

# UC Irvine

## UC Irvine Electronic Theses and Dissertations

### Title

The phenotypic investigation of mitochondria in cancer

### Permalink

<https://escholarship.org/uc/item/7dx3r48z>

### Author

Lefebvre, Austin

### Publication Date

2021

### Copyright Information

This work is made available under the terms of a Creative Commons Attribution License, available at <https://creativecommons.org/licenses/by/4.0/>

Peer reviewed|Thesis/dissertation

UNIVERSITY OF CALIFORNIA,  
IRVINE

The phenotypic investigation of mitochondria in cancer

DISSERTATION

submitted in partial satisfaction of the requirements  
for the degree of

DOCTOR OF PHILOSOPHY

in Biomedical Engineering

by

Austin Epiphane Yann Tung-Shan Lefebvre

Dissertation Committee:  
Associate Professor Michelle Digman, Chair  
Associate Professor Wendy Liu  
Associate Professor Devon Lawson  
Assistant Professor Daryl Preece



Chapter 3 © 2018 Springer Nature  
Portions of Chapter 4 © 2020 Springer Nature  
Chapter 5 © 2020 to all authors  
Chapter 6 © 2021 Springer Nature  
Portions of Chapter 4 and 7 © 2021 Alireza Sohrabi  
All other materials © 2021 Austin Epiphane Yann Tung-Shan Lefebvre

# DEDICATION

To all the parents, siblings, grandparents, children, and partners  
affected by their loved one's cancer

# TABLE OF CONTENTS

	Page
<b>LIST OF FIGURES</b>	<b>viii</b>
<b>ACKNOWLEDGMENTS</b>	<b>x</b>
<b>VITA</b>	<b>xii</b>
<b>ABSTRACT OF THE DISSERTATION</b>	<b>xxii</b>
<b>1 Historical context for phenotypic measurements of mitochondria in cancer</b>	<b>1</b>
1.1 Metabolic implications in cancer growth . . . . .	1
1.1.1 The Warburg effect . . . . .	1
1.1.2 A new hallmark of cancer . . . . .	4
1.2 Metabolic implications in cancer metastasis . . . . .	6
1.2.1 Metabolism of intravasation . . . . .	6
1.2.2 Metabolism of circulation . . . . .	9
1.2.3 Metabolism of colonization . . . . .	9
1.3 Existing methods for metabolism research . . . . .	11
1.3.1 Metabolomics and metabolic flux . . . . .	11
1.3.2 Immunostaining . . . . .	12
1.3.3 Cellular respiration . . . . .	13
1.4 Fluorescence lifetime imaging of cellular autofluorescence . . . . .	13
1.4.1 The brief history of fluorescence . . . . .	13
1.4.2 Cellular autofluorescence . . . . .	15
1.5 Mitochondrial morphology, motility, and dynamics in cellular function . . . . .	19
1.5.1 Mitochondrial organization in cellular health . . . . .	19
1.5.2 Problems with phenotypic measurements of mitochondria . . . . .	20
1.6 Summary . . . . .	21
<b>2 FLIM of NADH</b>	<b>22</b>
2.1 Fluorescence and its lifetime . . . . .	22
2.1.1 Fluorescence absorption and emission . . . . .	22
2.1.2 Fluorescence decay . . . . .	24
2.1.3 Measuring fluorescence lifetime . . . . .	25
2.1.4 Analyzing fluorescence lifetime . . . . .	29
2.2 NADH fluorescence . . . . .	33

2.2.1	NADH excitation and emission . . . . .	34
2.2.2	NADH conformations . . . . .	34
2.2.3	The phasor approach to NADH FLIM analysis . . . . .	35
2.3	Summary . . . . .	36
<b>3</b>	<b>Metabolic shifts of TNBC as a function of substrate density</b>	<b>38</b>
3.1	Abstract . . . . .	38
3.2	Introduction . . . . .	39
3.3	Results . . . . .	42
3.3.1	Collagen characterization measurements . . . . .	42
3.3.2	Triple-negative breast cancer cells shifts towards glycolytic signatures on denser collagen substrates . . . . .	44
3.3.3	Metabolism inhibition studies confirm that GLY and OXPHOS are modulated by collagen density . . . . .	48
3.4	Discussion . . . . .	49
3.5	Materials and Methods . . . . .	56
3.5.1	Cell culturing and transfections . . . . .	56
3.5.2	Collagen substrate monolayers . . . . .	56
3.5.3	Inhibition studies . . . . .	57
3.5.4	Characterization of collagen substrates . . . . .	58
3.5.5	Confocal and fluorescence lifetime imaging acquisition and analysis . . . . .	59
3.5.6	Statistical analysis . . . . .	60
3.6	Acknowledgements . . . . .	60
3.7	Author Contributions . . . . .	61
3.8	Summary . . . . .	61
<b>4</b>	<b>Metabolic shifts of invasive and metastatic cancer cells</b>	<b>62</b>
4.1	Substrate stiffness reprograms GBM metabolism . . . . .	62
4.1.1	Introduction . . . . .	63
4.1.2	Results . . . . .	65
4.1.3	Discussion . . . . .	67
4.1.4	Methods . . . . .	70
4.2	Transcriptional diversity and bioenergetic shift in human breast cancer metastasis revealed by single-cell RNA sequencing . . . . .	74
4.2.1	Introduction . . . . .	74
4.2.2	Results . . . . .	75
4.2.3	Discussion . . . . .	89
4.2.4	Methods . . . . .	92
4.2.5	Reporting Summary . . . . .	103
4.2.6	Data availability . . . . .	103
4.2.7	Code availability . . . . .	104
4.2.8	Acknowledgements . . . . .	104
4.2.9	Contributions . . . . .	105
4.3	Summary . . . . .	105

<b>5</b>	<b>Patient-derived xenograft culture-transplant system for investigation of human breast cancer metastasis</b>	<b>107</b>
5.1	Abstract . . . . .	107
5.2	Introduction . . . . .	108
5.3	Results . . . . .	110
5.3.1	Development of a 3D culture system for viable propagation of PDX cells as tumor spheres in vitro . . . . .	110
5.3.2	PDX tumor sphere cells maintain their global transcriptome program	114
5.3.3	PDX tumor sphere cells maintain tumorigenic potential and form spontaneous metastasis in vivo . . . . .	116
5.3.4	PDX tumor sphere cells can be genetically engineered for functional studies of metastasis in vivo . . . . .	120
5.3.5	PDX tumor sphere cells produce robust experimental metastasis in vivo	122
5.3.6	Validation of PDX culture-transplant system for authentic investigations of metastasis in vivo . . . . .	125
5.3.7	NME1 promotes lung metastasis from patient tumor cells . . . . .	127
5.4	Discussion . . . . .	132
5.5	Materials and Methods . . . . .	133
5.5.1	Harvesting and processing tumors into single cells . . . . .	133
5.5.2	Culturing PDX cells . . . . .	134
5.5.3	Generation of RNA sequencing dataset . . . . .	134
5.5.4	Processing and analysis of bulk RNA-seq data . . . . .	135
5.5.5	Mouse strains . . . . .	135
5.5.6	Orthotopic transplantation and i.c and i.v injection models of cultured PDX cells for modeling metastasis . . . . .	136
5.5.7	Analysis of primary tumors and metastasis in distal tissues . . . . .	136
5.5.8	Histology and pathological analysis . . . . .	137
5.5.9	Lentivirus transduction for genetic engineering of PDX cells . . . . .	137
5.5.10	Pharmacologic studies . . . . .	138
5.5.11	Cell death and viability assays . . . . .	138
5.5.12	NADH fluorescence lifetime imaging . . . . .	139
5.5.13	Phasor FLIM NADH fractional analysis . . . . .	139
5.5.14	Single cell analysis . . . . .	140
5.5.15	qPCR analysis . . . . .	140
5.5.16	Relapse-free survival analysis . . . . .	141
5.6	Funding . . . . .	141
5.7	Competing interests . . . . .	141
5.8	Author Contributions . . . . .	141
5.9	Acknowledgements . . . . .	142
5.10	Summary . . . . .	142
<b>6</b>	<b>Automated segmentation and tracking of mitochondria in live-cell time-lapse images</b>	<b>144</b>
6.1	Abstract . . . . .	144
6.2	Main . . . . .	145

6.3	Results . . . . .	148
6.3.1	Object-based segmentation of mitochondria . . . . .	148
6.3.2	Object-based tracking of mitochondria . . . . .	152
6.3.3	In silico validation of segmentation and tracking algorithms . . . . .	156
6.3.4	In vitro validation of segmentation and tracking algorithms . . . . .	160
6.3.5	Mitochondrial features may predict breast cancer subtype . . . . .	164
6.3.6	Metabolism of single mitochondria . . . . .	169
6.4	Discussion . . . . .	171
6.5	Methods . . . . .	173
6.5.1	Primary human mammary tissue dissociation and processing . . . . .	173
6.5.2	Collection and processing of PDX tumors . . . . .	174
6.5.3	Primary and PDX cell culture . . . . .	174
6.5.4	Three-dimensional culture of cell lines . . . . .	175
6.5.5	Two-dimensional culture of cell lines . . . . .	175
6.5.6	TMRM studies . . . . .	175
6.5.7	Nocodazole studies . . . . .	176
6.5.8	Fission and fusion studies . . . . .	176
6.5.9	Mitochondria and fluorescence lifetime imaging . . . . .	176
6.5.10	Statistical testing . . . . .	177
6.6	Reporting Summary . . . . .	177
6.7	Data availability . . . . .	178
6.8	Code availability . . . . .	178
6.9	Summary . . . . .	178
<b>7</b>	<b>Mitochondrial and metabolic phenotypes as a function of the cellular cytoskeleton</b>	<b>180</b>
7.1	Introduction . . . . .	180
7.2	Results . . . . .	182
7.2.1	Contractility inhibition on mitochondrial morphology and motility in breast cells . . . . .	182
7.2.2	Cytoskeletal effects on mitochondrial morphology and motility in breast cells . . . . .	184
7.2.3	Metabolic shifts following contractility inhibition in breast cells . . . . .	186
7.2.4	Integrins and CD44 directly mediate the metabolic switch in GBM cells . . . . .	188
7.2.5	ECM stiffness and CD44 alter mitochondrial morphology and motility . . . . .	190
7.3	Discussion . . . . .	192
7.4	Materials and Methods . . . . .	193
7.4.1	Cell culture . . . . .	193
7.4.2	Fluorescence imaging of mitochondria . . . . .	194
7.4.3	FLIM of NADH . . . . .	194
7.4.4	GBM receptor inhibition . . . . .	195
7.4.5	Statistical analysis . . . . .	195
7.5	Summary . . . . .	196

<b>8</b>	<b>Conclusions</b>	<b>197</b>
8.1	Solving problems . . . . .	197
8.2	Making new ones . . . . .	200
	<b>Bibliography</b>	<b>202</b>
	<b>Appendix A</b> NADH fraction calculation code	<b>226</b>
	<b>Appendix B</b> Collagen density modulates triple-negative breast cancer cell metabolism through adhesion-mediated contractility: Supplementary ma- terials	<b>228</b>
	<b>Appendix C</b> Mitometer manual	<b>235</b>
	<b>Appendix D</b> Automated mitochondria segmentation and tracking in live-cell time-lapse images: Supplementary materials	<b>263</b>

# LIST OF FIGURES

	Page
1.1 Schematic representation of the differences between oxidative phosphorylation, anaerobic glycolysis, and aerobic glycolysis (Warburg effect). . . . .	3
1.2 The Emerging Hallmarks of Cancer Metabolism. . . . .	5
1.3 Patterns of Metastatic Spread of Solid Tumors. . . . .	7
1.4 Reversibility of EMT during metastatic colonization. . . . .	8
1.5 Discrepancy in metabolic studies of cancer metastasis. . . . .	11
1.6 Stokes shift. . . . .	14
1.7 Jablonski diagram. . . . .	15
1.8 TCSPC FLIM data representation of the FRET standard. . . . .	16
1.9 Limiting conformations for NADH. . . . .	18
2.1 The Becquerel phosphoroscope (1873-1874) . . . . .	26
3.1 Quantification of collagen substrates . . . . .	43
3.2 Metabolic indexes of breast cells . . . . .	45
3.3 Metabolic indexes of other cancer cell lines . . . . .	47
3.4 MDA-MB-231 and MCF-10A metabolic indexes when treated with metabolic inhibitors. . . . .	50
4.1 Bulk RNA-sequencing results of GBM spheroids represented as heatmaps . .	66
4.2 FLIM of NADH of soft and stiff HA-encapsulated GBM spheroids . . . . .	67
4.3 GBM spheroids alter invasion and pH in HA gels . . . . .	68
4.4 NADH FLIM comparison of a GBM spheroid and GBM migratory population in soft hydrogels . . . . .	69
4.5 Single-cell RNA sequencing of micrometastatic and primary tumour cells. . .	77
4.6 Micrometastatic cells display a distinct transcriptome program. . . . .	78
4.7 Prognostic value of micrometastasis- associated genes in basal-like breast cancer patients. . . . .	80
4.8 Micrometastatic cells display increased mitochondrial OXPHOS. . . . .	82
4.9 Gene scoring identifies OXPHOS and glycolysis as top metabolic pathways differentially expressed between micrometastases and primary tumour cells. .	84
4.10 Oxidative phosphorylation is critical for lung metastasis. . . . .	86
4.11 Oligomycin treatment inhibits OXPHOS in MDA-MB-231 and 4T1-GFP cells. .	87
4.12 Model for metabolic shift associated with metastatic seeding in TNBC. . . .	90



5.1	Comparison of 3D culture methods for viable propagation of PDX tumor cells in vitro . . . . .	111
5.2	Comparison of PDX cell culture conditions . . . . .	113
5.3	PDX tumor sphere cells maintain their global transcriptome programme . . .	115
5.4	PDX tumor sphere cells maintain tumorigenic potential and form spontaneous metastasis in vivo . . . . .	117
5.5	Analysis of primary tumors and spontaneous metastases generated by cultured PDX cells . . . . .	118
5.6	PDX tumor sphere cells can be genetically engineered for functional studies of metastasis in vivo . . . . .	121
5.7	PDX tumor sphere cells produce robust experimental metastasis in vivo . . .	123
5.8	HCI-002 tumor spheres produce experimental metastasis in vivo . . . . .	124
5.9	Validation of PDX culture-transplant system for authentic investigations of metastasis in vivo . . . . .	126
5.10	Cytotoxicity and cell death analysis of PDX cells post drug treatment. . . .	128
5.11	NME1 promotes lung metastasis from patient tumor cells . . . . .	130
5.12	NME1 overexpression in cultured PDX cells and its relevance in patient breast cancer prognosis. . . . .	131
6.1	Object-based segmentation of individual mitochondria from fluorescence images.	149
6.2	Diffuse background removal surrounding objects of complex shapes. . . . .	150
6.3	Parameter exploration for choosing low-pass filter and threshold parameters.	151
6.4	Tracking of mitochondria via global minimization of morphological and displacement differences. . . . .	153
6.5	Flowchart for morphology and displacement-based global cost minimization tracking. . . . .	154
6.6	Flowchart for gap-closing scheme. . . . .	157
6.7	In silico validation of mitochondria segmentation and tracking algorithms. . .	159
6.8	In vitro validation of mitochondria segmentation and tracking algorithms. . .	162
6.9	Live-cell time lapse images with added noise. . . . .	163
6.10	Motility and morphology differences in mitochondria of normal breast epithelial cells and breast cancer cells. . . . .	165
6.11	Three-dimensional spheroid cultures. . . . .	166
6.12	Cancer-specific metabolic heterogeneity in single mitochondria. . . . .	170
7.1	Contractility inhibition on mitochondrial morphology and motility. . . . .	183
7.2	Cytoskeletal effects on mitochondrial morphology and motility. . . . .	185
7.3	Metabolic shifts following contractility inhibition in breast cells. . . . .	187
7.4	Integrins and CD44 directly mediate the metabolic switch in GBM cells. . .	189
7.5	ECM stiffness and CD44 alter mitochondrial morphology and motility. . . .	191

# ACKNOWLEDGMENTS

To my friends, family, and peers that have been with me through it all, you mean more to me than you can ever know.

To mama, thank you for giving me the love, the strength, the courage, and the independence I needed to get to where I am now, you have been my biggest role model in all aspects of my life. To papa, thank you for the endless love and support you have given me throughout the years. Your weekly phone calls always give me something to look forward to. To Marin and Manon, the best and most amazing siblings anyone could ask for, thank you for showing me what it means to stand up for what you believe in and to be 100% yourself, 100% of the time. You are two of the most supportive and exceptional people I know. To Y-Po and Y-Gong, thank you for building this amazing family, and showing me what it means to always put family and loved-ones first. To Jojo, auntie CC, Ian, Eric, and Greg, thank you for always being there for me, and supporting me through everything. À Amère et Apère, et la famille en France, merci pour tout l'amour et le soutien que vous m'avez donnés, même de l'autre côté du monde.

To Edward, my brother, thank you for dealing with me since 4<sup>th</sup> grade, throughout all my weird stages in life, and being the loudest and most loving hype man I've ever had.

To my Seattle crew, Mike, Jacob, Pierre, Ena, Nina, Meera, and Destiny, thank you for giving me some of the best memories that have kept me going through grad school, from tomato sauce, to sketchy airplane rides, to believing in life after love, you have gotten me through it all. To Julie, thank you for sticking by me since 1<sup>st</sup> grade and allowing me to truly unleash my weird self even to this day. To Kevin, thank you for always being the most supportive big, you've made a man out of me. To Jeremy, I probably would've dropped out without our surfy surf seshes, copious grilling, and beer fridays, and for all of that, I thank you. To my best roommates, Miraj, Jake, Ryan, Franco, and Param, thank you for being my biggest support group throughout my years in school, and for not kicking me out. To the Butter Baes, Ryan, Ben, Dat, and Chris, thank you for the weekly dinners and board game nights, it always gave me something to look forward to. To the OAC, Alfonso, Angie, and Evelia, thank you for the drinks, the talks, and the oysters that have gotten me through grad school, may we never get food poisoning again. Thank you to my teammates and rivals Balam, Lorenzo, Valeria, and Francesco for keeping me on my toes, may we never truly understand the rules of volleyball.

Thank you to Kritter cat for watching over me while I write this dissertation, and being a constant source of much needed darkness in my life.

Last but not least, thank you to Evelia, your love, support, and dance skills have helped me outlast the pandemic (so far) and have given me the motivation and clarity to make it to the end of graduate school. Thank you for being my guiding light.

This dissertation would also never have been possible without the endless support of my mentors, and funding sources.

First and foremost, thank you to my committee chair, Dr. Michelle Digman. Your mentorship taught me independence and gave me the freedom to grow and to thrive. Your kindness, patience, and the respect you have earned from all whom you interact with has taught me the importance of building real connections inside and outside of academia. Thank you especially for supporting my constant crazy ideas on Mitometer and helping to make them a reality. Thank you also to my other committee members, Dr. Wendy Liu, Dr. Devon Lawson, and Dr. Daryl Preece, for the support, motivation, and wonderful ideas you all have contributed towards my research. Thank you also to Dr. Enrico Gratton, for helping me put countless experiments in a bigger context, and for always giving me your time when I need to ask something.

To the LFD crew, thank you for the endless support, guidance, and occasional much needed harsh criticism. A special thank you to Francesco, who helped keep me sane throughout graduate school, from surfing, to volleyball, to pizza-making, to editing my papers, you have kept me going. Thank you Milka for pushing my introverted self to open up around the lab. Thank you to the youngsters, Balam, Song, and Karen, for keeping me from feeling like the 90 year old that I usually feel like. Thank you Suman for hundreds of interesting lunch conversations. Thank you Michael and Andrew for teaching me the ropes during my first year. Thank you Lorenzo for all your help in and out of lab. Thank you Giulia for the mental and gastronomical support you've given me, and for bringing Dede around. Thank you Alex, for the coding and microscopy support, and for reminding me I'm terrible at chess. Thank you Simon, for dealing with my RBF, helping me with anything in lab, and being a great desk neighbor.

Thank you to my collaborators, whose work has built a large portion of this dissertation. Dennis, I am thankful for our chance encounter (thanks to Jeremy) in the gym, may our gains never fade.

Thank you to my many undergraduates (or ducklings, as 3rd floor NS2 folks like to call them), who have helped make so much of this work a reality and have gone on to do bigger and better things. Thank you especially to my first undergraduates, Freddie and Elysia, for dealing with my crazy 2<sup>nd</sup> year weekly idea-changes that mostly never went anywhere.

I would like to express my sincere appreciation to my funding sources: the National Science Foundation's Graduate Research Fellowship Program, which helped fund my tuition and stipend for 3 years (DGE-1839285), and to the UC Irvine Dean's Dissertation Fellowship, which helped fund the last few months of my graduate career.

Thank you also to Springer Nature, the publisher of all the papers I have authored and co-authored within this dissertation, and to their amazing team of editors.

# VITA

Austin Epiphane Yann Tung-Shan Lefebvre

## EDUCATION

<b>Ph.D. in Biomedical Engineering</b> University of California, Irvine	<b>2021</b> <i>Irvine, California</i>
<b>M.S. in Biomedical Engineering</b> University of California, Irvine	<b>2020</b> <i>Irvine, California</i>
<b>B.S. in Biomedical Engineering, Magna Cum Laude</b> University of California, San Diego	<b>2017</b> <i>San Diego, California</i>

## RESEARCH EXPERIENCE

<b>Laboratory for Fluorescence Dynamics</b> University of California, Irvine	<b>2017–2021</b> <i>Irvine, California</i>
<b>Metallo Systems Biology Lab</b> University of California, San Diego	<b>2014–2017</b> <i>San Diego, California</i>
<b>Kim Multiscale Biofab. and Tissue Engineering Lab</b> University of Washington	<b>2013–2014</b> <i>Seattle, Washington</i>

## TEACHING EXPERIENCE

<b>Team Leader, USIBR</b> University of California, Irvine	<b>2018–2019</b> <i>Irvine, California</i>
<b>Team Leader, COSMOS</b> University of California, Irvine	<b>2018–2019</b> <i>Irvine, California</i>
<b>Teaching Assistant, BME 50B</b> University of California, Irvine	<b>2018</b> <i>Irvine, California</i>
<b>Teacher, Science and Engineering Night</b> Santiago K-12 School	<b>2017</b> <i>Irvine, California</i>

## COMMUNITY ENGAGEMENT

<b>President, Graduate Association of BME Students</b> University of California, Irvine	<b>2019–2021</b> <i>Irvine, California</i>
<b>Vice President, Graduate Association of BME Students</b> University of California, Irvine	<b>2018–2019</b> <i>Irvine, California</i>
<b>Founder and President, BME Journal Club</b> University of California, Irvine	<b>2017–2018</b> <i>Irvine, California</i>
<b>Publicist Chair, Engineering World Health</b> University of California, San Diego	<b>2015–2016</b> <i>San Diego, California</i>
<b>Media and Technology Chair, BMES</b> University of California, San Diego	<b>2014–2016</b> <i>San Diego, California</i>
<b>Assistant Projects Director, Engineers Without Borders</b> University of California, San Diego	<b>2013–2014</b> <i>San Diego, California</i>
<b>Booth Volunteer, Life Science Research Weekend</b> University of Washington	<b>2013</b> <i>Seattle, Washington</i>

## PUBLICATIONS

- Automated mitochondria segmentation and tracking in live-cell time-lapse images** 2021  
Nature Methods, 18, 1091–1102
- Patient-derived xenograft culture-transplant system for investigation of human breast cancer metastasis.** 2021  
Communications Biology, In Press
- Transcriptional diversity and bioenergetic shift in human breast cancer metastasis revealed by single-cell RNA sequencing.** 2020  
Nature Cell Biology, 22 (3), 310-320
- Patient-derived xenograft culture-transplant system for investigation of human breast cancer metastasis.** 2020  
bioRxiv
- Tracking Motility and Morphology of Individual Mitochondria Reveals Large Heterogeneities in Breast Cancer Subtypes.** 2021  
Biophysical Journal, 120 (3), 194a
- Non-destructively Analyzing the Metabolic Dysregulation of Invasive Cancer Cells on an Intracellular Scale.** 2020  
Biophysical Journal 118 (3), 307a
- A Non-Invasive Metabolic Investigation of Breast Cancer Invasion.** 2019  
Biophysical Journal 116 (3), 550a
- The Phasor FLIM Analysis Monitors Metabolic Changes at the Leading Edge in Response to Rac Photo-Activation and Mitochondrial Transport in MDA MB231 Cells.** 2019  
Biophysical Journal 116 (3), 442a

**Cancer Cells' Situational Awareness: The  
Mechanosensing Metabolic Shift of Invasive Breast  
Cells.** 2018

Molecular Biology of the Cell, 29 (26)

**Collagen density modulates triple-negative breast can-  
cer cell metabolism through adhesion-mediated contrac-  
tility.** 2018

Scientific Reports, 8 (1), 1-11

**LKB1 Promotes Metabolic Flexibility in Response to  
Energy Stress.** 2017

Metabolic Engineering, 43, 208-217

## ORAL PRESENTATIONS

- Tracking motility and morphology of individual mitochondria reveals large heterogeneities in breast cancer subtypes.** 2021  
Biophysical Society Annual Meeting, Virtual
- Measuring metabolic alterations on a single-mitochondrion level in living cells.** 2020  
NIH CSBC/PS-ON Annual Meeting, Virtual
- Measuring metabolism of single mitochondria in living cells.** 2020  
Center for Advanced Design and Manufacturing of Integrated Microfluidics (CADMIM)  
International Advisory Board Meeting, Virtual
- Analyzing metabolism of live single mitochondria.** 2020  
NIH CSBC/PS-ON Junior Investigators Meeting, Virtual
- Analyzing the Metabolism of Live Tissues and Cells in Breast Cancer** 2020  
Breast Disease Oriented Team, Chao Family Comprehensive Cancer Center, Irvine, CA
- Non-Destructively Analyzing the Metabolic Dysregulation of Invasive Cancer Cells on an Intracellular Scale.** 2020  
Biophysical Society Annual Meeting, San Diego, CA
- Embryologic** 2019  
New Venture Competition Life Sciences Pitch Competition, Irvine, CA
- Embryologic** 2019  
New Venture Competition Wayfinder Pitch Competition, Irvine, CA
- Actin Mediated Shifts of Mitochondrial Function in TNBC Cells.** 2019  
Mechanobiology Symposium, Irvine, CA
- Establishing a link between mitochondrial dynamics and metabolic reprogramming.** 2019  
NIH CSBC/PS-ON Junior Investigators Meeting, Bethesda, MD



<b>Metastasis: The Finger of Death.</b>	<b>2018</b>
Associated Graduate Students Symposium, Irvine, CA	
<b>EEG Powered Motor Intent Prediction for Prosthetic Limb Control.</b>	<b>2017</b>
UCSD Bioengineering Senior Design Final Presentation, San Diego, CA	
<b>Biosignal Prosthetics: The Future of Brain Powered Prosthetics.</b>	<b>2017</b>
NSF Innovation Corps Phase II, San Diego, CA	
<b>Biosignal Prosthetics: The Future of Brain Powered Prosthetics.</b>	<b>2016</b>
NSF Innovation Corps Phase I, San Diego, CA	
<b>The Use of EEG Controlled Prosthetics to Translate Motor Intent.</b>	<b>2016</b>
BMES-UC San Diego xSEED Pitch Competition, San Diego, CA	

## POSTER PRESENTATIONS

- Tracking mitochondria reveals metabolic and dynamic heterogeneity in breast cancers.** 2021  
AAAS Annual Meeting, Virtual
- Metabolic and dynamic heterogeneity of live single-cell mitochondria revealed via the phasor approach to FLIM.** 2020  
American Society for Cell Biology (ASCB—EMBO) Annual Meeting, Virtual
- Measuring metabolic alterations on a single-mitochondrion level in living cells.** 2020  
NIH CSBC/PS-ON Annual Meeting, Virtual
- Analyzing metabolism of live single mitochondria.** 2020  
NIH CSBC/PS-ON Junior Investigators Meeting, Virtual
- Non-Destructively Analyzing the Metabolic Dysregulation of Invasive Cancer Cells on an Intracellular Scale.** 2020  
Biophysical Society Annual Meeting, San Diego, CA
- The phasor FLIM analysis reveals metabolic modulation and cell migration through adhesion-mediated contractility.** 2020  
SPIE Photonics West, San Francisco, CA
- A Non-Invasive Metabolic Investigation of Breast Cancer Invasion** 2019  
BMES-UCI Student Symposium, Irvine, CA
- Inhibition of Mitochondrial Recruitment and Metabolic Shift in Metastatic Breast Cancer Cells** 2019  
BMES Annual Meeting, Philadelphia, PA
- Inhibition of Mitochondrial Recruitment and Metabolic Shift in Metastatic Breast Cancer Cells** 2019  
CSBC / PS-ON Junior Investigators Meeting, Bethesda, MD

<b>A Non-Invasive Metabolic Investigation of Breast Cancer Invasion</b> UC Irvine BME Visitation Day, Irvine, CA	<b>2019</b>
<b>A Non-Invasive Metabolic Investigation of Breast Cancer Invasion</b> Bench to Bedside Symposium, Irvine, CA	<b>2019</b>
<b>A Non-Invasive Metabolic Investigation of Breast Cancer Invasion</b> Biophysical Society Annual Meeting, Baltimore, MD	<b>2019</b>
<b>The Phasor FLIM Analysis Monitors Metabolic Changes at the Leading Edge in Response to Rac Photo-Activation and Mitochondrial Transport in MDA-MB-231 Cells</b> Biophysical Society Annual Meeting, Baltimore, MD	<b>2019</b>
<b>Cancer Cells' Situational Awareness: The Mechanosensing Metabolic Shift of Invasive Breast Cells.</b> ASCB — EMBO, San Diego, CA	<b>2018</b>
<b>Spectral Phasor Analysis Discriminates Changes in Fluidity of Invasive Tumor Cells</b> Synthetic and Chemical Biology Club, Irvine, CA	<b>2018</b>
<b>Spectral Phasor Analysis Discriminates Changes in Fluidity of Invasive Tumor Cells</b> UCI Campus-Wide Symposium on Basic Cancer Research, Irvine, CA	<b>2018</b>
<b>EEG Powered Motor Intent Prediction for Prosthetic Limb Control</b> Bioengineering Day, UC San Diego, San Diego, CA	<b>2017</b>
<b>Injectable Myocardial Matrix-Graphene Composite Hydrogels for Functional Cardiac Tissue Engineering</b> Institute for Stem Cell and Regenerative Medicine Symposium, Seattle, WA	<b>2014</b>

## **HONORS AND AWARDS**

<b>Graduate Dean's Dissertation Fellow</b> University of California, Irvine	<b>2021</b>
<b>1<sup>st</sup> Place, Art in Science</b> University of California, Irvine	<b>2021</b>
<b>2<sup>nd</sup> Place, Poster: Graduate Student, Cell Biology</b> AAAS/Science Annual Meeting	<b>2021</b>
<b>Awardee: Program for Excellence in Science</b> AAAS/Science Annual Meeting	<b>2020</b>
<b>Nominee: Microsoft Ph.D. Fellowship</b> University of California, Irvine	<b>2020</b>
<b>Biomedical Engineering Graduate Student of the Year</b> University of California, Irvine	<b>2019</b>
<b>New Venture Competition, Life Sciences 2<sup>nd</sup> Place</b> University of California, Irvine	<b>2019</b>
<b>New Venture Competition, Win the Future 2<sup>nd</sup> Place</b> University of California, Irvine	<b>2019</b>
<b>Biophysical Society Travel Award Recipient</b> Biophysical Society Annual Meeting	<b>2018</b>
<b>NSF GRFP Awardee</b> National Science Foundation	<b>2018</b>
<b>Magna Cum Laude</b> University of California, San Diego	<b>2017</b>
<b>NSF GRFP Honorable Mention</b> National Science Foundation	<b>2017</b>
<b>Stewart Society Member</b> University of California, San Diego	<b>2017</b>

<b>Phi Beta Kappa Honor Society Member</b> University of California, San Diego	<b>2016</b>
<b>Caledonian Society Member</b> University of California, San Diego	<b>2015</b>
<b>Purple and Gold Scholarship</b> University of Washington	<b>2013</b>

# ABSTRACT OF THE DISSERTATION

The phenotypic investigation of mitochondria in cancer

By

Austin Epiphane Yann Tung-Shan Lefebvre

Doctor of Philosophy in Biomedical Engineering

University of California, Irvine, 2021

Associate Professor Michelle Digman, Chair

Metastasis remains the leading cause of cancer mortality but its mitochondrial dysregulation - from its morphology and motility to its metabolic influence - in modulating cancer's progression is poorly understood. This dissertation describes the development and use of complex microphysiological culture systems to place cancer in its proper environmental context for mitochondrial phenotypic discoveries. FLIM of NADH is used to probe the metabolic differences between invasive and non- or less-invasive cancer cells and elucidate potential invasion-specific therapeutic targets. This dissertation also introduces Mitometer, an algorithm for fast, unbiased, and automated segmentation and tracking of mitochondria in live-cell two-dimensional and three-dimensional time-lapse images. Mitometer finds that mitochondria of triple-negative breast cancer cells are faster, more directional, and more elongated than those in their receptor-positive counterparts. Furthermore, Mitometer shows that mitochondrial motility and morphology in breast cancer, but not in normal breast epithelia, correlate with metabolic activity. Mitometer is then applied to investigate cellular contractility in the influence of mitochondrial phenotype. The goal of this dissertation as a whole is to accentuate the importance of creating new assays and techniques with the impact of context and translatability in mind.

# Chapter 1

## Historical context for phenotypic measurements of mitochondria in cancer

### 1.1 Metabolic implications in cancer growth

#### 1.1.1 The Warburg effect

Otto Warburg's seminal 1925 paper "The metabolism of carcinoma cells" provides as a noteworthy starting point for the study of cancer metabolism [[Warburg \(1925\)](#)]. He begins by detailing sea urchin egg fertilization, an event with rapid cell proliferation, displaying a six-fold increase in respiration as compared to its resting state. Warburg claims a similar upregulation in respiration should logically be expected in a carcinoma, where there is also a high activity of cell proliferation, compared to resting epithelium. Instead, the opposite was found to be true. When comparing the respiration (as measured in Ringer's solution at body temperature) of kidney and liver tumor sections to those of non-tumorigenic sections, the respiration was significantly reduced.

Despite many attempts at increasing the respiration in these tumor sections via modification of amino acids, fatty acids, and glucose in the media, the results were consistent. Interestingly, a suspicious amount of lactic acid was appearing in the Ringer's solution, and it was concluded that glycolysis was being modified, "the velocity of which is greater in growing tissues than in resting tissues." Even more importantly, not only did the rate of glycolysis increase, but it remained elevated even in the presence of oxygen, a process termed aerobic glycolysis, which we now call the Warburg effect (Fig. 1.1). He ends the paper contemplating reasons for this metabolic switch in carcinomas, vaguely hypothesizing on mitochondrial dysfunction as the cause, though he was cautious to limit his conclusions.

Only later in 1956 did Warburg elaborate on this idea in his most well-known work, "On the origin of cancer cells," where he states as fact the emergence of cancer as a cause of the "injuring of respiration" and the "increase of fermentation" [Warburg (1956)]. Since the acceptance of DNA mutations as a cause for cancer would not become generally accepted until the mid-1970's [Nowell (1976)], and the effects of ionizing radiation on DNA damage until even later, Warburg goes on to postulate about x-ray's harmful effects on cancer (and non-tumorigenic) cells:

"When one irradiates a tissue that contains cancer cells as well as normal cells, the respiration of the cancer cells, already too small, will decline further. If the respiration falls below a certain minimum that the cells need unconditionally, despite their increased fermentation, they die; whereas the normal cells, where respiration may be harmed by the same amount, will survive because, with a greater initial respiration, they will still possess a higher residual respiration after irradiation... But still further: the descendants of the surviving normal cells may in the course of the latent period compensate the respiration decrease by fermentation increase and, thence, become cancer cells."

Although this theory of x-rays as a respiration-based forming agent of cancer cells did not hold, nor did his theory of a defective oxidative metabolism as a necessary cause of tumor



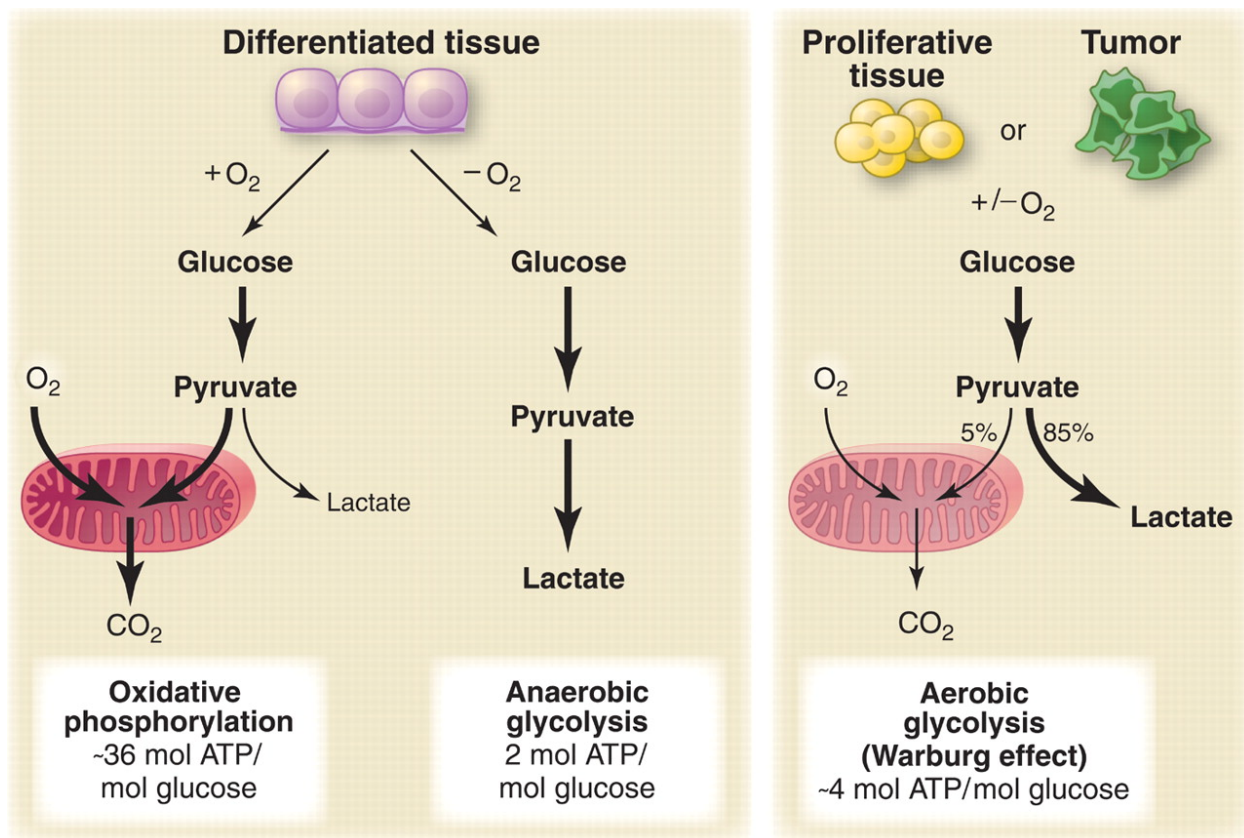


Figure 1.1: Schematic representation of the differences between oxidative phosphorylation, anaerobic glycolysis, and aerobic glycolysis (Warburg effect). In the presence of oxygen, nonproliferating (differentiated) tissues first metabolize glucose to pyruvate via glycolysis and then completely oxidize most of that pyruvate in the mitochondria to CO<sub>2</sub> during the process of oxidative phosphorylation. Because oxygen is required as the final electron acceptor to completely oxidize the glucose, oxygen is essential for this process. When oxygen is limiting, cells can redirect the pyruvate generated by glycolysis away from mitochondrial oxidative phosphorylation by generating lactate (anaerobic glycolysis). This generation of lactate during anaerobic glycolysis allows glycolysis to continue (by cycling NADH back to NAD<sup>+</sup>), but results in minimal ATP production when compared with oxidative phosphorylation. Warburg observed that cancer cells tend to convert most glucose to lactate regardless of whether oxygen is present (aerobic glycolysis). This property is shared by normal proliferative tissues. Mitochondria remain functional and some oxidative phosphorylation continues in both cancer cells and normal proliferating cells. Nevertheless, aerobic glycolysis is less efficient than oxidative phosphorylation for generating ATP. In proliferating cells, ~10% of the glucose is diverted into biosynthetic pathways upstream of pyruvate production. From [Heiden et al. (2009)]. Reprinted with permission from AAAS.

formation and proliferation [Moreno-Sanchez et al. (2007)], his quantitatively formed conclusions on the metabolic switch from oxidative phosphorylation to glycolysis were thoroughly corroborated in the succeeding decades.

### 1.1.2 A new hallmark of cancer

With conflicting findings, the cause of the Warburg effect was in question for several decades. A switch to glycolysis from the more efficient ATP production of oxidative phosphorylation seems counterintuitive, and reasonable causes for this switch would not start to be quantitatively explained until the end of the 20<sup>th</sup> century. The first reason for this switch is that, though less ATP is produced per mole of glucose via glycolysis, the glycolytic flux of these proliferative cells is upregulated, and thus the rate of ATP production is remarkably increased [Guppy et al. (1993); Pfeiffer et al. (2001)]. Additionally, this increased accessibility of glucose provides biosynthetic intermediates for these cells, allowing them the ingredients necessary for their proliferation [Vander Heiden et al. (2009)]. These alterations in energy metabolism were deemed so widespread that Hanahan and Weinberg declared it an emerging hallmark of cancer in their updated review, stating that the Warburg effect is another cancerous phenotype programmed by proliferation-inducing oncogenes [Hanahan and Weinberg (2011)].

Following its classification as an emerging cancer hallmark and the advancement and increase in accessibility of biochemical and biomolecular tools, the understanding of the biological basis and the importance of tumor-associated metabolic alterations exponentially increased in the following decade. Consequently, Pavlova and Thompson assigned cancer metabolism its own six hallmarks: “(1) deregulated uptake of glucose and amino acids, (2) use of opportunistic modes of nutrient acquisition, (3) use of glycolysis/TCA cycle intermediates for biosynthesis and NADPH production, (4) increased demand for nitrogen, (5) alterations in metabolite-driven gene regulation, and (6) metabolic interactions with the microenvironment” (Fig. 1.2) [Pavlova and Thompson (2016)]. Though these metabolic al-

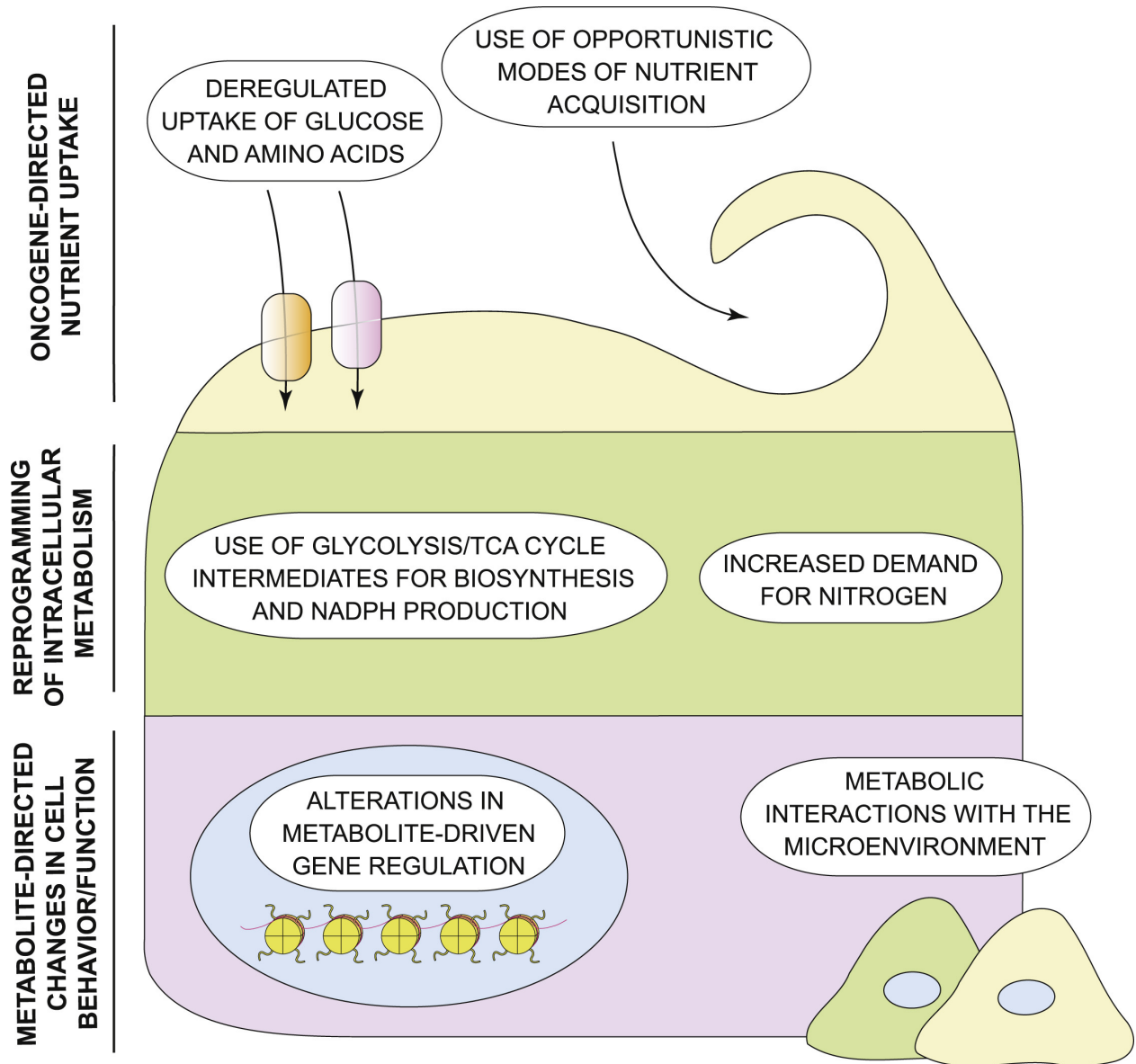


Figure 1.2: The Emerging Hallmarks of Cancer Metabolism. Cancer cells accumulate metabolic alterations that allow them to gain access to conventional nutrient sources as well as to unconventional nutrient sources, utilize these nutrients toward the creation of new biomass to sustain deregulated proliferation, and take advantage of the ability of select metabolites to affect the fate of cancer cells themselves as well as a variety of normal cell types within the tumor microenvironment. Three layers of cell-metabolite interaction are depicted, all of which become reprogrammed in cancer. On top are the adaptations that involve nutrient uptake (Hallmarks 1 and 2), followed by alterations to intracellular metabolic pathways (Hallmarks 3 and 4) in the middle. Finally, long-ranging effects of metabolic reprogramming on the cancer cell itself (Hallmark 5), as well as on other cells within its microenvironment (Hallmark 6), are depicted at the bottom. Reprinted from *Cell Metabolism*, Volume 23, Issue 1, Natalya N. Pavlova and Craig B. Thompson, The Emerging Hallmarks of Cancer Metabolism, Pages 27-47, 2016, with permission from Elsevier.

terations are becoming well understood, and increasingly therapeutically target-able, a large majority of these studies and pharmaceuticals revolve around cancer cells of primary tumor sites rather than secondary sites of metastatic tumor cells.

## 1.2 Metabolic implications in cancer metastasis

The research into specifically metastatic tumorigenic cell populations is only just beginning to emerge and already a number of studies have unveiled important insights into metastatic metabolic changes through the multistep invasion and colonization process. A recent but promising theory posits that the extent of a tumor’s metabolic plasticity determines its success at seeding, adapting to, and growing in “hostile environments,” i.e. the metastatic sites [Lehuédé et al. (2016)]. Indeed, a recent review proposes that tumor cells acquire specific metabolic signatures to adapt and thrive at specific metastatic sites, which dictate where they will form secondary tumors, and could help explain why certain primary tumors metastasize to specific organs (Fig. 1.3) [Obenauf and Massagué (2015); Schild et al. (2018)]. This metastatic evolution of metabolism begins at the intravasation process when cancer cells detach from their primary tumor site.

### 1.2.1 Metabolism of intravasation

This intravasation requires the revival of an embryonic process known as epithelial-to-mesenchymal transition (EMT), indicated by a large phenotypic shift and a high degree of cell plasticity (Fig. 1.4) [Nieto (2013)]. Studies around the metabolic adaptation of cells undergoing EMT seem to suggest a Warburg effect during this stage, allowing cells to avoid anchorage-dependent anoikis as they detach from the primary site [Dong et al. (2013); Kamarajugadda et al. (2012); Liu et al. (2016); Lu et al. (2015)]. It is evident, however, that these cells must evolve more metabolic remodeling after the intravasation process, as only 0.1% of cancer cells remain viable in circulation, and of those survivors, less than 0.01%

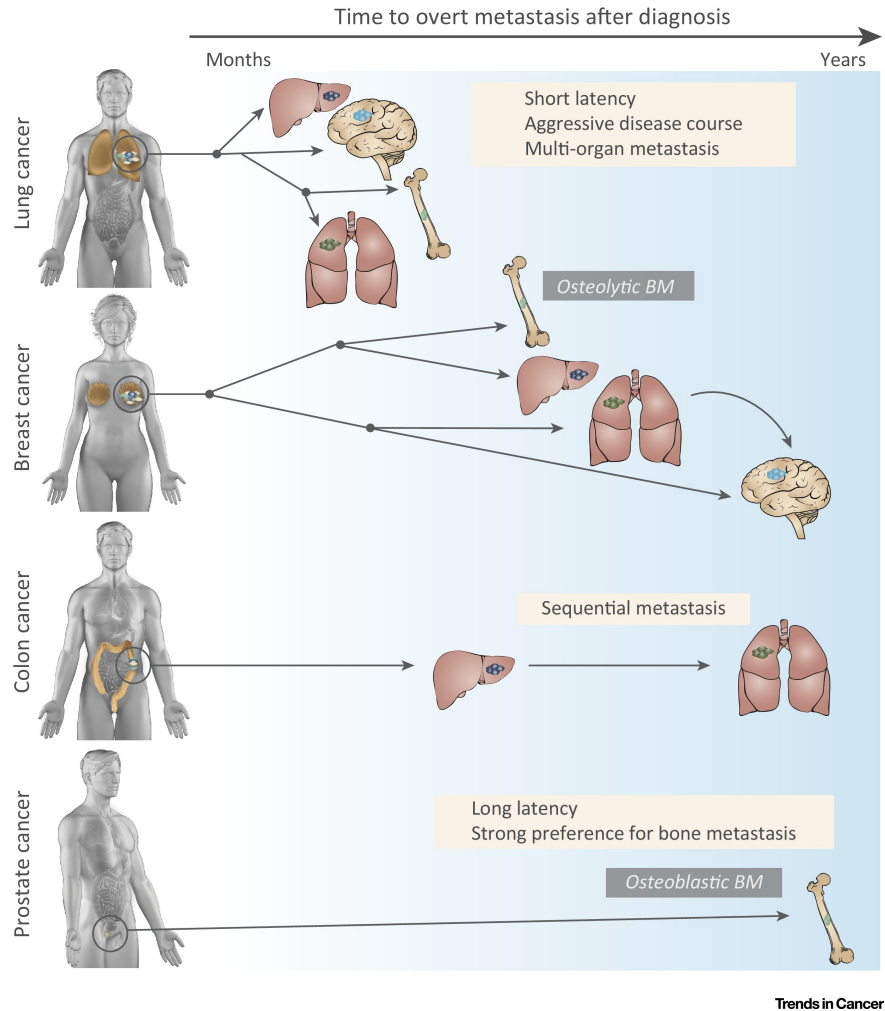


Figure 1.3: Patterns of Metastatic Spread of Solid Tumors. Different cancer types exhibit remarkable variability in their metastatic course, reflected in the length of the latency period (months to years), the organs affected (most commonly the liver, lung, bone, and brain) and the type of metastasis (e.g., osteolytic or osteoblastic bone metastasis). Latency period (denoted by the arrow on top of the figure – left: months, right: years after diagnosis): lung cancer metastasis typically occurs within months after initial diagnosis, whereas prostate cancer and some subtypes of breast cancer can produce distant relapse up to decades after initial diagnosis. Lung cancer is the main contributor to brain metastasis, whereas it is a late occurrence in breast cancer. Organ pattern (the most-frequently affected organ is located on the top of each cancer type): lung and breast cancers metastasize to different organs (with a different propensity), whereas colon cancer most frequently metastasizes to liver, and from established liver metastasis secondarily to lung. Prostate cancer typically although not exclusively metastasizes to bone. Different cancer types also vary in the type of metastatic lesions they induce, well illustrated by the development of osteolytic bone metastasis in breast and lung cancer, and osteoblastic bone metastasis in prostate cancer. Abbreviation: BM, bone metastasis. Reprinted from Trends in Cancer, volume 1, issue 1, Anna C. Obenauf and Joan Massagué, Surviving at a Distance: Organ-Specific Metastasis, Pages 76-91, Copyright 2015, with permission from Elsevier.



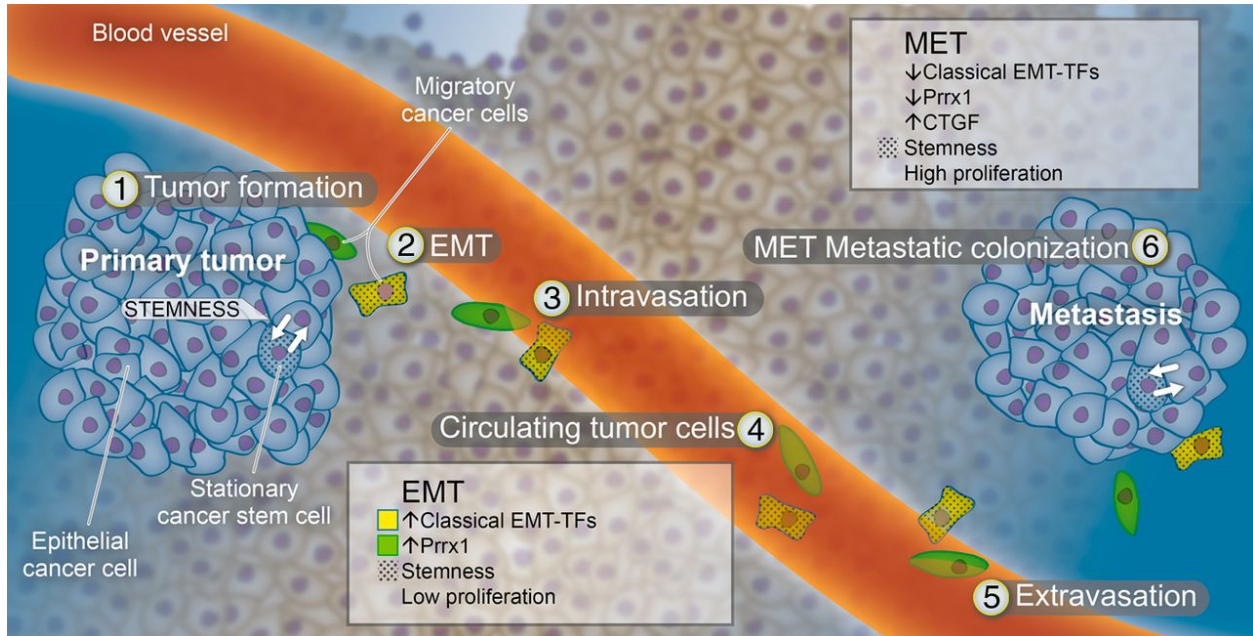


Figure 1.4: Reversibility of EMT during metastatic colonization. Cancer cells delaminate from the primary tumor-expressing EMT-TFs, which endow them with invasive properties to migrate through the extracellular matrix and enter the lymphatic and blood vessels. Those migratory cancer cells expressing classical EMT-TFs (Snail, Twist, and Zeb factors) present CSC properties, whereas those expressing Prrx1 do not. These two classes of CTCs are depicted, although whether the two types of EMT occur in parallel or are exclusive for individual tumors has not been shown. After extravasation, CTCs can colonize distant organs, undergoing a MET upon down-regulation of the EMT-TFs, which reverts them to the epithelial state and increases proliferation. Further work is necessary to characterize the signals that down-regulate the classical EMT-TFs while maintaining CSC properties. CTGF has been shown to induce MET concomitantly with CSC traits in cancer cells, a global effect that promotes metastatic colonization and is similar to that produced after Prrx1 down-regulation. Stationary cancer stem cells can be converted into differentiated tumor cells, and dedifferentiation of non-CSCs can generate cells with TIC. This bidirectional conversion (represented by white double arrows) adds a high degree of phenotypic plasticity in tumors that requires the design of improved therapeutic strategies. From [Nieto \(2013\)](#). Reprinted with permission from AAAS.

of them produce metastases [Fidler (1970)]. To complement EMT, cancer cells must also overcome the mechanical endothelial barrier, and interact with surrounding stromal cells to push their way into circulation. To achieve this, cells most notably upregulate matrix metalloproteinases (MMPs) via citrate metabolism and O-Glycosylation. These MMPs serve to degrade matrix proteins and facilitate infiltration, but also regulate signaling pathways to adjust cell growth, modify inflammation, and even promote angiogenesis [Kessenbrock et al. (2010)]. The cells then take advantage of nearby vessels, either hematogenous or lymphatic, to begin the dissemination process [Nathanson (2003); Wyckoff et al. (2000)].

### 1.2.2 Metabolism of circulation

Within these vessels, circulating tumor cells (CTCs) must adapt to harsh conditions in order to survive. Most notably, oxidative stress is increased when cells detach from their extracellular matrix (ECM), and only those that can plasticize their metabolism are able to survive the dissemination process [Piskounova et al. (2015)]. This survival is possibly dependent on the upregulation of fatty acid oxidation (FAO) during metabolic stress in order to maintain NADPH and ATP levels without increasing the generation of reactive oxygen species (ROS) and causing cell death [Li et al. (2018)]. Those that survive the exacting conditions then have a chance to begin the extravasation process into distant tissue.

### 1.2.3 Metabolism of colonization

As previously mentioned, though CTCs could potentially form metastases in any organ in the body, many times primary tumors will propagate metastases to specific secondary sites. An attractive hypothesis is that the metabolic requirements at the potential secondary sites match the metabolic reprogramming undergone by the surviving CTCs. In a sense, it is comparable to a natural selection process, where the most plastic tumor cells that form metastatic lesions have either the greatest ability to adapt or evolve the most beneficial

phenotypes for the circumstance, and thus are able to not only survive in circulation, but also in the specific organs that they begin to colonize. Consequently, those cancer cells that are most readily able to adapt to specific organ sites are likely already metabolically inclined in favor of those organs, simply based on their primary sites or the changes they had to undergo in order to intravasate out of the primary site. Schild et al. summarize and give credibility to this hypothesis quite comprehensively in a recent review, exemplifying this adaptation in several organs [Schild et al. (2018)].

### 1.2.3.1 Site-specific metabolic changes

In the brain, both normal cells and metastases are able to flexibly metabolize alternative fuel sources other than glucose [Albrecht et al. (2010); Chen et al. (2015); Ebert et al. (2003)]. Similarly, in the lungs, metastatic cells have an unusual propensity to combat oxidative stress, allowing them to thrive in regions of elevated ROS [LeBleu et al. (2014); St-Pierre et al. (2006)]. Alternatively, in the liver, triumphant metastatic cells are those that upregulate glycolysis and creatine secretion while downregulating mitochondrial metabolism to enhance biosynthetic fuel generation, both important processes for survival in the heterogeneously oxygenated environment of the liver [Dupuy et al. (2015); Loo et al. (2015)]. In the bone, colonizing metastatic cells typically express enzymes to synthesize serine and upregulate production of lactate, both of which help differentiate precursor cells into bone-degrading osteoclasts, helping the cancer to form metastatic niches [Lemma et al. (2017); Pollari et al. (2011)]. Finally, in the omentum, a fatty, metabolically active organ, metastatic colonizers upregulate fatty acid binding proteins to collect fatty acids from nearby adipocytes and use them for metabolic processes via  $\beta$ -oxidation [Choe et al. (2016); Nieman et al. (2011)]. Though these studies give many hints at the metabolic changes undergone by cancer cells during the metastatic process, a complete and unified story is still missing, and therapeutic targets are highly limited.



Metastasis is the leading cause of cancer mortality, with some cancer types' metastases accounting for over 90% of cancer deaths [Dillekås et al. (2019)]. Unfortunately, the number of metabolic studies done in relation to cancer metastasis, invasion, or migration is exceedingly lower than those of general cancer metabolism (Fig. 1.5). This discrepancy is likely in large

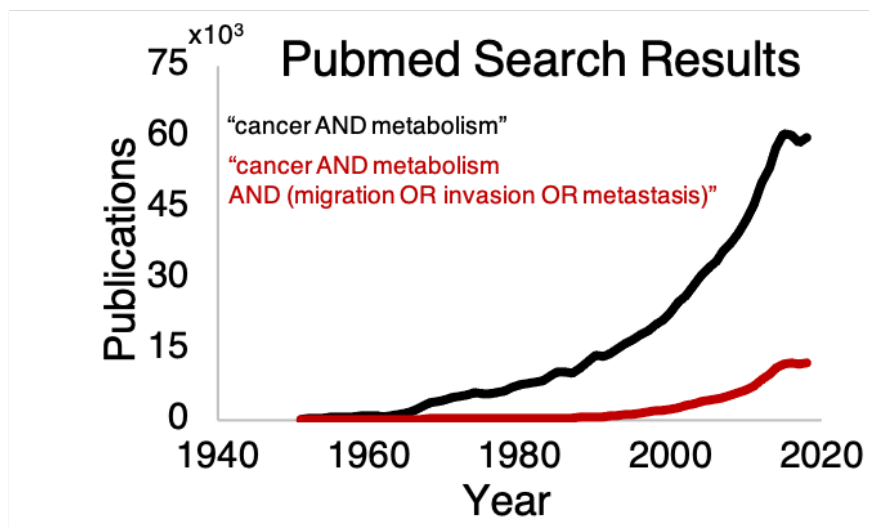


Figure 1.5: Discrepancy in metabolic studies of cancer metastasis. A pubmed search for “cancer AND metabolism” over the years (black) is shown in comparison a search for “cancer AND metabolism AND (migration OR invasion OR metastasis)” over the years (red).

part due to a lack of existing tools to study metastatic cells in their native environment (or a model thereof), and at a single-cell, or even intracellular resolution, which is required to investigate the heterogeneous subpopulations within tissues and the elusive migratory cancer cell subtypes.

## 1.3 Existing methods for metabolism research

### 1.3.1 Metabolomics and metabolic flux

There exist many commonly utilized methods to quantitatively investigate the metabolic changes in bulk cell environments. For example, metabolomics – the study of the metabolic composition of biological samples – can be performed using various state-of-the-art devices,

and allows for quantification of small molecule metabolites [Alonso et al. (2015)]. Two main methods exist for running metabolomics experiments, nuclear magnetic resonance (NMR), and mass spectrometry (MS). While both have their advantages, namely a high-throughput nature and the output of a large pool of quantifiable metabolic markers, they lack the ability for non-destructive analysis (e.g. in tissue samples or complex culture systems) and single-cell analysis, making it difficult to apply to metastatic metabolism research. In conjunction, one can also run metabolic flux analyses on metabolomics data, which allows for the quantification of metabolic activity by investigating the pathways by which intermediates are metabolized [Antoniewicz (2015)]. But again, though these methods are extensively utilized for primary tumor and cell monolayer research, they are extremely difficult to tailor for single-cell scales or for complex analyses of dynamic environments [Zenobi (2013)]. Consequently, several other methods have been exploited in an attempt to investigate the metabolic dysregulation of invasive and migrating cells.

### 1.3.2 Immunostaining

One such method is immunostaining. Using immunostaining procedures, which allows for single-cell level quantification of antigens, one group found that stromal cells lacking caveolin-1 surrounding particularly metastatic and recurrent breast tumor tissue fueled tumor cells via aerobic glycolysis, which they termed the reverse Warburg effect [Pavlidis et al. (2009)]. In contrast, the tumor cells themselves showed significantly higher staining of mitochondrial markers as compared to the surrounding stromal cells. Another study by the same group also showed this process to occur in metastases to lymph nodes [Sotgia et al. (2012)]. Though this method benefits by increasing the resolution at which cells can be analyzed, and thus better tease out the heterogeneities in biological samples, it suffers from a destructive fixation step that may modify the cells' environment and thus metabolic phenotypes, and also removes the capability of a temporally evolving analysis.

### 1.3.3 Cellular respiration

Alternatively, technological advancements in the past couple of decades have made it possible to measure cellular respiration rates, glycolysis, and ATP production non-destructively in tissue monolayers via the Seahorse XF analyzer [Wu et al. (2007)]. This technique has also been expanded to high-throughput scenarios, multicellular systems, and more complex culture systems, providing useful data on mitochondrial function and phenotypic drug discovery [Bond et al. (2018); Divakaruni et al. (2014); Luz et al. (2015); Rogers et al. (2011)]. Though useful, this method is impossible to use on a single-cell resolution in heterogeneous culture systems, and thus is limited in its usefulness for analyzing cancer cell migration and invasion. Evidently, a better way to analyze heterogeneous cell populations at a single-cell resolution without disrupting the surrounding complex culture system is needed.

## 1.4 Fluorescence lifetime imaging of cellular autofluorescence

One extremely useful technique for studying cells at a phenotypic level is the analysis of the fluorescence lifetime of endogenous cellular autofluorescence.

### 1.4.1 The brief history of fluorescence

Fluorescence itself is a long-observed phenomenon, but it became truly understood in 1852 with Sir George Stokes' seminal paper "On the change of refrangibility of light," where he explained in detail the process on how a substance that absorbs light at a short wavelength can emit that light at a longer wavelength, now known as the Stokes' shift (Fig. 1.6 [Stokes (1852)]). In brief, when electrons of a fluorescent molecule are promoted to an excited state via the absorption of a photon, the electrons lose some energy via vibrational (among other possible pathways) decay but remain in their excited state. The electrons then drop back

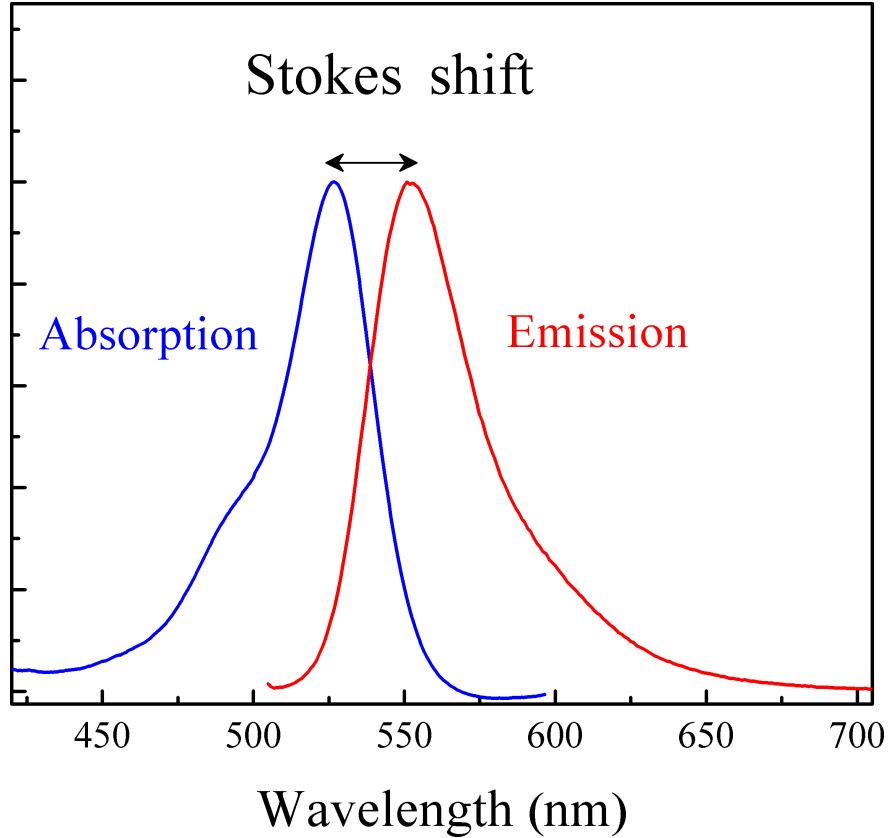


Figure 1.6: A Stokes shift of around 25 nm between the absorption (blue) and emission (red) spectra of Rhodamine 6G.

down to their ground state via the emission of a photon but starting from a lower vibrational level in the excited state, thus emitting a photon with a lower amount of energy – and thus higher wavelength – than of that with which it was excited. This process can be visualized via a Jablonski energy level diagram (Fig. 1.7) [Jabłoński (1935)]. More than half a century later, theories on the possibility of a quantifiable temporal process of this shift from the excited state back to the ground state (i.e. fluorescence lifetime) began to emerge [STERN (1919)], and eventually these theories were confirmed with experimental measurements (Fig. 1.8) [Gaviola (1926)].

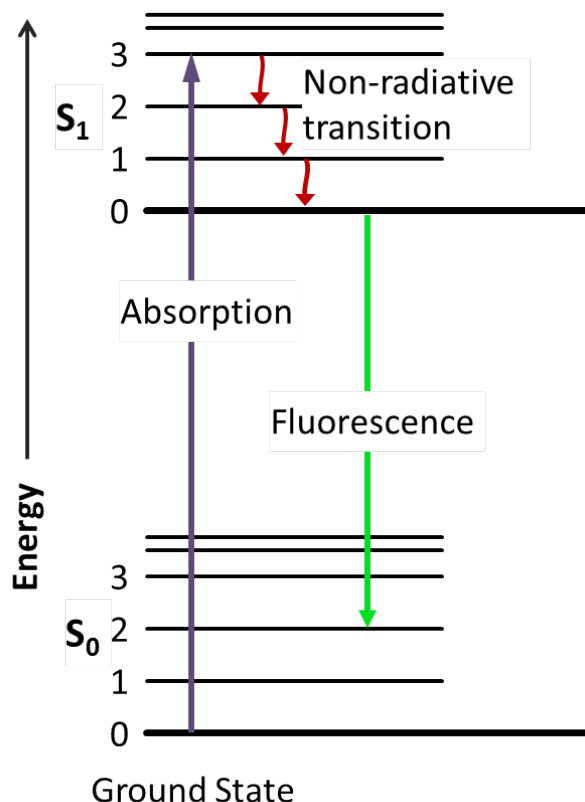


Figure 1.7: A Jablonski diagram showing the ground state ( $S_0$ ), the first excited state ( $S_1$ ), vibrational energy levels within the states, and the absorption (purple), non-radiative decay (red), and fluorescence (green) processes.

### 1.4.2 Cellular autofluorescence

By a stroke of chemical luck, many molecules within living cells display endogenous fluorescence properties when excited with proper wavelengths of light. The two metabolically related cofactors in the cell most responsible for this endogenous fluorescence are flavin adenine dinucleotide (FAD) and the reduced form of nicotinamide adenine dinucleotide (NADH). Several recent reviews will satisfy the further exploration of the functions and importance of these cofactors in cellular function, should they wish to be understood in detail [Cantó et al. (2015); Covarrubias et al. (2021); Okabe et al. (2019); Xiao et al. (2018b); Yaku et al. (2018); Yang and Sauve (2016)]. Although the fluorescence properties of these molecules

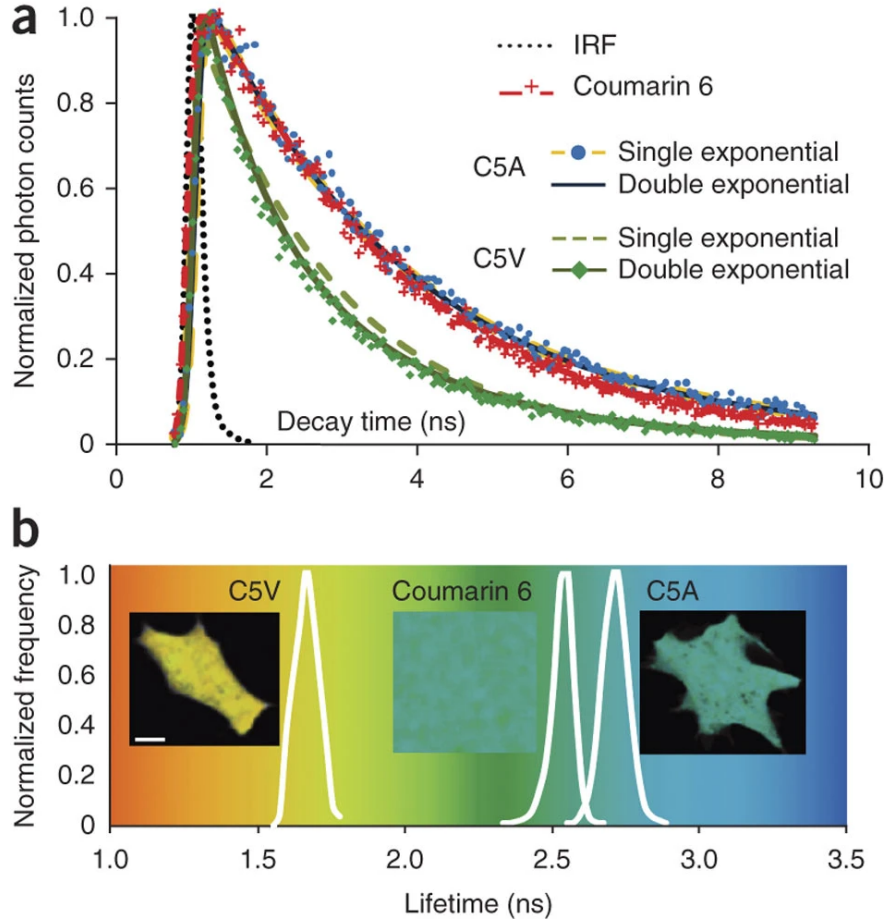


Figure 1.8: TCSPC FLIM data representation of the FRET standard. (a) The representative Coumarin 6, C5A (donor-alone control) and C5V (FRET standard) raw decay data and corresponding fitting curves are shown. Fittings were carried out using the measured instrument response function (IRF) with a full width at half maximum of  $\sim 300$  ps. The fluorescent lifetime decay kinetics for Cerulean in the C5A and C5V constructs was determined through the comparisons of fitting the decay data into both single- and double-exponential decay models. There was little difference observed between the single- and double-exponential fits of the C5A decay data, confirmed by the calculated  $\chi^2$ s-1.08 (single) versus 1.07 (double). However, the C5V FRET standard was better represented by the double-exponential fit ( $\chi^2 = 1.07$ ) compared with the single-exponential fit ( $\chi^2 = 2.38$ ). The results clearly show the quenched state of Cerulean (the donor) in the presence of Venus (the acceptor) resulting from FRET. (b) The lifetime distributions in representative Coumarin 6, C5A or C5V lifetime (overlaid with intensity) images are shown (the apparent lifetime for C5V, see equation (2) [of the corresponding publication]). Scale bar, 10  $\mu\text{m}$ . Reprinted by permission from Springer Nature, Nature protocols, [Sun et al. \(2011\)](#), Copyright 2011.

were known essentially since their functions were discovered, the usefulness of this fluorescence was limited until now-Nobel laureates Paul Boyer and Hugo Theorell realized that the fluorescence properties of NADH differed when bound to alcohol dehydrogenase (ADH) compared to free in solution [Boyer et al. (1956)].

#### 1.4.2.1 Understanding NADH and FAD fluorescence

These changes in NADH fluorescence - due to a change in the ratio of NADH to NAD (of which NAD does not fluoresce) - were soon cleverly exploited to analyze redox states, first in isolated mitochondria, then in-vivo in rats by biochemist Britton Chance and collaborators [Chance and Baltscheffsky (1958); Chance et al. (1962)]. Chance also described a method to derive these redox states from the intensity ratio of FAD and NADH, since FAD only fluoresces in the oxidized form whereas the opposite is true for NAD, and used this method to characterize fresh rabbit and cow corneas [Chance and Lieberman (1978); Chance et al. (1979)]. The use of the fluorescence lifetime of these cofactors was not evident, however, until a series of papers on the characterization of the emission properties of FAD and NADH revealed a change in lifetime when in folded and unfolded configurations (Fig. 1.9) [Elodi and Szabolcsi (1959); Scott et al. (1970); Shifrin and Kaplan (1959); Spencer and Weber (1969); Weber (1950,5,5)]. Indeed, it was soon after discovered that the lifetime of these coenzymes changed due to the unfolding upon binding to enzymes (i.e. ADH) [Gafni and Brand (1976)].

These enzyme-bound and free states would not be correlated with redox states, and thus metabolism, in cells until 2005 by Bird et al., after the advent of FLIM and its use for NADH lifetime imaging in live-cells was introduced [Bird et al. (2005); König et al. (1996); Lakowicz et al. (1992); Piston et al. (1992)]. It is important to mention that the fluorescence lifetime and spectrum of NADH exactly overlays that of its phosphate derivative NADPH, and because NADPH's fluorescence contribution is minimal, we will hereafter refer to NADH/NADPH jointly as NADH for simplicity [Blacker et al. (2014); Wakita et al. (1995)].

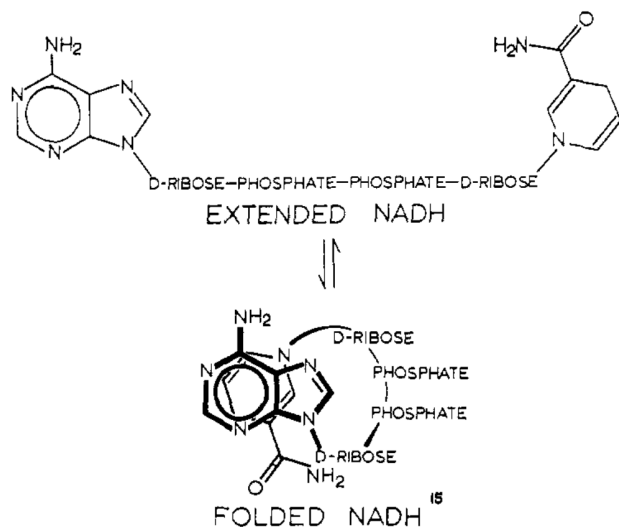


Figure 1.9: Limiting conformations for NADH. Reprinted with permission from [Scott et al. \(1970\)](#). Copyright 1970 American Chemical Society.

#### 1.4.2.2 Exploiting NADH and FAD fluorescence

Since the advent of this method of label-free metabolic fluorescence lifetime imaging, it has been used to uncover important insights of cellular processes such as to quantify metabolic differences among germ cells in *C. elegans*, metabolic shifts during stem cell differentiation, metabolic response in insulinoma cells after glucose stimulation, and even to generate a metabolic map of liver tissue and the human retina [[Ferri et al. \(2020\)](#); [Rodimova et al. \(2020\)](#); [Schweitzer et al. \(2007\)](#); [Stringari et al. \(2011,1\)](#)]. A large proportion of these insights, however, center on tumor metabolism.

FLIM of NADH has been crucial to studying these tumoral metabolic processes nondestructively in live cells. This technique can readily be used to analyze metabolic states in simple 2D monolayer tumor cell cultures such as to compare metabolic profiles across tumor subpopulations [[Trinh et al. \(2017\)](#)], and in response to drug treatments [[Davis et al. \(2020\)](#)]. But its usefulness is especially evident in circumstances where other analysis methods would otherwise disrupt important cellular processes in question. These situations can vary from metabolic shifts in cancer cells cultured in 3D microenvironments such as collagen [[Mah et al. \(2018\)](#); [Scipioni et al. \(2021\)](#)], matrigel [[Lefebvre et al. \(2021\)](#); [Ma et al. \(2020\)](#)], and



hyaluronic acid [Sohrabi (2021)] hydrogels, to metabolic alterations during active cellular processes such as collective cancer cell migration [DeCamp et al. (2020)] and cancer cell mitochondrial motility [Lefebvre et al. (2021)]. The expanded use of FLIM of NADH for characterization of these complex culture systems and heterogeneous cell populations will be the focus of several of the proceeding chapters of this dissertation.

## 1.5 Mitochondrial morphology, motility, and dynamics in cellular function

### 1.5.1 Mitochondrial organization in cellular health

As Warburg had posited in his original paper on cell metabolism, the mitochondrion and its dysfunction lie at the center of tumorigenesis and progression. Mitochondria are the main sources of energy production (see: powerhouse) in the cell and the roles of both its structure and function on the impact of healthy and diseased cells are currently under active scrutiny. Although its functional importance in oxidative phosphorylation is well studied and its mechanism heavily characterized, the importance of mitochondrial shape, motility, and fission and fusion dynamics are still debated. In neurons, a field in which mitochondrial motility is most heavily investigated, their localization throughout the cell has been shown to be important for regulating spatial bioenergetic demands [Baloh (2008)], recycling dysfunctional mitochondria [Westermann (2010)], and even have an influence in the differentiation of neuronal precursors post-mitosis [Iwata et al. (2020)]. Impairment of these important processes has been associated with a wide range of neurological diseases, including Alzheimer's disease [Pigino et al. (2003); Rui et al. (2006)], Huntington's disease [Trushina et al. (2004)], and Parkinson's disease [Wang et al. (2011)].

Interestingly, these dynamic processes have been shown to be highly dysregulated in cancer cells [Senft and Ronai (2016)], and influence metastatic dissemination of cancer cells

via the same important mitochondrial regulatory pathways as neuronal cells [Caino et al. (2016,1)]. This dysregulation is likely necessary to allow for the fueling of the different parts of the metastatic cascades as mentioned previously, namely EMT, intravasation, circulation, extravasation, and colonization, all of which require ATP-demanding cytoskeletal processes at distal ends of the cells.

### 1.5.2 Problems with phenotypic measurements of mitochondria

Both basic and preclinical mitochondrial research have been delayed by the current gold standard of analysis – manual annotation and tracking. This highly biased and time-consuming procedure has made it difficult to include mitochondrial phenotypic analysis in the arsenal of metrics quantified by cell biologists. Instead, many rely on generalized approaches to tease out mitochondrial features, such as Gaussian fitting, which works well only for spherical and elliptical particles, and cannot tease out reliable morphological information for complex shapes [Cheezum et al. (2001); Tang et al. (2015); Tinevez et al. (2017)]. A better approach for investigating these mitochondria is via object-based tracking methods, but these methods require a reliable way to first segment the objects in question, which is a non-trivial procedure in itself. A deep learning model exists for mitochondrial segmentation, including a transfer learning procedure for tailoring the model to specific cell or microscope types, but requires manual annotation, which may introduce bias [Fischer et al. (2020)]. Existing tracking methods also fall short, as many rely on linear landscapes common in neurons, and typically require heavily biased user-determined settings [Alsina et al. (2017); Miller et al. (2015); Vallmitjana et al. (2017); Winter et al. (2012)]. Most also completely ignore the fission or fusion of mitochondria, or else rely on high spatiotemporal resolution to connect objects in a pixel-wise fashion between frames [GIEDT et al. (2012); Kandel et al. (2015)].

Evidently, a novel method for an unbiased, automated segmentation and tracking of mitochondria is necessary for teasing out peculiarities in both normal and diseased cells. This will serve to advance mitochondrial research on both a basic and preclinical level, and for the

case of this dissertation, be used to understand the intricacies of phenotypic mitochondrial dysregulation in the advancement of metastatic progression. Indeed, the development of algorithms for the automated segmentation and tracking of mitochondria in live-cell time-lapse images, and its applications in cancer metastasis will be the primary topic for several upcoming chapters of this dissertation.

## 1.6 Summary

Much is already known about the metabolic and mitochondrial dysregulation occurring in primary tumor cells to fuel complex proliferative processes and allow tumors to grow. However, there is little consensus about a unified theory on metabolic shifts that occur during the metastatic cascade as tumor cells begin to invade, spread, and colonize different organs. As mitochondria are central to metabolism and bioenergetics of cancer cells (and cells in general), their phenotypic changes are of great interest to study metabolic dysregulation and its consequences, but existing techniques are lacking in their usefulness. In this dissertation, a detailed investigation of the phenotypic metabolic intricacies of invasive cancers will be presented, along with the creation of two important techniques, (1) a technique to create reliable organoid cultures for the study of cancers in a complex 3D environment, and (2) a technique to probe phenotypic changes of mitochondria in these cancers. Finally, these mitochondrial features will be correlated with metabolic and cytoskeletal features in an attempt to understand how these qualities are connected with and influence one another.

# Chapter 2

## FLIM of NADH

Throughout multiple projects within this dissertation, I make use of the phasor approach to NADH FLIM. It thus seems necessary to describe this method and the method from which it extends in greater detail before introducing experimental results. In this chapter, I will briefly explain what FLIM is, how it is used to exploit NADH for metabolic information, and how we use the Fourier domain for a more intuitive and useful analysis over its time domain derivative. Although these topics have been lightly introduced in the previous chapter, its mathematics and necessary hardware and software components have not, and will comprise the majority of this chapter.

### 2.1 Fluorescence and its lifetime

#### 2.1.1 Fluorescence absorption and emission

Fluorescence is a phenomenon that occurs when electrons of a molecule are excited from their ground state to a higher energy state - a so-called excited state - then subsequently returns to its ground state by releasing that energy in the form of a photon. The absorption and emission of a photon occurs in and is measured by discrete quanta. Each quantum has

a certain energy as expressed by Planck’s Law in Equation 2.1.

$$E = h\nu = \frac{hc}{\lambda} \quad (2.1)$$

Where  $h$  is Planck’s constant,  $c$  is the speed of light,  $\nu$  represents the frequency of a photon, and  $\lambda$  represents its wavelength. By Planck’s Law, the wavelength of an incoming photon is inversely proportional to its energy. The wavelength of the light wave from which the photon is a part of directly determines whether an impacted molecule’s electrons are raised to the excited state - if the wavelength is short enough (i.e. there is enough energy) the electrons will transition to a higher energy state, and any excess will raise its vibrational and rotational states, but if the wavelength is too long, no absorption will occur.

A molecule is able to typically absorb a large range of wavelengths due to its variation in vibrational energy levels and thermal motion, which allows for a variety of photon energies to promote a transition. The range of absorption wavelengths constitutes that molecule’s absorption spectrum.

Once a photon’s energy is absorbed by a molecule, and its electrons are excited to a higher state, many processes can occur, each with varying probabilities, and will depend on the molecule and its environment. Most typically, the molecule will, within this excited state, relax from a higher vibrational level to the lowest vibrational level in the first excited state, a process termed internal conversion.

Finally, the molecule will release the stored energy to relax to its ground state, and if this energy is released in the form of a photon, the molecule is considered fluorescent. The excitation spectrum of a molecule constitutes the emission intensity of the molecule at a single wavelength for various absorption wavelengths.

Although some other relaxation pathways exist to compete with the fluorescence emission, such as intersystem crossing (leading to phosphorescence, or delayed fluorescence) and

collision-based non-radiative processes (such as quenching), they are out of the scope of this dissertation, and its discussion can be found elsewhere.

Because some energy is lost between the excitation and emission of a photon, the resulting emitted photon will have a higher wavelength than the one used for excitation. As mentioned previously, this process is known as a Stokes shift, and is helpful for the use of fluorescence, experimentally.

### 2.1.2 Fluorescence decay

The excitation of a molecule's electronic state occurs in the order of femtoseconds ( $10^{-15}$  seconds). Once in its excited state, it decays to that state's lowest vibrational energy level, which occurs in the order of picoseconds ( $10^{-12}$  seconds). As mentioned previously, a combination of radiative (fluorescent) and non-radiative processes can occur to demote an excited molecule back to its ground state. These processes' probabilities of occurrence are described by decay rate constants ( $k$ ), and are used to characterize a molecule's fluorescence lifetime. This lifetime ( $\tau$ ) is defined as the time it takes for a molecule in the excited state to decay by a factor of  $e$ . With these parameters in mind, the probability of the emission of a photon can be determined using Equation 2.2.

$$dI(t) = -\frac{1}{\tau(t)}I(t)dt \tag{2.2}$$

Where  $I(t)$  is the probability of emission at given time  $t$  for a decay time of  $\tau(t)$  after exciting the molecule at time 0. When solved for the case of a constant lifetime (i.e.  $\tau(t)=\tau_0$ ), we are presented with a classic monoexponential decay function (Equation 2.3).

$$I(t) = A_0 e^{-\frac{t}{\tau_0}} \tag{2.3}$$

Where  $A_0$  is a variable describing the amplitude of the system, called the pre-exponential factor.

In a multiexponential system (i.e. multiple fluorescent molecules with different decay times) the differing decay rates must be taken into account, and the system's decay can be described via Equation 2.4.

$$I(t) = \sum_{i=k}^N A_k e^{-\frac{t}{\tau_k}} \quad (2.4)$$

Where  $A_k$  is a variable describing the amplitude and  $\tau_k$  the lifetime of the N exponential decay systems.

For a fluorescent molecule, this decay back down to the electronic ground state occurs at a much slower timescale than its excitation and internal conversion, in the order of nanoseconds ( $10^{-9}$  seconds), and can be precisely measured using conventional hardware.

### 2.1.3 Measuring fluorescence lifetime

The measurement of a molecule's excited state decay was first performed in the middle of the 19<sup>th</sup> century with phosphorescent substances. In fact, it was originally believed that fluorescent compounds stopped emitting immediately after the removal of the excitation source, whereas phosphorescent compounds held on to this energy, and could keep emitting for even as long as a several hours after excitation. For those longer decay times, a simple clock could be used to measure its lifetime, however, for those substances that took less than a second to decay, more advanced techniques needed to be developed.

In an inspiration from a rotating cog device used by a physicist to measure the speed of light, Becquerel created a rotating wheel to measure phosphorescence at time intervals as short as  $10^{-4}$  seconds. This device consisted of two rotating disks with holes on each, arranged such that the holes on opposite disks never overlap. A phosphorescent material is placed between the two disks and light is fed through one hole, exciting the material, whose

emission can then be viewed from the opposite disk's hole. The disks are then rotated at a known speed, which allows for the quantification of the substance's lifetime (Fig. 2.1). Eventually, the development of fast light sources and shutters using polarizers and reservoirs

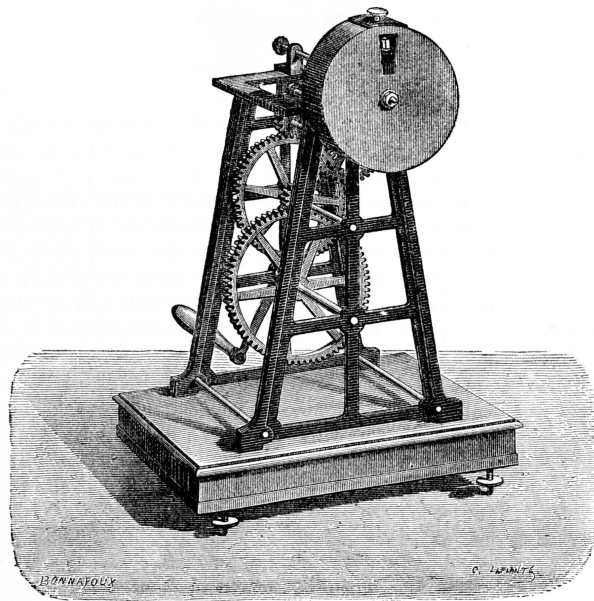


Figure 2.1: The Becquerel phosphoroscope (1873-1874)

of liquids highly sensitive to electric fields (termed Kerr cells) made it possible to generate light flashes on the order of  $10^{-8}$  seconds (Gottling (1923)). Using a modified version of these techniques, Gaviola created what he called a fluorometer, the first instrument to measure fluorescence lifetime, and published his well-known paper measuring lifetimes of Rhodamine B and fluorescein (both on the order of  $10^{-9}$  seconds) [Gaviola (1926)].

Today, instruments to measure a sample's fluorescence lifetime have become more compact and easy to use than ever before, and are able to measure fluorescence lifetimes either in the time domain, or the frequency domain. Though the technique of measurement between these two domains are different, their data can be used interchangeably by converting them through the Fourier transform (and its inverse).



### 2.1.3.1 Time domain acquisition

To measure fluorescence lifetime in the time domain, a fluorescent sample is excited by an extremely narrow pulse of light that is pulsed in such a way to avoid another excitation during the molecule's decay. Two devices, a time-correlated single photon counter (TCSPC) module, and a FastFLIM FLIM box are commonly used approaches for time-domain measurements, in which photomultiplier tubes (PMTs) or photodiodes record single photon arrivals, and their arrival times as measured by synchronized clocks are used to build up a decay curve to calculate the sample's fluorescence lifetime. Though both are useful for their own reasons, the FLIMbox benefits from a higher duty cycle, a higher range of frequencies at which it records complete decays, and a shorter dead time, which produces more complete data. These benefits result in more accurate phasor transformations than its TCSPC counterparts [Ranjit et al. (2018)].

### 2.1.3.2 Frequency domain acquisition

Alternatively, in the frequency domain, the excitation light is sinusoidally modulated at high frequencies (rather than pulsed) as in Equation 2.5.

$$E(t) = E_0(1 + M_E \sin(\omega t)) \quad (2.5)$$

Where  $E(t)$  is the excitation intensity at time  $t$ ,  $E_0$  is the excitation intensity at time 0,  $M_E$  is the excitation's modulation factor,  $\omega$  is the angular modulation frequency of the excitation source, and  $t$  is the time.

This modulated excitation consequently produces a modulated emission of the sample as in Equation 2.6.

$$F(t) = F_0(1 + M_F \sin(\omega t + \phi)) \quad (2.6)$$

Where  $F(t)$  is the sample's emission intensity at time  $t$ ,  $F_0$  is the emission intensity at time 0,  $M_F$  is the emission's modulation factor,  $\omega$  is the angular modular frequency of the excitation source,  $t$  is the time, and  $\phi$  is the phase shift between the excitation and emission sources.

This modulated emission mirrors the modulation of the excitation source, but is modified slightly via a phase delay and amplitude reduction, both of which can be used to calculate the sample's lifetime by solving for  $\tau$  in Equations 2.7 and 2.8.

$$\omega = \tau_p \tan(\phi) \quad (2.7)$$

Where  $\omega$  is the angular modular frequency of the excitation source,  $\tau_p$  is the lifetime derived from the phase shift, and  $\phi$  is the phase shift between the excitation and emission sources.

$$M = \frac{1}{\sqrt{1 + (\omega\tau_m)^2}} \quad (2.8)$$

Where  $M$  is the amplitude reduction (demodulation),  $\omega$  is the angular modular frequency of the excitation source, and  $\tau_m$  is the lifetime derived from the demodulation.

The amplitude reduction is calculated from the ratio of the emission amplitude  $M_F$  to excitation amplitude  $M_E$ , as in Equation 2.9.

$$M = \frac{M_F}{M_E} \quad (2.9)$$

Which in turn are calculated from the ratio of their respective AC and DC signal components as in Equations 2.10 and 2.11.

$$M_F = \frac{AC_F}{DC_F} \quad (2.10)$$

$$M_E = \frac{AC_E}{DC_E} \tag{2.11}$$

PMTs or charge-coupled devices (CCDs) are then used to capture the emission signal.

## 2.1.4 Analyzing fluorescence lifetime

Just as the fluorescence lifetime of a sample can be collected in either the time or frequency domain, the analysis of its data can be performed in either domain as well. A time domain acquisition can be analyzed in the frequency domain via the data's Fourier transformation, and frequency domain acquisition can be analyzed in the time domain via the data's inverse Fourier transformation.

### 2.1.4.1 Time domain analysis

The time domain analysis of fluorescence decay data has long been the gold-standard of analysis. Its main approach is to fit the acquired photon arrival measurements to a sum of first order kinetic processes as a sum of exponential decays (Equation 2.4). A problem occurs, however, when this fitting fails to take into consideration the instrument response function (IRF) of a time-domain acquisition, which is convoluted with the sample's exponential decay. The IRF must thus be deconvoluted before a proper fitting of the sample's decay can be performed. Several time consuming techniques exist for this deconvolution process.

Following IRF considerations, decay curves (numbering on the order of a million) must be analyzed for a single image on a pixel-by-pixel basis to account for multi-exponential sample decays, which becomes extremely computationally expensive. Several techniques exist to fit these decay curves, which all have their own advantages and disadvantages, and (along with many other methods) are described in great detail in a wonderful recent review [Datta et al. (2020)]. The most common techniques are least squares fitting, maximum likelihood

estimation, global analysis, and bayesian analysis, all of which require prior assumptions about the number of components contributing to the decay, and other electronic variations contributing to the signal [Maus et al. (2001); Verveer et al. (2000); Wang et al. (2019)].

#### 2.1.4.2 Frequency domain analysis

Alternatively, lifetime data can be analyzed in the frequency domain via the phasor approach to fluorescence lifetime imaging by transforming the decay data (from the time domain) or mapping the phase shift and modulation (from the frequency domain) to the phasor plot (a Cartesian representation of polar coordinates) in 2D space - the method I will be using for FLIM data analysis throughout this dissertation. The phasor approach to FLIM allows for near-instantaneous analysis of FLIM data, as no iterative fitting procedures are required [Ranjit et al. (2018)]. This approach also makes FLIM analysis graphically intuitive, and its results accessible to a less familiar audience [Wouters and Esposito (2008)].

The mathematics for the phasor transformation of lifetime decay data were first described by Weber [Weber (1981)] and used as a graphical representation by Jameson soon after [Jameson et al. (1984)]. Instead of x and y coordinates, the phasor plot is classically represented by g and s coordinates. To transform time domain data to phasor coordinates, Equations 2.12 and 2.13 are used.

$$g_{i,j}(\omega) = \frac{\int_0^T I_{i,j}(t) \cos(\omega t) dt}{\int_0^T I_{i,j}(t) dt} \quad (2.12)$$

$$s_{i,j}(\omega) = \frac{\int_0^T I_{i,j}(t) \sin(\omega t) dt}{\int_0^T I_{i,j}(t) dt} \quad (2.13)$$

Where  $g_{i,j}(\omega)$  and  $s_{i,j}(\omega)$  are the x and y coordinates of the phasor transformation of an image's pixel  $(i,j)$ ,  $\omega$  is the angular modular frequency of the excitation source,  $T$  is the

repeat frequency of the acquisition, and  $I_{i,j}(t)$  is the intensity of pixel  $(i,j)$  as a function of  $t$ , time.

To transform frequency domain data to phasor coordinates, Equations 2.14 and 2.15 are used.

$$g_{i,j}(\omega) = M_{i,j} \cos(\phi_{i,j}) \quad (2.14)$$

$$s_{i,j}(\omega) = M_{i,j} \sin(\phi_{i,j}) \quad (2.15)$$

Where  $M_{i,j}$  is the modulation and  $\phi_{i,j}$  is the phase shift of pixel  $(i,j)$ 's emission as compared to the excitation source. In polar coordinates, these transformations show  $M$  as the modulation of the phasor, and  $\phi$  as the phase. These equations are reminiscent of a description of a circle in polar coordinates:

$$x = r \cos(\theta), y = r \sin(\theta)$$

Where  $x=g$ ,  $y=s$ ,  $r=M$ , and  $\phi=\theta$ .

These coordinates can also be expressed as a function of the repetition frequency and lifetime by integrating equation 2.4 via Equations 2.12 and 2.13, giving Equations 2.16 and 2.17.

$$g(\omega) = \sum_{k=1}^N \frac{A_k \tau_k}{1 + (\omega \tau_k)^2} / \sum_{k=1}^N A_k \tau_k \quad (2.16)$$

$$s(\omega) = \sum_{k=1}^N \frac{A_k \omega \tau_k^2}{1 + (\omega \tau_k)^2} / \sum_{k=1}^N A_k \tau_k \quad (2.17)$$

Where  $A_k$  and  $\tau_k$  describes the amplitude and the lifetime of specie  $k$ , respectively for  $N$  species, and  $\omega$  is the repetition frequency of the excitation source.

By these equations, we find that all monoexponential decays ( $N=1$ ) fall on the semicircle between  $g = 0$  and  $1$ , and  $s = 0$  and  $0.5$ , centered at  $0.5$ , termed the universal circle. At a lifetime of  $0$ , the position of the point on the phasor lies at a  $(g,s)$  of  $(1,0)$ . As the lifetime increases, the phasor position of that point moves counter-clockwise along the universal circle, where an infinite lifetime lies at  $(0,0)$ . Multiexponential decays ( $N>1$ ) instead fall within the universal circle, but never on the circle.

An important rule to note, which I will often make use of in the following sections, is the rule of linear addition in the phasor space. This rule states that any multiexponential decay which contains a mixture of monoexponential decays will fall on the linear trajectory connecting the phasor plot positions of the individual monoexponential decays. For example, if a pixel  $(i,j)$  in an image contains fluorescence lifetime decay data of two monoexponential fluorescent species, we can derive its coordinates as a combination of both species by Equation 2.18.

$$I(t)_{i,j} = A_1 e^{-\frac{t}{\tau_1}} + A_2 e^{-\frac{t}{\tau_2}} \quad (2.18)$$

Using equations 2.16 and 2.17 for  $N=2$ , we apply the phasor transform and get Equations 2.19 and 2.20.

$$g_{i,j}(\omega) = \left( \frac{A_1 \tau_1}{1 + (\omega \tau_1)^2} + \frac{A_2 \tau_2}{1 + (\omega \tau_2)^2} \right) / (A_1 \tau_1 + A_2 \tau_2) \quad (2.19)$$

$$s_{i,j}(\omega) = \left( \frac{A_1 \tau_1 \omega \tau_1}{1 + (\omega \tau_1)^2} + \frac{A_2 \tau_2 \omega \tau_2}{1 + (\omega \tau_2)^2} \right) / (A_1 \tau_1 + A_2 \tau_2) \quad (2.20)$$

Its point on the phasor plot will lie on the line connecting the positions representing the decay of the two monoexponential species. We can represent the fractional contribution of specie  $k$  by defining  $f_k$  in Equation 2.21 [Ranjit et al. (2019)].

$$f_k = \frac{A_k \tau_k}{\sum_{k=1}^N A_k \tau_k} \quad (2.21)$$

For our  $N=2$  example, we rewrite Equations 2.19 and 2.20 as Equations 2.22 and 2.23

$$g_{i,j}(\omega) = f_1 \frac{1}{1 + (\omega \tau_1)^2} + f_2 \frac{1}{1 + (\omega \tau_2)^2} \quad (2.22)$$

$$s_{i,j}(\omega) = f_1 \frac{\omega \tau_1}{1 + (\omega \tau_1)^2} + f_2 \frac{\omega \tau_2}{1 + (\omega \tau_2)^2} \quad (2.23)$$

Where  $f_1$  and  $f_2$  are the fractional contributions of species 1 and 2, respectively, to the  $g$  and  $s$  positions on the phasor plot. These equations can of course be used to represent a pixel with  $N$  monoexponential species by Equations 2.24 and 2.25.

$$g_{i,j}(\omega) = \sum_{k=1}^N \frac{f_k}{1 + (\omega \tau_k)^2} \quad (2.24)$$

$$s_{i,j}(\omega) = \sum_{k=1}^N \frac{f_k \omega \tau_k}{1 + (\omega \tau_k)^2} \quad (2.25)$$

## 2.2 NADH fluorescence

NADH is an important coenzyme lying at the center of metabolic processes within the cell. Its main use is to manage electron availability, but does so both in the cytoplasm to regulate glycolysis, and within the mitochondrion to regulate oxidative phosphorylation. In

glycolysis, NAD is reduced to NADH during glucose’s transition to pyruvate. Alternatively, in mitochondria, NAD is reduced to NADH in the tricarboxylic acid cycle, then subsequently oxidized back to NAD in the electron transport chain to create the necessary electron gradient between the mitochondrial matrix and intermembrane space for the generation of ATP. Importantly, NADH is endogenously fluorescent, and depending on how it’s being used, can phenotypically reveal important alterations in metabolism.

### **2.2.1 NADH excitation and emission**

NADH has an absorption spectrum with two peaks at relatively short wavelengths, 250 nm and 340 nm. More importantly, however, NADH has a useful two-photon cross section at 720 nm, allowing for multiphoton excitation for better sample penetration and decreased cellular photodamage. In our studies, and many others, a two-photon excitation wavelength of 740 nm is used, in order to avoid exciting pyridoxines.

NADH has a relatively broad emission spectrum, from 420 nm to 550 nm, though bandpass filters are typically used to capture only the lower part of this spectrum, as FAD overlaps quite strongly with the higher portion of the NADH spectrum. Additionally, a bandpass filter serves to block the shorter peak emission wavelengths of collagen and elastin, which are both excited at similar wavelengths to NADH. In our studies, we use a bandpass filter of 460/80 nm to capture NADH emission between 420-500 nm.

### **2.2.2 NADH conformations**

Upon binding to a protein, NADH changes conformation from its natural free state. In its free state, NADH has a closed conformation where, post-excitation, part of the energy in the excited adenine moiety is transferred to the dihydronicotinamide moiety, adding a quenching-based decay component, and increasing the overall fluorescence decay lifetime [Scott et al. (1970)]. In NADH’s bound conformation, the molecule instead unfolds, separating the ade-



nine and dihydronicotinamide moieties, and thus the molecule’s fluorescence lifetime is less affected by quenching and increases in decay time. As mentioned previously, these bound and free states of NADH represent changes in NAD<sup>+</sup>/NADH ratios, which in turn represent changes in metabolism. In the bound conformation, NADH has a lifetime of roughly 3.4 ns, compared to its free state, which has a lifetime of roughly 0.4 ns. These metabolic changes have been extensively experimentally validated using glycolytic and metabolic inhibitors, and have been analyzed in both the time and frequency domain [Mah et al. (2018); Murata et al. (2019); Tiede et al. (2007); Trinh et al. (2017); Yu and Heikal (2009)].

### 2.2.3 The phasor approach to NADH FLIM analysis

The frequency domain makes it fast and intuitive to analyze metabolic shifts using the change in NADH fluorescence lifetime. As NADH typically assumes two conformations, (I say typically, because NADH can be bound to different enzymes, each which give different lifetimes, but 3.4 ns is a good approximation) bound and free, which have two different monoexponential decays, we know that any sample which contains a mixture of bound and free NADH (a biexponential decay) will have a phasor position that lies within the universal circle. More specifically, according to the rule of linear addition in the phasor space, this sample’s position will lie within the linear trajectory between the phasor position of purely free and purely bound NADH. This linear trajectory between free and bound NADH is termed the metabolic trajectory. From Equation 2.4, we get a two-component decay system described by Equation 2.18.

Using the metabolic trajectory, we can calculate the fractional contribution of bound and free NADH to quantify shifts in metabolism. Phasor transformation gives its  $g$  and  $s$  coordinates represented by Equations 2.22 and 2.23, where  $f_1$  represents the fractional contribution of free NADH and  $f_2$  represents the fractional contribution of bound NADH (or vice-versa) to the  $g$  and  $s$  coordinates of pixel  $(i,j)$ . Since  $g$ ,  $s$ ,  $\omega$ , and both  $\tau$  are known in this equation, we are left only with 2 unknowns of  $f_1$  and  $f_2$  in a system of 2 equations. In practice,

we add in a third component representing the background signal of our acquisition system, giving us a third unknown, but as we know that the sum of all fractional contributions must be equal to 1, we have a third equation to add to our system. This system is represented by Equations [2.26](#), [2.27](#), and [2.28](#)

$$g_{i,j} = f_{free} \frac{1}{1 + (\omega\tau_{free})^2} + f_{bound} \frac{1}{1 + (\omega\tau_{bound})^2} + f_{bg} \frac{1}{1 + (\omega\tau_{bg})^2} \quad (2.26)$$

$$s_{i,j} = f_{free} \frac{\omega\tau_{free}}{1 + (\omega\tau_{free})^2} + f_{bound} \frac{\omega\tau_{bound}}{1 + (\omega\tau_{bound})^2} + f_{bg} \frac{\omega\tau_{bg}}{1 + (\omega\tau_{bg})^2} \quad (2.27)$$

$$1 = f_{free} + f_{bound} + f_{bg} \quad (2.28)$$

Thus, we can solve for  $f_{free}$ ,  $f_{bound}$ , and  $f_{bg}$ . The MATLAB code for solving these equations is provided in Appendix [A](#).

## 2.3 Summary

FLIM of NADH is a useful and quantitative tool for analyzing metabolic shifts in live cells. Combining FLIM of NADH with the phasor transformation simplifies and expedites analysis, making visualization and quantification more readily approachable for a general scientific audience, and removes the need for a fitting-based analysis. In this chapter, I have laid out the mathematics and background of the phasor approach to the analysis of FLIM of NADH, which should provide clarity on this method during its uses in the following chapters. The other methods used in this dissertation were either created by me (or with my help) and

expounded upon thoroughly within their respective chapter, or are only pertinent to a specific chapter, and thus discussed within its context.

# Chapter 3

## Metabolic shifts of TNBC as a function of substrate density

This chapter is a slightly modified version of a paper from: Mah et al., Collagen density modulates triple-negative breast cancer cell metabolism through adhesion-mediated contractility, Scientific Reports, published 2018, Springer Nature and has been reproduced here with the permission of the copyright holder under a [Creative Commons Attribution 4.0 International License](#).

Its supplementary materials can be found in Appendix [B](#).

### 3.1 Abstract

Extracellular matrix (ECM) mechanical properties upregulate cancer invasion, cell contractility, and focal adhesion formation. Alteration in energy metabolism is a known characteristic of cancer cells (i.e., Warburg effect) and modulates cell invasion. There is little evidence to show if collagen density can alter cancer cell metabolism. We investigated changes in energy metabolism due to collagen density in five breast cell lines by measuring the fluorescence lifetime of NADH. We found that only triple-negative breast cancer cells, MDA-MB-231

and MDA-MB-468 cells, had an increased population of bound NADH, indicating an oxidative phosphorylation (OXPHOS) signature, as collagen density decreased. When inhibiting ROCK and cell contractility, MDA-MB-231 cells on glass shifted from glycolysis (GLY) to OXPHOS, confirming the intricate relationship between mechanosensing and metabolism. MCF-10A cells showed less significant changes in metabolism, shifting towards GLY as collagen density decreased. The MCF-7 and T-47D, less invasive breast cancer cells, compared to the MDA-MB-231 and MDA-MB-468 cells, showed no changes regardless of substrate. In addition, OXPHOS or GLY inhibitors in MDA-MB-231 cells showed dramatic shifts from OXPHOS to GLY or vice versa. These results provide an important link between cellular metabolism, contractility, and collagen density in human breast cancer.

## 3.2 Introduction

Cancer cells can modulate their energy metabolism to meet nutritional, biosynthesis, and respiration requirements for maintaining malignancy. One of these factors is the metabolic state of the cancer cell due to their tendency to undergo aerobic glycolysis, known as the Warburg Effect [[Heiden et al. \(2009\)](#); [Liberti and Locasale \(2016\)](#); [Warburg et al. \(1927\)](#)]. Although it produces less ATP per molecule of glucose, glycolysis (GLY) is a more rapid way of producing ATP and is able to meet the high demands of energy to fuel processes such as invasion, migration, and matrix degradation [[Caino and Altieri \(2015\)](#); [Cunniff et al. \(2016\)](#); [Desai et al. \(2013\)](#); [Zhao et al. \(2013\)](#)]. Along with high turnover of ATP production, a byproduct of lactic acid and high acidification also has been shown to benefit cancer cell survival and upregulate invasiveness [[Estrella et al. \(2013\)](#)].

Mechanical properties of the extracellular matrix (ECM) are also a known factor that regulates cell migration and cancer invasion [[Alexander et al. \(2008\)](#); [Artym et al. \(2015\)](#); [Paszek et al. \(2005\)](#); [Seewaldt \(2014\)](#)]. Cells interact with the surrounding ECM through integrin-mediated adhesions and focal adhesions (FAs), that are clusters of over 150 pro-

teins [Kanchanawong et al. (2010); Liu et al. (2015)]. These complexes tether to the cell’s mechanosensing network through actin filaments and regulate processes such as adhesion, migration, and proliferation [Bugyi and Carlier (2010); Gardel et al. (2010); Hirata et al. (2014); Ponti et al. (2004)]. Recent studies have shown that integrin-mediated adhesions interact with the metabolic pathway of the cell through the PI3K/AKT/mTOR pathway and that this could be a potential method of switching the Warburg effect [Ata and Antonescu (2017); Levental et al. (2009); Yang et al. (2015)]. Many of these studies use biochemical assays which are invasive and often lose information which exists in live cell samples. In our approach, we used a non-invasive fluorescence imaging technique to measure ECM density, study live cell behavior, and map energy metabolism within each cell.

Fluorescence lifetime imaging microscopy (FLIM) has been shown to be a powerful technique to measure metabolic indices of live-cells [Bird et al. (2005); Cinco et al. (2016); Datta et al. (2015); Ma et al. (2016); Provenzano et al. (2009); Sameni et al. (2016); Stringari et al. (2012a)]. By looking at the fluorescence lifetime of nicotinamide adenine dinucleotide (NADH), a metabolite involved in OXPHOS and GLY, we can determine the population of free and bound NADH due to their difference in lifetime decay. This will allow us to quantify the “metabolic trajectory”, known as the “M trajectory”, of the cell at every pixel of our image and determine if the cell is undergoing OXPHOS or GLY [Stringari et al. (2012a)]. This trajectory has also been shown to correlate with results found in conventional biochemical assays when OXPHOS or GLY inhibitors are used to shift metabolic signatures towards one another [Cinco et al. (2016); Stringari et al. (2012a,1)]. The advantage of this imaging technique is that it is non-invasive and is able to image real-time changes in metabolism.

For this study, we measured free and bound populations of NADH within different cancer cell lines and a non-tumorigenic cell line when seeded on collagen substrates of different concentrations (1.2 mg/mL and 3.0 mg/mL) and on glass. The microstructural properties of this substrate, including collagen density and fiber diameter, were measured using image correlation spectroscopy [Raub et al. (2008)]. The 3.0 mg/mL and 1.2 mg/mL collagen

substrate had collagen fibers of similar size, but the 3.0 mg/mL collagen substrate gave rise to a denser ECM than the 1.2 mg/mL substrate by 3X. The 3.0 mg/mL collagen substrate was also determined by rheology to be one order of magnitude stiffer than the 1.2 mg/mL collagen substrate. In this paper, we will refer to the density of the collagen as our means to distinguish the difference between the two ECM substrates. We are also aware that each cell line requires different media conditions for culturing, and these affect the metabolism. However, we are interested in the effects of collagen density on each cell line independently. The highly metastatic triple-negative breast cancer cell (TNBC) lines, MDA-MB-231 and MDA-MB-468 were grown on collagen and glass substrate to observe their metabolic shifts. MDA-MB-231 showed a shift towards a more glycolytic signature as collagen density increased, and as compared to cells plated on glass. Inhibition of cell contractility with the addition of Y-27632 shifted all the cells on all substrates to a more OXPHOS signature compared to their uninhibited controls. This further shows that integrin-mediated adhesions behave as mechanosensors, and these adhesions can alter metabolism. MDA-MB-468 cells did not show changes in response to collagen density, however, the cells showed increase OXPHOS on both collagen substrates when compared to glass. MCF-7 and T-47D, the less invasive breast cancer cells, were also tested and did not show changes in metabolic signatures.

Non-tumorigenic breast cell line MCF-10A showed slight changes in NADH free:bound ratio only on the low-density collagen surface, indicating that this property is more prominent in MDA-MB-231 and MDA-MB-468 cell lines. Other cancer cell types, U-251 MG glioma and A-375 MM melanoma cell lines, were evaluated under the same conditions. The U-251 MG cells had no significant differences in their NADH free:bound ratio in response to collagen density. A-375 MM cells did not adhere well to the collagen substrates could be a reason for their lack of change in their NADH free:bound ratio, indicating that the mechanosensing network must be established in order to undergo metabolic reprogramming. Inhibition of OXPHOS or GLY in MDA-MB-231 cells showed shifts in NADH free:bound

ratio with respect to each treatment towards their metabolic counterparts across all surfaces, and further confirmed that it is indeed the metabolism that is being altered by the ECM. MCF-10A cells showed a shift when OXPHOS was inhibited only on our denser collagen substrate and on glass when GLY was inhibited. The results found in our work here show that both the mechanosensing and metabolism pathways are interconnected and can be modulated through ECM mechanical properties. This will provide further information to develop cancer therapies which target either or both of these pathways to decrease cancer cell invasion.

## 3.3 Results

### 3.3.1 Collagen characterization measurements

Tilghman et al. postulated that cellular metabolism can be altered when MDA-MB-231 cells are cultured on soft (300 Pa) versus stiff (19200 Pa) matrices due to the fact that cells stayed in the G1 phase cell cycle phase longer [Tilghman et al. (2012)]. Indeed, their results using cell lysates with ATPlite assay and protein synthesis assays confirmed their hypothesis. The substrates used in those experiments were limited to polyacrylamide gels that have a large rigidity/flexibility range, but it is not physiological. In our approach, we used collagen monolayers prepared at two different concentrations of 1.2 mg/mL and 3.0 mg/mL. Second harmonic generation (SHG) images were taken to measure the fiber thickness, and density was measured using image correlation spectroscopy (ICS) (Fig. 3.1a. Previously in our lab, we have shown that the mechanical properties of collagen obtained through SHG and ICS correlated to those obtained by rheology or scanning electron microscopy images [Chiu et al. (2013); Raub et al. (2008)]. For this analysis, the  $\omega_o$  value gives the waist of the auto-correlation function and based on the size of the point spread function of the laser (roughly  $0.3 \mu\text{m}$  at the waist). A larger  $\omega_o$  indicates thicker fibers.  $1/G(0)$  quantified the density of the matrix which is the height of the auto-correlation function extrapolated from the first



measured point. A smaller  $1/G(0)$  value corresponds to denser matrices. 3.0 mg/mL and 1.2 mg/mL collagen substrates showed similar average values of  $\omega_o$  of 2.55 and 2.29 (Fig. 3.1c). However, the 3.0 mg/mL collagen has a significantly larger average value of  $1/G(0)$  of 5.54 compared to that of the 1.2 mg/mL collagen at 1.09 (Fig. 3.1d). This confirms that the 3.0 mg/mL collagen substrates have a denser network of collagen although their fiber thicknesses are similar. Rheology measurements were also done to quantify the modulus of the substrates. 3.0 mg/mL and 1.2 mg/mL collagen substrates were measured and have averages of 38.12 Pa and 5.66 Pa, respectively (Fig. 3.1b), showing that the 3.0 mg/mL collagen substrates are about one order of magnitude stiffer than the 1.2 mg/mL substrate.

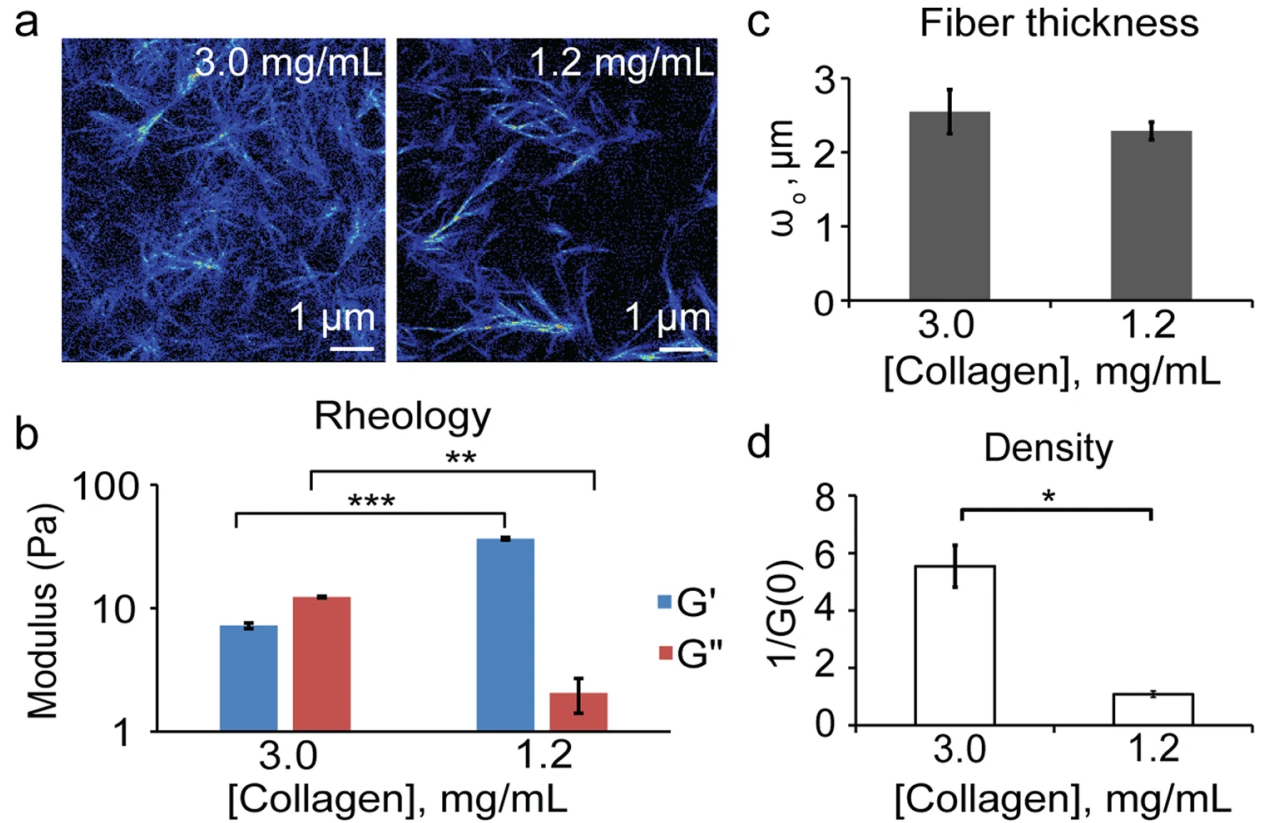


Figure 3.1: Quantification of collagen substrates. (a) Second harmonic generation images of 3.0 mg/mL ( $n=9$ ) and 1.2 mg/mL collagen substrates ( $n=7$ ); where  $n$ =total number of collagen samples measured. (b) Modulus of collagen substrates at 10% strain and 1 Hz. (c) Quantification of fiber size ( $\omega_o$ ) and (d) density of collagen substrates. \* $p<1e-3$ , \*\* $p<1e-26$ , \*\*\* $p<1e-57$ .

### 3.3.2 Triple-negative breast cancer cells shifts towards glycolytic signatures on denser collagen substrates

By measuring NADH fluorescence lifetimes with FLIM, we were able to non-invasively determine spatial shifts in the metabolism of different cell lines in response to collagen density. NADH has two different lifetimes when it is free in the cytosol, 0.4 ns, or bound to a protein, ranging from 1.4 ns to 9 ns [Jameson et al. (1989); Skala et al. (2007)]. Thus, we are able to distinguish the ratio of free and bound NADH at each pixel. For our studies, the lifetime of NADH bound to lactate dehydrogenase (LDH, 3.4 ns) is used when quantifying the population of bound NADH, although there are many other possible enzymes [Datta et al. (2015); Ma et al. (2016)].

The lifetime decay measured is Fourier transformed and displays a graphical representation of fluorescence lifetime on the phasor plot where all single exponential decay lifetimes are plotted on the semi-circle (called the universal circle) and all multi-exponential lifetimes are inside the semicircle representing the sum of linear combinations of single-exponential lifetimes. Figure 3.2a depicts the fluorescence lifetime of free NADH (0.4 ns) and 100% bound (3.4 ns) NADH to LDH. If the binding is not complete, we can calculate the ratio of bound to free NADH from the pure free and bound linear combination of lifetimes. In our control, the population of the percentage bound to NADH was 75% . This linear trajectory is indicative of GLY and OXPHOS state in live cells [Digman et al. (2008); Stringari et al. (2012a)].

Highly invasive MDA-MB-231 cells were seeded on collagen and glass substrates to observe changes in free:bound ratios of NADH. In addition, the free:bound ratio of NADH in non-tumorigenic breast cells MCF-10A were used as a control for a non-tumorigenic cell line. MDA-MB-231 cells showed an 8.0% and 11.8% increase of bound NADH on 3.0 mg/mL and 1.2 mg/mL substrates, respectively, relative to those on glass (Fig. 3.2b). This indicates that as collagen density increased, the MDA-MB-231 cells shifted from OXPHOS (white/cyan)

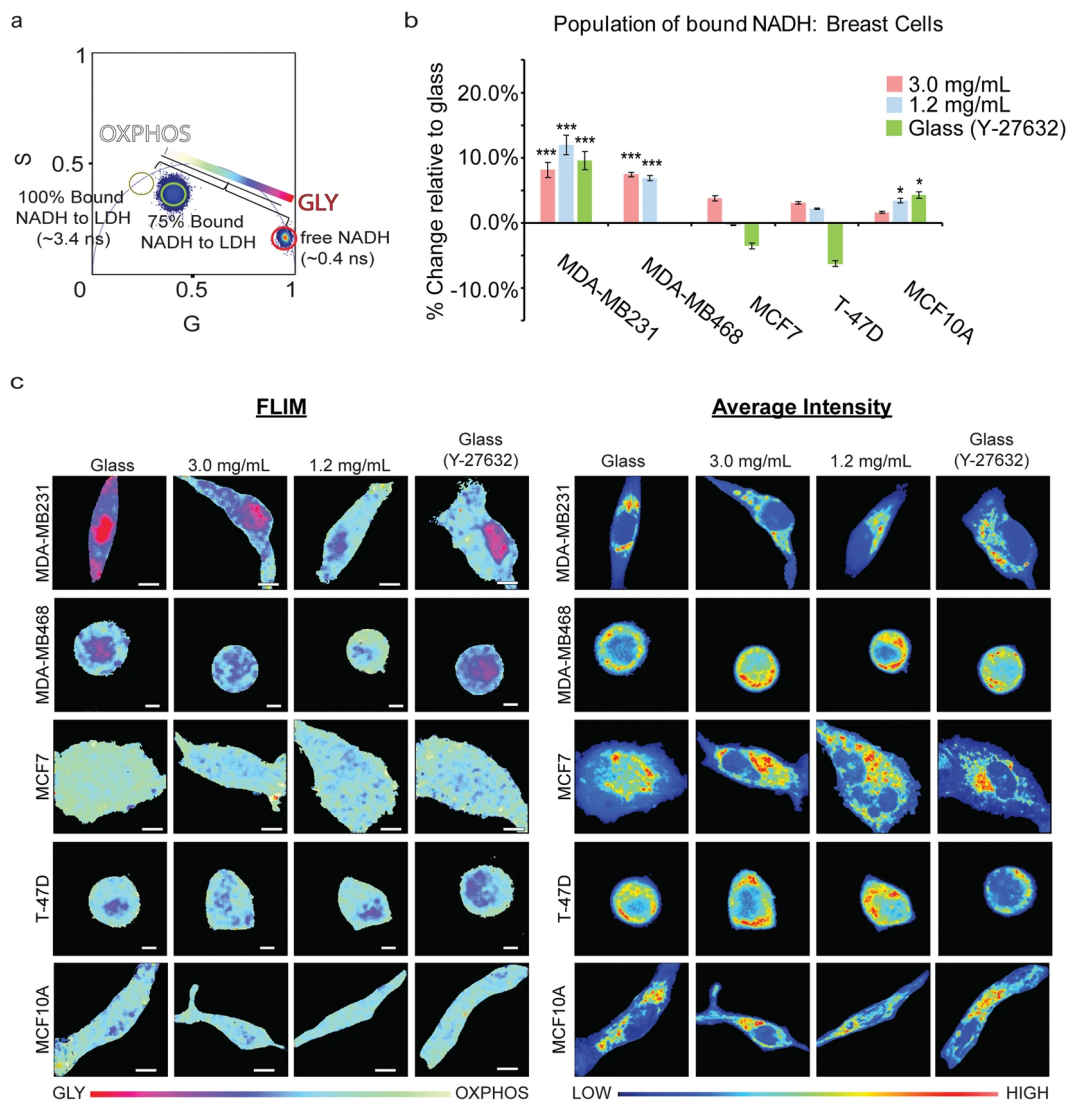


Figure 3.2: Metabolic indexes of MDA-MB-231 (3.0 mg/mL: n=71; 1.2 mg/mL: n=53; Glass: n=77; Glass (Y-27632): n=33), MDA-MB-468 (3.0 mg/mL: n=20; 1.2 mg/mL: n=20; Glass: n=5; Glass (Y-27632): n=5), MCF-7 (3.0 mg/mL: n=20; 1.2 mg/mL: n=21; Glass: n=20; Glass (Y-27632): n=21), T-47D (3.0 mg/mL: n=5; 1.2 mg/mL: n=5; Glass: n=5; Glass (Y-27632): n=5), and MCF-10A (3.0 mg/mL: n=64; 1.2 mg/mL: n=59; Glass: n=63; Glass (Y-27632): n=26) cells on various collagen densities. (a) An increased population of bound NADH to LDH (long lifetime NADH, cyan) is indicative of a more OXPPOS signature while an increased population of free NADH (short lifetime NADH, red) would indicate GLY. These two extremes create a linear “M-trajectory” where a mixed population of bound and free NADH, for example 75%, will lie between these two points. (b) Percent increase of bound NADH in MDA-MB-231, MDA-MB-468, MCF-7, T-47D, and MCF-10A cells relative to glass. (c) Colored images of FLIM of NADH and the average intensity of NADH within MDA-MB-231, MDA-MB-468, MCF-7, T-47D, and MCF-10A cells. n=total number of cells measured. \*p<0.05, \*\*p<0.01, and \*\*\*p<0.001 by Student’s t-test. Scale bar: 5  $\mu$ m. Error bars are based on standard deviation.

to GLY (pink/red) (Fig. 3.2c). Similarly, MDA-MB-468 showed a 7.4% and 6.9% increase in bound NADH on the 3.0 mg/mL and 1.2 mg/mL substrates, respectively, marking a highly significant change ( $p < 0.001$ ) when compared to the cells plated on glass. These results indicate that MDA-MB-468 cells shift to an increased OXPHOS signature when cultured on a less dense substrate.

These cells on glass were then treated with 10  $\mu$ M Y-27632, a ROCK inhibitor that decreases cell contractility, to assess if inhibiting the cell's mechanosensing ability would shift the metabolism towards OXPHOS. Indeed, we see a significant change in the metabolic index (9.5% increase in bound NADH) in MDA-MB-231 cells when Y-27632 was added (Fig. 3.2b). Similar results were seen on MDA-MB-231 cells on glass when treated with 3.5  $\mu$ M blebbistatin, showing a 16.1% increase relative to untreated glass samples (Fig. B.1). Interestingly, unlike the MDA-MB-231 cells, MDA-MB-468 cells showed no significant difference in bound NADH compared to the cells plated on glass when treated with 10  $\mu$ M of Y-27632. We also used both treatments on MDA-MB-231 cells plated on 1.2 mg/mL and 3.0 mg/mL collagen and detected an increase in the bound NADH population as well (Fig. B.2). MCF-10A cells also showed this shift in metabolism in response to collagen density but to a less drastic compared to the MDA-MB-231 cells (Fig. 3.2b,c). MCF-7 and T-74D cells also showed similar trends in the average increase of bound NADH relative to when they are grown on glass, although the changes were not significant. We also examined other cancer cell lines to determine if they also had the same response to collagen density. These results are shown below.

Melanoma, A-375 MM, and glioblastoma, U-251 MG, cell lines showed different results than that of the TNBCs. A-375 MM cells showed no significant change in the free:bound ratio of NADH when on the 1.2 mg/mL or 3.0 mg/mL collagen substrates or glass (Fig. 3.3a,b). We noticed that these cells did not adhere as well on the collagen substrates due to their round morphology (Fig. 3.3c) which could be the reason why there was no change in metabolism as seen in the TNBCs. This further supports our hypothesis that the mechanosensing pathway

plays an important role in cancer cell metabolism. The U-251 MG cells showed increased glycolytic signatures on average as collagen density decreased, although the results were not statistically significant. Previous studies have also shown that MDA-MB-231 and U-251 MG have opposite trends of matrix degradation and invadopodia formation when they are cultured in different media supplemented with GLY or OXPHOS inhibitors [van Horssen et al. (2013)]. This may explain our results, but further studies will need to be conducted to confirm them.

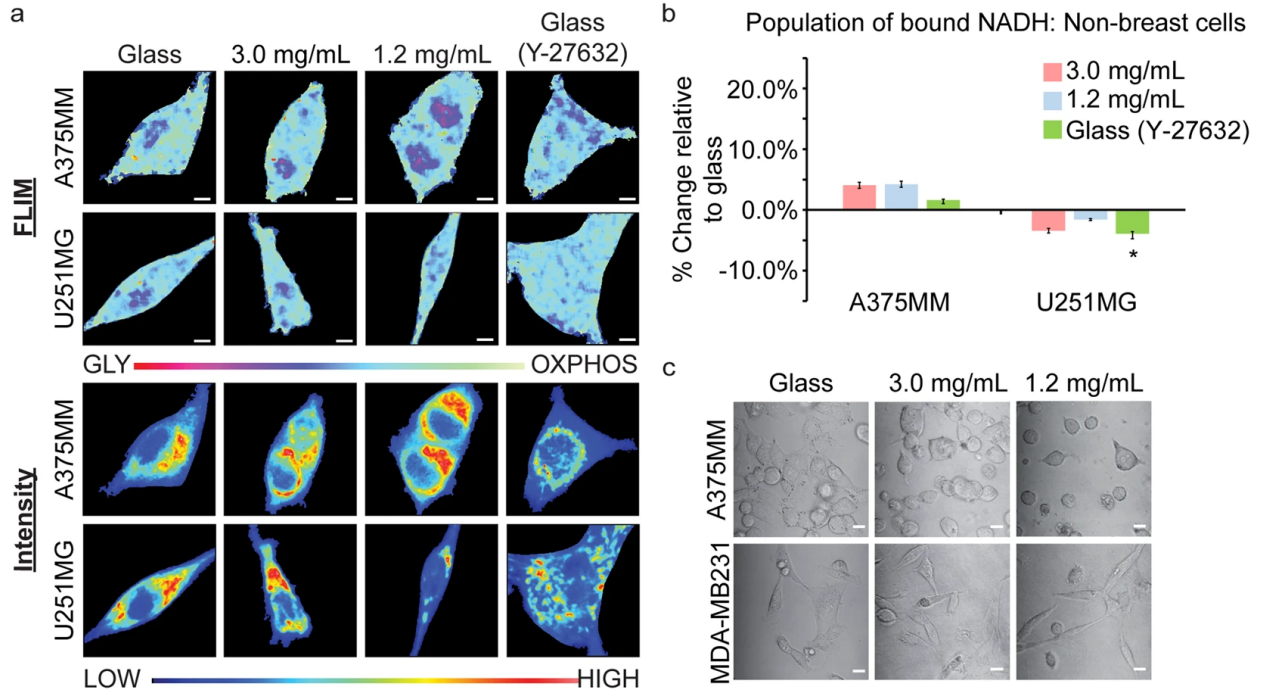


Figure 3.3: Metabolic indexes of A-375 MM (3.0 mg/mL: n=24; 1.2 mg/mL: n=23; Glass: n=24; Glass (Y-27632): n=28) and U-251 MG (3.0 mg/mL: n=28; 1.2 mg/mL: n=30; Glass: n=26; Glass (Y-27632): n=22) cells on various collagen densities. (a) FLIM and average intensity images of NADH within A-375 MM melanoma and U-251 MG glioma cell lines. (b) Quantification of the percent change of NADH within A-375 MM and U-251 MG cell lines on various substrates relative to those on glass. (c) Transmitted optical images of A-375 MM and MDA-MB-231 cells on different substrates. n=total number of cells measured. \*p<0.05, by Student's t-test. Scale bar: 5  $\mu$ m. Error bars are based on standard deviation.

We isolated the metabolic phasor signature of the nucleus and the cytoplasm and compare them here across all surfaces in each cell line (Fig. B.3). Generally, the nucleus of the cell lines has a more GLY signature than the cytoplasm, but this did not significantly affect the

results we found when looking at the entire cell within MDA-MB-231 and MCF-10A cells. However, within A-375 MM cells seeded on 3.0 mg/mL or 1.2 mg/mL collagen substrates, their populations of bound NADH were similar; but when looking at their nuclei and cytoplasmic, we began to see a separation between the two conditions, especially in the nuclei alone. The nuclei in A-375 MM cells on 3.0 mg/mL collagen substrates show a shift towards GLY where their population of bound NADH decreased by 29.5% compared to those on glass. U-251 MG cell nuclei metabolic indices were similar on all surfaces except for those on glass and treated with blebbistatin, which showed a 13.3% decrease in the population of bound NADH. We also looked at NIH-3T3 fibroblast cells to observe if these changes can be seen in other cell types, but the results showed no change (Fig. B.4).

The rest of this report will focus mainly on the MDA-MB-231 and MCF-10A cells to compare the results of cancerous and non-tumorigenic cell lines. In order to confirm that the fraction of free:bound ratio of NADH is modulated through collagen density, we conducted metabolism inhibition studies of each cell line when seeded on both collagen and glass substrates.

### **3.3.3 Metabolism inhibition studies confirm that GLY and OXPHOS are modulated by collagen density**

In order to ensure that the collagen density alters metabolism in MDA-MB-231 and MCF-10A cells and that these changes correlate with lifetime positions along the M trajectory, we treated these cell lines with oxidative phosphorylation and glycolysis inhibitors. We treated MDA-MB-231 cells with 50 mM 2-deoxyglucose and 100 mM dichloroacetate (2DG&DCA) for GLY inhibition and 50 nM rotenone and 50 nM antimycin A (R&A) for OXPHOS (Fig. 3.4a,b). These inhibitors are known used to shift the metabolic signatures towards OXPHOS or GLY [Caino and Altieri (2015); Cinco et al. (2016); Morris et al. (2016); Stringari et al. (2012a)]. 2DG&DCA treatment showed an increased population of bound NADH of 20.5%, 11.7% and 10.6% for cells plated on glass, 3.0 mg/mL collagen, and 1.2 mg/mL collagen



surfaces, respectively, relative to untreated cells (Fig. 3.4c). When MDA-MB-231 cells were treated with R&A on glass, 3.0 mg/mL and 1.2 mg/mL collagen substrates, they showed significant decreases in the population of bound NADH,  $p < 0.0001$ , of 8.17% , 14.2% and 13.2% , respectively, relative to untreated cells. These treatments were also applied to MCF-10A cells where we observed a significant decrease in the population of bound NADH only on 3.0 mg/mL collagen substrates, 3.39% , and glass, 10.7% , when treated with R&A (Fig. 3.4d). No changes were seen on the 1.2 mg/mL collagen substrates. However, there was a significant increase of 11.3% in these cells which were treated with 2DG&DCA.

### 3.4 Discussion

The Warburg effect is the hallmark of cancer cell metabolism, described as an oncogene-directed glycolytic state even when oxygen is present [Heiden et al. (2009); Liberti and Locasale (2016); Ward and Thompson (2012)]. This could be due to the high turnover of ATP production through glycolysis for energy production with glucose, although the alternative process of oxidative phosphorylation creates more product of energy per glucose molecule. Cancer cell invasion has also been shown to be modulated by changes in metabolism through changing cell media additives for energy consumption [Scott et al. (2012); van Horsen et al. (2013)] or the ECM stiffness and density [Artym et al. (2015); Gould and Courtneidge (2014); Paszek et al. (2005); Provenzano et al. (2008); Seewaldt (2014)]. However, the link between ECM stiffness or density and cell metabolic state (OXPHOS or GLY) is not clear. Recent studies that look at alterations of metabolism use invasive biochemical assays that do not report the spatial heterogeneous changes of metabolic response within cellular compartments, nor their cellular metabolic state. Our study used FLIM of NADH to measure real-time metabolic indexes of different cancer cell types in response to collagen density. This allows us to characterize which metabolic process occurs with pixel resolution in live cells. It is important to note that since different additives change cellular metabolism, our culture

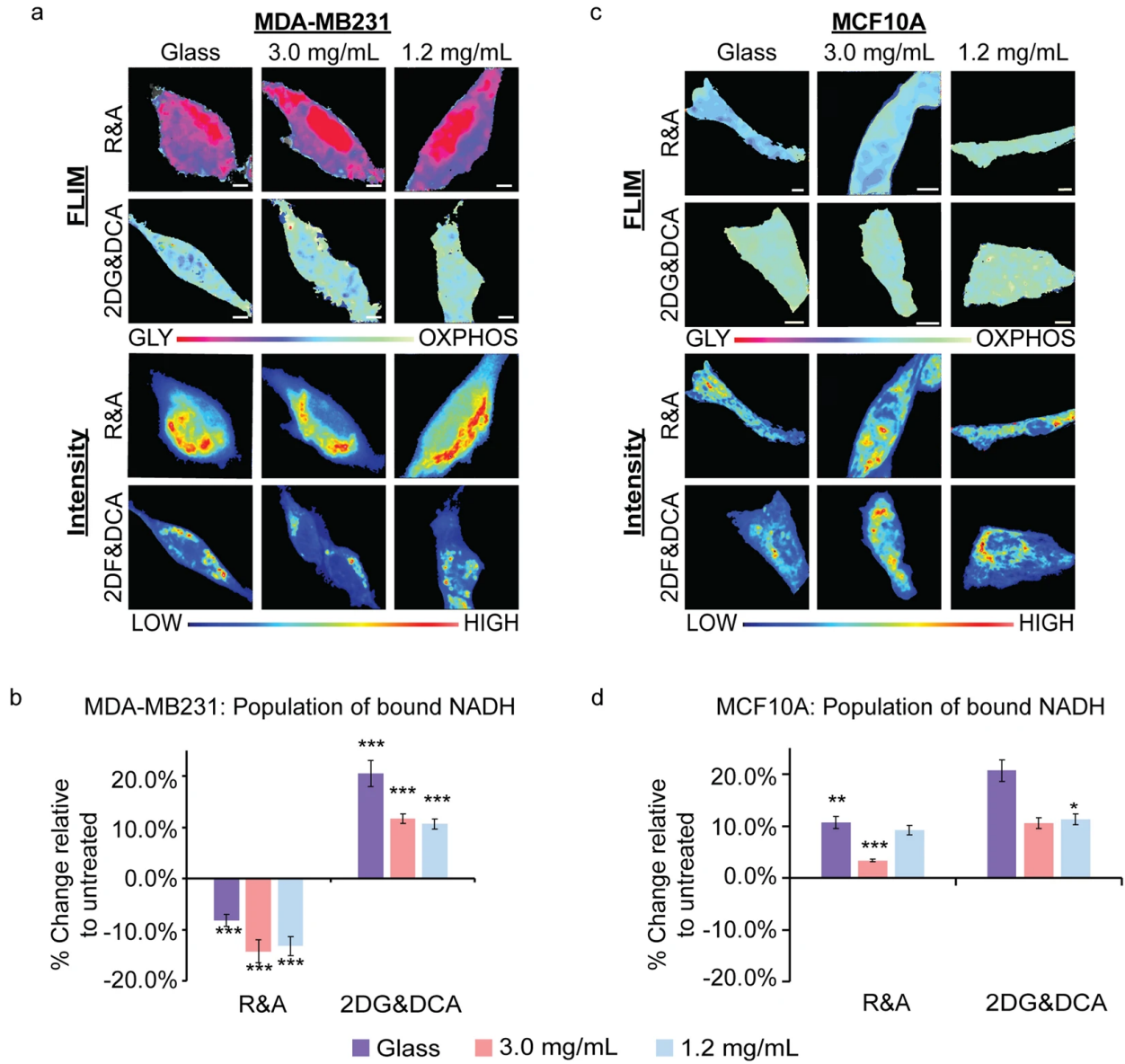


Figure 3.4: MDA-MB-231 and MCF-10A metabolic indexes when treated with metabolic inhibitors. (a) MDA-MB-231 and (b) MCF-10A cells treated with rotenone and antimycin A (R&A) or 2-deoxyglucose and dichloroacetate (2DG&DCA) for OXPHOS or GLY inhibition, respectively. FLIM images show the shifts in metabolic indexes with respective intensity images below. (c) Quantification of the change of bound NADH in MDA-MB-231 with R&A (Glass: n=29; 3.0 mg/mL: n=29; 1.2 mg/mL: n=29) or 2DG&DCA (Glass: n=29; 3.0 mg/mL: n=19; 1.2 mg/mL: n=21) relative to untreated cells. (d) Quantification of the change of bound NADH in MCF-10A with R&A (Glass: n=25; 3.0 mg/mL: n=20; 1.2 mg/mL: n=15) or 2DG&DCA (Glass: n=21; 3.0 mg/mL: n=24; 1.2 mg/mL: n=22) relative to untreated cells. n=total number of cells measured. \*p<0.05, \*\*p<0.01, and \*\*\*p<0.001 or less by Student's t-test. Scale bar: 5  $\mu$ m. Error bars are based on standard deviation.



conditions for our cells remained the same through the study. Each cell line required different culturing conditions independently, but their media used was the same when measurements were taken. Thus, we are able to observe their respective metabolism changes in response to collagen density.

We have found that MDA-MB-231, MDA-MB-468, and MCF-10A cells on substrates on two different collagen densities have an increasing population of free NADH, showing a more glycolytic signature of metabolism. The effect was even greater on the MDA-MB-231 and MDA-MB-468 TNBC metastatic cells. This correlates with previous studies in that breast cancer cells have increased migration and aggressiveness within denser collagen matrices [Haage and Schneider (2014); Levental et al. (2009); Paszek et al. (2005)]. In addition, cancer cells undergo aerobic glycolysis for energy production, thus increased collagen density could be a contributor to the metabolic shift towards glycolysis [Liberti and Locasale (2016); Morris et al. (2016)]. The ECM plays a key role in the cancer cell's mechanosensing pathway through integrin signaling, and there is increasing evidence that this regulates cell migration and matrix degradation [Alexander et al. (2008); Beaty et al. (2013); Chiu et al. (2013); van Horssen et al. (2013)]. Increased ECM stiffness and density signals actin polymerization, upregulated integrin signaling, and stabilization of the focal adhesion complexes [Ciobanaru et al. (2013); Gardel et al. (2010); Hirata et al. (2014)]. This increase of integrin signaling has been shown to also upregulate the PI3K/AKT/mTOR pathways and possible metabolism switching in cancer cells [Ata and Antonescu (2017); Caino and Altieri (2015); Lien et al. (2016); Yang et al. (2015)]. In addition, stimulating the actin-contraction of cells through external forces by shear flow or pulling of the cell membrane elevates glucose uptake [Bays et al. (2017); Hayashi et al. (1998)]. Bays et al. has shown that this increased glucose uptake was also shown to increase ATP production for actin polymerization and stabilize E-cadherin contacts [Bays et al. (2017)]. Our results expanded on these studies by looking at the specific metabolic indexes of cancer cells when introduced to various collagen density. We speculate

that these same pathways are being activated in the TNBCs and are stimulated passively through focal adhesion-mediated interactions with the ECM.

When cells grown on glass substrates were treated with Y-27632 or blebbistatin, we inhibited their ability to undergo contraction through myosin-II and caused focal adhesion detachment from the substrate [Martin et al. (2016)]. This, in turn, showed shifts in metabolic indexes from GLY to OXPHOS in MDA-MB-231 and MCF-10A cells. This confirms that it is through actin-mediated cell contractility that modulated these shifts in metabolism. Interestingly, the MDA-MB-231 cells treated with Y-27632 had a similar NADH free:bound ratio as those grown on 3.0 mg/mL, which could mean that their degrees of contractility were similar to each the respective conditions. Those treated with blebbistatin had a much larger shift towards OXPHOS, surpassing the population of bound NADH of cells grown on 1.2 mg/mL collagen. Since blebbistatin directly affects myosin-II and is more potent than Y-27632, this was as expected. Previous studies have shown that stable adhesions have a developed mechanosensing network of actin, and these adhesions can grow in response to forces or increasing substrates stiffness [Bieling et al. (2016); Kim and Wirtz (2013); Petit and Thiery (2000); Wells (2008)]. Thus, cells on the denser substrates should have the most stable adhesions. In turn, they would also have increased FAK which promotes glucose consumption and plays a key role in the OXPHOS and GLY balance within cancer cells [Palorini et al. (2013)].

The human melanoma cell lines, A-375 MM, in this study attached to 1.2 mg/mL and 3.0 mg/mL collagen substrates but did not spread as well as all other cells. This was an indication that their adhesions are not stable or favorable on these substrates [Calderwood et al. (2013); Cavalcanti-Adam et al. (2007); Massia and Hubbell (1991)] and their mechanosensing ability could have been compromised and reduce mitochondria activity [Ochsner et al. (2010)]. Consequently, this would fail to change the metabolic indexes of these cells as shown in our results; where the NADH free:bound of A-375 MM on 1.2 mg/mL or 3.0 mg/mL have no

difference. This phenotype showed that there is a confirmed link between focal adhesion-mediated mechanosensing and cellular metabolism.

Glioblastoma cells, U-251 MG also showed no change in the population of bound NADH as collagen density decreased. It is important to note that there are many other possible uses for pyruvate aside from OXPHOS in the mitochondria. Downstream of GLY are intermediates of the tricarboxylic acid cycle, such as citrate, which allows for the synthesis of lipids, proteins and nucleic acids, a demand for highly proliferating cells [DeBerardinis et al. (2008)]. There is also fatty acid synthesis through citrate which is shown to correlate with the formation of invadopodia, which are actin-rich protrusions used for matrix invasion [Gould and Courtneidge (2014); Morris et al. (2016); Scott et al. (2012)]. In addition, the pentose phosphate pathway could further increase the GLY and fraction of free NADH. All of the pathways mentioned could be elevated within MDA-MB-231 cells, which could contribute to their difference in metabolic trends from the U-251 MG cells when collagen density is varied.

There is still the question of whether or not the shifts in metabolic signatures are unique to TNBCs. Based on the results reported here, this seems to be the case. Since we are changing the concentration of collagen to tune the density of the substrates, the density of ligands for integrin binding also varies. At the same time, an increase of substrate stiffness has been shown to upregulate FA signaling as well [Indra and Beningo (2011); Ng and Brugge (2009)]. Thus, it is possible that the increase of integrin expression itself is the primary cause of the metabolism shifts [Artym et al. (2015); Beaty et al. (2013)]. Within in vivo systems, an increase in collagen density results in a stiffer ECM, which our system aimed to represent.

The TNBCs have a significant decrease in the fraction of bound NADH when plated on glass, 3.0 mg/mL and 1.2 mg/mL collagen, respectively. Although the percent of bound NADH of MDA-MB-468 cells on both collagen substrates increased compared to glass, there is no significant difference of bound NADH between the two collagen substrates. This variation from the MDA-MB-231 cell line could be due to the cell's phenotype. MDA-MB-468

cells are much rounder than the MDA-MB-231 cells in every condition. This roundness likely indicates a decreased adherence to the substrate, and thus, when plated on the two much less dense collagen substrates, may have reached a plateau in its adhesion. This lack of change in adherence may be the cause of the non-significant changes in the free:bound ratio between the two collagen substrate conditions, however additional work is required to confirm this hypothesis. MCF-7 and T-47D cells were shown to have similar trends of their average bound NADH when comparing them side-by-side. These two cell lines are similar in their genotype of ER+, PR+, and HER2-. Expression levels of ER+, PR+, HER2- are known to play an important role in cellular metabolism, thus these results are not surprising [Walsh et al. (2012)].

We confirmed that the changes in the metabolic trajectory of the MDA-MB-231 cells were reflective in cellular metabolism using the OXPHOS and GLY inhibitors. When these inhibitors were added, cells shifted their metabolism accordingly to their inhibitors but there were no significant metabolic differences across collagen densities within these changes (Fig. B.5a). However, the MCF-10A cell lines did not show any changes in metabolic indexes across substrate densities in their untreated conditions. They did show substrate sensitivity only when OXPHOS was inhibited. When R&A was added to inhibit OXPHOS in MCF-10A cells on the 3.0 mg/mL and glass substrates, there was a maximum decrease to around 63.8% of the population of bound NADH; however, those on 1.2 mg/mL collagen showed no significant change (Fig. B.5b). This could mean that on denser collagen substrates, these cells were more susceptible to metabolic changes when introduced to inhibitors. Additionally, this could also indicate that the metabolism of the MCF-10A cells was behaving more like the MDA-MB-231 cells on the denser matrices. When 2DG&DCA was added to inhibit GLY in MCF-10A cells, we see an increase in the population of bound NADH to around 71.8% when grown on 1.2 mg/mL collagen substrate. Since OXPHOS and an environment with less collagen is preferable for the MCF-10A cells, this could mean that this ECM provides an extra boost towards OXPHOS pathway when GLY is inhibited.

The phasor approach to FLIM of NADH allows isolation of the metabolic signature within sub-cellular compartments of the cells. Here, we focused on comparing the nuclei and cytoplasm of MDA-MB-231, MCF-10A, A-375 MM, and U-251 MG cell lines (Fig. B.3). We were able to see that the metabolic shifts within the nuclei and cytoplasm of MDA-MB-231 and MCF-10A cells are similar to their whole cell signature. However, within A-375 MM cells we were able to make distinctions of the population of bound NADH between surfaces, which were not detected when averaging over the entire cell. The nuclei of A-375 MM cells on 3.0 mg/mL collagen substrates has a significant decrease in the population of bound NADH with respect to those on glass. Thus, looking at the nuclear metabolic indexes can separate subtle changes that are hidden in whole cell readings. These distinctions seen could be due to nuclear processes, such as transcription or DNA repair, which has also been shown to affect the ratio of bound and free NADH [Aguilar-Arnal et al. (2016); Wright et al. (2012)].

We have shown that focal adhesion-mediated contractility modulates cell metabolism in MDA-MB-231 cancer cells. With the use of FLIM of NADH, we were able to non-invasively measure metabolic changes of cancer cell lines MDA-MB-231, MDA-MB-468, T-47D, MCF-7, A375M, U-251 MG and within non-tumorigenic lines MCF-10A, and NIH-3T3. Particularly in triple-negative breast cancer lines, MDA-MB-231 and MDA-MB-468, we saw that less dense collagen substrates shifted cells to have a more OXPHOS metabolic signature due to their increased population of bound NADH. Further studies by inhibiting myosin-II contractility increased the population of bound NADH in MDA-MB-231 cells across all surfaces and confirmed our hypothesis. This further supports that ECM mediated adhesions are up-regulated due to substrate density and modulates metabolic signatures. We also confirmed that the changes in NADH free:bound in MDA-MB-231 and MCF-10A cells were due to GLY or OXPHOS by inhibiting these pathways with dichloroacetate and 2-deoxyglucose or rotenone and antimycin A, respectively. With our results combined with what is known in literature, there is a relationship between the mechanosensing and metabolism pathway in cancer cells and both play a critical role in regulating cancer invasiveness. This provides

insight to develop therapies which target mechanosensing abilities of cancer cells to revert their metabolism similar to a more non-tumorigenic cell type or decrease their invasiveness.

## **3.5 Materials and Methods**

### **3.5.1 Cell culturing and transfections**

MDA-MB-231, MDA-MB-468, T-47D, MCF-7, NIH-3T3, and A-375 MM cells were cultured in Dulbecco's Modified Eagle's Medium (DMEM) with high glucose, L-glutamate, and sodium pyruvate (Genesee Scientific, San Diego, CA) supplemented with 10% heat-inactivated Fetal Bovine Serum (Thermofisher Scientific, USA) and 1% Penicillin - Streptomycin 100X Solution (Genesee Scientific, San Diego, CA). U-251 MG cells were cultured in DMEM / F12 with also with high glucose, sodium pyruvate and L-glutamine (Thermofisher Scientific, USA) supplemented with 10% heat-inactivated Fetal Bovine Serum (Thermofisher Scientific, USA) and 1% Penicillin-Streptomycin 100X Solution (Genesee Scientific, San Diego, CA). MCF-10A cells were also cultured in DMEM/F12 with high glucose, sodium pyruvate and L-glutamine (Thermofisher Scientific, USA) supplemented with 5% horse serum (Thermofisher Scientific, USA), 20 ng/mL epidermal growth factor, 0.5 mg/mL Hydrocortisone (Sigma-Aldrich, St. Louis, MO), 100 ng/mL cholera toxin (Sigma-Aldrich, St. Louis, MO), 10  $\mu$ g/mL insulin (Sigma-Aldrich, St. Louis, MO), and 1% Penicillin-Streptomycin 100X Solution (Genesee Scientific, San Diego, CA). All cell lines were incubated at 37 °C, 5% CO<sub>2</sub>.

### **3.5.2 Collagen substrate monolayers**

Substrates were made on 35 mm glass bottom imaging dishes which were treated for 5 minutes with UV-ozone. 1% v/v of 3-aminopropyltriethoxysilane (APTES) in deionized water were added and allowed to sit for 25 minutes at room temperature. The dishes were washed

thoroughly with deionized water and brought to the biosafety hood for sterile handling. 1 mL of sterilized MilliQ water used to rinse the dish before collagen was added.

For collagen preparation, microcentrifuge tubes and reagents used were kept on ice for as long as possible while handling. Collagen I from rat tail (Corning, Corning, NY) was diluted with deionized water such that the final concentration was either 1.2 mg/mL or 3.0 mg/mL. 100  $\mu$ L of 10X phosphate buffer saline (Thermofisher Scientific, USA) containing phenol red was added dropwise while vortexing as a pH indicator. 0.5 N NaOH was then added dropwise to the mixture with periodic vortexing until the solution became a slight pink (pH 7). The collagen was then added to the treated imaging dish (total volume of 1 mL) and incubated at 20 °C for 1 hour and then at 37 °C, 5% CO<sub>2</sub> overnight. 0.25e6 cells were then added to each dish the next day and then allowed to incubate at 37 °C, 5% CO<sub>2</sub> overnight again before imaging took place.

### **3.5.3 Inhibition studies**

Contractility inhibition was done with Y-27632 (Selleckchem, US) or blebbistatin (Sigma-Aldrich, St. Louis, MO) at a working concentration of 10  $\mu$ M and 3.5  $\mu$ M, respectively. Each inhibitor was incubated for 10 minutes at room temperature before conducting FLIM/NADH imaging. MDA-MB-231 or MCF-10A cells were treated with sodium dichloroacetate (Sigma-Aldrich, St. Louis, MO) and 2-deoxyglucose (Sigma-Aldrich, St. Louis, MO) at a working concentration of 100 mM and 50 mM, respectively, for 6 hours at 37 °C, 5% CO<sub>2</sub> to inhibit glycolysis. Similarly, cells were treated for 10 minutes with 50 nM rotenone and 50 nM antimycin A at 37 °C, for oxidative phosphorylation inhibition studies before NADH lifetimes were measured.

### 3.5.4 Characterization of collagen substrates

Rheology measurements of collagen substrates were conducted to obtain the storage ( $G'$ ) and loss ( $G''$ ) moduli. The collagen substrates were pre-made on 15 mm glass slides that were treated with UVO and APTES as described above. Collagen solutions of 1.2 mg/mL or 3.0 mg/mL were carefully pipetted onto the round glass slides and allowed to incubate at 20 °C for 1 hour and then at 37 °C overnight for 2 nights to mimic culturing conditions for imaging. The glass slides were placed on the stage of the AR-G2 rheometer (TA Instruments, New Castle, DE) that was kept at a constant temperature of 37 °C. A sand-blasted parallel plate geometry with a diameter of 25 mm was lowered to a gap distance of 0.3 mm so that it was in close contact with the surface of the collagen. Rheology measurements were conducted at a constant sinusoidal frequency of 1 Hz and 10% peak-to-peak strain and outputs of  $G'$  and  $G''$  were recorded for a total of 10 minutes. A data point was taken every 60 seconds.

Second harmonic generation imaging of collagen substrates was conducted to characterize substrate density as previously [Chiu et al. (2013); Raub et al. (2007)]. Briefly, 2-photon excitation at 900 nm was used to generate second harmonics of collagen and collected with a bandpass filter at 460/80 nm with external photon-multiplier tubes (H7422P-40, Hamamatsu, Japan) and FastFLIM FLIMBox (ISS, Champaign, IL). 100 frames were collected and analyzed using image correlation spectroscopy on SimFCS (LFD, UCI). Spatial correlations were applied to each pixel at coordinate (x, y) of the compiled SHG images with equation 3.1:

$$G_S(\xi, \phi) = \frac{\langle I(x, y) * I(x + \xi, y + \phi) \rangle_{x,y}}{\langle I(x, y) \rangle_{x,y}^2} - 1 \quad (3.1)$$

where  $I$  is the intensity.  $\xi$  and  $\phi$  are the spatial shifts in the x and y directions, respectively.



### 3.5.5 Confocal and fluorescence lifetime imaging acquisition and analysis

FLIM images for MDA-MB-231, U-251 MG, and A-375 MM cells were imaged on the Zeiss LSM 710 (Carl Zeiss, Jena, Germany), LSM 880 (Carl Zeiss, Jena, Germany), and Olympus Fluoview respectively. MCF-10A, T-47D, and MDA-MB-468 cells were also imaged on the LSM710. Metabolism inhibition studies of MDA-MB-231 and MCF-10A cells were imaged on the Olympus Fluoview. Images ( $256 \times 256$  pixel size) were taken at a pixel dwell time of  $25.21 \mu\text{s}$ ,  $16.38 \mu\text{s}$ , and  $20 \mu\text{s}$  for the LSM710, LSM880, and Fluoview, respectively. All microscope systems were coupled to with a two-photon Ti: Sapphire laser (Spectra-Physics MaiTai, Mountain View, CA) for NADH excitation at 740 nm with an Olympus 40X/0.8 NA water objective. The emission was separated at 690 nm in all systems followed by two bandpass filter at 460/80 nm and 540/50 nm with a with a dichroic mirror 495 nm long-pass filter. The signal was collected with an external photomultiplier tube (H7422P-40, Hamamatsu, Japan). A320 FastFLIM FLIMbox (ISS, Champaign, IL) was used to acquire the frequency domain of the lifetime of NADH until enough statistics were obtained. The experiments for all cells (except for the T-47D and MDA-MB-468 cells) were repeated in triplicate. Images of coumarin-6 in ethanol were also taken as reference and calibration for FLIM measures across all microscopes.

SimFCS (LFD, UCI) was used to analyze the fluorescence lifetime of NADH at every pixel. The lifetime decay at each pixel was Fourier transformed and plotted on a phasor plot as previously described where each point on the phasor represents one pixel [Digman et al. (2008)]. Each cell's cluster of phasor points was averaged to obtain their S, G, and fraction bound value. Calculations for S and G for the in-phase and out-of-phase signals are shown in equations 3.2 and 3.3 respectively. I is the intensity of the pixel at point (x, y) and  $\omega$  is the angular frequency of the light modulation. Average phasor plots of the data are shown

in Figure B.6.

$$S_{x,y} = \frac{\int_0^{\text{inf}} I_{x,y}(t) \sin(\omega t) dt}{\int_0^{\text{inf}} I_{x,y}(t) dt} \quad (3.2)$$

$$G_{x,y} = \frac{\int_0^{\text{inf}} I_{x,y}(t) \cos(\omega t) dt}{\int_0^{\text{inf}} I_{x,y}(t) dt} \quad (3.3)$$

The fraction of bound NADH is calculated based on the fact that any two points on the phasor plot (e.g. 100% free NADH and 100% bound NADH to LDH) can be connected by a line and any points along that line will be a linear representation of the two extremes. Thus, the experimental data will exist between 100% free NADH and 100% bound NADH, signifying samples that have a mixture of free and bound NADH. Those points that are closer to the phasor of bound NADH to LDH will have a higher population of bound NADH.

### 3.5.6 Statistical analysis

Statistical significance was determined for experiments with the Student's t-test (two-sample, variance based on F-test) in Microsoft Excel.

## 3.6 Acknowledgements

The authors sincerely thank Dr. Enrico Gratton, Director of the Laboratory for Fluorescent Dynamics, for his advice on image correlation spectroscopy; Michael Murata, Andrew Trinh, Ning Ma, and Sara Sameni for their advice on NADH FLIM data; Jeremy Jacinto for organizing figures for this manuscript; the Daniela Bota Lab at UC Irvine for donating U-251 MG cells, the Feng Liu-Smith lab at UC Irvine for donating A-375 MM cells, and the Olga Razorenova Lab at UC Irvine for donating T-47D and MDA-MB-468 cells. This work was supported by the National Institutes of Health grant 2P41GM103540, in part by

the American Cancer Society Institutional Research Grant 129801-IRG-16-187-13-IRG from the American Cancer Society, and by the National Science Foundation Graduate Research Fellowship award DGE-1839285.

### **3.7 Author Contributions**

E.J.M. conducted all studies relating to cell mechanosensing and metabolism along with their FLIM analysis of MDA-MB-231, MCF-7, MCF-10A, A-375 MM, U-251 MG, and NIH-3T3 cells. A.E.Y.T.L. conducted all studies relating to cell mechanosensing and metabolism along with their FLIM analysis of MDA-MB-468 and T-47D cells. Metabolism inhibition image collection and FLIM analysis were done by G.E.M. Second harmonic generation of collagen and rheology measurements and analysis were conducted by E.J.M. Collagen substrates were prepared by E.J.M., A.E.Y.T.L. and G.E.M for their respected experiments. E.J.M., A.E.Y.T.L., G.E.M., A.F.Y. and M.A.D. contributed to data interpretation and manuscript preparation.

### **3.8 Summary**

In this chapter, we presented results that connect invasive triple-negative breast cancer cell metabolism with mechanosensation of surrounding collagen extracellular matrix. These modified cellular environments contribute to a diverse range of factors influencing the metastatic cascade including modifying cellular signaling pathways, physical cytoskeletal rearrangements, and ultimately invasion. However, thus far we have only presented data on a single-cell level in collagen, which is a step in the right direction to mimic physiological conditions. In the following chapter, we present data of metabolic alterations in models of increasing complexity, namely, 3D organoid cultures of cancer cells in hyaluronic acid hydrogels, and comparison of cancer cell metabolisms in primary and secondary metastatic sites.

# Chapter 4

## Metabolic shifts of invasive and metastatic cancer cells

The first section of this chapter, on glioblastoma multiforme spheroids in hyaluronic acid hydrogels, consists of unpublished data as of the time of writing this dissertation, and materials have been used with permission from co-authors. The second section on breast cancer transcriptomes in primary and secondary sites has been published in: Davis et al., Transcriptional diversity and bioenergetic shift in human breast cancer metastasis revealed by single-cell RNA sequencing, Nature Cell Biology, published 2020, Springer Nature and has been, in part, reproduced here.

### 4.1 Substrate stiffness reprograms GBM metabolism

Our first model is that of patient-derived glioblastoma multiforme (GBM) tumor spheroids within a 3D hyaluronic acid (HA) hydrogel culture. This project is a wonderful collaboration with Dr. Stephanie Seidlits and her post-doctoral student Dr. Alireza Sohrabi, who have designed the culture system and have grown multiple GBM cell lines within these HA gels for us to image and analyze.

### 4.1.1 Introduction

Glioblastoma multiforme is a highly invasive and prevalent type of brain cancer. Despite of this, it is incurable, and median survival time remains at a paltry 3 months in untreated cases, and only up to 20 months for standard of care treatment [[Malmström et al. \(2012\)](#); [Stupp et al. \(2017\)](#)]. For the most part the cellular origins of GBMs remain unknown, though astrocytes are a primary suspect. As GBM is the most aggressive and most common type of glioma, most brain cancer research surrounds its growth and invasion. Despite the amount of research being done, very little advancement in the palliative, much less curative, abilities of GBM therapies has been made. Consequently, new methods and techniques must be applied to GBM research in order to understand it mechanistically and phenotypically so as to discover new potentially therapeutically targetable pathways. One such approach is to understand the tumor microenvironment and how its mechanical and molecular composition contributes to the evolution and invasion of GBM cells.

Similar to breast tumors, glioblastoma multiforme (GBM) have heavily modified tumor microenvironments. In fact, gliomas rarely metastasize out of the brain, but instead invade surrounding tissue via blood vessels, tracts of white matter, and subarachnoid space [[Cuddapah et al. \(2014\)](#)]. In comparison to normal brain ECM, tumor ECM typically has a much stiffer composition, which the tumor cells themselves modify, along with their own cytoskeleton, in order to invade through cellular barriers as both a collective unit and as individual cells [[Claes et al. \(2007\)](#); [Cuddapah et al. \(2014\)](#); [Friedl and Wolf \(2003\)](#)]. To accomplish this, GBM cells modulate integrins, among other proteins. These integrins act as a sensor to the surrounding ECM, relaying back to intracellular signaling proteins to regulate a wide variety of pathways.

As we have seen in the previous chapter, one such mechanism regulated by mechanosensitive pathways is metabolism. As with other cancer types, an altered cellular metabolism is a hallmark of GBM as well. Indeed, GBMs have been shown to alter their metabolism in line with the Warburg effect in an effort to support molecular biosynthesis and generation

of ATP for enhanced growth [Marbaniang and Kma (2018)]. Interestingly, many different combinations of genetic variability in various GBM tumors have been shown to lead to very similar metabolic alterations, hinting that a metabolically-targeted therapeutic intervention may prove as a promising pathway for GBM-wide therapies.

Existing studies have mostly targeted glycolytic genes in an attempt to shut down this Warburg fueled GBM growth. The knockdown of a variety of glycolytic genes all proved to strongly and selectively inhibit the growth of GBM tumors [Muller et al. (2012); Sanzey et al. (2015)]. Conversely, the upregulation of glycolytic pathways via hypoxia, MYC amplification, and mTORC1/2 all seem to promote GBM tumor development [Cancer Genome Atlas Research Network (2008); Masui et al. (2013); Tateishi et al. (2016)]. Logically, a glycolysis-inhibiting therapeutic intervention should mitigate GBM growth and survival.

Indeed, therapies relying on depletion of glycolytic enzymes did decrease tumor proliferation and angiogenesis [Wolf et al. (2011)]. Surprisingly, this depletion also helped to fuel invasion of the GBM in the surrounding stroma, which may point to an oxidative phosphorylation mechanism during the invasion process. In support of this theory, experiments knocking down IDH1, an important enzyme in the TCA cycle, seemed to increase overall sensitivity of these GBM models to therapy [Calvert et al. (2017)]. Unfortunately, most studies rely on bulk methods of studying metabolism, which ignore the important heterogeneities both within tumors, and between the tumor core and invasive sites. Additionally, most models fail to recapitulate native tumoral environment necessarily leading to inconsistencies in results between model and patient systems. For both of these reasons, little progress has been made in the way of metabolism-based therapeutic GBM interventions, and a revised model and methodology must be utilized to advance the field.

In this section, we use FLIM of NADH to tease out large metabolic shifts in patient-derived GBM cells under differing conditions. We compare phenotypically soft and stiff HA hydrogel-cultured GBM spheroid metabolism on a spheroid-wide level. Furthermore, we compare the metabolic shifts between the spheroid core of the GBM cells cultured in

soft HA hydrogels to its invading arms to gain insights into the complex process-dependent alterations of metabolism during GBM evolution.

## **4.1.2 Results**

### **4.1.2.1 ECM stiffness alters GBM metabolic gene expression**

In order to investigate the effects of ECM stiffness on GBM cell protein expression, we performed bulk RNA sequencing from a pool of hydrogels in both soft and stiff conditions. As a control, we also extracted RNA from spheres in gliomasphere culture. Interestingly, in two different patient-derived GBM cell lines, we found mitochondrially-encoded genes (denoted by MT-) to be highly differentially expressed between the soft and stiff conditions, where these genes were consistently and significantly enriched in the stiff hydrogels, and downregulated in the soft hydrogels (Fig. 4.1). All of these dysregulated mitochondrial genes are involved within the mitochondrial electron transport chain (ETC), which acts to generate ATP within the mitochondria to produce energy for the cell [Zhao et al. (2019)]. Additionally, many of these dysregulated genes specifically belong to complex I and complex IV of the ETC, suggesting potentially complex-specific dysregulation influencing the mechanosensitive metabolic changes in these GBM cells.

### **4.1.2.2 GBM spheroid metabolism depends on the ECM stiffness**

As we saw in from our bulk RNA sequencing experiments, GBM spheroids in stiff hydrogels upregulate transcripts coding for proteins involved in oxidative phosphorylation as compared to those spheroids cultured in soft hydrogels (Fig. 4.1). In order to further probe the potential metabolic changes in consequence of these modified transcriptomes, and to do so in a live-cell and gel-specific context, we performed FLIM of NADH on these soft and stiff hydrogel-cultured GBM conditions. Our results reinforced our findings from the previous section, showing a higher fraction of bound NADH in stiff hydrogel cultures (indicating

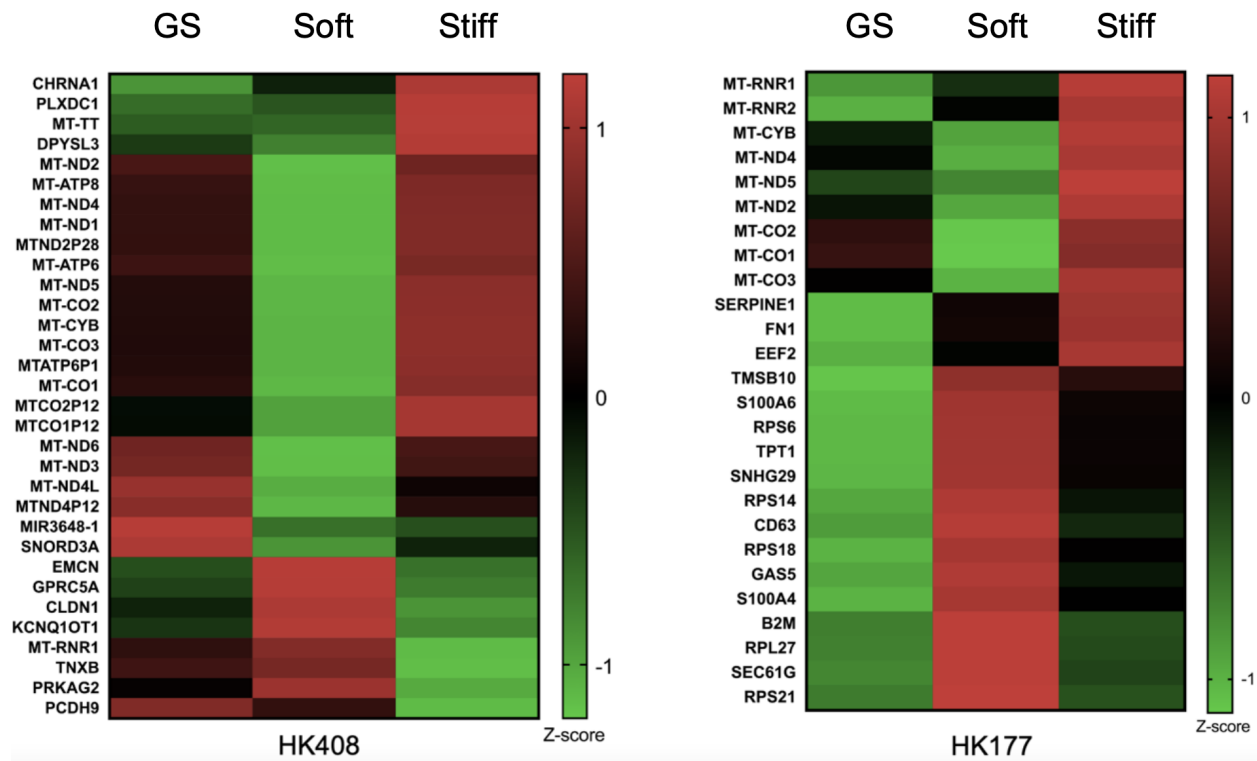


Figure 4.1: Bulk RNA-sequencing results of GBM spheroids represented as heatmaps. For both cell lines, mitochondria-encoded genes (denoted by MT-) are differentially overexpressed in stiff hydrogels when compared to soft. (GS: Gliomasphere)

an upregulation of oxidative phosphorylation mechanisms) as compared to the soft hydrogel cultures. These findings indicate a substrate stiffness-dependent modulation of cellular metabolism (Fig. 4.2).

#### 4.1.2.3 GBM cell invasion and metabolism

In the previous section, we talked only about the metabolic consequences that the HA-hydrogels confirmed upon GBM spheroids. However, their invasive potential is also modulated by substrate stiffness. Indeed, we found that a stiff HA microenvironment inhibits GBM cell migration (Fig. 4.3). In soft hydrogels, we found that GBM cells migrated on average  $165.54 \pm 58.65 \mu\text{m}$  away from their core of origin. Interestingly, in stiff hydrogels no significant migration was found. In performing pH measurements via the absorption of phenol red at 560 nm, we found a significant reduction in absorption in media of GBM



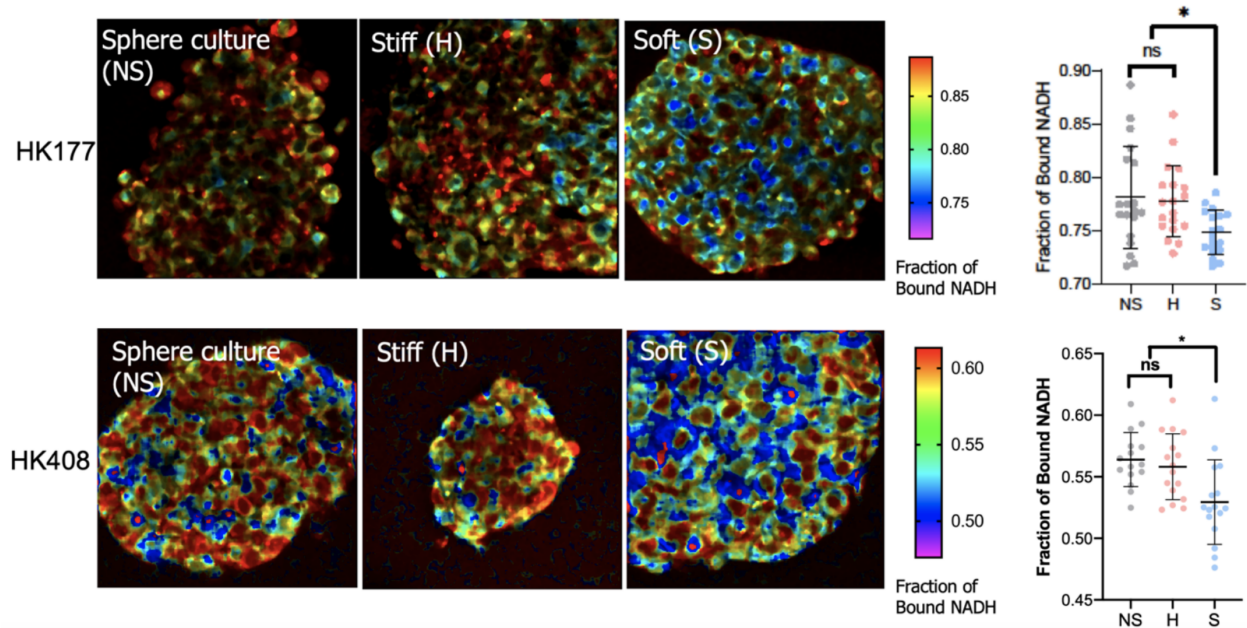


Figure 4.2: FLIM of NADH of soft and stiff HA-encapsulated GBM spheroids. In both cell lines, less fraction of bound NADH was observed in spheres encapsulated in soft hydrogels, compared to the ones in stiff hydrogels. Lower fraction of bound NADH indicates that GBM cells switch to a more glycolytic metabolism pathway in soft hydrogels. NS = no HA gel, H = stiff HA gel, S = soft HA gel.

spheroids cultured in soft hydrogels at longer time points, as compared to the media of those GBM spheroids cultured in stiff hydrogels, indicating a lower pH (Fig. 4.3) [Held (2018)]. At day 3, the measurements of phenol red absorbance were  $0.1367 \pm 0.011$  and  $0.1274 \pm 0.013$  for soft and stiff conditions, respectively ( $p=0.1137$ ). At day 6, the measurements of phenol red absorbance were  $0.149 \pm 0.007$  and  $0.161 \pm 0.011$  for soft and stiff hydrogels, respectively ( $p<0.01$ ). Interestingly, we also saw that, specifically in the invading arms of the soft-hydrogel GBM cultures, there was an upregulation of bound NADH as compared to its spheroid-based cells, where the fraction of bound NADH increased from  $0.500 \pm 0.018$  in gliomaspheres to  $0.550 \pm 0.015$  in the migratory population ( $p<0.0001$ ) (Fig. 4.4).

### 4.1.3 Discussion

Understanding the metabolic and mitochondrial landscape defining the invasion process in GBM is critical for developing new therapeutic interventions for the prevention of cancer

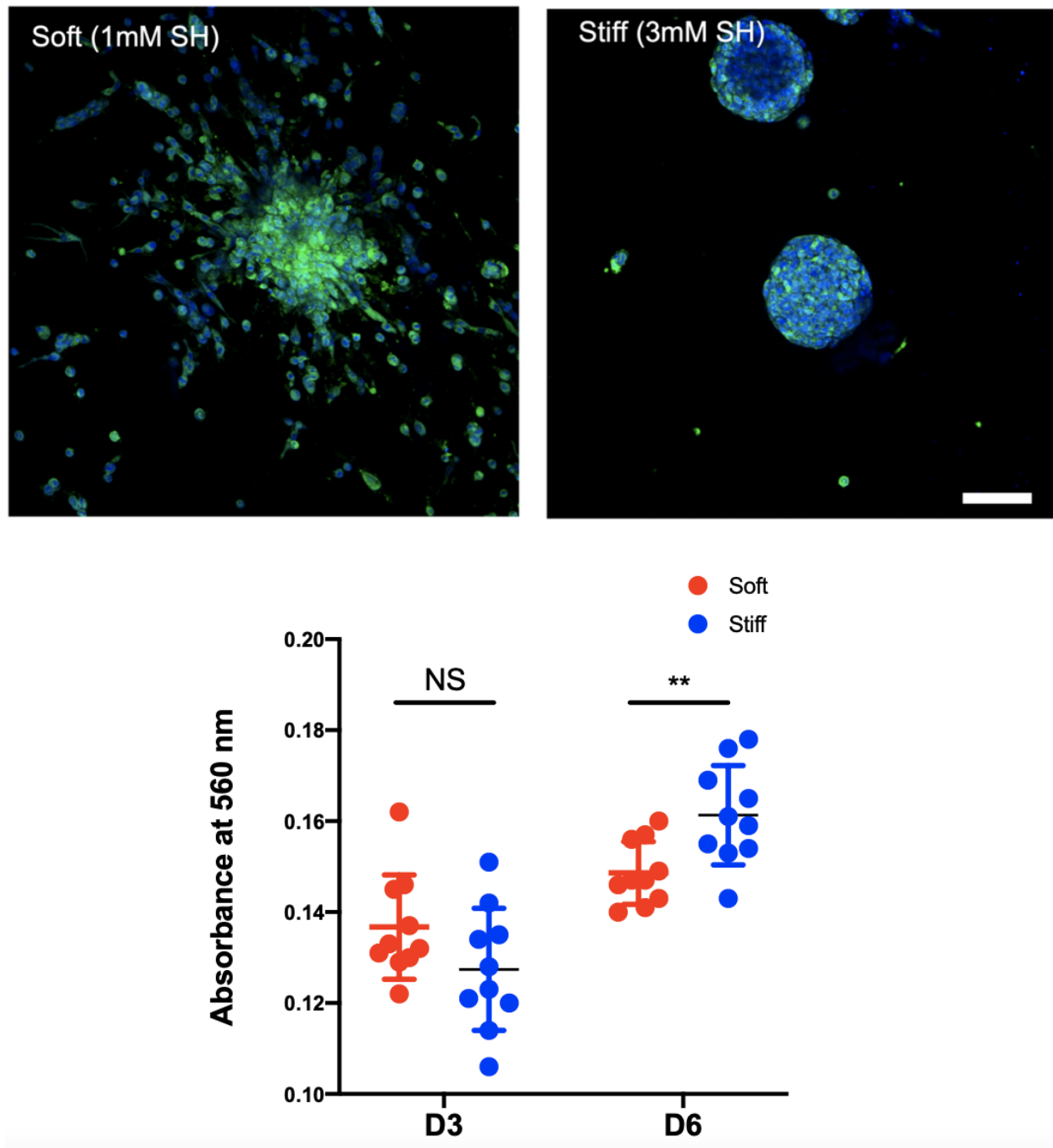


Figure 4.3: (Top) GBM spheroids encapsulated in soft hydrogels exhibit strong migratory phenotype whereas in stiff conditions no cell migration was observed. (scale bar = 100  $\mu\text{m}$ ) (Blue: Hoechst staining of nuclei, Green: Phalloidin staining of actin). (Bottom) Phenol-red absorbance measurement at 560 nm shows at day 6, the environment is more acidic around soft gels compared to stiff ones.

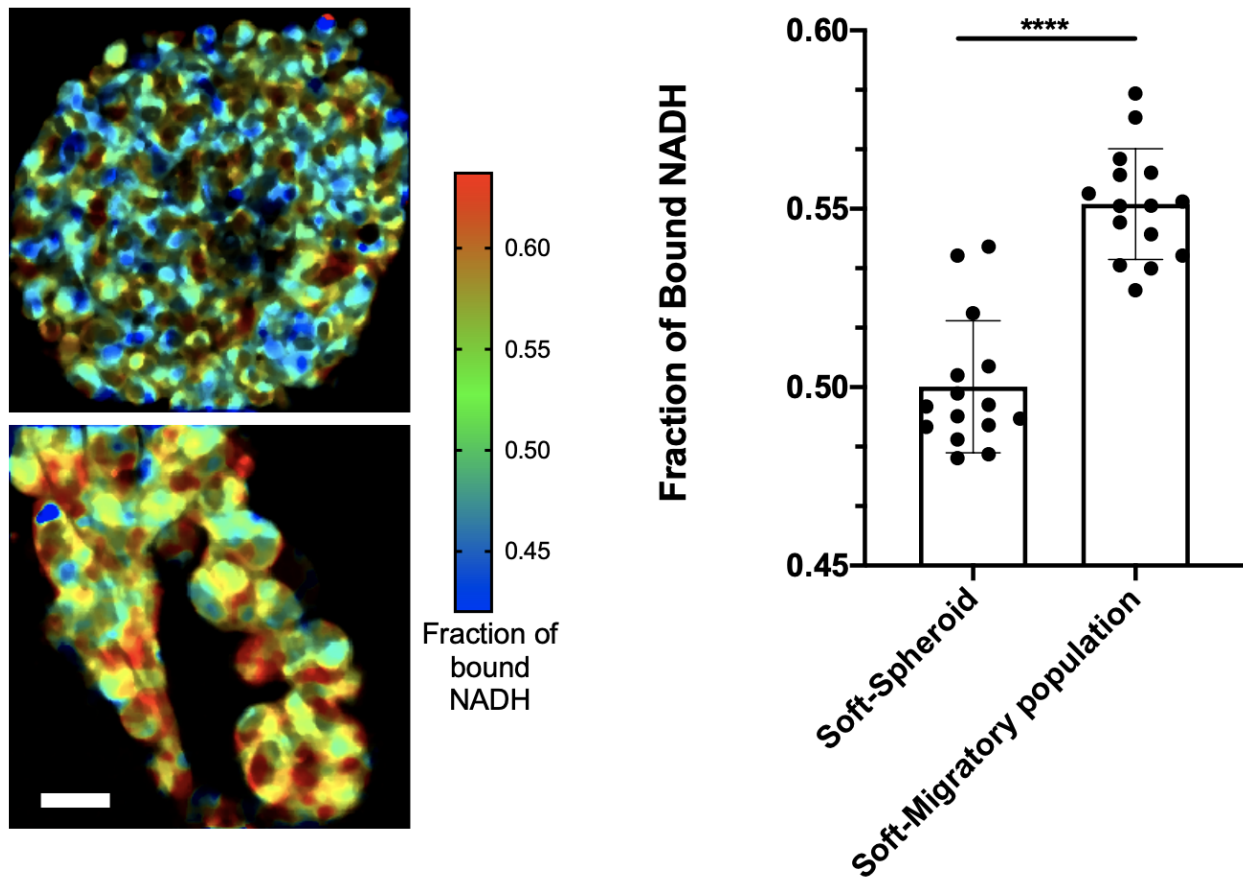


Figure 4.4: NADH FLIM comparison of a GBM spheroid and GBM invasive population in soft hydrogels. The migratory cells, originating from the same sphere on top, shift towards a higher OXPHOS metabolic pathway. (Scale bar = 50  $\mu\text{m}$ ) (\*\*\*\*: p-value < 0.0001).

progression. Here, we have first used bulk RNA sequencing to show that GBM spheroids in stiff hyaluronic acid hydrogels present a higher signature of mitochondrial activity as compared to GBM spheroids in soft hydrogels. Interestingly, we also saw more matrix invasion in the soft hydrogels, indicating a connection between this cancer's progression and its mitochondrial activity. To explore this connection, we used FLIM of NADH to look at phenotypic shifts in oxidative phosphorylation and glycolysis. We found, in agreement with our bulk RNAseq data, that in stiff hydrogels, GBM spheroids shift their metabolism towards oxidative phosphorylation, as compared to in soft hydrogels. Interestingly, we found that the actual invading arms of the soft hydrogel-cultured GBM spheroids showed a similar

shift towards oxidative phosphorylation, as compared to the core of the spheroid, showing a shift towards glycolysis.

These results suggest a shift from a glycolytic spheroid core metabolism during growth to a more oxidative phosphorylation, mitochondria-reliant invasion metabolism. To understand these metabolic shifts in a cancer-wide context, we must move to another cancer model. In the next section, we explore how breast cancer changes its metabolic landscape through an investigation of both genotypic and phenotypic diversity of metabolism during its growth and metastatic dissemination.

#### **4.1.4 Methods**

##### **4.1.4.1 Hydrogel formation**

Hyaluronic acid-based hydrogels were formed according to a previously published protocol [Xiao et al. (2018b)]. In brief, HA-SH (0.5% w/v), 4-arm thiol terminated polyethylene glycol (PEG), 8-arm norbornene terminated PEG, 0.025% w/v lithium phenyl-2,4,5 trimethylbenzoylphosphinate, and 0.25 mM thiolated RGD was dissolved in 20 mM HEPES buffer at a pH of 7. The solution was then cast into 4 mm silicone molds, which were irradiated with 365 nm UV light for 15 seconds. 1mM SH was used for soft hydrogels, and 3 mM SH was used for stiff hydrogels.

##### **4.1.4.2 Cell culture**

Two patient derived GBM cell lines, a mesenchymal-type HK177, and a proneural type HK408, were provided by Dr. Harley Kornblum at UC Los Angeles. Cell lines were collected in adherence with the UC Los Angeles Institutional Review Board protocol 10-000655. Cell lines were kept in complete media, consisting of DMEM/F12 media supplemented with 1xG21, 1% v/v noromycin, 50 ng/mL EGF, 20 ng/mL FGF-2, and 25 mg/mL heparin.

Aggrewell well plates were used to maintain constant spheroid sizes prior to hydrogel encapsulation. The wells were filled with 1 mL of 5% w/v pluronic F-127 solution, which were then centrifuged at 3000 G for 5 minutes, then incubated for 30 minutes at room temperature. Wells were then washed with 1 mL of complete media, GBM cells were added to the wells, and 1 mL of complete media was added. The plates were then centrifuged at 300 G for 3 minutes.

The next day, spheroids were collected from the wells, briefly centrifuged at 200 G for 1 minute, and resuspended in the hydrogel precursor solution. The hydrogels were formed as described above, then transferred to 24-well plates and cultured in 500  $\mu$ L of complete media. 250  $\mu$ L of media was replaced every two days.

#### **4.1.4.3 RNA-sequencing**

A pool of 6 spheroid-embedded hydrogels were used for RNA extraction. RNA extraction was performed using the Qiagen RNeasy Micro kit. Briefly, hydrogels were incubated in a lysis buffer (RLT) and disintegrated using a 1 mL syringe with a 20 G needle [Xiao et al. (2018a)]. The lysate was flown through a Qiagen Qias shredder column at 17000 G for 2 minutes. The lysates were then transferred to the RNeasy micro column and RNA was extracted based on manufacturer protocol.

RNA sequencing was performed at UC Los Angeles Technology Center for Genomics and Bioinformatics (TCGB). RNA concentration and quality were checked with a Nanodrop spectrophotometer. Libraries for RNA-Seq were prepared with KAPA stranded mRNA-Seq kit. The workflow consists of mRNA enrichment and fragmentation, first strand cDNA synthesis using random priming followed by second strand synthesis converting cDNA:RNA hybrid to double-stranded cDNA (dscDNA), and incorporates dUTP into the second cDNA strand. cDNA generation is followed by end repair to generate blunt ends, A-tailing, adaptor ligation and PCR amplification. Different adaptors were used for multiplexing samples in one lane. Sequencing was performed on an Illumina NovaSeq6000 for PE 2x150 run. Data quality

check was done on Illumina SAV. Demultiplexing was performed with Illumina Bcl2fastq v2.19.1.403 software. The reads were mapped by STAR 2.27a [Dobin et al. (2013)] and read counts per gene were quantified using human Ensembl GRCh38.98 GTF file. In Partek Flow, read counts were normalized by CPM  $+1.0 \times 10^{-4}$ . All results of differential gene expression analysis utilized Partek's statistical analysis tool, GSA. For differentially expressed gene list, p-values and fold change (FC) filters were applied. The filter was  $p < 0.05$  and  $FC > 2$  for all differential gene expression results. Ingenuity Pathway Analysis (IPA) software [Krämer et al. (2014)] was used for pathway analysis. Using the list of significantly ( $p < 0.05$ ) differentially expressed ( $FC > 2$ ) genes, the Canonical Pathway analysis, Disease and Function analysis, and networks analysis were performed by IPA.

#### 4.1.4.4 Fluorescence lifetime imaging of NADH

NADH fluorescence lifetime images were acquired with an LSM 880 confocal microscope (Zeiss) with a 40x 1.2NA C-Apochromat water-immersion objective coupled to an A320 FastFLIM acquisition system (ISS). A Ti:Sapphire laser (Spectra-Physics Mai Tai) with an 80 MHz repetition rate was used for two-photon excitation at 740 nm. The excitation signal was separated from the emission signal by a 690 nm dichroic mirror. The NADH signal was passed through a 460/80 nm bandpass filter and collected with an external photomultiplier tube (H7522P-40, Hamamatsu). Cells were imaged within a stage-top incubator kept at 5% CO<sub>2</sub> and 37°C. FLIM data were acquired and calibrated with the SimFCS 4 software developed at the Laboratory for Fluorescence Dynamics at UC Irvine. Calibration of the system was performed by acquiring FLIM images of coumarin 6 (roughly 10  $\mu$ M), which has a known lifetime of 2.5 ns in ethanol, to account for the instrument response function.

#### 4.1.4.5 Phasor-based FLIM analysis of NADH

NADH assumes two main physical states, a closed configuration when free in solution, and an open configuration when bound to an enzyme [Hull et al. (2001)]. These two physical states

have differing lifetimes, 0.4 ns when in its free configuration, and 3.4 ns when in its bound configuration [Mah et al. (2018); Ranjit et al. (2018)]. To quantify metabolic alterations, we perform fractional analysis of NADH lifetime by calculating individual pixel positions on the phasor plot along the linear trajectory of purely free NADH lifetime (0.4 ns) and purely bound NADH lifetime (3.4 ns). We quantify the fraction of free NADH by simply calculating the distance of the center of mass of a spheroid’s cytoplasmic NADH FLIM pixel distribution to the position of purely bound NADH divided by the distance between purely free NADH and purely bound NADH on the phasor plot. To ensure avoiding contribution from background fluorescence which may be present in the media, we perform a three-component analysis post-background calibration to linearly unmix its contribution. We also use an empirically determined intensity threshold for each file to exclude any low-intensity background signal arising from the surrounding ECM and media. These segmentation and phasor analysis methods are described in detail in Chapter 2.

#### 4.1.4.6 Statistical testing

D’Agostino and Pearson omnibus normality tests were used to test for normality in data sets. For those that were considered normally distributed, a one-way ANOVA and t-test were used to determine statistical differences between groups. For non-normally distributed data, a non-parametric Mann-Whitney test was used. All statistical analyses were done in Prism 8.



## 4.2 Transcriptional diversity and bioenergetic shift in human breast cancer metastasis revealed by single-cell RNA sequencing

Our next model is that of patient-derived xenograft breast tumors displaying spontaneous metastases to various organs within in vivo mouse models. This project was the start of a fruitful collaboration with Dr. Devon Lawson's and Dr. Kai Kessenbrock's lab at UC Irvine. Here, we find interesting results in the metabolic genotype and phenotype of breast cancer metastases that are quite similar to those found in patient-derived GBM spheroid models, in that the metastatic/invasive cells upregulate a mitochondrial-based metabolic signature as compared to the core/primary tumor cells. As previously mentioned, this work has been published in: Davis et al., Transcriptional diversity and bioenergetic shift in human breast cancer metastasis revealed by single-cell RNA sequencing, Nature Cell Biology, published 2020, Springer Nature and has been, in part, reproduced here. Its supplementary tables and materials can be found in the online version.

### 4.2.1 Introduction

Despite major advances in the detection and treatment of early stage disease, metastasis remains the cause of nearly all mortality associated with breast cancer [[Bianchini et al. \(2016\)](#)]. Previous work suggests that metastasis is seeded by rare primary tumour cells with unique biological properties that enable them to surpass each step in the metastatic cascade [[Hermann et al. \(2007\)](#); [Lawson et al. \(2018\)](#); [Oskarsson et al. \(2014\)](#)]. Although the properties promoting cell motility and migration have been well studied, the mechanisms governing the seeding and establishment of micrometastasis in distal tissues are poorly understood. This is in part because metastatic seeding cannot be studied in humans and because it is technically challenging to detect and analyse rare cells at this transient stage in animal models. Further



insights into the mechanisms driving metastatic seeding are critical to inspire new strategies for the prevention of metastatic spread and reduction in mortality of patients with breast cancer.

We have developed a robust approach for the capture and analysis of individual cancer cells during the seeding of micrometastasis in human patient-derived-xenograft (PDX) models using single-cell RNA sequencing (scRNA-seq) technology. This enabled us to study the role of tumour heterogeneity in metastasis and identify cellular programs upregulated in micrometastatic cells that promote metastatic seeding. We found that micrometastases display a distinct transcriptome program and identified mitochondrial oxidative phosphorylation (OXPHOS) as a top pathway upregulated during metastatic seeding. This was confirmed at the molecular level, where we demonstrated that micrometastatic cells display increased mitochondrial membrane potential and a distinct metabolic profile. We further found that the pharmacological inhibition of OXPHOS, specifically in cancer cells, attenuates metastatic seeding in the lungs using two different breast cancer experimental metastasis models. These data show that OXPHOS is functionally important for metastasis and suggest that different metabolic strategies may be advantageous for cells to complete discrete stages of the metastatic cascade.

## **4.2.2 Results**

### **4.2.2.1 Single-cell RNA sequencing of matched primary tumours and micrometastases**

To identify fundamental cellular programs important for seeding in metastatic tissues, we investigated transcriptome programs uniquely expressed by cancer cells during the seeding and establishment of micrometastatic lesions. We utilized PDX models of breast cancer because of their human disease authenticity, including intra-tumour heterogeneity, which is critical for determining the role of cellular heterogeneity in metastasis [DeRose et al. (2011);

[Hochhauser and Caldas \(2017\)](#); [Izumchenko et al. \(2017\)](#); [Lodhia et al. \(2015\)](#)]. We analysed three previously established PDX models of triple-negative breast cancer (TNBC): HCI001, HCI002 and HCI010 (Fig. 4.5a) [[DeRose et al. \(2011\)](#)]. As in many patients with breast cancer, metastatic progression is slow and sporadic in these models, where most animals display dispersed micrometastases in the lung and lymph nodes and very low metastatic burden at the endpoint (primary tumour diameter of 20-25 mm; Fig. 4.5b,c) [[DeRose et al. \(2011\)](#); [Lawson et al. \(2015\)](#)]. This enabled us to investigate the transcriptional changes associated with early events in the seeding and establishment of micrometastasis.

#### **4.2.2.2 Micrometastatic cells display a distinct transcriptome program**

To determine whether micrometastatic cells possess unique transcriptome programs that may facilitate seeding in distal tissues, we performed supervised analysis to directly compare gene expression in primary tumour and micrometastatic cells (Fig. 4.6a)[[Butler et al. \(2018\)](#); [Satija et al. \(2015\)](#)]. This identified 330 differentially expressed genes ( $P < 0.05$ ;  $\log[\text{fold change (FC)}] > 0.25$ ), including 116 genes specifically upregulated in micrometastatic cells conserved in all three PDX models (Fig. 4.6b and Supplementary Table 3 (online)). Top micrometastasis-associated genes included several heat shock proteins (HSPB1, HSPE1 and HSPA8), which are protein chaperones upregulated in response to environmental stress that play pleiotropic roles in protein folding, wound healing, antigen presentation, protection from apoptosis, and cellular proliferation and differentiation (Fig. 4.6c) [[Creagh et al. \(2000\)](#); [Ikwegbue et al. \(2018\)](#)]. Several cytokeratins (KRT14, KRT16, KRT7 and KRT17) were also upregulated in micrometastatic cells from all three models as well as ACTG2, which encodes a smooth muscle protein involved in cell motility (Fig. 4.6c). Micrometastatic cells also expressed higher levels of several genes with lesser known roles in metastasis such as CKB, PHLDA2, NME1, ASHA1, NOP16 and S100A16 (Fig. 4.6c).

We next performed a series of survival analyses, logistic regression and in situ validation experiments to confirm increased expression of micrometastasis-associated genes in PDX

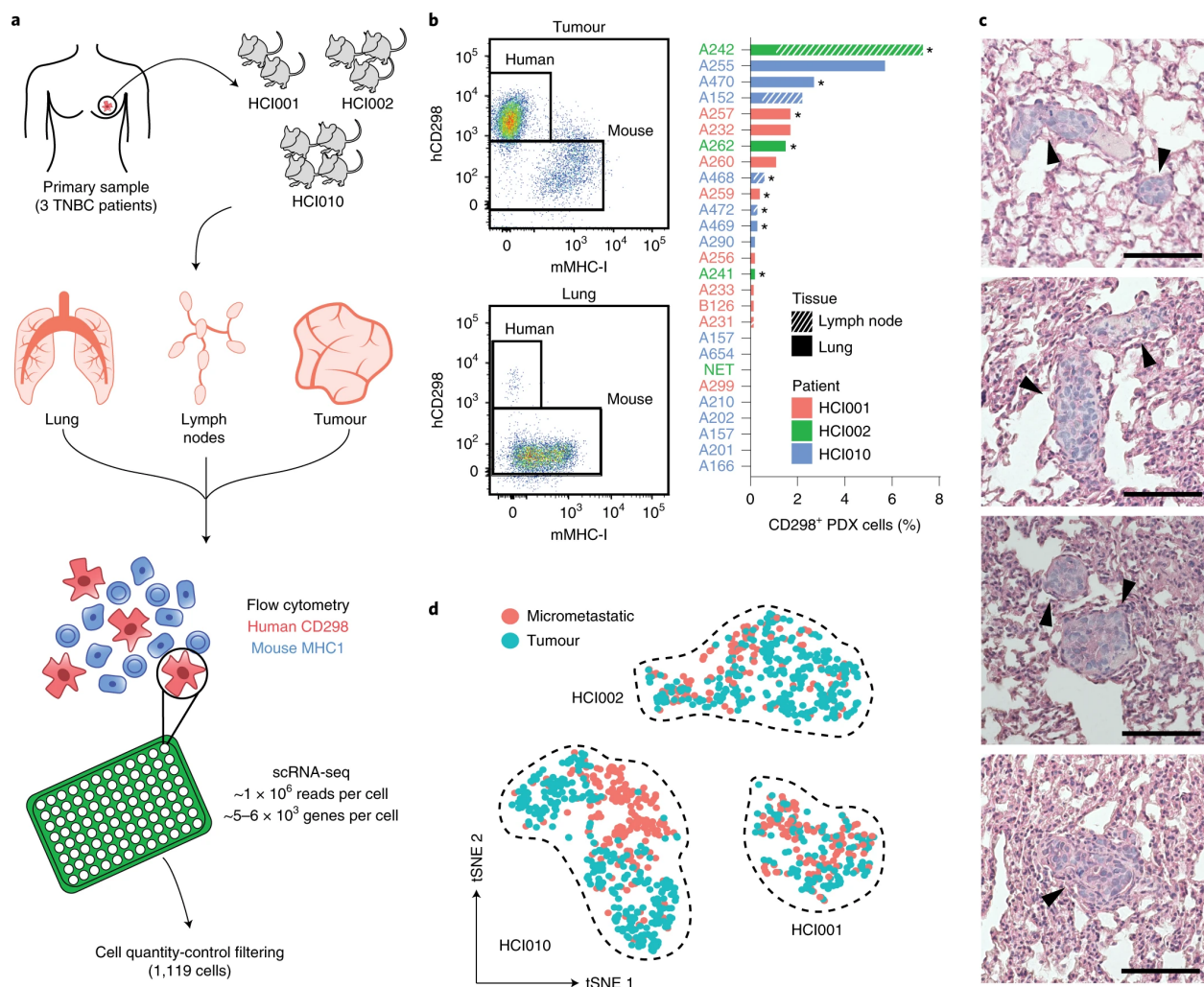


Figure 4.5: Single-cell RNA sequencing of micrometastatic and primary tumour cells. **a**, Overview of the experimental workflow. The primary tumour, lungs and lymph nodes of each PDX animal were digested to make single-cell suspensions. Single CD298+MHC-I- human tumour cells were isolated by flow cytometry, deposited into individual wells of 96-well plates and single-cell cDNA libraries were prepared using Smartseq2 chemistry. Matched primary tumour and micrometastatic cells from nine mice and three PDX models (HCI001, HCI002 and HCI010) were analysed, and 1,119 cells passed quality-control filtering. **b**, Left, flow cytometry-based strategy for the isolation of human CD298+MHC-I- cells from micrometastatic (bottom) and primary tumour (top) cells. Right, frequency of CD298+MHC-I- cells in a cohort of PDX mice. Mice that were selected for sequencing are indicated with an asterisk. **c**, Haematoxylin and eosin stains of micrometastases in the lungs of HCI001 mice. Data are representative of n=8 biologically independent samples. Micrometastatic lesions are indicated by the arrows. Scale bars, 100 μm. **d**, T-distributed stochastic neighbour embedding (tSNE) plot showing clustering of 1,119 metastatic and primary tumour cells from the HCI001, HCI002 and HCI010 models.

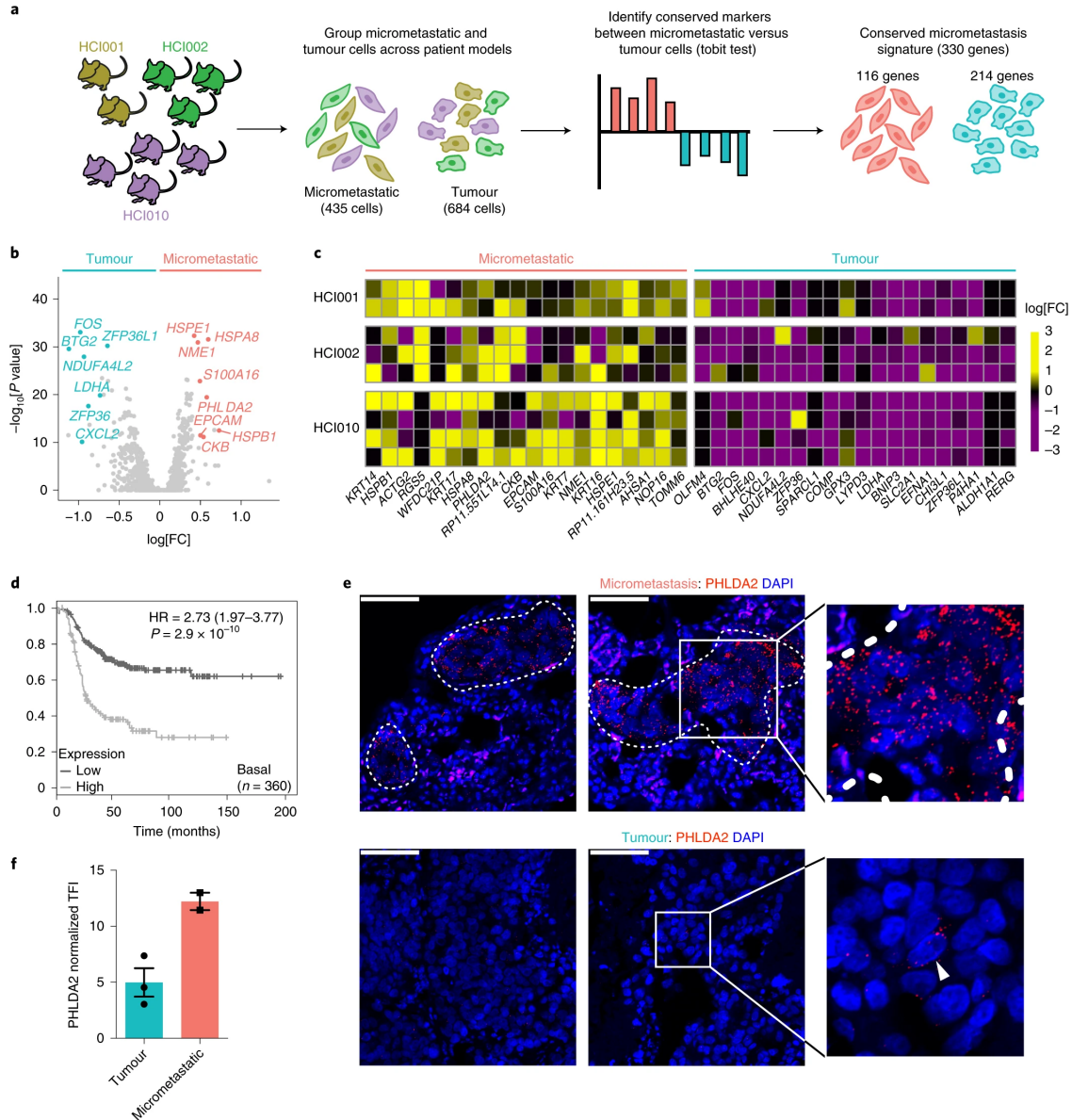


Figure 4.6: Micrometastatic cells display a distinct transcriptome program. **a**, Schematic of the analysis method to identify genes that were differentially expressed between micrometastatic and primary tumour cells. **b**, Volcano plot showing differentially expressed genes between micrometastases and tumours. **c**, Heat map of the top-20 marker genes. The average FC of each gene (x axis) was plotted for each mouse (y axis). Yellow indicates higher expression in micrometastatic cells and purple indicates higher expression in tumour cells. **d**, Kaplan-Meier survival curve showing decreased relapse-free survival in patients with basal-like breast cancer (n=360) who expressed high levels of the top-15 micrometastasis-associated genes. **e**, Representative fluorescent in situ hybridization for PHLDA2 (RNAscope) on primary tumour (bottom) and lung micrometastases (top) from the PDX model HCI001. Insets, higher magnification of individual puncta. The white arrow indicates a tumour cell with high expression of PHLDA2. Scale bars, 50  $\mu\text{m}$ . **f**, Normalized total fluorescent intensity (TFI) of PHLDA2. Data are shown as the mean  $\pm$  s.e.m.

mice and evaluate the disease relevance in patients with breast cancer. We first explored whether increased primary tumour expression of micrometastasis-associated genes is predictive of poor survival in patients with basal-like breast cancer using microarray data from the KM Plotter database (879 patients) [Györfy et al. (2010)]. This was done to determine whether micrometastasis-associated genes are higher in more biologically aggressive tumours and whether they have value as predictive biomarkers for disease progression in patients. Remarkably, we found that 15 of our top-20 micrometastasis-associated genes were significantly predictive of relapse in basal-like patients (two genes were not predictive and the data for three genes were not available;  $P < 0.05$ , hazard ratio (HR)  $> 1.4$ ; Fig. 4.7a). Combining all 15 genes further increased the power for predicting patient relapse in this cohort, showing a nearly threefold increased risk (HR=2.73,  $P = 2.9 \times 10^{-10}$ ; Fig. 4.6d).

We next utilized a stepwise logistic-regression model to identify the top biomarker candidates for micrometastasis in our dataset. We utilized the Akaike information criterion to determine the optimal number of genes to include in each subsampling ( $n=5$ ) and constructed ten models on equal subsamplings of micrometastatic and primary tumour cells in our dataset (Fig. 4.7b,c). Using this approach, the top candidates will appear the most often in the ten data subsamplings. We found that PHLDA2 was the top candidate for micrometastatic cells and was present in eight of ten models (Fig. 4.7d).

PHLDA2 is a maternally imprinted gene that regulates placental growth and increases xenograft engraftment and cell invasion in vitro but has limited prior association with breast cancer metastasis [Moon et al. (2015); Tunster et al. (2016)]. Our survival analysis showed that PHLDA2 was significantly predictive of increased relapse ( $P = 7.4 \times 10^{-3}$ ; HR=1.44) in patients with basal-like breast cancer (Fig. 4.7a). We compared the PHLDA2 transcript levels in primary tumour and micrometastases using high-resolution single-molecule fluorescence in situ hybridization (RNAscope) to determine whether the PHLDA2 transcripts are upregulated in micrometastatic lesions in situ. We found that the levels of PHLDA2 transcripts were at least twofold higher in micrometastases relative to primary tumours,



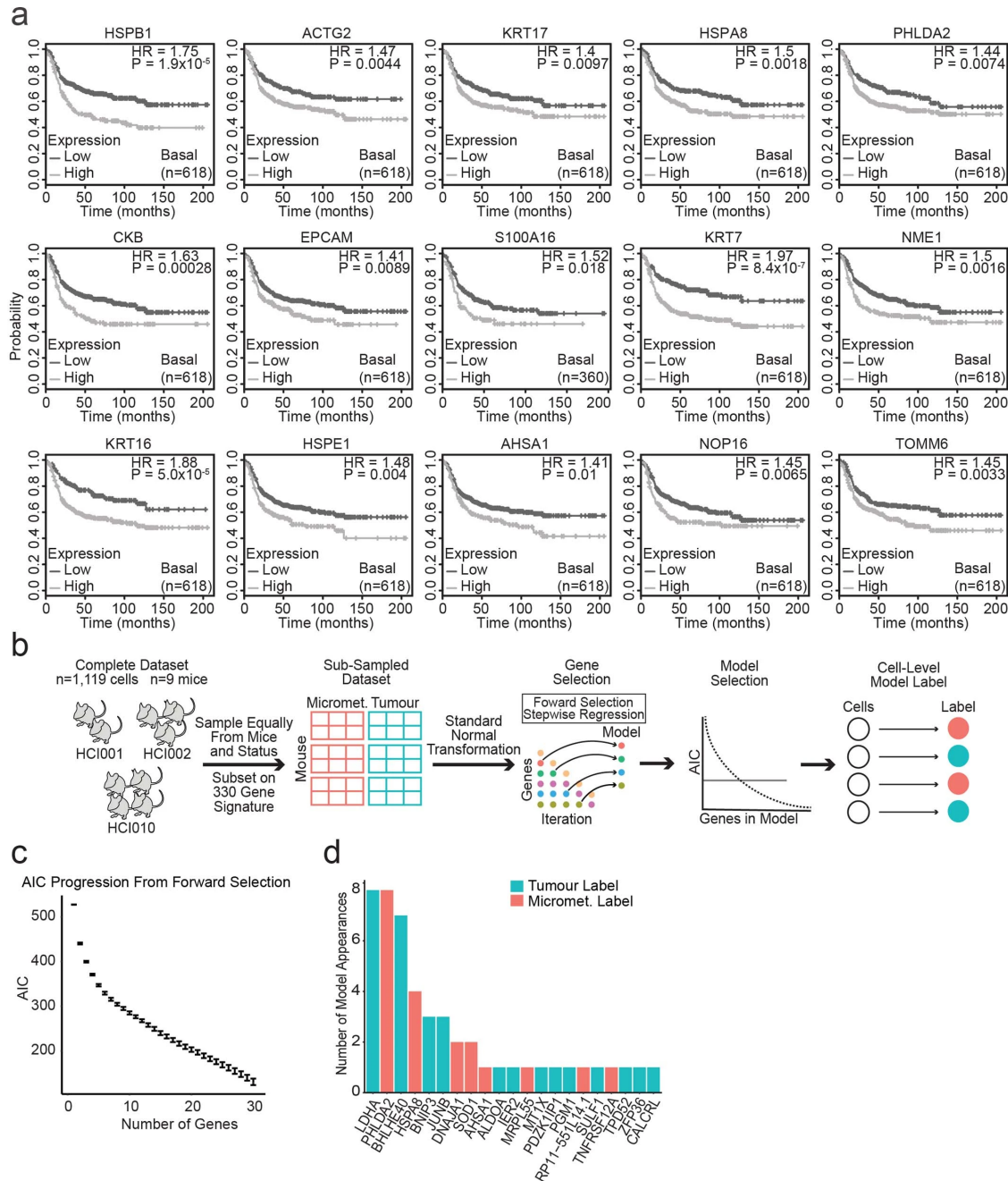


Figure 4.7: Prognostic value of micrometastasis- associated genes in basal-like breast cancer patients. **a**, Kaplan-Meier curves show relapse free survival (RFS) in basal-like breast cancer patients. **b**, Schematic for the construction of a stepwise logistic regression model to identify top biomarker candidates descriptive of primary tumour or micrometastatic cells. **c**, Plot demonstrating the AIC versus the number of genes included in the model. Data is presented as the 10% and 90% quantiles of the 10 data subsamplings. **d**, Bar plot showing the number of model appearances for each gene out of 10 data subsamplings.

validating our approach for identifying genes upregulated in micrometastasis (Fig. 4.6e,f). Interestingly, only rare primary tumour cells expressed PHLDA2, raising the question of whether it marks pre-metastatic cells (Fig. 4.6e). These data highlight our dataset as a resource for the identification of potential drivers of metastatic seeding and biomarkers to predict metastatic progression in patients with breast cancer.

#### 4.2.2.3 Micrometastatic cells upregulate mitochondrial OXPHOS

We performed GO term analysis on our 330-gene signature to identify pathways and cellular properties upregulated in cancer cells during metastatic seeding (Supplementary Table 4 (online)). The top GO terms for micrometastatic cells included ‘epidermis development’ (CALML5, KRT17, KRT16, KRT14 and KLK5) and ‘response to unfolded protein’ (DNAJA1, HSPA8, HSPB1, HSPE1 and HSPD1; Fig. 4.8a and Supplementary Table 4 (online)). Interestingly, many top GO terms centred on mitochondrial biology and metabolism and included ‘respiratory electron transport chain’, ‘ATP metabolic process’, ‘mitochondrial transport’ and ‘oxidative phosphorylation’ (Fig. 4.8a). In contrast, ‘canonical glycolysis’ and ‘pyruvate metabolic process’ were top GO terms for primary tumour cells, suggesting clear metabolic differences between primary tumour and micrometastatic cells (Fig. 4.8a and Supplementary Table 4 (online)). The analysis of the GO term-associated genes showed that 27 genes related to OXPHOS, glycolysis and mitochondrial complexes were differentially expressed ( $P < 0.05$ ; Fig. 4.8b). Micrometastatic cells expressed higher levels of numerous mitochondrial electron transport chain (ETC) genes, including NDUFS6, NDUFAB1, NDUFB2, NDUF4A, UQCRC3 and COX6A as well as the ATP synthase subunits ATP5I, ATP5G1 and ATP5J2 (Fig. 4.8b). Micrometastatic cells also expressed higher levels of the mitochondrial transport genes TOMM5, TOMM6 and TIMM13 as well as the mitochondrial ribosome genes MRPL14, MRPL55 and MRPL51, which translate mitochondrial genes encoding ETC proteins (Fig. 4.8b). Superoxide dismutase 1 (SOD1)—which encodes a mitochondrial enzyme that converts superoxide radicals to  $O_2$  and  $H_2O_2$ , and may thus





protect micrometastatic cells from apoptosis due to oxidative stress from increased ETC activity—was also upregulated in micrometastatic cells (Fig. 4.8b). In contrast, primary tumour cells expressed higher levels of genes associated with glycolysis, including the glycolytic enzymes ALDOA, ALDOB, ALDOC, PGM1 and PGK1 (Fig. 4.8b). Our logistic regression analysis also identified LDHA, which promotes aerobic glycolysis by catalysing the conversion of pyruvate to lactate and diverting it from entry into the citric acid cycle (CAC), as the top gene most descriptive of primary tumour cells (Fig. 4.7d).

We evaluated the expression of 1,402 genes associated with 37 metabolic pathways—such as the pentose phosphate pathway, the citric acid cycle and fatty-acid metabolism—to further investigate the metabolic differences between primary tumour cells and micrometastases (Fig. 4.8c, Fig. 4.9 and Supplementary Table 5 (online)). Gene scoring for each pathway showed that glycolysis ( $P=2.20\times 10^{-16}$ ) and OXPHOS ( $P=2.20\times 10^{-16}$ ) were the most significantly differentially expressed of all 37 pathways (Fig. 4.8c). Importantly, we found that >70% of the genes were detected and passed quality filtering in 33 of the 37 pathways, indicating sufficient coverage across the metabolic pathways for comparative analysis (Fig. 4.9).

We next performed several studies for molecular validation of the metabolic differences between primary tumour and micrometastasis cells. As conventional oxygen-consumption assays are not amenable to the small cell numbers extracted from micrometastases, we performed a combination of flow cytometry and high-resolution metabolomic analyses. We compared the mitochondrial activity of primary tumour and metastatic cells through flow cytometry using tetramethylrhodamine methyl ester (TMRM), which is a fluorescent dye that accumulates in the mitochondria as a result of a difference in membrane potential (Fig. 4.8d) [Scaduto and Grotyohann (1999)]. We found that HCl010 primary tumours contain TMRM<sup>high</sup> and TMRM<sup>low</sup> populations, where TMRM<sup>high</sup> cells are the minor population (Fig. 4.8e). Quantitative PCR analysis of sorted TMRM<sup>high</sup> and TMRM<sup>low</sup> cells confirmed that TMRM<sup>high</sup> cells express higher levels of the genes involved in mitochondrial biogenesis and the ETC, validating the TMRM assay in PDX cells (Fig. 4.8e). We stained matched pri-

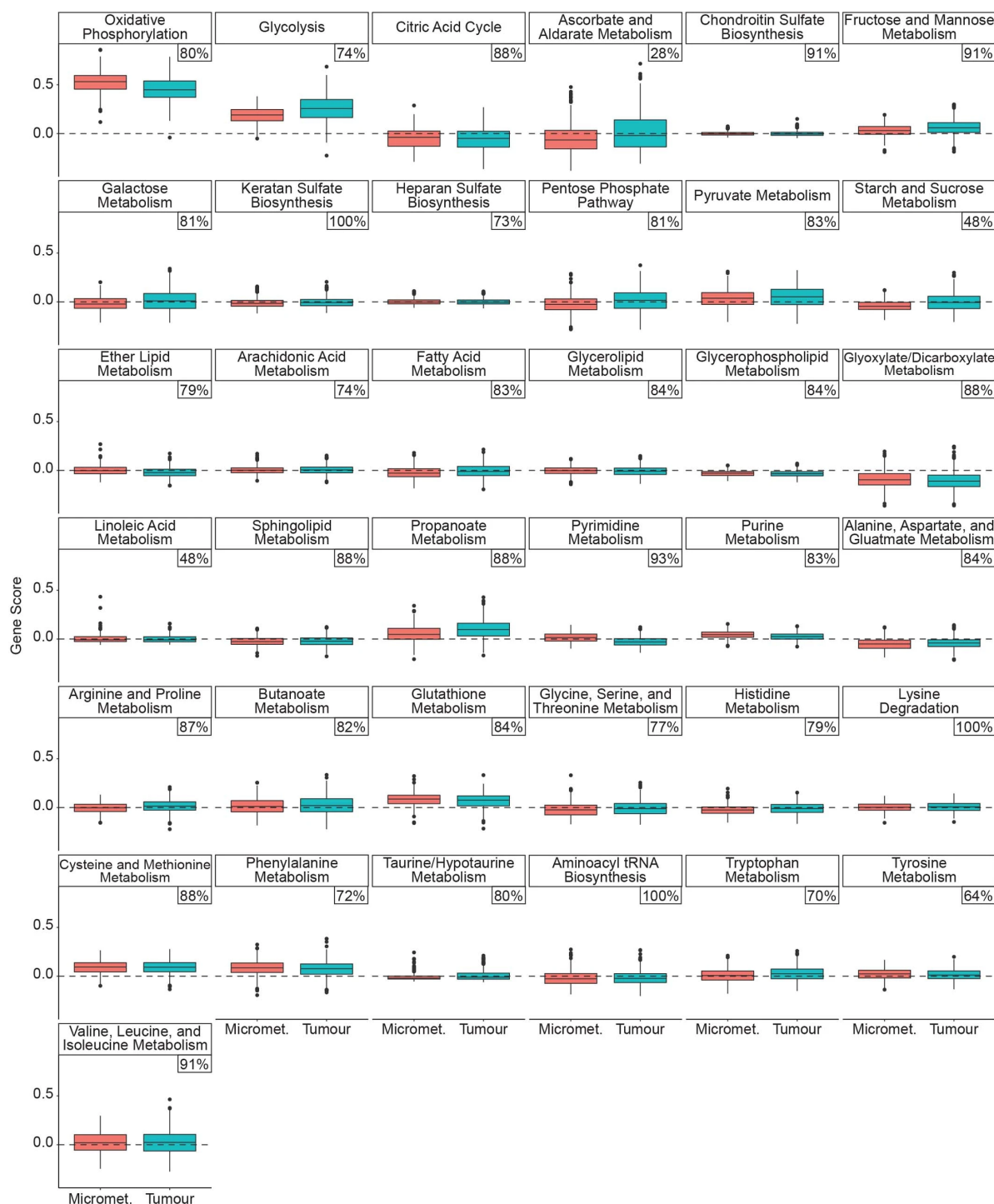


Figure 4.9: Gene scoring identifies OXPHOS and glycolysis as top metabolic pathways differentially expressed between micrometastases and primary tumour cells. Gene scores for each metabolic pathway in micrometastatic (red, n=435 cells) or primary tumour cells (blue, n=684 cells). Each cell in the dataset was scored by calculating the difference between the average gene expression for all the genes in each metabolic pathway versus the average gene expression of a randomly selected background gene set.

mary tumour and lung cell suspensions from six HCl010 PDX mice with TMRM. The cells were co-stained with a viability dye (Sytox), CD298, MHC-I and MitoTracker to identify viable human cells and assess the mitochondrial membrane potential relative to mitochondrial mass. Flow cytometry analysis showed that the mitochondrial membrane potential of micrometastases was threefold higher than primary tumour cells ( $P=0.0331$ ; Fig. 4.8f). These data, combined with transcriptome analyses, strongly suggest that micrometastases utilize higher levels of OXPHOS for cellular metabolism.

#### 4.2.2.4 Oxidative phosphorylation is critical for lung metastasis

We next investigated whether increased OXPHOS is functionally important for metastasis or simply represents a response to increased oxygen availability in the metastatic site. We used two experimental metastasis models of TNBC that metastasize to the lung with reproducible kinetics following intravenous delivery—that is, mouse 4T1 and human MDA-MB-231 cells. We used the complex V inhibitor oligomycin to inhibit OXPHOS in vitro and then measured its effects on metastatic outgrowth in the lung (Fig. 4.10a,b). We chose oligomycin because it is a highly selective inhibitor of OXPHOS with limited off-target effects [Fernyhough and McGavock (2014)]. Oligomycin induces cells to shift to glycolysis to produce ATP and has been used to study the consequences of this metabolic shift in diverse settings [Choi et al. (2009); Dayan et al. (2009); Hao et al. (2010); Ward et al. (2000)].

Given that oligomycin is cytotoxic if cells are unable to switch to increased glycolysis [Hao et al. (2010)], we performed a series of analyses to test the health and metabolic state of MDA-MB-231 and 4T1 cells post treatment (Fig. 4.11a,b). Flow cytometry analysis of propidium iodide and annexin V staining showed that oligomycin does not reduce cell viability, increase apoptosis or alter cell morphology 72h post treatment (Fig. 4.11c,d). Furthermore, proliferation assays showed no decrease in the growth rate of treated cells (Fig. 4.11e,g). Using the Seahorse XF assay, we found that oligomycin induces a sustained reduction in the oxygen-consumption rate (OCR) and a corresponding increase in the extracellular acid-

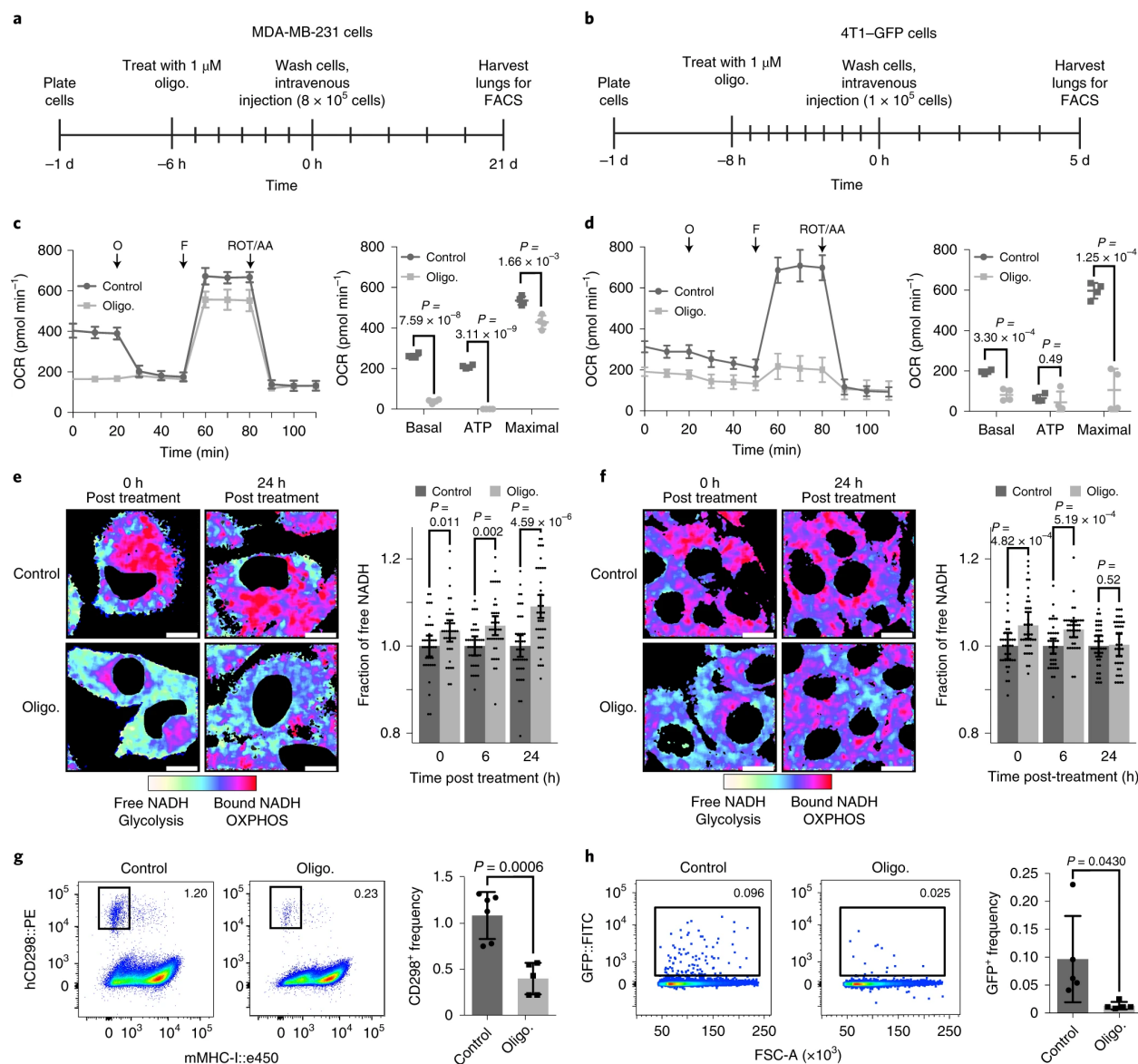


Figure 4.10: Oxidative phosphorylation is critical for lung metastasis. **a,b**, Schematic of the experimental approach used to determine the effects of complex V inhibition via oligomycin on metastasis of MDA-MB-231 (**a**) and 4T1-GFP cells (**b**). **c,d**, Left, OCR of MDA-MB-231 (**c**) and 4T1-GFP cells (**d**) versus control cells after treatment with oligomycin for 6-8h in vitro. Right, basal, ATP and maximal respiration rates for each condition. **e,f**, Left, representative FLIM images of the fluorescence lifetime of NADH in cultured MDA-MB-231 (**e**) or 4T1-GFP cells (**f**). Right, quantification of the free-NADH fraction in the FLIM images normalized to the control. **g,h**, Flow cytometry analysis of the metastatic burden in the lungs of the animals injected intravenously with oligomycin-treated or control cells. Left, FACS plots show MDA-MB-231 cells (**g**), identified as CD298<sup>+</sup>MHC-I<sup>+</sup>, and 4T1-GFP cells (**h**), identified by GFP, in representative animals. Right, frequency of metastatic cells.

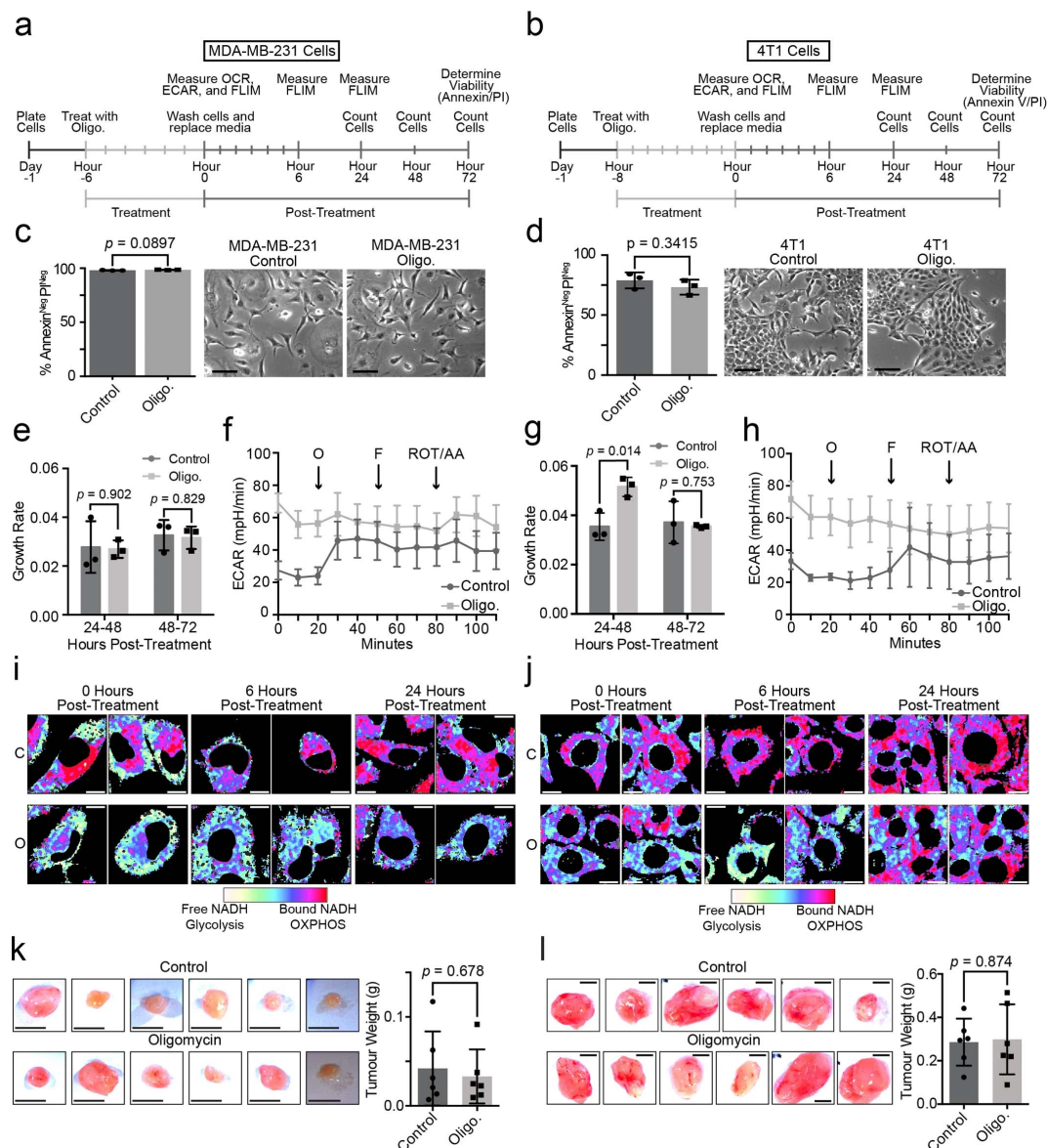


Figure 4.11: Oligomycin treatment inhibits OXPHOS in MDA-MB-231 and 4T1-GFP cells. **a,b**, Schematic of the experimental setup to determine the effects of oligomycin treatment on MDA-MB-231 (**a**) or 4T1-GFP (**b**) cells. (**c-d**) Bar graph (left) of the viability of MDA-MB-231 (**c**) or 4T1-GFP (**d**) cells 72-hours post-treatment determined via flow cytometry. Brightfield images (right) of in vitro MDA-MB-231 (**c**) or 4T1-GFP (**d**) cells 72 hours after cessation of oligomycin treatment. Scale bar=100  $\mu$ m. **e**, Growth rate of MDA-MB-231 cells for the indicated time period after cessation of oligomycin treatment. **f**, Extracellular acidification rate (ECAR) of MDA-MB-231 treated with oligomycin compared to control cells. **g**, Same as (**e**) for 4T1-GFP cells. **h**, Same as (**f**) for 4T1-GFP cells. (**i,j**) Additional FLIM images of the fluorescence lifetime of NADH in cultured MDA-MB-231 (**i**) or 4T1-GFP cells (**j**) as shown in Fig. 4.10e,f. (**k-l**) Brightfield images of tumours from orthotopically injected control or oligomycin treated MDA-MB-231 (**k**) or 4T1-GFP (**l**) cells. Scale bar=0.5 cm.



ification rate (ECAR; Fig. 4.10c,d and 4.11f,h), suggesting the cells shift from OXPHOS to glycolysis. We further utilized phasor fluorescence lifetime imaging (FLIM) of NADH to determine the durability of the metabolic shift. Fluorescence lifetime imaging relies on the fact that the fluorescence lifetime of NADH is longer when bound to enzymes involved in mitochondrial metabolism (approximately 3.4 ns) than when free floating in the cell during glycolysis (approximately 0.4 ns) [Digman et al. (2008); Sameni et al. (2016)]. Analysis of the FLIM 6-24h after treatment showed a significant decrease in bound NADH, indicating a durable shift from OXPHOS to glycolysis in both cell lines ( $P < 0.05$ ; Fig. 4.10e,f and 4.11i,j). Collectively, these data demonstrate that oligomycin induces MDA-MB-231 and 4T1 cells to shift from OXPHOS to glycolytic metabolism without compromising cell viability or proliferation.

We injected NOD/SCID mice intravenously with oligomycin-treated or control MDA-MB-231 cells ( $8 \times 10^5$ ) and harvested lungs of the mice 21d later (Fig. 4.10a). Flow cytometry analysis showed an almost threefold decrease in the frequency of metastatic cells in the lungs of the treatment group (Fig. 4.10g), showing that OXPHOS inhibition attenuates the metastatic capacity of MDA-MB-231 cells. We used a similar approach to test the effects of OXPHOS inhibition on 4T1 cell metastasis (Fig. 4.10b). We injected green fluorescent protein (GFP)-labelled 4T1 cells ( $1 \times 10^5$ ) into BALB/c mice and harvested the lungs of the mice 5d later, as 4T1 cells metastasize rapidly in the lung. Remarkably, the animals injected with oligomycin-treated 4T1-GFP cells displayed a sevenfold decrease in metastatic cells in their lungs at this early time point (Fig. 4.10h), suggesting OXPHOS is important to facilitate early events in the metastatic cascade.

Finally, we tested the effects of oligomycin treatment on primary tumour growth to determine whether OXPHOS is specifically important for metastasis or generally important for cancer cell function. We treated 4T1 and MDA-MB-231 cells with oligomycin in vitro, performed bilateral orthotopic injections ( $1 \times 10^6$  cells), and harvested tumours 14 and 17d later, respectively (Fig. 4.11k,l). We found no significant difference in engraftment efficiency or

tumour size in control versus oligomycin-treated tumours (Fig. 4.11k,l), further establishing a role for OXPHOS in mediating the lung metastasis (Fig. 4.12).

### 4.2.3 Discussion

Defining the molecular mechanisms that facilitate specific stages of the metastatic cascade is critical to understand how cells metastasize and inspire new strategies to prevent metastatic spread in cancer patients. We have developed a robust approach for the capture and analysis of rare cells during the seeding and establishment of micrometastasis in PDX models using scRNA-seq. We found that micrometastases display significant transcriptional heterogeneity but also display a distinct expression program that is predictive of poor survival in patients with breast cancer. We identify mitochondrial OXPHOS as the top pathway upregulated in micrometastases, in contrast to primary tumour cells that score higher for genes associated with aerobic glycolysis (Fig. 4.12). We validated this by flow cytometry and HR-LCMS, where we found that micrometastases display a distinct metabolic profile and higher levels of several metabolites that feed into OXPHOS. Most importantly, we found that pharmacological inhibition of OXPHOS substantially attenuates lung metastasis, showing that OXPHOS is functionally critical for metastatic spread.

Our work sheds light on the controversial role of metabolism in metastasis. Historically, tumours were thought to contain dysfunctional mitochondria and be principally sustained by Warburg metabolism [Koppenol et al. (2011); Warburg (1956)]. Recent work has challenged this dogma, showing the importance of glutamine [Dornier et al. (2017); Rodrigues et al. (2016); Yang et al. (2014)], fatty-acid [Antalis et al. (2011); Camarda et al. (2016)], proline [Elia et al. (2017)] and pyruvate carboxylase-mediated metabolism [Christen et al. (2016)] in metastatic progression [Elia et al. (2018); Teoh and Lunt (2018)]. Recent work using the 4T1 mouse model also showed that circulating cancer cells utilize increased OXPHOS and that suppression of a central regulator of mitochondrial biogenesis (PGC1a) reduces cancer-cell invasion and metastasis [LeBleu et al. (2014)]. Another study showed increased expression

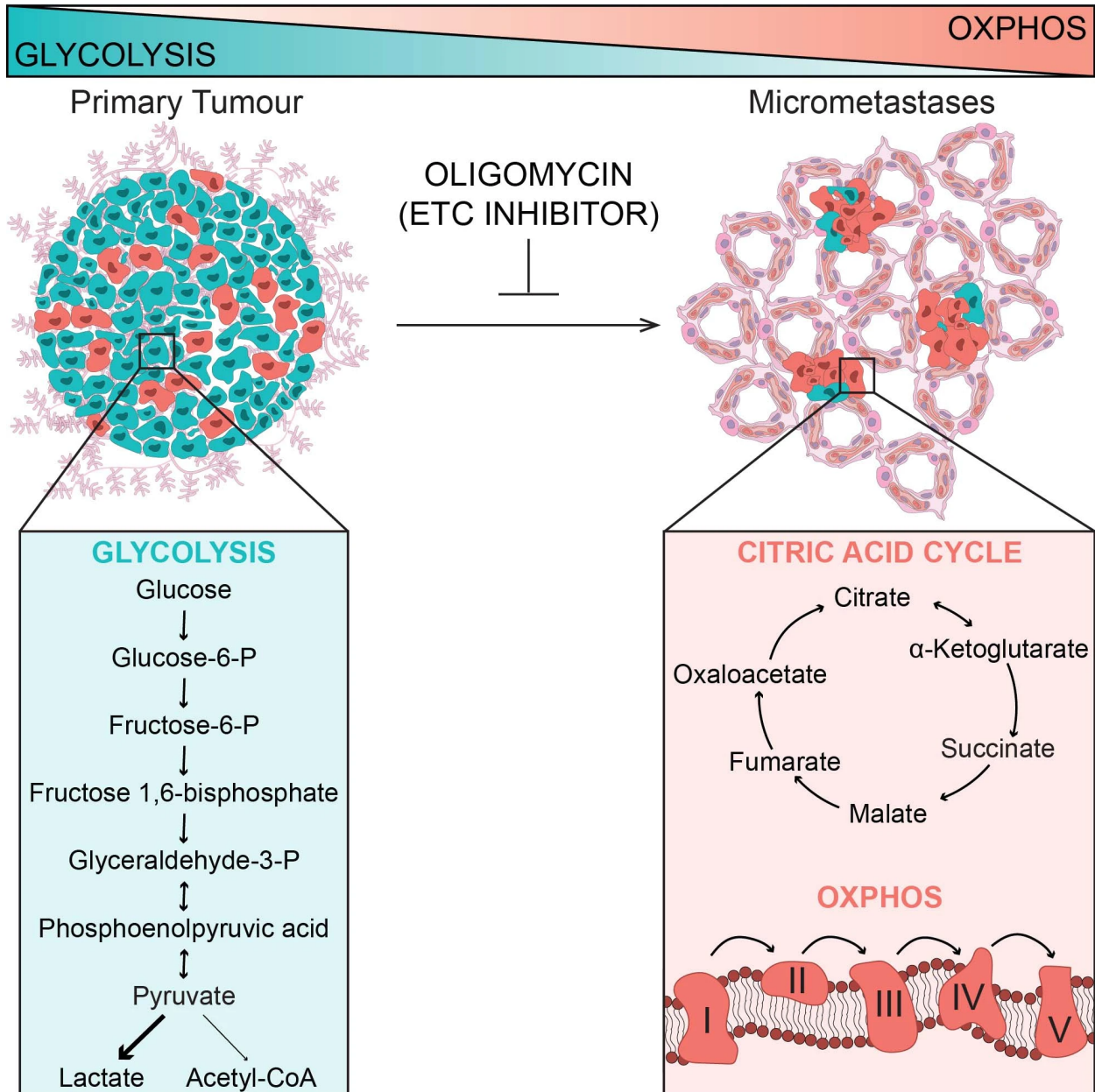


Figure 4.12: Model for metabolic shift associated with metastatic seeding in TNBC. Metastatic cells in the lung and lymph nodes display increased OXPHOS, in contrast to primary tumour cells that express higher levels of genes associated with aerobic glycolysis. Pharmacological inhibition of OXPHOS with the complex V inhibitor oligomycin substantially attenuates lung metastasis in experimental models of TNBC, showing that OXPHOS is functionally important for metastasis.



of mitochondrial complex I and oxidative stress in lung micrometastases using in situ RNA sequencing [Basnet et al. (2019)]. Our work utilized an unbiased transcriptomic approach to discover that OXPHOS promotes metastasis, specifically during the seeding step of the metastatic cascade, in three distinct human patient models of TNBC. Interestingly, many metabolic pathways implicated in metastasis—such as glutamine, fatty-acid and proline metabolism—also converge on or produce critical metabolites to drive OXPHOS, raising the question of whether OXPHOS represents an underlying mechanistic link between them.

Oxidative phosphorylation may promote metastatic seeding in several ways. Increased ATP generation through OXPHOS may provide energy for cytoskeleton remodelling for motility or to survive anoikis during cell detachment and migration [Schafer et al. (2009)]. Increased ROS production through OXPHOS may promote cell motility by activating oncogenic signalling, as mitochondrial ROS-inducing mutations are sufficient to trigger metastasis [Dai et al. (2015); Giannoni et al. (2008); Ogura et al. (2012); Porporato et al. (2014); Zielonka and Kalyanaraman (2008)]. Epidemiological data in humans also support a role for OXPHOS in cancer progression, showing that treatment with the diabetes drug metformin (complex I inhibitor) is protective against the relapse and metastasis of breast cancer [Bodmer et al. (2011); Col et al. (2012); Kumar et al. (2013); Romero et al. (2012)]. Several drugs targeting mitochondrial metabolism are already FDA approved or in clinical trials (for example, IACS-010759 (ref. [Yap et al. (2019)]), plumbagin [Hafeez et al. (2015,1)] and atovaquone [Fiorillo et al. (2016); Lv et al. (2018)]), providing an opportunity for re-indication in breast cancer patients to prevent metastasis. However, further studies are needed to define which specific steps of the metastatic cascade OXPHOS is critical for to determine when it might be applied for clinical benefit against metastasis.

## 4.2.4 Methods

### 4.2.4.1 PDX models

The samples from patients were provided by A. L. Welm at the Department of Oncological Sciences at the Huntsman Cancer Institute (HCI). All of the tissue samples were collected with informed consent from individuals being treated at the Huntsman Cancer Hospital and the University of Utah under a protocol approved by the Institutional Review Board of the University of Utah. HCI001 was acquired from a primary tumour biopsy of a female patient diagnosed with Stage IV ER-PR-Her2- basal-like invasive ductal carcinoma with no previous systemic treatment. HCI002 was acquired from a primary tumour biopsy of a female patient diagnosed with Stage IIIA ER-PR-Her2- basal-like medullary-type invasive ductal carcinoma with no previous systemic treatment. HCI010 was acquired from a pleural effusion of a female patient diagnosed with Stage IIIC ER-PR-Her2- basal-like (PAM50) invasive ductal carcinoma treated with several rounds of chemotherapies. The samples were collected and de-identified by the Huntsman Cancer Institute Tissue Resource and Application Core facility before being obtained for implantation. The study is compliant with all of the relevant ethical regulations regarding research involving human participants.

### 4.2.4.2 Animal experiments

The Institutional Animal Care and Use Committee of the University of California, Irvine reviewed and approved all of the animal experiments. Orthotopic transplants of serially passaged human tumour samples were performed on immunocompromised three- to four-week-old NOD/SCID or NSG mice after clearing the mammary fat pads following established protocols [[Lawson et al. \(2015\)](#)]. Tumour growth was monitored by weekly caliper measurements and volumes were calculated as:  $\text{length} \times \text{width}^2 \times 0.51$ . The animals were euthanized and tissues were harvested when the tumours reached a length or width of 2.0-2.5 cm. For the experimental metastasis studies, cultured MDA-MB-231 or 4T1-GFP cells were

suspended in 100  $\mu$ L sterile PBS and injected into the tail vein of eight- to ten-week-old female NOD/SCID (MDA-MB-231) or BALB/c (4T1-GFP) mice. The mice were euthanized by asphyxiation with CO<sub>2</sub> followed by cervical dislocation and perfusion with 10 mM EDTA in D-PBS 21d (MDA-MB-231) or 5d (4T1-GFP) post injection. For the cell-line orthotopic tumour injections, the mice were placed under isoflurane anaesthesia (1.5-2.0%). The area was shaved and cleaned with an alcohol swab before injection. MDA-MB-231 or 4T1-GFP cells ( $1 \times 10^6$  cells in 100  $\mu$ L PBS) were injected bilaterally into the fourth mammary fat pad of 10- to 12-week-old NSG mice. The study is compliant with all of the relevant ethical regulations regarding animal research.

#### **4.2.4.3 Tissue harvest and dissociation**

Animals at the endpoint were euthanized by asphyxiation with CO<sub>2</sub> followed by cervical dislocation and perfusion with 10 mM EDTA in D-PBS. Evan's Blue (Sigma-Aldrich, cat. no. E2129-10G) was injected into the footpads and ears of the anaesthetized mice before perfusion to aid visualization of the lymph nodes. The solid tissues from the mice—which included the primary tumour, lungs and lymph nodes—were processed for flow cytometry by mechanical chopping with blades, followed by collagenase IV (Sigma-Aldrich cat. no. C5138-1G) digestion in medium (DMEM-F12 medium with 5% FBS, 5  $\mu$ g ml<sup>-1</sup> insulin and 1% penicillin/streptomycin solution) for 45 min at 37°C. The cell suspensions were washed with 2  $\mu$ g ml<sup>-1</sup> DNase I (Worthington Biochemical, cat. no. LS002139) for 5 min and further dissociated with 0.05% trypsin for 10 min. Following a wash with Hanks balanced salt solution with 2% FBS, the cells were passed through a 70- $\mu$ m filter. Lung and primary tumour cells were treated with  $1 \times$  RBC lysis buffer, followed by resuspension in DMEM-F12 with 10% FBS for FACS.

#### 4.2.4.4 Cell culture

MDA-MB-231 and 4T1-GFP cells were cultured in either 10 cm or six-well plates (Genesee Scientific, cat. no. 25-105) containing DMEM-F12 (Fisher Scientific, cat. no. MT10090CV), 5% heat-inactivated fetal bovine serum (Sigma-Aldrich, cat. no. 12306C) and 1% penicillin-streptomycin 100 $\times$  solution (Hyclone, cat. no. SV30010). The cells were passaged with 0.05% trypsin (Corning, cat. no. 25-052-CI) after reaching 70% confluency. For the control-treated cells, the medium was replaced with fresh medium. For the oligomycin-treated cells, medium containing 1  $\mu$ M oligomycin was added for either 6h (MDA-MB-231) or 8h (4T1-GFP), the cells were then washed and fresh medium was added. For the FLIM analysis, 4T1-GFP mouse breast cancer cells and MDA-MB-231 human breast cancer cells were cultured in DMEM (Thermo Fisher Scientific, cat. no. 11965092) supplemented with 10% heat-inactivated fetal bovine serum (Thermo Fisher Scientific, cat. no. 10082139) and 1% penicillin-streptomycin 100 $\times$  solution (Hyclone, cat. no. SV30010). The cells were plated at a confluency of  $2 \times 10^4$  cells  $\text{cm}^{-2}$  in eight-well glass-bottomed fibronectin-coated imaging dishes (Thermo Fisher Scientific, cat. no. 155411) approximately 24h before drug treatment and left to adhere. The medium was replaced the following day with medium containing 1  $\mu$ M oligomycin (MP Biomedicals, cat. no. 0215178610), whereas the control cells had their medium replaced. The cells were washed with PBS and their medium was replaced after 8h (4T1-GFP) or 6h (MDA-MB-231) of treatment. The cells were then imaged at 0, 6 and 24h post washout for no more than 1h per experimental condition. For the proliferation studies,  $2 \times 10^5$  MDA-MB-231 cells were seeded on six-well plates (Genesee Scientific, cat. no. 25-105) containing DMEM-F12 (Fisher Scientific, cat. no. MT10090CV), 10% heat-inactivated fetal bovine serum (Sigma-Aldrich, cat. no. 12306C), 1% penicillin-streptomycin 100 $\times$  solution (Hyclone, cat. no. SV30010) and 5 mM HEPES (Gibco, cat. no. 15630-080) approximately 24h before drug treatment and left to adhere; 4T1 ( $2 \times 10^5$ ) cells were seeded on six-well plates (Genesee Scientific, cat. no. 25-105) containing DMEM-F12 (Fisher Scientific, cat. no. MT10090CV), 5% heat-inactivated fetal bovine serum (Sigma-Aldrich, cat. no. 12306C)

and 1% penicillin-streptomycin 100× solution (Hyclone, cat. no. SV30010) approximately 24h before drug treatment and left to adhere. The medium was replaced the following day with medium containing 1  $\mu$ M oligomycin (MP Biomedicals, cat. no. 0215178610), whereas the control cells had their medium replaced. The cells were washed with PBS and their medium was replaced after 8h (4T1-GFP) or 6h (MDA-MB-231) of treatment. The cells were collected with 0.05% trypsin (Corning, cat. no. 25-052-Cl) at 24, 48 and 72h post treatment and counted using a Countess II automated cell counter (Thermo Fisher Scientific, cat. no. AMQAX1000). The growth rate between 24 and 48h, and between 48 and 72h post treatment was calculated using the following equation:

$$Growth - rate = \frac{\ln\left(\frac{N(t)}{N(0)}\right)}{t}$$

Where  $N(t)$  is the number of cells at either 48 or 72h,  $N(0)$  is the number of cells at either 24 or 48h and  $t$  is the time between measurements.

#### 4.2.4.5 Flow cytometry

We used the human-specific antibody CD298 (diluted 1:100; PE; BioLegend, cat. no. 341704) and the mouse-specific antibody MHC-I (diluted 1:150; APC; Thermo Fisher Scientific, cat. no. 17-5957-80). Flow cytometry was performed using a BD FACSAria Fusion cell sorter. Cell viability was determined by negative staining with SYTOX blue (diluted 1:1,000; Thermo Fisher Scientific, cat. no. S34857). The forward-scatter area by forward-scatter width (FSC-H×FSC-A) and side-scatter area by side-scatter width (SSC-H×SSC-A) was used to discriminate single cells from doublet and multiplet cells. Mouse cells were excluded by gating out CD298-MHC-I+ cells. Human primary tumour cells and metastatic cells were selected by gating on Sytox-CD298+MHC-I- cells. For the mitochondrial membrane potential readouts, the cells were stained with TMRM (diluted 1:500; Thermo Fisher

Scientific, cat. no. T668), MitoTracker-Green (diluted 1:100 from a 10  $\mu$ M stock; Thermo Fisher Scientific, cat. no. M7514), human-specific antibody CD298 (diluted 1:100; APC; BioLegend, cat. no. 341706) and the mouse-specific antibody MHC-I (diluted 1:100; PE/Cy7; BioLegend, cat. no. 114717). Cell viability was determined by negative staining with SYTOX blue (diluted 1:1,000; Thermo Fisher Scientific, cat. no. S34857). Compensation controls and fluorescence minus one controls were used to determine the TMRM<sup>high</sup> and TMRM<sup>low</sup> populations in the PDX tumour cells. For the analysis of the MDA-MB-231 metastatic burden, FSC-W $\times$ FSC-A and SSC-W $\times$ SSC-A was used to discriminate single cells from doublet and multiplet cells. The MDA-MB-231 cells were defined by gating on Sytox-CD298<sup>+</sup>MHC-I<sup>-</sup> cells and the level of metastatic burden was determined using the frequency of that population. One mouse from the oligomycin-treated group did not contain any detectable MDA-MB-231 cells by flow cytometry and was thus excluded from the analysis. For the analysis of the 4T1-GFP metastatic burden, FSC-H $\times$ FSC-A and SSC-H $\times$ SSC-A was used to discriminate single cells from doublet and multiplet cells. The 4T1-GFP cells were defined by gating on Sytox-GFP<sup>+</sup> cells and the level of metastatic burden was determined using the frequency of that population. For the analysis of cell viability following oligomycin treatment, the cells were stained with annexin V-FITC (diluted 1:100; GeneTex, cat. no. GTX14082) and propidium iodide (diluted 1:100; Thermo Fisher Scientific, cat. no. P3566). FSC-W $\times$ FSC-A and SSC-W $\times$ SSC-A was used to discriminate single cells from doublet and multiplet cells. Viability was determined by the frequency of annexin V-propidium iodide-cells in the population.

#### **4.2.4.6 Generation of scRNA-seq data**

Single cells were sorted directly into each well of a skirted 96-well PCR plate (Fisher Scientific, Eppendorf, cat. no. E951020443) containing lysis buffer (0.2% Triton X-100 (Sigma-Aldrich, cat. no. T9284), 2U $\mu$ l<sup>-1</sup> RNaseOUT (Thermo Fisher Scientific, cat. no. 10777019), 10  $\mu$ M oligo-dT30VN and 10  $\mu$ M dNTPs (Thermo Fisher Scientific, cat. no. 18427088)). The

plates were snap frozen on dry ice and stored at  $-80^{\circ}\text{C}$  until further processing. Total RNA was converted into complementary DNA using the SmartSeq2 protocol and prepared for Illumina sequencing using the Nextera XT DNA library preparation kit (Illumina, cat. no. FC-131-1096). The cells were sequenced at a depth of  $1 \times 10^6$  reads per cell on a HiSeq 2500 system.

#### 4.2.4.7 Processing of scRNA-seq data

Files from the HiSeq 2500 were demultiplexed and converted to FASTQ files. Paired-end 100bp reads were aligned to the Gencode 21 human transcriptome using Bowtie 2 and quantified using RSEM with the following parameters: `rsem-calculate-expression -p $CORES --bowtie2 --paired-end READ1 READ2 gencodehg21`. The expression values were log-transformed into  $\log[\text{transcripts per kilobase million} + 1]$  matrices and loaded into the Seurat analysis package with the following parameters: `p10<- CreateSeuratObject(raw.data=p10.mat, min.cells=8, min.genes=1,000, project='HCI010')`. We removed any cells identified as visual outliers by library complexity ( $<2,500$  genes per cell) or overrepresentation of mitochondrial gene expression ( $>50\%$ ) as a further quality control. In addition, we removed any genes that were not represented in a robust population of cells ( $<8$  cells per gene) from the downstream analysis. This resulted in a final analysis of 1,119 single-cell profiles. Using the RegressOut feature in Seurat, we calculated the z-score residuals using `nGene` and `percent.mito` as co-variates, which was used to perform principal-component analysis and tSNE. A G1/S and G2/M score was calculated using the gene score method described below and regressed out as well for HCI001 and HCI010.

#### 4.2.4.8 Dimensionality reduction, cell cluster identification and differential gene expression analysis

Dimensionality reduction and differential gene expression was performed using the Seurat analysis package version 2.1.0 (refs. [Butler et al. (2018); Satija et al. (2015)]). For the com-

binned and individual patient analysis, highly variable genes in our dataset were identified using the `MeanVarPlot` function with the following parameters: `FindVariableGenes(object = comb, mean.function = ExpMean, dispersion.function = LogVMR, x.low.cutoff = 0.0125, x.high.cutoff = 3, y.cutoff = 0.5)`. These variable genes were then used for principal-component analysis. The principal components generated were then used to perform tSNE of the data. For the individual patient analysis, using the `FindClusters` function in Seurat and a granularity parameter of 1.0, we identified distinct subpopulations and defined marker genes for each of them with the `FindAllMarkers` function in Seurat with the default settings for the `FindAllMarkers` function and the ‘bimod’ statistical test. For the generation of the 330-micrometastatic-gene signature, metastatic cells from all PDX models were grouped together separate from tumour cells and we calculated a differential expression test in Seurat using the ‘tobit’ test with the following parameters: `comb<- FindAllMarkers(object=comb, only.pos=TRUE, min.pct=0.1, logfc.threshold=0.25, test.use='tobit', latent.vars='orig.ident')`. The ‘orig.ident’ command in the ‘latent.vars’ variable represents the patient ID (that is, HCI001, and so on). By including this variable, the tobit model identifies conserved marker genes [Butler et al. (2018); Satija et al. (2015)]. The ‘min.pct’ variable in Seurat’s differential expression (DE) tobit test is defined as the minimum percent of cells per group that must express a gene ( $\log(\text{TPM}+1) > 0$ ) to be considered in the output of the test. Gene Ontology analysis was performed using the Enrichr web resource, where the input gene set for each population was the markers identified by `FindAllMarkers`. For the analysis of specific OXPHOS and glycolysis genes, we calculated the average  $\log_2[\text{FC}]$  of the raw matrix values using the `FetchData(use.raw=T)` function in Seurat.

#### **4.2.4.9 Development of logistic regression model for identifying candidate biomarkers**

To calculate the logistic regression model used to identify candidate biomarker targets, the gene expressions were normalized across all cells such that each gene had a mean expression



of zero and a s.d. of one. For model fitting, the data were sampled equally ten times from each mouse and cell-identity (tumour versus micrometastasis) category to avoid systematic bias. For each sampling, a stepwise regression with forward selection was performed, where at each step the model that minimized the Akaike information criterion was chosen to be used as a base model for the next step. Our logistic regression model used a conservative cutoff of five genes based on the elbow in the Akaike information criterion plot to minimize the size of our gene set while maintaining descriptive power.

#### **4.2.4.10 Gene scoring**

To quantitatively compare gene groups (for example, glycolysis and OXPHOS) in our cell populations, we utilized individual gene scores as described previously. A curated list of genes was obtained from the Kyoto Encyclopedia of Genes and Genomes, a database used for GO term enrichment. We utilized the `AddModuleScore()` function from Seurat to calculate the gene scores for each population. Full gene lists for all pathways used in the gene-scoring analysis are provided in Supplementary Table 5 (online).

#### **4.2.4.11 Relapse-free-survival analysis**

For the relapse-free-survival analysis, we generated Kaplan-Meier survival curves on primary tumour microarray data of patients with basal-like breast cancer from the KM Plotter database for the top-20 micrometastasis-associated genes in our 330-gene signature [gyorffy 2010, Nagy 2018]. We found that two genes were not predictive and the data for three genes were not available, and these genes were thus excluded. To generate the combined survival analysis, we calculated a weighted average of the 15 predictive genes analysed using the ‘Use Multiple Genes’ function in KM Plotter. All Kaplan-Meier plots are displayed using the ‘auto select best cutoff’ parameter.

#### 4.2.4.12 Histology

Tumour and lung tissues from the PDX mouse models were fixed overnight in 4% paraformaldehyde and then dehydrated and processed for paraffin embedding in a Leica tissue processor using standard protocols. The paraffin blocks were cut into 5- $\mu$ m-thick sections using a Leica microtome, rehydrated and then stained with haematoxylin and eosin. Bright-field imaging was performed using a BZ-X700 Keyence microscope.

#### 4.2.4.13 Fluorescent in situ hybridization

Fluorescent in situ hybridization was performed on formalin-fixed paraffin-embedded sections using the RNAscope multiplex fluorescent reagent kit v2 (ACD, cat. no. 323110) according to the manufacturer's instructions. Briefly, the formalin-fixed paraffin-embedded sections were rehydrated in HistoClear and 100% ethanol before antigen retrieval using the RNAscope antigen retrieval solution and mild boiling at 100°C for 15min. PHLDA2 probe (ACD, cat. no. 551441) amplification was performed according to the manufacturer's instructions with the TSA plus cyanine 3 (diluted 1:1,000; PerkinElmer, cat. no. PN NEL744001KT) fluorophore, stained with DAPI and mounted with Prolong Gold. The slides were visualized using a Zeiss LS700 confocal microscope. Image analysis was performed in ImageJ. The normalized total fluorescence intensity of the PHLDA2 probe was calculated on regions of interest across at least five different fields of view on two mouse lungs and three tumours from HCI001 according to the following equation:

$$Normalized - TFI = \frac{Fluorescence - integrated - density}{Area - of - region - of - interest}$$

The surrounding mouse stroma was excluded from the analysis for the quantification of lung micrometastatic regions of interest and the necrotic regions or mouse stroma were excluded from the analysis for the tumour regions of interest.

#### **4.2.4.14 Quantitative real-time PCR**

Total RNA was extracted using a Quick-RNA MicroPrep kit (Zymo, cat. no. R1050). The messenger RNA was reverse transcribed into cDNA using the iScript cDNA synthesis kit (BioRad, cat. no. 1708891) according to the manufacturer's protocol. The quantitative real-time PCR reactions were performed using PowerUp SYBRGreen master mix (Applied Biosystems, cat. no. A25742). The primer sequences used for each gene are listed in Supplementary Table 7 (online).

#### **4.2.4.15 OCR and ECAR measurements**

MDA-MB-231 or 4T1-GFP ( $8 \times 10^4$ ) cells were seeded into Seahorse XF24 microplates (Agilent, cat. no. 100850), and the XF24 cartridge (Agilent, cat. no. 100850) was calibrated in the Seahorse prep station (Agilent) overnight. The medium was replaced with 0.5 ml XF base medium (Agilent, cat. no. 102353) supplemented with 10 mM glucose, 2 mM glutamine and 1 mM pyruvate before the assay. The cells were incubated at 37°C for 1h in the Seahorse prep station. Next, 56  $\mu$ l oligomycin (2  $\mu$ M; Sigma, cat. no. 75351), 62  $\mu$ l FCCP (2  $\mu$ M; Sigma, cat. no. C2920) and 69  $\mu$ l rotenone with antimycin A (1  $\mu$ M; Sigma, cat. no. 557368, A8674) were added into the cartridge wells. The OCR and ECAR levels were determined using Seahorse bioscience XF24 extracellular flux analyzer (Agilent) and each cycle of measurement involved mixing (3min), waiting (2min) and measuring (3min) cycles. To quantify the basal respiration, we calculated the difference in the average OCR before the addition of oligomycin and the average OCR after the addition of rotenone with antimycin A. For ATP-dependent respiration, we calculated the difference in average OCR before and after the addition of oligomycin. The maximal respiration rates were calculated as the difference in average OCR after the addition of FCCP and the average OCR after the addition of oligomycin. Any negative values were set to zero for visualization and when calculating differences between groups.

#### 4.2.4.16 FLIM

All FLIM imaging experiments were performed as previously described [Mah et al. (2018)]. The FLIM images were acquired on an inverted laser scanning confocal microscope with a  $\times 40/1.2$  numerical aperture water-immersion objective with cells kept under biological conditions throughout. The cells (4T1-GFP and MDA-MB-231) were excited at approximately 2 mW with a two-photon Ti:Sapphire laser (Spectra-Physics, MaiTai) at 740 nm, which was passed through a 690 nm dichroic filter. The fluorescence emission was separated through a bandpass filter (442/46 nm) to capture the cell auto-fluorescence and exclude any GFP emission, and was then detected using a photomultiplier tube (Hamamatsu, cat. no. H7422P-40). The fluorescence lifetime decays were captured in the frequency domain via an A320 FastFLIM box (ISS) and subsequently mapped onto the phasor plot using the SimFCS software—developed at the Laboratory for Fluorescence Dynamics at the University of California, Irvine—for quantitative NADH lifetime analysis. Coumarin-6 in ethanol, with a known single exponential fluorescence lifetime of  $2.5 = \text{ns}$ , was imaged before each experiment and used as a calibration sample for the instrument response time.

#### 4.2.4.17 FLIM data analysis

Each pixel of the FLIM image was Fourier transformed and plotted on the phasor plot in SimFCS, as previously described [Mah et al. (2018)]. Each FLIM image was individually masked to exclude any nuclei from the analysis. The cluster of phasors of each masked frame were then averaged to obtain its G and S coordinate, which was then used to determine the fraction of free NADH of each cluster. This free NADH fraction was calculated on the fact that 100% free NADH has a decay of approximately 0.4 ns and 100% bound NADH has a decay of approximately 3.4 ns. Any pixel with a fluorescence decay containing a mixture of both free and bound NADH will lie within the linear combination of 100% free and 100% bound NADH when on the phasor plot in the frequency domain. Consequently, the fraction of free NADH of the cluster can be calculated by the mathematical distance between the

positions of the 100% free NADH and 100% bound NADH on the universal circle of the cluster. For each independent experiment, the fraction of free NADH of the treated sample was subtracted from the average of the fraction of free NADH of the control sample to obtain the fraction of free NADH difference. Significance was determined using a two-tailed Student's t-test with homoscedasticity determined using an F-test. The error bars represent the s.e.m.

#### **4.2.4.18 Statistics and reproducibility**

Quantitative data are presented as either the mean $\pm$ s.e.m. or mean $\pm$ s.d. from at least three independent experiments unless otherwise specified. When appropriate, statistically significant differences between groups were analysed using a two-way unpaired Student's t-test. Differences were considered significant at  $P < 0.05$ . All samples—if preserved and properly processed—were included in the analyses and no samples or animals were excluded, unless otherwise specified. No statistical method was used to predetermine the sample sizes and the female mice were randomly assigned PDX tumours for transplant. The investigators were not blinded to allocation during experiments and outcome assessment.

#### **4.2.5 Reporting Summary**

Further information on research design is available in the Nature Research Reporting Summary linked to this article.

#### **4.2.6 Data availability**

The authors declare that all data supporting the findings of this study are available within the article and its supplementary information files or from the corresponding author on reasonable request. All RNA-seq data files along with their associated metadata have been deposited in the GEO database under the accession code GSE123837. Previously published

microarray data that were reanalysed here with KM Plotter [Györfy et al. (2010); Nagy et al. (2018)] are available under the following accession codes: E-MTAB-365, E-TABM-43, GSE11121, GSE12093, GSE12276, GSE1456, GSE16391, GSE16446, GSE16716, GSE17705, GSE17907, GSE18728, GSE19615, GSE20194, GSE20271, GSE2034, GSE20685, GSE20711, GSE21653, GSE2603, GSE26971, GSE2990, GSE31448, GSE31519, GSE32646, GSE3494, GSE37946, GSE41998, GSE42568, GSE45255, GSE4611, GSE5327, GSE6532, GSE7390 and GSE9195.

#### 4.2.7 Code availability

Custom scripts are available at [https://github.com/lawsonlab/Single\\_Cell\\_Metastasis](https://github.com/lawsonlab/Single_Cell_Metastasis).

#### 4.2.8 Acknowledgements

We thank G. Gutierrez and M. Masoud for technical assistance and animal handling. We thank N. Pervolarakis for helpful advice on data analysis. We thank K. Kessenbrock for thoughtful feedback on experimental design and careful review of the manuscript. We thank A. L. Welm for providing the PDX samples. Image acquisition was made possible in part through access to the Optical Biology Core Facility of the Developmental Biology Center, a shared resource supported by the Cancer Center Support Grant (grant no. CA-62203), with assistance from A. Syed and a Center for Complex Biological Systems Support Grant (grant no. GM-076516) at the University of California, Irvine. This study was supported by funds from the National Cancer Institute (grant nos R01 CA057621 and U01 CA199315 to Z.W., and grant no. K22 CA190511 to D.A.L.), National Institutes of Health (grant no. R01HD073179 to E.M., P41-GM103540 to M.A.D. and A.E.Y.T.L., and T32CA009054 to M.B.G. and R.T.D., through matched university funds through matched university funds), National Science Foundation (grant no. 1847005 to M.A.D. and NSF GRFP DGE-1839285 to A.E.Y.T.L.), Team Michelle and Friends non-profit organization, Suzette Kirby Breast

Cancer Research Fund, V Foundation (grant no. V2019-019) as well as an Opportunity Award funded by the UCI Center for Complex Biological Systems (CCBS; NIGMS, grant no. P50-GM076516 to R.T.D., K.B., D.Maurer, E.M. and D.A.L.). H.A. was supported by the University of Hail, Hail, Saudi Arabia for the PhD Fellowship. D.Ma was supported by a Canadian Institutes of Health Research Postdoctoral Fellowship.

### **4.2.9 Contributions**

D.A.L., E.M., M.K., M.A.D., J.W.L. and Z.W. designed and supervised the research. R.T.D., Y.Y., K.B., M.B.G., D.Ma, A.E.Y.T.L., A.T.P., H.A., G.A.H., J.L. and D.A.L. performed the research. R.T.D., K.B., Z.X. and D.Maurer performed the bioinformatic analyses. R.T.D. and D.A.L. wrote the manuscript, and all authors discussed the results and provided comments and feedback.

## **4.3 Summary**

In this chapter, we presented results that differentiated metabolic processes on both the genotypic and phenotypic level between tumors and their invasive and metastatic fronts. In the first section, our data showed that patient-derived GBM cells shifted their metabolic functions when they were cultured in soft vs. stiff HA hydrogels. Specifically, we showed that in soft hydrogels, the GBM spheroids become more invasive and upregulate glycolytic RNA expression and NADH fractions as compared to those in stiff hydrogels. However, the invading arms of the soft hydrogel-cultured GBM spheroids differed from their core, showing a phenotypic upregulation of oxidative phosphorylation NADH fractions. Similarly, in patient-derived xenografted breast cancer mouse models, the metastatic tumor populations had both genotypically and phenotypically upregulated oxphos metabolism mechanisms as compared to the primary tumor site. We showed that upon inhibition of oxidative phosphorylation, there was a reduction in metastasis in breast cancer cells.

This chapter developed on ideas described in the previous chapter by using more physiologically relevant experimental models. Though extremely powerful, the metastatic model used in the second section is limited in its flexibility for phenotypic assays in live cells. In the next chapter, we create a 3D breast cancer tumor spheroid culture-transplant system to facilitate the expansion and modulation of PDX cells to run functional metastatic assays. This model will be used in future chapters to help run phenotypic mitochondrial experiments.



# Chapter 5

## Patient-derived xenograft culture-transplant system for investigation of human breast cancer metastasis

This chapter is again part of the wonderful collaboration with Dr. Devon Lawson and Dr. Kai Kessenbrock and is a slightly modified version of a paper from: Ma et al., Patient-derived xenograft culture-transplant system for investigation of human breast cancer metastasis, bioRxiv, posted 2020 and has been reproduced here with the permission of the copyright holders.

### 5.1 Abstract

Metastatic disease carries a poor prognosis and its study is limited by the availability of authentic experimental models. Here, we present a 3D tumor sphere culture-transplant system that facilitates expansion and modulation of patient-derived xenograft (PDX) cells

for use in functional experimental metastasis assays. RNA sequencing shows PDX tumor spheres maintain fundamental properties of native tumor cells. In vivo transplantation studies demonstrate cultured cells yield robust spontaneous and experimental metastasis following orthotopic and intravenous or intracardiac delivery, respectively. Pharmacologic inhibition of previously reported metastasis-promoting pathways also inhibits metastasis of PDX cells after culture, validating our approach. Finally, we used our culture-transplant system to demonstrate a new role of the metabolic enzyme NME1 in promoting breast cancer metastasis. Thus, we present a novel method for authentic propagation, engineering and transplantation of PDX models for functional studies of metastasis using bona fide patient tumor cells.

## 5.2 Introduction

Metastasis is the cause of >95% of breast cancer patient mortality, causing death in >40,000 women per year [DeSantis et al. (2016); Lambert et al. (2017)]. There are limited effective treatments for metastasis, and the identification of new therapeutic targets has been hindered by a lack of experimental models that faithfully recapitulate metastatic disease. Most metastasis research has been conducted with a handful of genetically engineered mouse models (GEMM) and cell lines that have limitations for accurately modeling metastasis in humans [Frese and Tuveson (2007); Neve et al. (2006)]. PDX models, where patient tumors are propagated in mice, offer increased authenticity as they maintain intratumoral heterogeneity, molecular markers and pathological characteristics of the original patient tumor [DeRose et al. (2011); Hidalgo et al. (2014); Tentler et al. (2012)]. PDX models have been used extensively in pre-clinical studies for drug testing in vivo, but their use in metastasis research has been limited by technical challenges. Functional studies of metastasis often involve genetic or pharmacologic perturbation of cancer cells in culture followed by transplantation in vivo to determine the effect of a gene or pathway of interest on metastatic dissemination. Al-

though studies have reported transient cultures of PDX cells for drug testing in vitro [Bruna et al. (2016); DeRose et al. (2013); Sachs et al. (2018)], they are typically only maintained for 24-72 hours and not used for viral engineering or transplantation. Development of a robust method for the propagation, engineering and transplantation of PDX tumor cells would enable new functional investigations of metastasis using patient tumor cells.

Although human cancer cell lines are typically maintained in 2D culture, previous work has shown that 3D cultures provide several advantages for cultivating primary tumor cells. Since they are 3D, they more closely recapitulate the physiologic conditions found in normal tissues where cell phenotype and function is heavily influenced by cell-cell and cell-extracellular matrix (ECM) interactions [Chaicharoenaudomrung et al. (2019)]. 3D conditions can be generated using various conditions, such as the hanging drop method used to maintain embryonic stem (ES) cells [Höpfl et al. (2004); Keller (1995); Martin (1981)], suspension in low-adhesion conditions as used for neurosphere cultures [Weiss et al. (1996)], or embedding in ECM scaffolds such as collagens, Matrigel, or synthetic hydrogels, which have been used to enrich for cancer stem cells (CSCs) [Sachs et al. (2018)]. Here, we screened several 3D culture conditions and present an optimized method for propagation of PDX cells as tumor spheres. RNA sequencing (RNA-seq) analysis shows PDX sphere cells maintain gene expression signatures characteristic of uncultured PDX tumor cells. Sphere cells can be engineered with lentivirus and produce tumors that recapitulate native PDX tumors following orthotopic transplantation in vivo. Importantly, we find that PDX sphere cells yield robust spontaneous metastasis from orthotopic tumors, as well as experimental metastasis following intravenous (i.v.) and intracardiac (i.c.) delivery in vivo. Inhibition of known metastasis-promoting pathways attenuates metastasis following tumor sphere culture, validating our approach for authentic investigations of metastasis from patient tumor cells. Finally, we investigate the role of nucleoside diphosphate kinase A (NME1), a gene we previously found upregulated during metastatic seeding of PDX tumor cells [Davis et al. (2020)]. We find that NME1 overexpression promotes metastasis of orthotopically-transplanted, cultured PDX cells, providing

proof-of-principal for the value of this culture-transplant system for facilitating functional analyses of new genes of interest in patient tumor cells.

## 5.3 Results

### 5.3.1 Development of a 3D culture system for viable propagation of PDX cells as tumor spheres in vitro

We screened several culture conditions to develop an optimal method for viable expansion of PDX tumor cells in vitro (Fig. 5.1a). We assessed two 3D growth methods: 1) suspension, where cells are grown in ultra-low attachment (ULA) plates [Byun et al. (2014); Yu et al. (2014)], and 2) Matrigel, where cells are grown in a basement membrane-rich semi-solid substratum [Edmondson et al. (2014)] (Fig. 5.1a). We also tested two media conditions: 1) Mammary Epithelial Cell Growth Medium (MEGM), which supports short-term cultures of PDX cells for drug testing [Bruna et al. (2016)], and 2) EpiCult™-B (EpiCult), which is commonly used for breast epithelial cell culture [Shafee et al. (2008); Shimono et al. (2009)] (Fig. 5.1a).

We used the previously established breast cancer PDX models, HCI-001, HCI-002, HCI-010 (ER-PR-Her2-; basal-like), and HCI-011 (ER+PR+Her2-, luminal B) [DeRose et al. (2011)] (Fig. 5.1a). We screened the culture conditions using HCI-010 and then validated the results using the other models. HCI-010 tumors were harvested from PDX mice after 2-5 months of growth in vivo, digested to single cell suspensions and plated into four culture conditions: i) ULA plates and EpiCult (ULA-E); ii) ULA plates and MEGM (ULA-M); iii) Matrigel and EpiCult (MAT-E); and iv) Matrigel with MEGM (MAT-M) (Fig. 5.1a). Microscopy 7-14 days later showed ULA-E and MAT-E both produced spheroid structures, while ULA-M and MAT-M produced limited growth (Fig. 5.1b). Flow cytometry analysis of cell viability by annexin V (aV) and propidium iodide (PI) staining showed that MAT-E

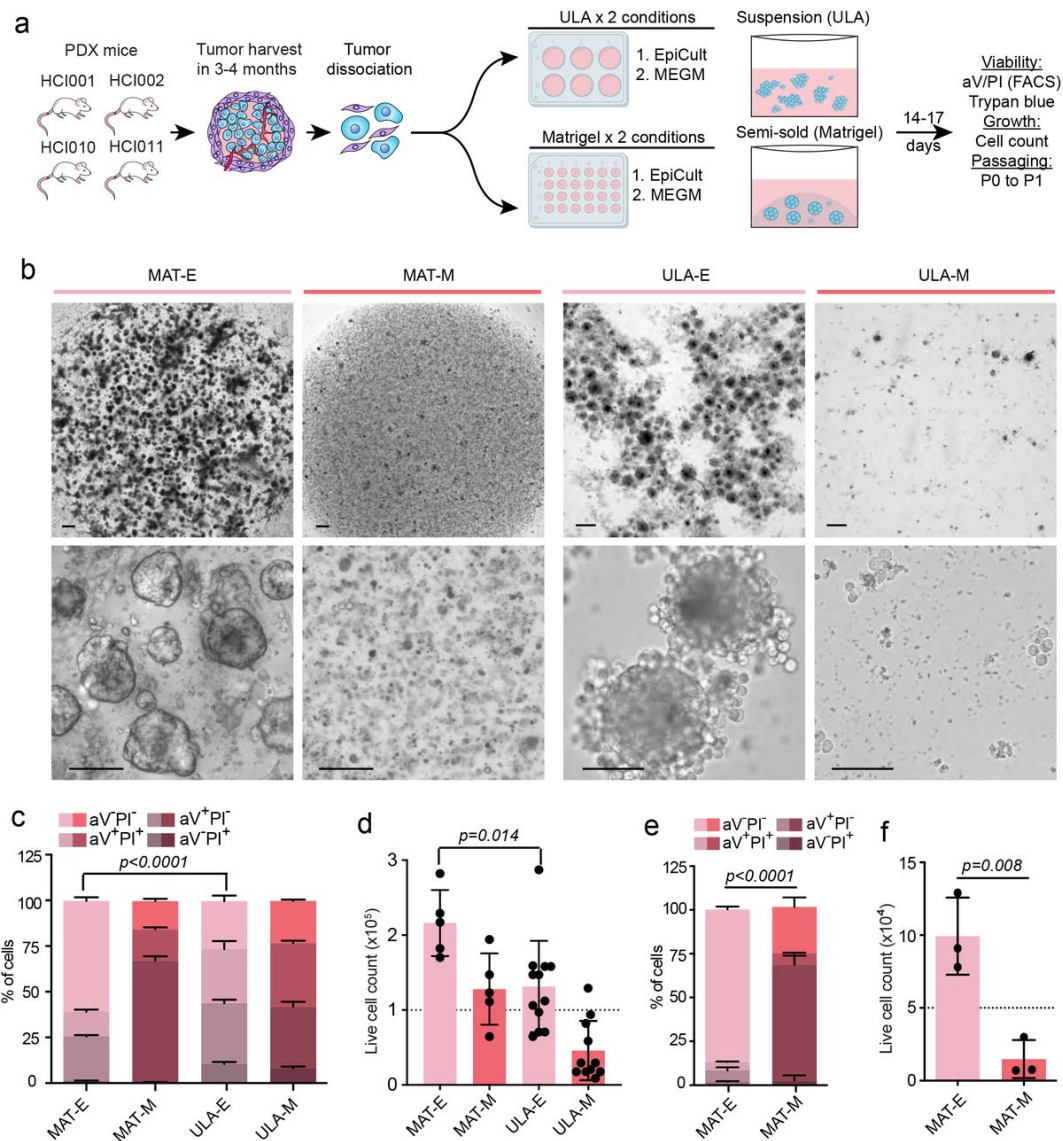


Figure 5.1: Comparison of 3D culture methods for viable propagation of PDX tumor cells in vitro. **(a)** Schematic summarizes culture conditions compared and readouts for PDX cell viability, growth and passaging capacity. **(b)** Representative brightfield images show spheroid structures generated 7-14 days after plating  $2.5 \times 10^5$  HCl010 cells in MAT-E, MAT-M, ULA-E, and ULA-M conditions. Scale bars =  $300 \mu\text{m}$  (top row),  $100 \mu\text{m}$  (bottom row). **(c)** Flow cytometry analysis of HCl010 cell viability post culture by aV and PI staining. Bar graph shows percent of aV-PI- (live), early apoptotic (aV+PI-) and dead (aV+PI+, aV-PI+) HCl010 cells in each condition. **(d)** Total viable HCl010 cell number in each condition at the conclusion of culture. Cells were plated at  $1.0 \times 10^5$  cells/well (dashed line), and quantified nine days later by trypan blue exclusion. **(e)** Flow cytometry analysis of HCl010 cell viability in each condition post passaging by aV and PI staining. HCl010 cells were cultured for 2 weeks, dissociated, re-plated at  $5.0 \times 10^4$  cells/well in MAT-E and MAT-M and analyzed 21 days later. **(f)** Total viable HCl010 cell number in each condition after passaging as described in (e).

produced the highest percentage of aV-PI-viable cells ( $60.6 \pm 2.0\%$ ;  $p < 0.0001$ ) (Fig. 5.1c, Extended Data Fig 1a). ULA-E showed 2.3-fold ( $p < 0.0001$ ) lower viability than MAT-E and 1.4-fold ( $p < 0.0001$ ) more aV+PI-cells in early apoptosis (Fig. 5.1c, 5.2a), indicating MAT-E is superior for producing viable PDX sphere growth.

We next compared the culture conditions for their ability to expand and passage PDX cells. Live cell number was determined before plating and after nine days of culture. Cell counts showed that MAT-E produced a 2.2-fold cell expansion, which was greater than ULA-E ( $p = 0.014$ ) and the other conditions that produced minimal or negative expansion (Fig. 5.1d). Passaging experiments showed MAT-E could also support extended viable growth of PDX cells. First generation (P0) spheres were harvested, dissociated and re-plated for an additional 14-17 days to produce P1 spheres (Fig. 5.1a). Flow cytometry analysis of P1 cells showed that MAT-E produced 4-fold greater viability than MAT-M ( $p < 0.0001$ ) (Fig. 5.1e). Cell counts showed that MAT-E produced a 2-fold expansion of viable cells, which was greater than MAT-M ( $p = 0.008$ ) that reduced total cell number (Fig. 5.1f).

Further evaluation of MAT-E showed it is sufficient to support growth of other PDX models. HCI-001, HCI-002 and HCI-011 tumors were harvested from PDX mice, dissociated to single cell suspensions and plated in MAT-E conditions. Microscopy analysis showed clear outgrowth of spheres from all three models (Fig. 5.2b). We also confirmed that spheres were generated from PDX tumor cells and not contaminating mouse epithelium using a flow cytometry assay previously developed by our laboratory [Lawson et al. (2015)]. Spheres generated from each PDX model were dissociated and stained with species-specific antibodies for CD298 (human) and MHC-I (mouse). Flow cytometry analysis showed that  $>90\%$  of cells were CD298+MHC-I-human tumor cells (Fig. 5.2c). These data show that MAT-E is superior for the viable growth and expansion of human PDX tumor cells in vitro. Figure 5.2d shows the kinetics of sphere growth in MAT-E conditions using time lapse imaging.



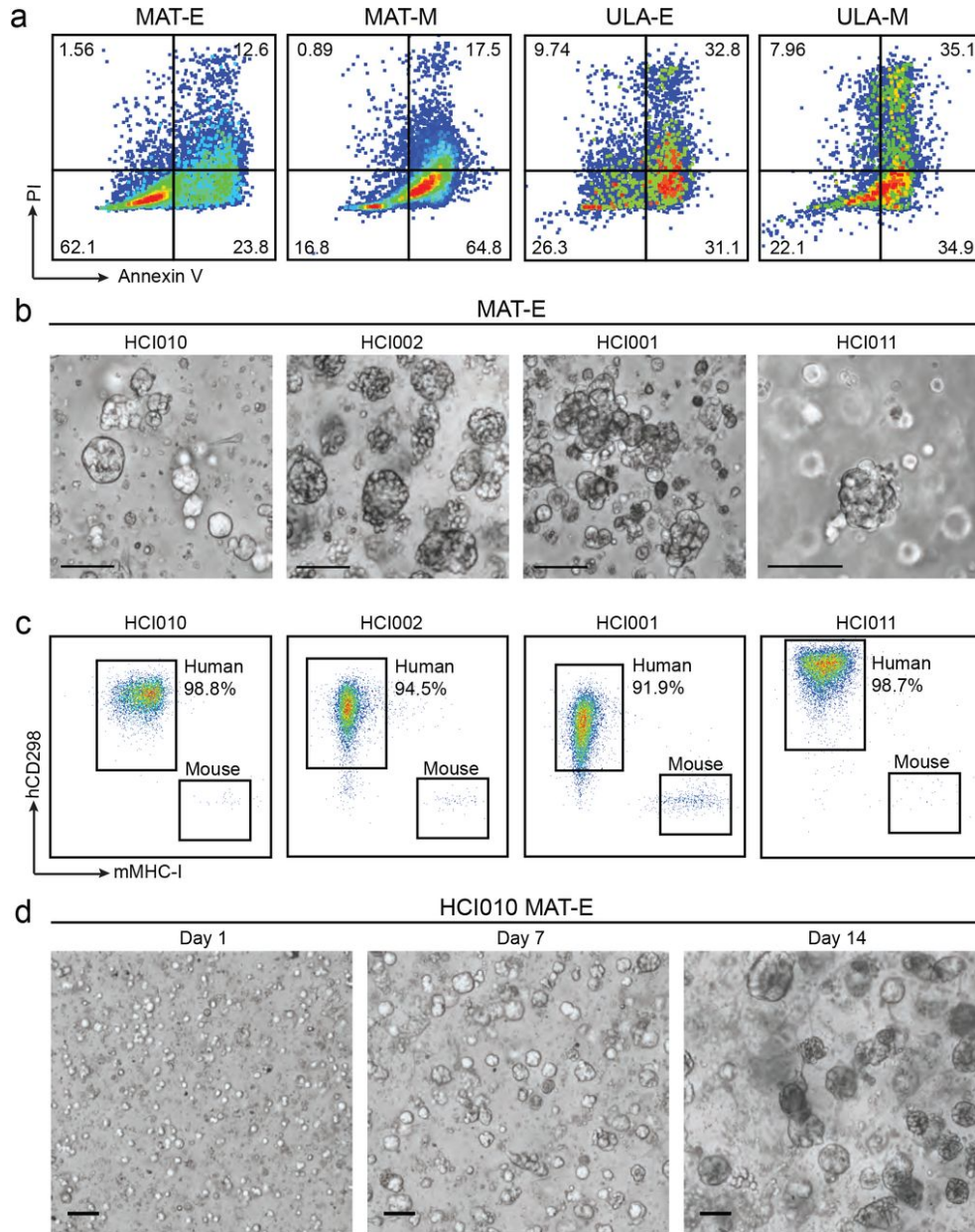


Figure 5.2: Comparison of PDX cell culture conditions (a) Representative flow cytometry plots show viability of HCI-010 cells by aV and PI staining after culture as described in Fig 5.1a. (b) Representative brightfield images show spheres generated by HCI-010, HCI-002, HCI-001 and HCI-011 tumor cells grown in MAT-E culture conditions. Scale bar = 100  $\mu$ m (c) Flow cytometry analysis to determine species identity of spheres generated in (b). Representative plots show the percent of human CD298+MHCI-tumor cells in each culture. (d) Timelapse imaging of sphere growth from HCI-010 cells in MAT-E conditions. Representative brightfield images at day 1, 7, and 14 are shown. Scale bar = 100  $\mu$ m.

### 5.3.2 PDX tumor sphere cells maintain their global transcriptome program

To determine whether PDX cells maintain their native state following MAT-E culture, we compared the global transcriptome profiles of cultured and uncultured cells by RNA sequencing (Fig. 5.3a). Cells from HCI-002 (n=3) and HCI-010 (n=3) tumors were dissociated and split into two matched groups, one for culture in MAT-E (cultured 1-3) and the other for immediate library preparation (uncultured 1-3) (Fig. 5.3a). CD298+MHC-I- cells from both groups were sorted by flow cytometry to enrich for human tumor cells and sequenced at 35 million paired end reads per sample. Reads were aligned to the human hg38 reference genome, and differentially expressed genes were identified using DESeq2 [Love et al. (2014)].

Gene expression was compared in paired cultured and uncultured samples from each PDX model by Pearson’s correlation test (Fig. 5.3b). This showed that gene expression was strongly correlated in most pairs, indicating that culture does not substantially alter cell state (Fig. 5.3b). Differential expression analysis identified 1,732 genes up and downregulated following MAT-E culture that were conserved across all pairs ( $\log_{2}FC > 2.0$ ,  $p < 0.05$ ) (Fig. 5.3c). This represents only 7.7% of the total transcriptome, further indicating that culture does not substantially alter cell state. Notably, canonical breast cell differentiation genes and molecular markers (KRT8, KRT18, KRT14, TP63, ERBB2, ESR1, PGR) were not differentially expressed suggesting the cells maintain their differentiation state and tumor subtype.

Gene Ontology (GO) analysis of the differentially expressed genes revealed several pathways up and downregulated following MAT-E culture (Fig. 5.3d). Pathways significantly upregulated include ‘cytokine-mediated signaling pathway,’ ‘extracellular matrix (ECM) organization,’ ‘interferon-gamma (IFN $\gamma$ )-mediated signaling pathway’ ‘regulation of cell proliferation,’ and ‘epithelial to mesenchymal (EMT) transition’ (Fig. 5.3d). Analysis of the genes within each GO term identified numerous chemokines (CXCL1, CXCL8 CXCL5), cytokines



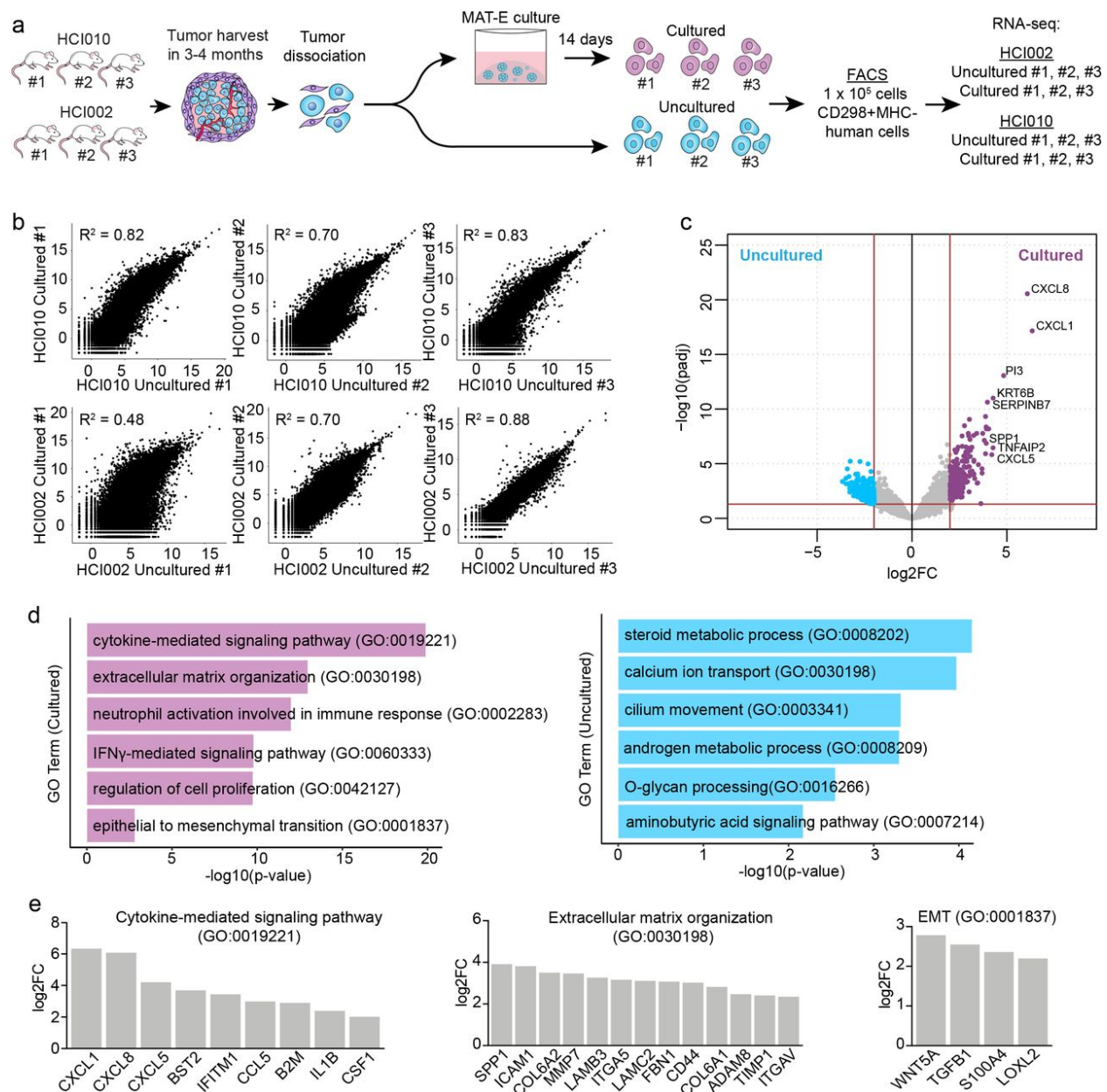


Figure 5.3: PDX tumor sphere cells maintain their global transcriptome programme (a) Workflow schematic for generation of RNA sequencing dataset to compare transcriptome signatures in paired cultured and uncultured cells from HCI-002 and HCI-010. (b) Scatter plots show correlation of gene expression across the entire transcriptome in paired cultured and uncultured samples ( $n=22,446$  genes). Pearson's correlation coefficient ( $R^2$ ) is shown for each pair. (c) Volcano plot shows genes significantly upregulated in cultured ( $n=277$  genes) or uncultured ( $n=1455$  genes) cells that are conserved in all pairs. (d) Bar graph shows GO terms associated with genes upregulated in cultured ( $n=277$  genes) and uncultured ( $n=1455$  genes) cells. (e) Select GO term-associated genes upregulated in cultured cells. See Supplementary Table 1 for full gene list.

(CSF1, CCL5, IL1 $\beta$ ) and IFN-response genes (BST2, B2M, HLA), suggesting that culture induces a stress-related or inflammatory response (Fig. 5.3e). We also observed upregulation of 23 ECM-related genes, including ICAM1, COL6A2, MMP7, ITGA5 and LAMC2 (Fig. 5.3e). Interestingly, cultured cells also displayed increased expression of the EMT-associated genes WNT5A, TGFB1, S100A4, and LOXL2, as well as the CSC marker CD44 (Fig. 5.3e). Prior work has shown that normal and breast cancer stem cells display EMT features [Mani et al. (2008); Pattabiraman and Weinberg (2014)]. This may therefore indicate that MAT-E culture selects for stem-like cells, which is consistent with prior reports using 3D culture conditions [Tachibana (2018); Visvader and Lindeman (2012)]. However, it is also possible that MAT-E culture induces upregulation of these transcriptome programs.

### 5.3.3 PDX tumor sphere cells maintain tumorigenic potential and form spontaneous metastasis in vivo

Spontaneous metastasis models are often considered more authentic than experimental metastasis models since the cells must progress through each step of the metastatic cascade in order to metastasize [Gómez-Cuadrado et al. (2017)]. Prior work has shown that HCI-002 and HCI-010 develop basal-like primary tumors and spontaneous metastasis following orthotopic transplantation [DeRose et al. (2011); Lawson et al. (2015)]. We investigated whether PDX cells maintain these capabilities following sphere culture. We cultured and expanded HCI-002 and HCI-010 cells in MAT-E for two weeks and orthotopically transplanted serial dilutions of cells into NOD/SCID mice (Fig. 5.4a). Similar to prior reports with uncultured PDX cell transplants [Lawson et al. (2015)], we observed primary tumor growth from nearly 100% of animals transplanted with cultured cells at each dilution (Fig. 5.4b, 5.5a).

We next compared histopathological and molecular features of MAT-E-cultured and native PDX tumors (Fig. 5.4c, 5.5b). All HCI-010 tumors were poorly vascularized, necrotic and showed no epithelioid differentiation, with little nodularity or ductal structure (Fig. 5.4c). HCI-002 tumors showed scant intervening myxoid stroma and thin walled vessels, less necro-

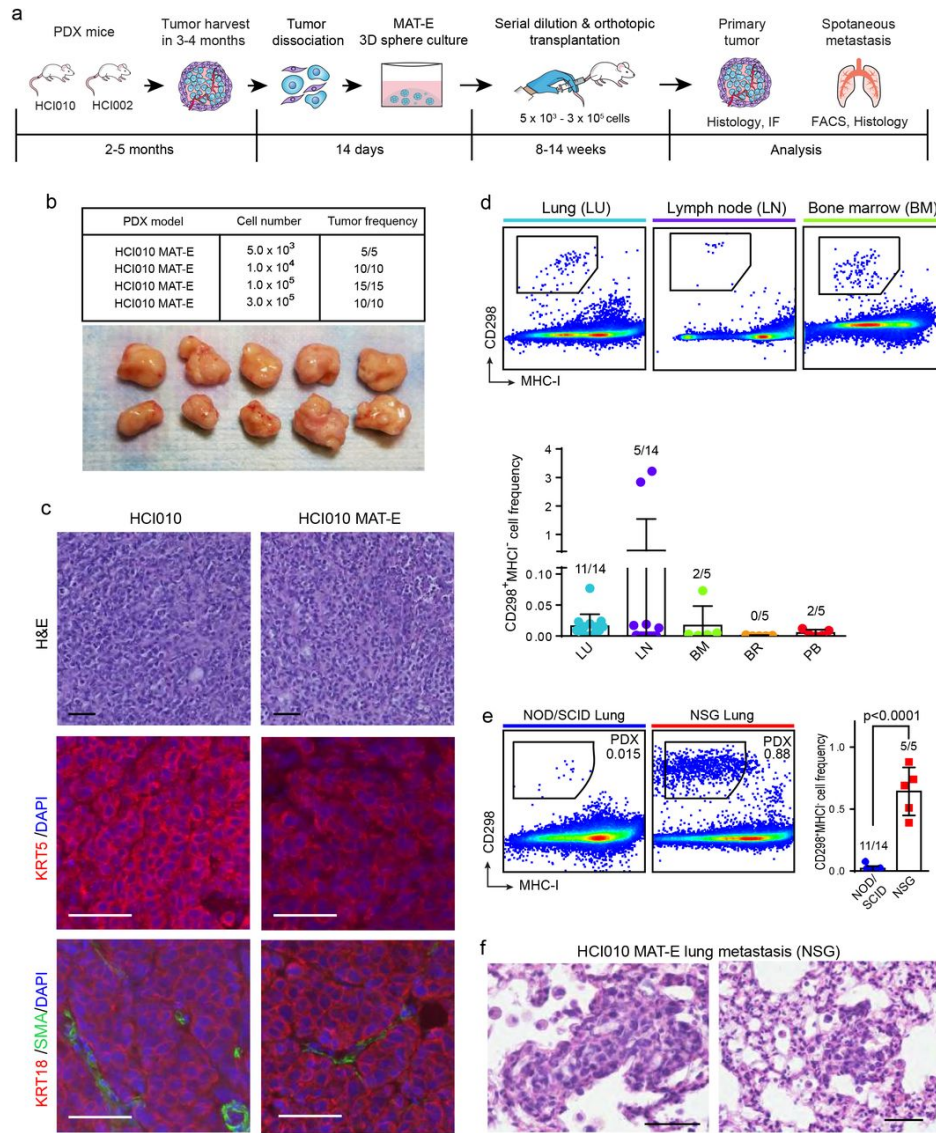


Figure 5.4: PDX tumor sphere cells maintain tumorigenic potential and form spontaneous metastasis in vivo (a) Schematic overview of workflow and timeline for assessing the capacity of cultured PDX cells to generate primary tumors and spontaneous metastasis following orthotopic transplantation. (b) Frequency of tumors generated at each dilution. Scale bar = 1 cm. (c) Histopathological and molecular marker analysis of tumors generated from uncultured (HCI-010) and cultured (HCI-010 MAT-E) cells. Scale bar = 50  $\mu$ m. (d) Quantification of spontaneous metastasis in animals transplanted with 1E05 cultured HCI-010 cells. (e) Comparison of lung metastatic burden in NOD/SCID and NSG animals transplanted orthotopically with 1E05 cultured HCI-010 cells. CD298<sup>+</sup>MHC-I<sup>+</sup> human metastatic PDX cells in the lungs 8 weeks after transplant by flow cytometry. Frequency of metastatic cells in a cohort of transplanted animals. (f) Representative images of metastatic lesions in the lungs of NSG animals transplanted with cultured HCI-010 cells identified by H&E staining and histopathological analysis. Scale bar=50 $\mu$ m.



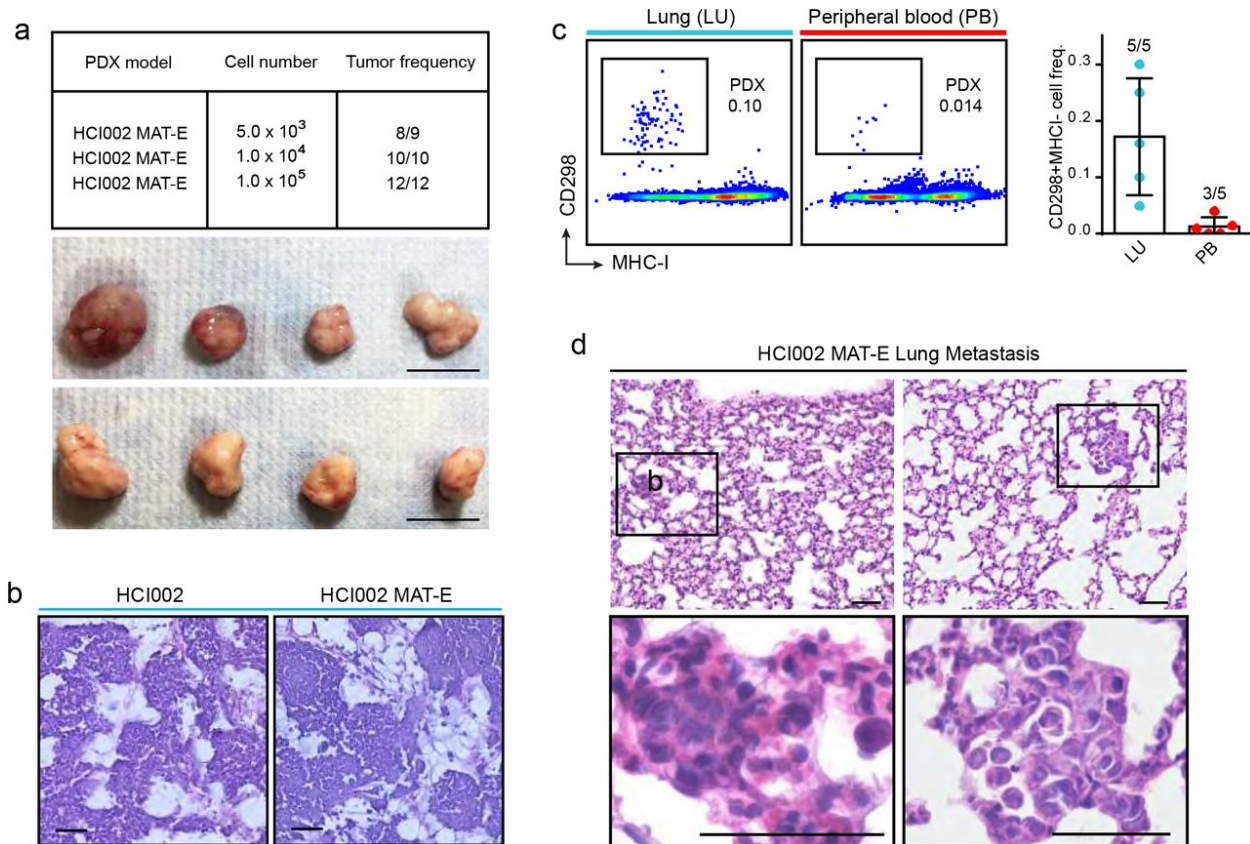


Figure 5.5: Analysis of primary tumors and spontaneous metastases generated by cultured PDX cells **(a)** Serial dilution and transplantation analysis to determine tumorigenic capacity of cultured cells. HCI-002 cells were cultured in MAT-E conditions and injected orthotopically into NOD/SCID mice at increasing dilution ( $5.0 \times 10^3$  –  $1.0 \times 10^5$ ). Table (top) shows the frequency of tumors generated at each dilution. Representative images (bottom) show primary tumors generated from orthotopic transplantation of  $1 \times 10^5$  cells after 12 weeks in vivo. Scale bar = 1 cm. **(b)** Histopathological analysis of tumors generated from uncultured (HCI-002) and cultured (HCI-002 MAT-E) cells. Representative images show tumor sections stained with hematoxylin and eosin (H&E). Scale bar =  $50 \mu\text{m}$ . **(c)** Quantification of spontaneous metastasis in animals transplanted with  $1 \times 10^5$  cultured HCI-002 cells. Representative plots (left) show CD298+MHC-I- human metastatic PDX cells in the lung and peripheral blood by flow cytometry. Bar graph (right) shows quantification of frequency of metastatic cells in a cohort of transplanted animals ( $n=5$ ). Fractions indicate the number of tissues with metastasis, defined by  $>0.005\%$  CD298+MHC-I- cells. Data are represented as the mean  $\pm$  s.d. LU = Lung, PB = peripheral blood. **(d)** Representative images of metastatic lesions in the lungs of animals transplanted with cultured HCI-002 cells identified by H&E staining and histopathological analysis. Scale bar =  $50 \mu\text{m}$ .

sis, and retained some small areas of nodular aggregates but were mostly undifferentiated (Fig. 5.5b). We observed no pathological differences between native and cultured tumors. Immunofluorescence (IF) staining for canonical basal (KRT5), myoepithelial (SMA) and luminal (KRT18) cell markers further indicated that HCI-010 MAT-E tumors maintain their native differentiation state (Fig. 5.4c). Tumors from both conditions displayed widespread KRT5 and KRT18 expression, and limited SMA expression, as expected for basal-like tumors (Fig. 5.4c).

We further evaluated the capacity of orthotopic tumors to produce spontaneous metastasis. Flow cytometry analysis identified CD298+MHC-I<sup>+</sup> human metastatic cells in the lungs (11/14), lymph nodes (5/14), bone marrow (2/5), and peripheral blood (2/5) but not the brains (0/5) of transplanted animals (Fig. 5.4d). Metastatic burden was low in most tissues, which is consistent with prior reports (Fig. 5.4d,e) [Lawson et al. (2015)]. We therefore tested the capacity of cultured cells to produce spontaneous metastasis in NOD scid gamma (NSG) mice, which lack natural killer (NK) cells and support greater human cell engraftment [Lawson et al. (2015)]. Remarkably, NSG mice displayed >32-fold higher metastatic burden in the lungs than NOD/SCID mice ( $p < 0.0001$ ) (Fig. 5.4e), and metastatic lesions were detectable by histopathological analysis (Fig. 5.4f). This is consistent with reports demonstrating the importance of NK cells in controlling metastasis, and shows that different immunodeficient strains can be used to achieve specific experimental contexts [López-Soto et al. (2017)]. Importantly, we also observed spontaneous metastasis from HCI-002 transplants, which displayed lung metastasis (5/5 mice) and circulating tumor cells in the peripheral blood (3/5 mice) (Fig. 5.5c,d). These data show that PDX cells maintain their tumorigenic and metastatic potential after sphere culture, and highlight the utility of our culture-transplant system for studies of spontaneous metastasis from human patient cells.

### 5.3.4 PDX tumor sphere cells can be genetically engineered for functional studies of metastasis in vivo

The ability to genetically perturb genes of interest is critical for functional investigations of metastasis. We investigated whether PDX tumor sphere cells can be genetically engineered and transplanted to generate spontaneous metastasis in vivo. Using a GFP lentiviral construct, we tested the infection efficiency of HCI-002 and HCI-010 sphere cells grown in MAT-E conditions (Fig. 5.6a). PDX cells were grown for 2-3 weeks to generate P0 spheres and then harvested and dissociated to generate cell suspensions. P0 cell suspensions were transduced using a combined centrifugation and suspension infection protocol (see Methods), and re-plated in MAT-E conditions for 2-3 weeks to expand and generate P1 spheres (Fig. 5.6a). Fluorescence microscopy revealed robust GFP expression both within and between P1 spheres (Fig. 5.6b,c). Quantification of infection efficiency by flow cytometry showed successful transduction with  $75.2 \pm 6.4\%$  and  $23.2 \pm 7.6\%$  of HCI-010 and HCI-002 cells positive for GFP, respectively (Fig. 5.6d). We next determined whether transduced P1 sphere cells could retain GFP signal and produce spontaneous metastasis following orthotopic transplantation in vivo. Flow cytometry sorted GFP+ HCI-002 and HCI-010 P1 sphere cells were transplanted, and primary tumors and lungs were collected and analyzed 60 days later. Whole mount imaging showed that GFP expression was retained in primary tumors (Fig 5.6e), and quantification by flow cytometry showed that  $>90\%$  of CD298+MHC-I- human PDX tumor cells retained GFP signal (Fig 5.6f). Analysis of lung tissue sections showed the presence of GFP positive metastatic lesions (Fig 5.6g), and flow cytometry analysis of lung cell suspensions identified CD298+MHC-I- GFP+ human metastatic cells (Fig 5.6h).

Remarkably,  $>95\%$  of CD298+MHC-I- human metastatic cells in the lung also retained GFP expression (Fig 5.6h). Thus, we demonstrate PDX sphere cells can be robustly engineered, maintain their capacity to form primary tumors and spontaneous metastasis, and retain their genetic alterations in vivo.

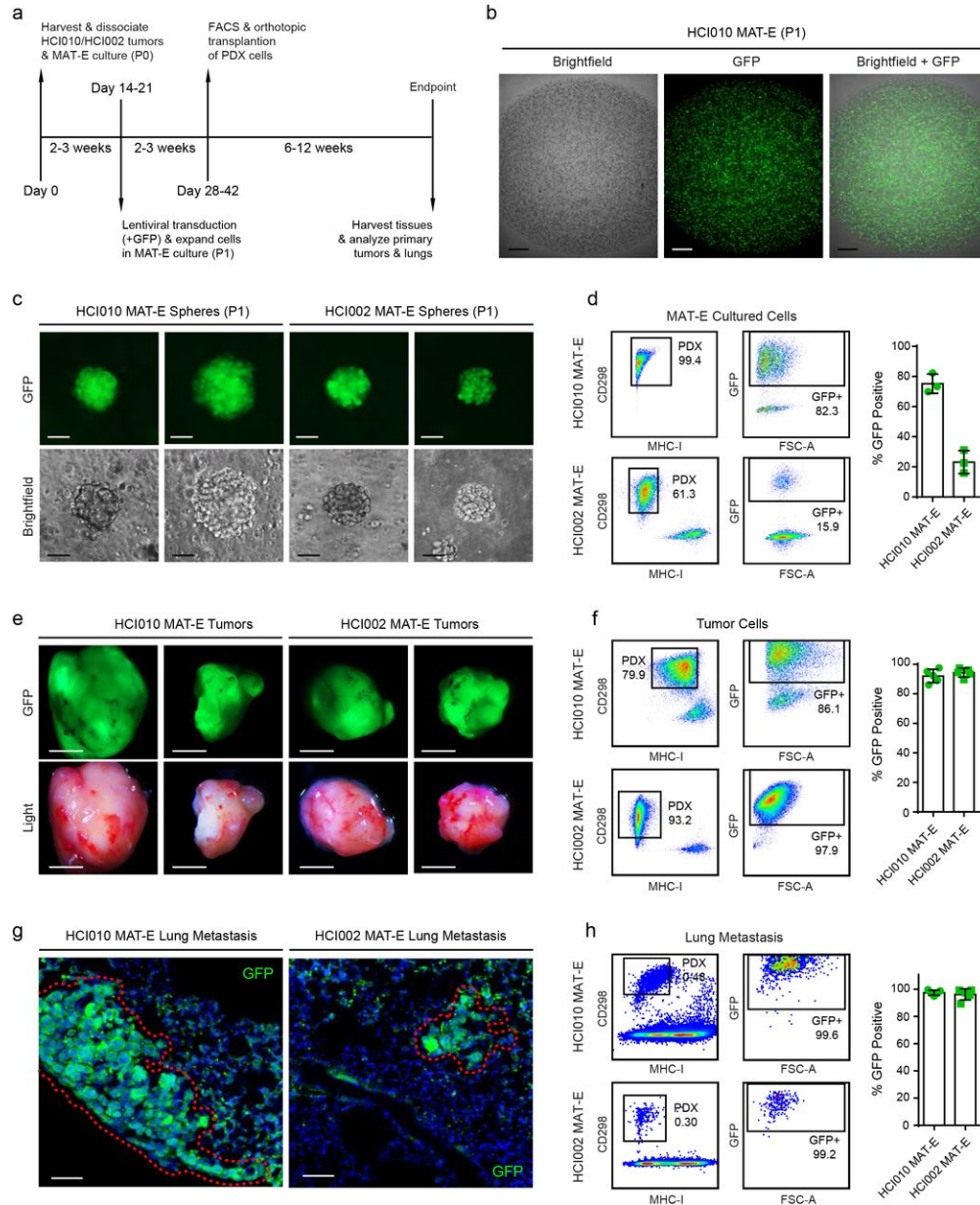


Figure 5.6: PDX tumor sphere cells can be genetically engineered for functional studies of metastasis in vivo (a) Lentiviral engineering of PDX sphere cells in vitro followed by analysis. (b) GFP expression in PDX sphere cultures following lentiviral transduction in vitro. Scale bar = 800  $\mu$ m. (c) GFP expression in P1 PDX spheres two weeks post transduction and expansion in MAT-E culture. Scale bar = 50  $\mu$ m. (d) Flow cytometry plots show transduction efficiency of P1 PDX sphere cells. (e) PDX tumors 60 days post orthotopic transplantation. Scale bar = 5 mm. (f) Flow cytometry plots show percent of human CD298+MHC-I-human tumor cells that retain GFP expression following tumor growth in vivo. (g) GFP+ metastatic lesions in the lungs of transplanted animals from (e). Dashed red outline highlights perimeter of lesions. Scale bar = 50  $\mu$ m. (h) Flow cytometry plots show percent of human CD298+MHC-I-human metastatic cells in the lung that retain GFP expression.

### 5.3.5 PDX tumor sphere cells produce robust experimental metastasis in vivo

In experimental metastasis models, cells are injected directly into the circulation via i.v. or i.c. delivery. I.v. injection introduces cells into the venous circulation and favors lung metastasis, while i.c. injection delivers cells into arterial circulation and supports bone and brain metastasis [Bos et al. (2009); Davis et al. (2020); Richert et al. (2005)]. These approaches produce metastasis with more robust, rapid and reproducible kinetics than spontaneous models and enable direct investigation of later steps in the metastatic cascade, such as survival in the blood stream, extravasation and seeding in the distal tissue. We investigated whether PDX cells expanded in culture will metastasize following i.v. or i.c. delivery in vivo.

We harvested HCI-010 and HCI-002 tumors from PDX mice and cultured the cells for two weeks in MAT-E conditions (Fig. 5.7a). 5E05 P0 sphere cells were injected i.v. or i.c. into NOD/SCID mice and peripheral tissues were harvested and analyzed by flow cytometry and histology eight weeks later (Fig. 5.7a). In i.c. injected animals, we observed CD298+MHC-I-human HCI-010 cells in the lungs (4/5 mice), bone marrow (3/5 mice), brain (5/5 mice) and peripheral blood (5/5 mice), but not the lymph nodes (0/5 mice) (Fig. 5.7b). Metastatic burden was remarkably robust in the brain, where HCI-010 cells constituted >50% of live cells in three of the mice (Fig. 5.7b). We also observed metastasis in the lungs, brain and peripheral blood of animals injected i.c. with HCI-002 cells (Fig. 5.8a). Like HCI-010, metastasis was most robust in the brain, demonstrating the utility of our culture-transplant system for studies of brain metastasis using patient tumor cells.

In i.v. injected animals, we observed CD298+MHC-I-HCI-010 human cells in the lungs (5/5 mice), bone marrow (1/5 mice), and peripheral blood (1/5 mice), but not the lymph nodes (0/5 mice) (Fig. 5.7c). As expected, i.v. delivery yielded the highest frequency and burden in the lungs ( $0.96 \pm 0.48\%$ ) (Fig. 5.7c). Analysis of mice injected i.v. with HCI-002 cells showed limited metastasis (Fig. 5.8b). We subsequently tested whether i.v. injection



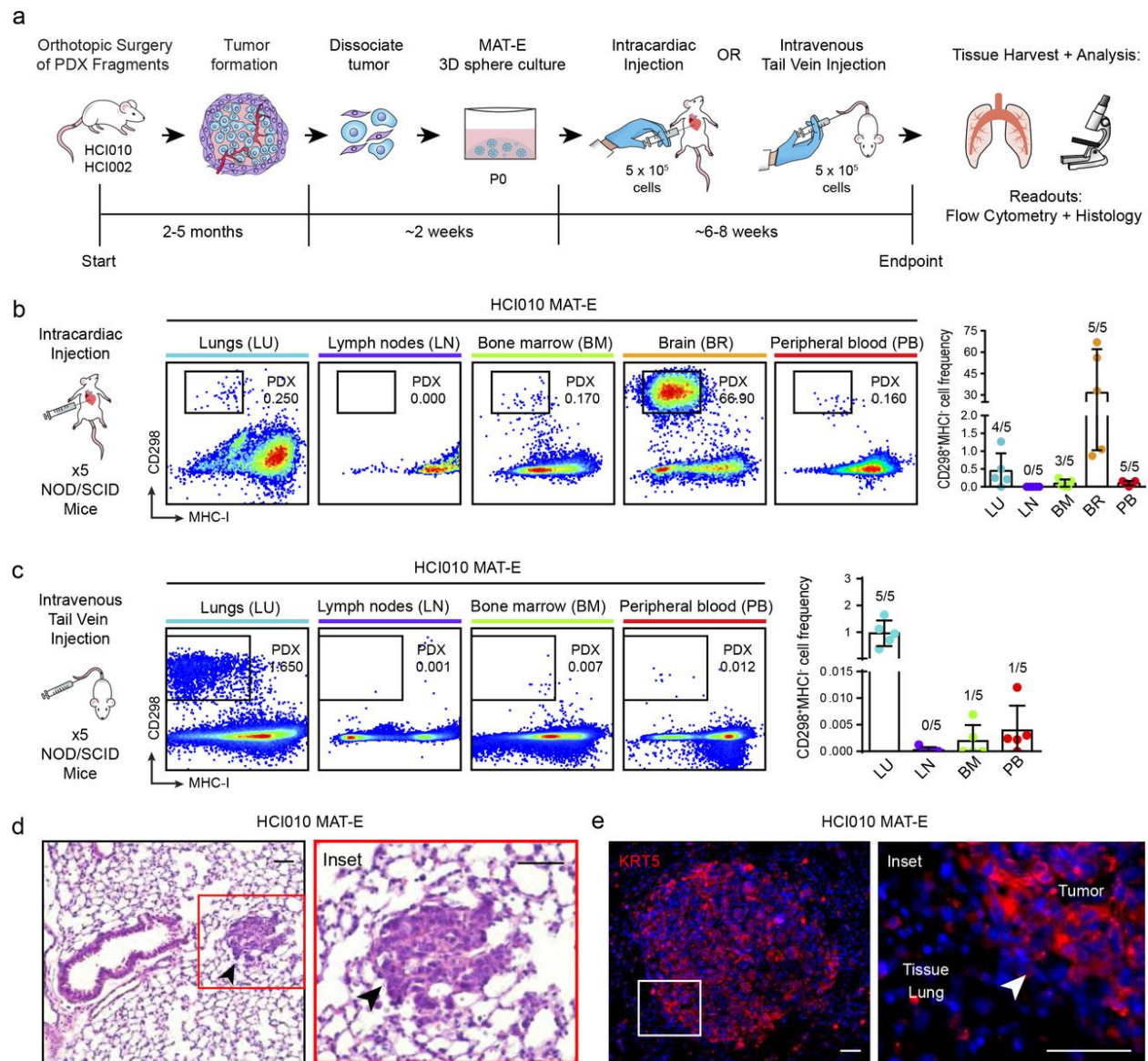


Figure 5.7: PDX tumor sphere cells produce robust experimental metastasis in vivo (a) Assessing the capacity of cultured PDX cells to metastasize using i.c. and i.v. experimental metastasis models. Metastatic spread following i.c. (b) and i.v. (c) injection of cultured PDX cells in vivo. Flow cytometry plots show human CD298<sup>+</sup>MHC-I<sup>+</sup> human metastatic cells. Bar graph shows quantification of frequency of metastatic cells. Fractions indicate the number of tissues with metastasis. (d) Metastatic lesions identified by histopathological analysis of H&E stained sections of lung tissue from animals described in (c). (e) IF staining for KRT5 in lung metastatic lesions from animals described in (c). Arrows indicate metastatic lesions. Scale bar = 50  $\mu$ m.

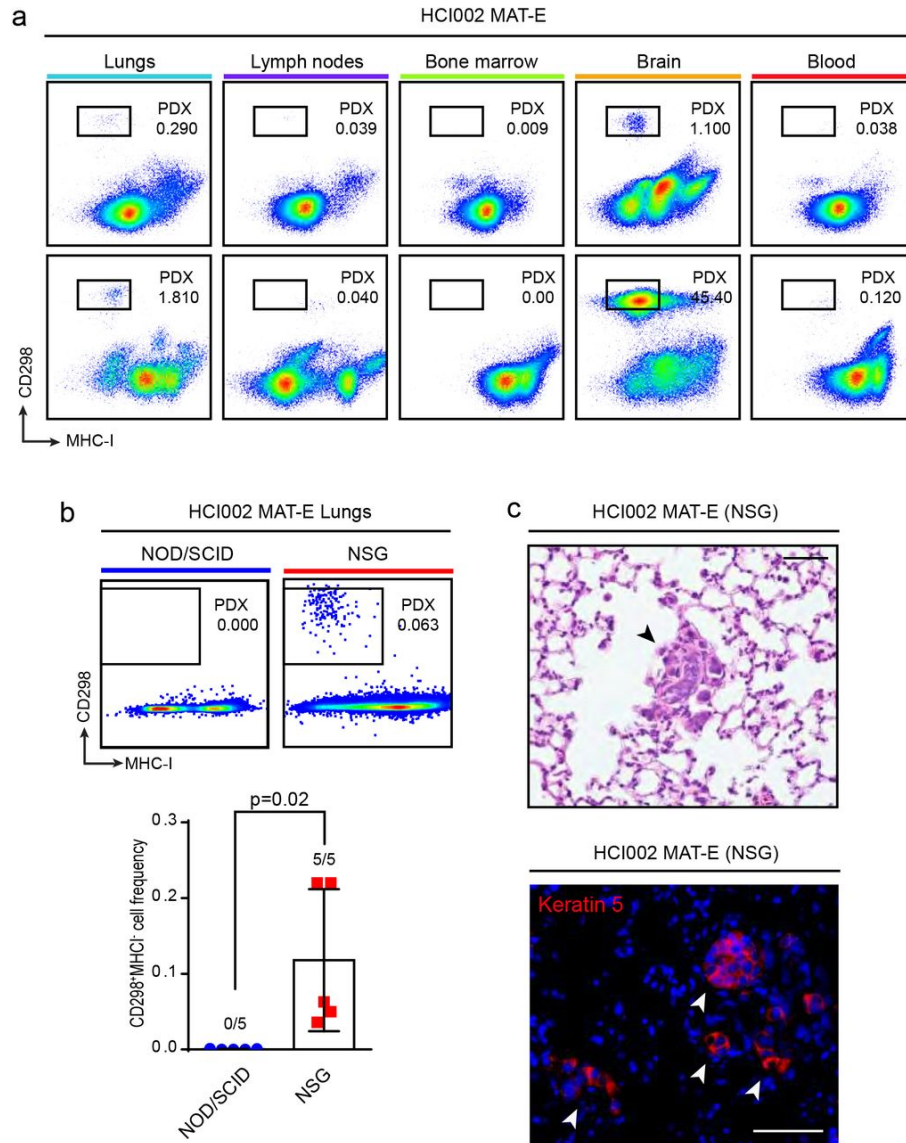


Figure 5.8: HCI-002 tumor spheres produce experimental metastasis in vivo (a) Analysis of metastatic spread following i.c. injection of cultured HCI-002 cells in vivo. Representative flow cytometry plots show CD298<sup>+</sup>MHC-I<sup>+</sup> human metastatic cells in the lungs, lymph nodes, bone marrow, brain, and blood 8 weeks following i.c. injection of 5E05 cultured HCI-002 cells into NOD/SCID mice. (b) Comparison of experimental metastasis from cultured HCI-002 cells in NOD/SCID and NSG mice. Flow cytometry plots show percent of human CD298<sup>+</sup>MHC-I<sup>+</sup> metastatic cells in the lungs of representative mice 8 weeks following i.v. injection of 5E05 HCI-002 cultured cells (top plots). Bar graph shows quantification of frequency of metastatic cells in a cohort of transplanted animals (n=5) (bottom). Fractions indicate the number of lungs with metastasis, as defined by >0.005% CD298<sup>+</sup>MHC-I<sup>+</sup> cells. Data is represented as the mean  $\pm$  s.d. P-value was determined by unpaired t-test. (c) Images show representative metastatic lesions (arrows) in the lungs of NSG mice identified by H&E staining (top) and IF staining for KRT5 (bottom). Scale bar = 50  $\mu$ m.

into NSG mice would support greater metastasis of HCI-002, since NSG mice supported more robust spontaneous metastasis (Fig. 5.4e). Indeed, flow cytometry analysis showed 5/5 NSG mice developed lung metastasis, compared to 0/5 NOD/SCID mice (Fig. 5.8b). Histopathological analysis confirmed the presence of metastatic lesions in the lungs, and IF staining showed specific expression of the basal cancer subtype marker KRT5 (Fig. 5.7d,e, 5.8c). These data demonstrate that patient tumor cells can be expanded in culture and used in experimental metastasis assays.

### 5.3.6 Validation of PDX culture-transplant system for authentic investigations of metastasis in vivo

To investigate whether our culture-transplant system can be used to faithfully study metastasis, we tested whether known pharmacological inhibitors of metastasis have a similar effect on PDX cells post culture. In prior work, we found that mitochondrial oxidative phosphorylation (OXPHOS) is upregulated in spontaneous lung metastases in PDX mice, and that inhibition of OXPHOS with the complex V inhibitor Oligomycin (Oligo) attenuates lung metastasis [Davis et al. (2020)]. However, functional studies were performed using surrogate cell line models, since functional experiments could not be performed with PDX cells. Here, we determined whether OXPHOS is also critical for the metastatic spread of patient tumor cells using our culture-transplant system (Fig. 5.9a).

We first confirmed that Oligo treatment does not affect PDX cell viability. HCI-002 cells were grown in MAT-E culture for two weeks (P0), treated with Oligo for 72 hours and assessed for viability by trypan blue exclusion and aV and PI staining. In contrast to treatment with cytotoxic agents, we observed no overt changes in PDX sphere morphology following Oligo treatment (Fig. 5.10a). Trypan blue exclusion analysis showed there was no significant difference in the percentage of live cells in control ( $72.3 \pm 3.1\%$ ) and Oligo ( $72.3 \pm 10.2\%$ ) treated conditions ( $p=0.999$ ) (Fig. 5.10b). Analysis of aV and PI by flow cytometry

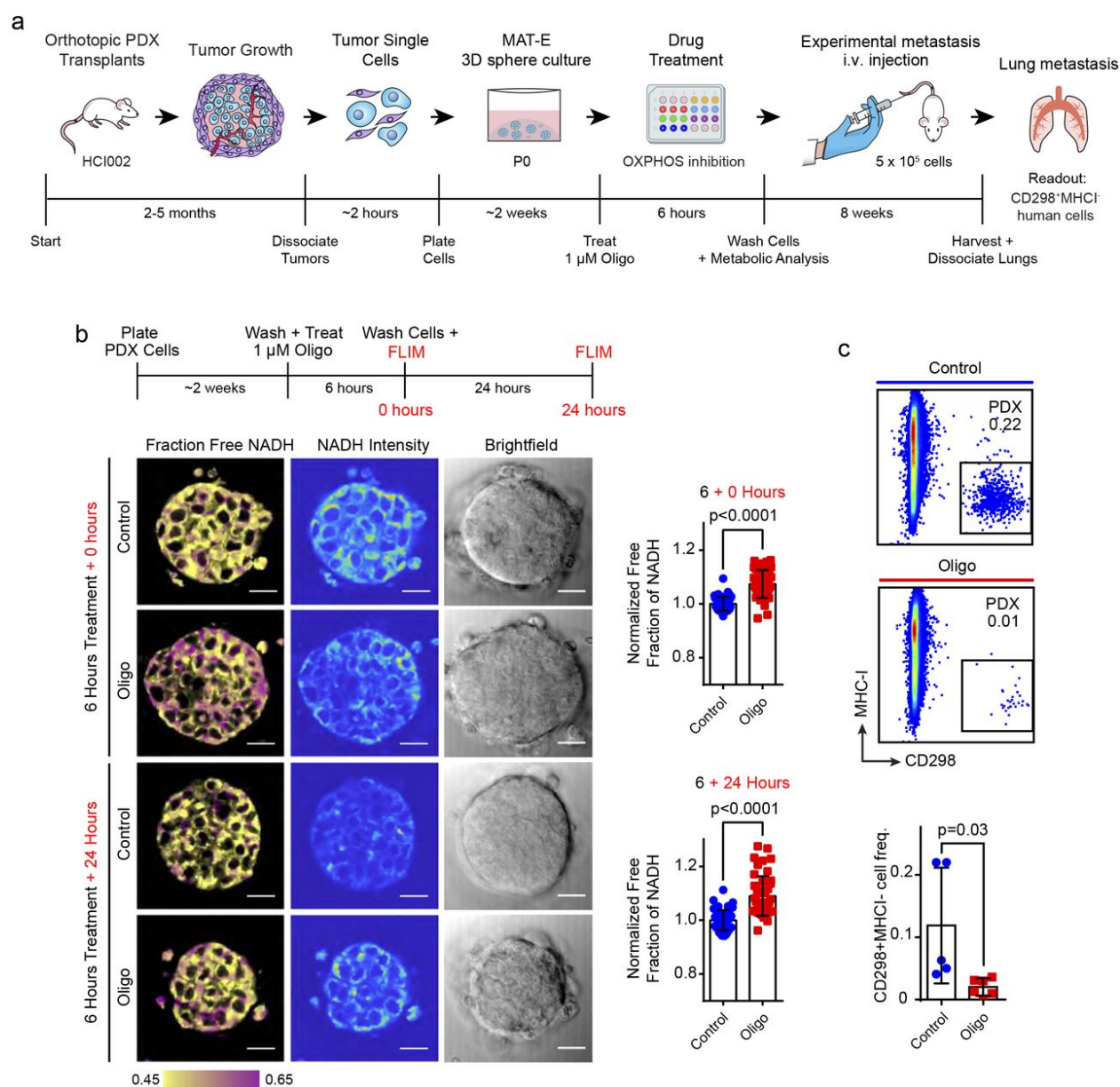


Figure 5.9: Validation of PDX culture-transplant system for authentic investigations of metastasis in vivo (a) Experimental workflow to test the effects of OXPHOS inhibition on the metastatic capacity of cultured HCI-002 PDX cells following i.v. injection in vivo. (b) Oligo treatment on OXPHOS in PDX tumor spheres by FLIM imaging. FLIM images show NADH fluorescence signal in representative HCI-002 spheres immediately after treatment with 1  $\mu$ M Oligo or vehicle and replacement with drug-free medium and 24 hours later. Scale bar = 20  $\mu$ m. Free NADH fractions at 0 and 24 hours (right panels). (c) Comparison of metastatic burden in mice transplanted with Oligo vs. vehicle treated PDX cells. Flow cytometry plots show the percent of human CD298<sup>+</sup>MHC-I<sup>+</sup> metastatic cells. Bar graph shows frequency of metastatic cells in a cohort of control (n=5) and Oligo (n=6) animals.



further showed no difference in the percentage of live cells (Oligo,  $77.8 \pm 1.9\%$ ; Control,  $81.0 \pm 3.1\%$ ) ( $p=0.206$ ) (Fig. 5.10c,d).

We next confirmed that Oligo treatment inhibits OXPHOS in PDX cells using fluorescence lifetime (FLIM) imaging. Previous work has shown that Oligo induces cells to shift from OXPHOS to glycolysis for ATP production [Choi et al. (2009); Davis et al. (2020); Hao et al. (2010)]. This shift can be observed using FLIM imaging of NADH, since the fluorescence lifetime of NADH is longer when bound to enzymes involved in OXPHOS (3.4 ns) than when free floating in the cytoplasm during glycolysis (0.4 ns) [Chance (2004); Stringari et al. (2012a)]. We treated HCI-002 spheres with Oligo for 6 hours, and washed and replaced the media fresh drug-free media (Fig 5.9b). FLIM showed a  $7.4 \pm 0.8\%$  increase in the fraction of free NADH at 0 hours ( $p<0.0001$ ), which was sustained and slightly increased at 24 hours ( $8.9 \pm 0.1\%$ ) ( $p<0.0001$ ) (Fig. 5.9b), confirming that Oligo induces a shift from OXPHOS to glycolysis in cultured PDX cells.

We determined whether OXPHOS inhibition suppresses the metastatic capacity of cultured PDX cells following i.v. injection. HCI-002 P0 sphere cells were treated with Oligo or vehicle control and injected i.v. (Fig 5.9a). Lungs were harvested eight weeks later and the frequency of human CD298+MHCI- metastatic cells in each condition was compared by flow cytometry. This revealed a 5.9-fold lower frequency of metastatic cells in mice injected with Oligo ( $0.02 \pm 0.01\%$ ,  $n=5$ ) compared to vehicle ( $0.12 \pm 0.09\%$ ,  $n=6$ ) treated cells ( $p=0.03$ ) (Fig. 5.9c). These data validate our culture-transplant system for authentic investigations of metastasis and show that OXPHOS is critical for metastasis of actual patient tumor cells.

### 5.3.7 NME1 promotes lung metastasis from patient tumor cells

We next used our culture-transplant system to investigate potential mechanisms underlying OXPHOS-mediated lung metastasis in PDX animals. In prior work, we found that nucleoside diphosphate kinase A (NME1) is upregulated in spontaneous lung metastases that display increased OXPHOS (Fig. 5.11b) [Davis et al. (2020)]. Increased NME1 expression

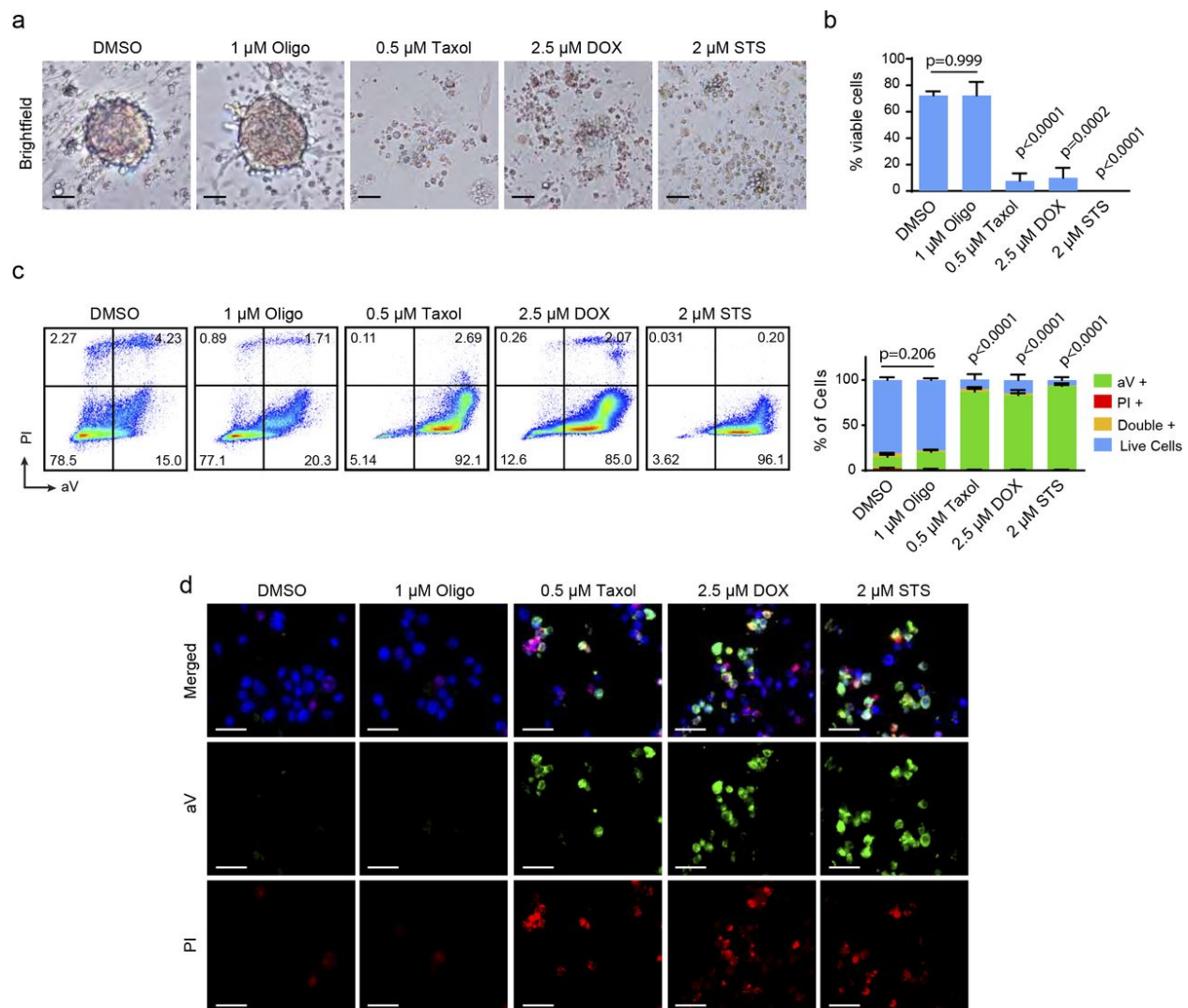


Figure 5.10: Cytotoxicity and cell death analysis of PDX cells post drug treatment. (a) Z-stack brightfield images of representative HCI-002 MAT-E spheroids grown for two weeks and treated with the indicated drugs for 72 hours. Scale bar = 50  $\mu$ m. Oligo = oligomycin; DOX = doxorubicin; STS = staurosporine. (b) Trypan blue exclusion viability assay of HCI-002 MAT-E cells grown for two weeks and treated with the indicated drugs for 72 hours. Values expressed as mean  $\pm$  s.d. from triplicate wells ( $n=3$ ). P-values were determined by unpaired t-tests of each condition vs. the DMSO control group. Taxol, DOX and STS were used as positive controls for cell death. (c) Representative flow cytometry plots of aV and PI dead cell analysis of HCI-002 MAT-E cells treated for 72 hours. Bar graph shows percent of live and dead HCI-002 cells by aV and PI. Data represented as mean  $\pm$  s.d. ( $n=3$ ). P-values were determined by unpaired t-tests of each condition vs. the DMSO control group for the percent of aV-PI-viable cells. Taxol, DOX and STS were used as positive controls for cell death. (d) Representative aV and PI fluorescence micrographs of HCI-002 MAT-E cells treated for 72 hours. Blue = Hoechst nuclear counterstain. Scale bar = 25  $\mu$ m.

in primary breast tumors is also associated with worse prognosis in breast cancer patients (Fig. 5.12a). NME1 catalyzes the transfer of a phosphate from nucleoside triphosphates (NTPs) to nucleoside diphosphates (NDPs), primarily from ATP to GDP to produce GTP for use in G protein signalling [Boissan et al. (2018)]. Several G proteins such as RAC1 and CDC42 promote cell migration and growth and have established pro-metastatic functions [Maldonado et al. (2020)]. We hypothesized that OXPHOS promotes metastasis in PDX cells through NME1, and tested whether NME1 overexpression promotes metastasis using our culture-transplant system.

HCI-010 cells were cultured in MAT-E conditions for two weeks (P0) and transduced with lentivirus to overexpress NME1 and GFP (+NME1-GFP) or GFP alone (+GFP) (Fig. 5.11a). Transduced P0 cells were re-plated and expanded in culture for 3 weeks (P1) (Fig. 5.12b), and human GFP+ CD298+MHCI-PDX cells were isolated by flow cytometry and transplanted orthotopically into recipient mice for 60 days (Fig. 5.12c). qPCR analysis for NME1 showed 3.9-fold increased expression in +NME1-GFP compared to +GFP transduced cells ( $p=0.0005$ ), confirming successful overexpression (Fig. 5.12d). Analysis of primary tumor growth showed no difference in the growth kinetics or mass of +NME1-GFP ( $n=6$ ) and +GFP ( $n=6$ ) groups (Fig. 5.11c). However, whole mount fluorescence microscopy analysis of lung tissues showed substantially more GFP signal in the +NME1-GFP group, indicating higher metastatic burden (Fig. 5.11d). This was confirmed by flow cytometry, which showed a >4-fold increase in the frequency of GFP+ CD298+MHC-I- human metastatic cells in the lungs of +NME1-GFP ( $0.98 \pm 0.25\%$ ) compared to +GFP ( $0.23 \pm 0.15\%$ ) control mice (Fig. 5.11e). These findings reveal a pro-metastatic function for NME1 in breast cancer lung metastasis and provide proof-of-principle for the value of our PDX culture-transplant system for functional investigations of new genes in metastasis using patient tumor cells.

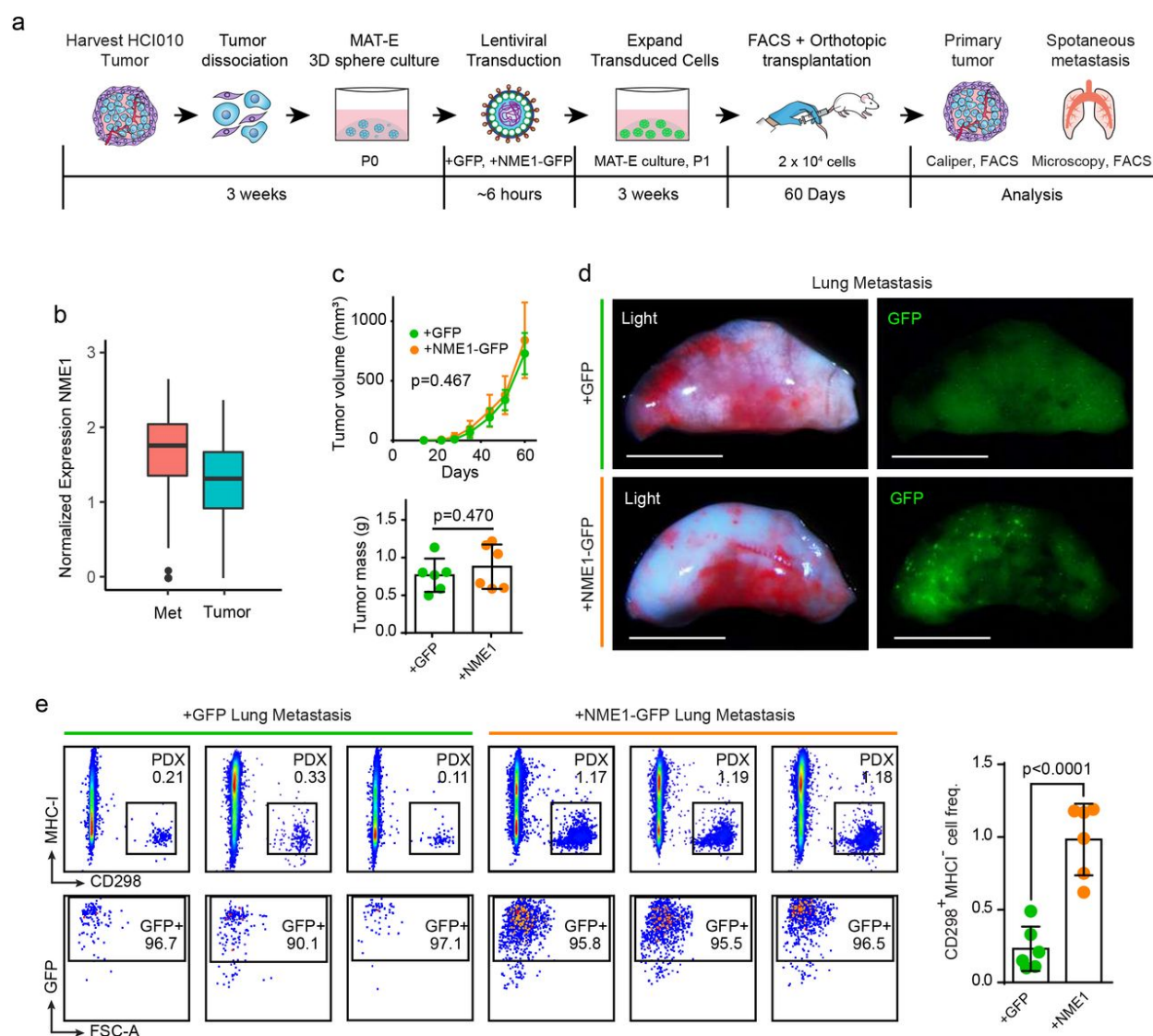


Figure 5.11: NME1 promotes lung metastasis from patient tumor cells (**a**) Workflow to investigate the effect of NME1 overexpression on spontaneous metastasis from cultured PDX tumor cells. (**b**) Normalized gene expression of NME1 in metastatic (red,  $n=435$  cells) and primary tumour cells (blue,  $n=684$  cells). (**c**) Primary tumor weight and growth kinetics. Line graph shows tumor volume calculated by caliper measurements (Top). Bar graph shows tumor weight measured at endpoint (Bottom). (**d**) GFP signal identifying metastatic nodules in representative lungs from orthotopically transplanted mice from (**c**). Scale bar = 5 mm. (**e**) Comparison of lung metastatic burden generated from control versus NME1-overexpressing PDX cells. Flow cytometry plots show the percentage of human metastatic cells in the lungs of three representative mice per group, identified by CD298<sup>+</sup>MHC-I<sup>-</sup> (top left panels) and GFP (bottom left panels). Bar graph quantifies the frequencies of CD298<sup>+</sup>MHC-I<sup>-</sup> metastatic cells in the lungs of each animal in the cohort. Values are expressed as mean  $\pm$  s.d. P-value determined by unpaired t-test.



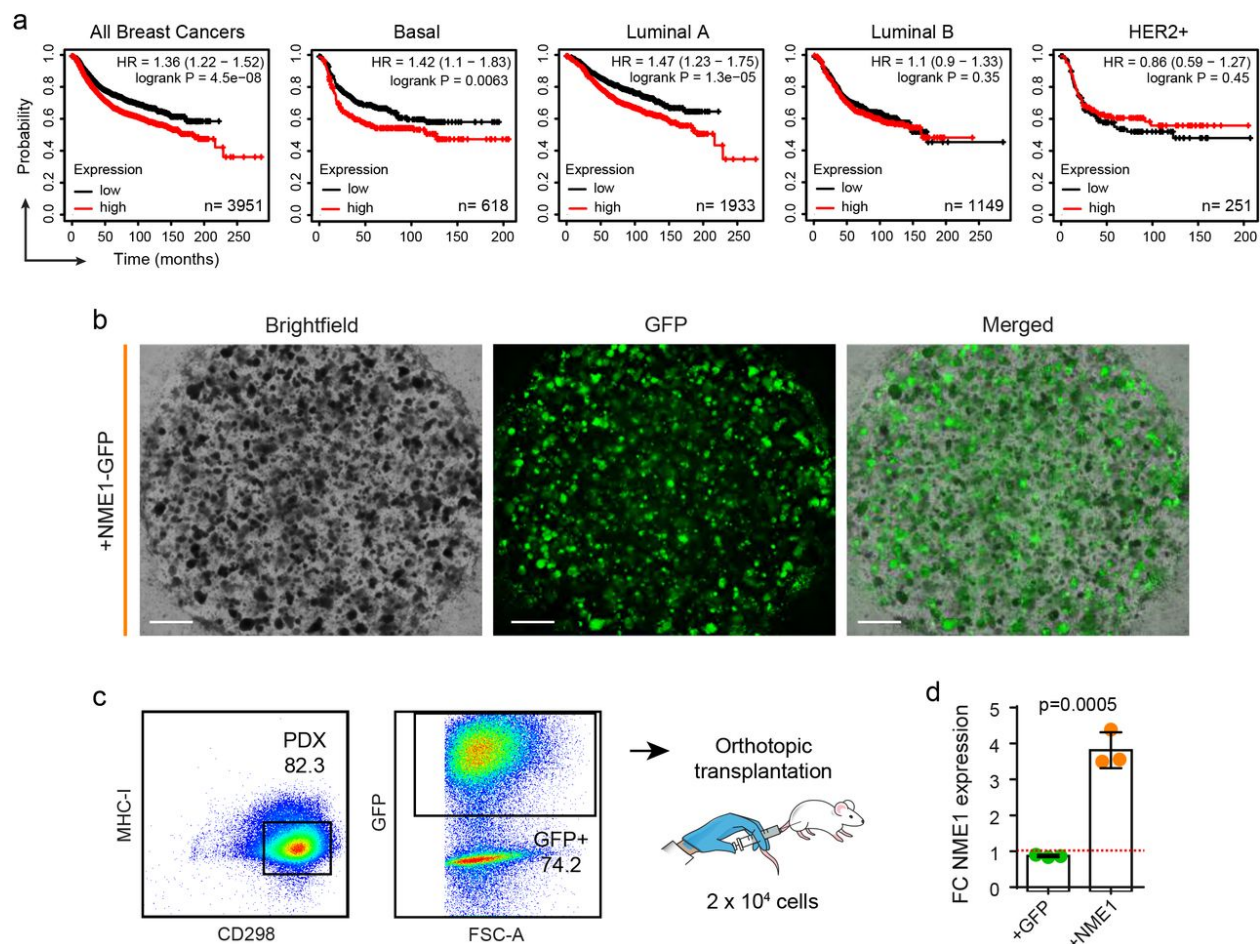


Figure 5.12: NME1 overexpression in cultured PDX cells and its relevance in patient breast cancer prognosis. (a) Kaplan-Meier (KM) curves show relapse free survival (RFS) in breast cancer patients by tumor subtype using the KM plotter database, based on their primary tumor expression of NME1. P-values were determined via a log-rank test. (b) Images show GFP expression in PDX spheres cultures following lentiviral transduction in vitro. HCI-010 sphere cells were transduced with +NME-GFP lentivirus at MOI=25 and re-seeded in MAT-E culture at a density of 2E05 cells per well. Images show z-stack micrographs of individual wells containing P1 spheres 3 weeks later. Scale bar = 800  $\mu$ m. (c) Flow cytometry plots show gating strategy for sorting transduced human GFP+CD298+MHCI- PDX cells for orthotopic transplantation and qPCR analysis. (d) Bar graph shows qPCR quantification of NME1 expression in control (+GFP) and NME1-GFP (+NME1) transduced cells. Values are plotted as fold change (FC) in NME1 expression in +NME1 relative to +GFP cells and represented as mean  $\pm$  s.d. P-value determined by unpaired t-test.

## 5.4 Discussion

Despite improvements in outcomes for early-stage patients, survival rates for metastatic patients have shown limited improvement and metastasis continues to be the major cause of death for cancer patients. A significant roadblock to progress has been the limited availability of models that faithfully recapitulate the biological complexities of metastasis in patients. Despite recent efforts to build large banks of human PDX models to improve authenticity in cancer research, their application in metastasis has been limited by the technical challenges of culturing patient cells in vitro for subsequent functional studies [Daniel et al. (2009); Whittle et al. (2015)]. Here, we develop a robust approach for the viable propagation, engineering and expansion of PDX cells in 3D culture for functional studies of metastasis. Using orthotopic transplantation and RNA sequencing, we show that cultured cells maintain tumorigenic potential and display minimal transcriptome changes, indicating that our method facilitates authentic long-term culture of patient tumor cells. We show PDX cells engineered in vitro display robust capacity for spontaneous and experimental metastasis, demonstrating the value of our culture-transplant system for functional studies of metastasis in diverse contexts. To our knowledge, this represents the first adaptation of PDX models for metastasis research in vivo, presenting an important technical advance that may help drive innovation for the development of more efficacious therapeutic strategies tailored specifically for metastatic disease.

In addition to technical advances, our study highlights the critical importance of cellular metabolism in breast cancer metastasis. Despite the historical focus on Warburg metabolism in tumor biology, we and others have recently shown that mitochondrial OXPHOS is critical for metastatic progression. However, these studies were conducted using cell line models [Andrzejewski et al. (2017); Davis et al. (2020); LeBleu et al. (2014)], so it remained unclear to what degree OXPHOS is important for metastasis in breast cancer patients.

Here, we used our culture-transplant system to find that OXPHOS inhibition significantly attenuates the lung metastatic capacity of patient tumor cells. We further investigated the potential role of the metabolic enzyme NME1 in OXPHOS-mediated metastasis [Davis et al. (2020)]. Although prior work in melanoma established NME1 as a metastasis suppressor gene, [Jarrett et al. (2013); Steeg et al. (1988); Zhang et al. (2011)] we recently reported its upregulation in lung metastases that display increased OXPHOS. Given that the main function of NME1 is to transfer phosphate from ATP to produce GTP, we hypothesized that NME1 may use ATP generated through OXPHOS to create GTP for G protein signaling pathways that promote metastasis [Boissan et al. (2018); Maldonado et al. (2020)]. Using our culture-transplant system, we found that NME1 overexpression results in a 4-fold increase in spontaneous lung metastasis. These results reveal a new pro-metastatic role for NME1 in breast cancer, suggesting its function is tissue-context specific, and open the door to future studies investigating the mechanistic link between NME1 and OXPHOS and their potential as therapeutic targets for metastatic disease. Our study also provides key proof-of-principle for the value of our PDX culture-transplant system for functional investigations of new genes in metastasis using patient tumor cells.

## 5.5 Materials and Methods

### 5.5.1 Harvesting and processing tumors into single cells

After 3-6 months of growth, tumors were collected from mice and mechanically dissociated, followed by 2 mg/mL collagenase (Sigma-Aldrich, cat. no. C5138-1G) digestion in medium (DMEM F-12 medium with 5% FBS) at 37°C for 45 minutes on a standard shaker. The digested tumor was washed with PBS, incubated with trypsin (Corning, cat. no. 25-052-Cl) for 10 minutes at 37°C, washed again, and then treated with DNaseI (Worthington Biochemical, cat. no. LS002139). The cells were filtered through a 100  $\mu$ m strainer. Live

cell concentration was checked using the Countess II automated cell counter (ThermoFisher Scientific Inc., Carlsbad, CA, USA).

### 5.5.2 Culturing PDX cells

PDX tumors were dissociated into single cells and plated in various culture conditions. PDX cells were plated in 6-well ULA plates (Fisher Scientific, cat. no. 07-200-601) at  $2.5 \times 10^5$  cells/well and topped off with 1 mL of either EpiCult™ Medium (StemCell Technologies, cat. no. 05610) supplemented with 5% FBS, 10 ng/mL human epidermal growth factor, and 10 ng/mL basic fibroblast growth factor or MEGM™ culture medium (Lonza, cat. no. CC-3150), completed as per manufacturer's protocol. Medium was changed when necessary.

PDX single cells were also cultured in standard flat bottom 24-well plates. The cells were plated at a seeding density of  $1.0 \times 10^5$  to  $2.5 \times 10^5$  cells/well in a 1:1 mix of Matrigel (growth factor reduced) (Corning, cat. no. 356231) and EpiCult™ or MEGM™. 1 mL of EpiCult medium was added to each well, and changed as necessary. Cells were harvested anytime between day 9-21 using dispase (StemCell Technologies, cat. no. 07913) and trypsin to dissociate Matrigel and spheres. All PDX cells from all culture conditions were grown at 37°C and 5% CO<sub>2</sub>.

### 5.5.3 Generation of RNA sequencing dataset

We generated a dataset of 3 biological replicates of paired HCI-010 uncultured and cultured cells, and paired HCI-002 uncultured and cultured cells. We harvested and dissociated HCI-010 and HCI-002 PDX tumors using methods described above. We split our single cell suspension in half and stained half of the uncultured HCI-010 and HCI-002 cells for FACS using fluorescent labeled antibodies for human specific CD298 (Biolegend, cat. no. 341704) and mouse-specific MHC-I (eBioscience, cat. no. 17-5957-82).  $1.0 \times 10^5$  uncultured cells were sorted for each patient for RNA isolation. The other half of the cell suspension was used for

culturing. HCI-010 and HCI-002 PDX cells were plated in 24-well plates at a seeding density of  $2.5 \times 10^5$  cells/well and topped off with 1 mL of EpiCult. Cells were grown in culture for 2 weeks, and then harvested using dispase and trypsin. Cultured cells were stained for FACS using fluorescent labeled antibodies for human-specific CD298 and mouse-specific MHC-I.  $1.0 \times 10^5$  cultured cells were sorted for each patient. After sorting, uncultured and cultured cells were processed for RNA extraction, followed by cDNA synthesis and amplification. Library construction was performed with the Takara Clontech SMARTer Stranded Total RNA-seq kit v2. The libraries were sequenced at a depth of 35 million paired end reads for each sample on the NovaSeq 6000. RNA sequencing Data are available on the GEO database under the accession code GSE153887.

#### **5.5.4 Processing and analysis of bulk RNA-seq data**

Quality of reads was accessed using FastQC software. Reads were aligned to reference genome GRCh38/hg38 from UCSC using Spliced Transcripts Alignment to a Reference (STAR) software. The un-normalized count matrix was filtered to exclude any genes with 0 reads, and we designated the uncultured samples as the reference level. We then performed differential gene expression analysis using DESeq2 1.28.1 in R 4.0.0.

#### **5.5.5 Mouse strains**

NOD/SCID and NSG mice were purchased from The Jackson Laboratory (Bar Harbor, Maine, USA). All mice were maintained in a pathogen-free facility. All mouse procedures were approved by the University of California, Irvine, Institutional Animal Care and Use Committee.

### **5.5.6 Orthotopic transplantation and i.c and i.v injection models of cultured PDX cells for modeling metastasis**

PDX cells were harvested after two to three weeks of culture in Matrigel and EpiCult. Dispase and trypsin were used to dissociate Matrigel and spheres to single cells. For orthotopic transplants,  $2.0 \times 10^4$  -  $1.0 \times 10^5$  cells were suspended in 15-20  $\mu\text{L}$  of a 1:1 mixture of PBS and Matrigel and injected into the number 4 mammary fat pads of NOD/SCID and NSG mice using a 25  $\mu\text{L}$  Hamilton syringe. For experimental metastasis models, cells were suspended at a concentration of  $5 \times 10^6$  cells/mL.  $5 \times 10^5$  cells in 100  $\mu\text{L}$  of PBS were injected into the right ventricle of each NOD/SCID or NSG mouse for i.c. injections or into the tail vein for i.v. injections.

### **5.5.7 Analysis of primary tumors and metastasis in distal tissues**

Following 8-14 weeks post orthotopic transplants, or ~8 weeks post i.c. or i.v. injections, primary tumors and peripheral tissues including lungs, lymph nodes, bone marrow, peripheral blood, and brains were harvested, dissociated to single cells and stained with fluorescent conjugated antibodies for CD298 (Biolegend, cat. no. 341704) and MHC-I (eBioscience, cat. no. 17-5957-82), and flow cytometry was used to analyze and quantify disseminated CD298+MHC-I- PDX cells using the BD FACS Aria Fusion cell sorter (Becton, Dickinson and Company, Franklin Lakes, NJ, USA) as described previously [[Lawson et al. \(2015\)](#)]. Primary tumor volumes were calculated using caliper measurements with the equation: volume of an ellipsoid =  $1/2(\text{length} \times \text{width}^2)$ . Whole mount images of primary tumors and lungs were taken with a Leica MZ10 F modular stereo microscope (Leica Microsystems, Buffalo Grove, IL, USA).

### 5.5.8 Histology and pathological analysis

Tissues were harvested from mice. The lungs and tumors were fixed in 4% formaldehyde. After overnight fixation at 4°C, the tissues were processed for paraffin embedding using standard protocols. The paraffin-embedded tissues were cut into 7- $\mu$ m sections using a Leica microtome, rehydrated, and stained with haematoxylin and eosin. For immunofluorescent staining, slides were subjected to antigen retrieval in a 10 mM citric acid buffer (0.05% Tween 20, pH 6.0). We then blocked non-specific binding with a blocking buffer (0.1% Tween 20 and 10% FBS in PBS) for 20 minutes, and then incubated tissues overnight at 4°C with primary antibodies. Slides were washed with PBS, and then incubated at room temperature with secondary antibodies for an hour, followed by washing with PBS, and mounting with VECTASHIELD Antifade Mounting Medium with DAPI (Vector Laboratories, H-1200-10). Images were taken using a BZ-X700 Keyence microscope (Keyence Corp. of America, Itasca, IL, USA). Pathological analysis was performed by Dr. Robert A. Edwards, a board-certified pathologist and the director of the Experimental Tissue Resource in the UC Irvine Health Chao Family Comprehensive Cancer Center.

### 5.5.9 Lentivirus transduction for genetic engineering of PDX cells

PDX cells were cultured for approximately 2-3 weeks in Matrigel and EpiCult, removed from Matrigel with dispase, dissociated to single cells with trypsin, neutralized with DMEM medium with 10% FBS, and washed with PBS with a 5 min centrifugation at  $300 \times g$ . Cells were suspended in premade lentivirus solution at a multiplicity of infection (MOI) of 25 and the final volume was topped off to no greater than 100  $\mu$ L with Opti-MEM™ I Reduced Serum Medium (ThermoFisher Scientific, Cat No. 31985070). GFP control (+GFP) and NME1 (+NME1) lentiviral expression vectors were packaged into lentiviral particles and purchased from VectorBuilder Inc., Chicago, IL, USA (+GFP Cat. No. VB190812-1255tza, +NME1 Cat. No. VB180802-1083ueg). Cells were subjected to an hour long spinfection at

300 × g at 4°C, resuspended and incubated in the same lentivirus solution for an additional 4-5 hours in 96-well round bottom ultra low attachment plate wells at 37°C and 5% CO<sub>2</sub>. Cells were centrifuged for 5 min at 300 × g, seeded in Matrigel and EpiCult as described above and expanded for an additional 2-3 weeks at 37°C and 5% CO<sub>2</sub>. Medium was replaced as needed. After 2-3 weeks in Matrigel and EpiCult cultured, PDX cells were removed from Matrigel with dispase, dissociated to single cells with trypsin to form single cell suspensions for transplantation into mice. Cell sorting for GFP-positive CD298+MHC-I- PDX cells with fluorescently tagged antibodies for CD298 (Biolegend, cat. no. 341704) and MHC-I (eBioscience, cat. no. 17-5957-82) was performed using the BD FACSaria Fusion cell sorter (Becton, Dickinson and Company, Franklin Lakes, NJ, USA).

#### **5.5.10 Pharmacologic studies**

Cells were treated with oligomycin (Oligo) (MP Biomedicals, Cat. No. 0215178610) for the inhibition of OXPHOS and treated with Taxol (Sigma-Aldrich Canada, Cat. No. T7402), staurosporine (STS) (Sigma-Aldrich Canada, Cat. No. S4400), and doxorubicin (DOX) (Sigma-Aldrich Canada, Cat. No. D1515) as positive controls for cell death. All compounds were prepared as concentrated stock solutions in DMSO and cells were treated with diluted working solutions in culture medium at DMSO concentrations no greater than 0.5% (v/v) using drug doses based off previous studies [[Davis et al. \(2020\)](#); [Ma et al. \(2017\)](#)].

#### **5.5.11 Cell death and viability assays**

Trypan Blue exclusion assays were performed with the Countess II automated cell counter (ThermoFisher Scientific Inc., Carlsbad, CA, USA). For analysis of cell death, cells were stained with aV-FITC, diluted 1:100 (GeneTex Cat. No. GTX14082) and PI, diluted 1:100 (ThermoFisher Scientific Cat. No. P3566) for 15 minutes in aV binding buffer (10 mM HEPES, 140 mM NaCl, 2.5 mM CaCl<sub>2</sub>, pH 7.4). Fluorescence microscopy was performed



with the BZ-X700 Keyence microscope (Keyence Corp. of America, Itasca, IL, USA), and flow cytometry analysis was performed using the BD FACSAria Fusion cell sorter (Becton, Dickinson and Company, Franklin Lakes, NJ, USA).

### 5.5.12 NADH fluorescence lifetime imaging

NADH fluorescence lifetime images were acquired with an LSM 880 confocal microscope (Zeiss) with a 40×1.2 NA C-Apochromat water-immersion objective coupled to an A320 FastFLIM acquisition system (ISS). A Ti:Sapphire laser (Spectra-Physics Mai Tai) with an 80 MHz repetition rate was used for two-photon excitation at 740 nm. The excitation signal was separated from the emission signal by a 690 nm dichroic mirror. The NADH signal was passed through a 460/80 nm bandpass filter and collected with an external photomultiplier tube (H7522P-40, Hamamatsu). Cells were imaged within a stage-top incubator kept at 5% CO<sub>2</sub> and 37°C. FLIM data was acquired and analyzed with the SimFCS 4 software developed at the Laboratory for Fluorescence Dynamics at UC Irvine. Calibration of the system was performed by acquiring FLIM images of coumarin 6 (~10  $\mu$ M), which has a known lifetime of 2.5 ns in ethanol, to account for the instrument response function.

### 5.5.13 Phasor FLIM NADH fractional analysis

NADH assumes two main physical states, a closed configuration when free in solution, and an open configuration when bound to an enzyme [Hull et al. (2001)]. These two physical states have differing lifetimes, 0.4 ns when in its free configuration, and 3.4 ns when in its bound configuration [Datta et al. (2015); Kolb and Weber (1975); Ma et al. (2016)]. To quantify metabolic alterations, we performed fractional analysis of NADH lifetime by calculating individual pixel positions on the phasor plot along the linear trajectory of purely free NADH lifetime (0.4 ns) and purely bound NADH lifetime (3.4 ns). We quantified the fraction of free NADH by calculating the distance of the center of mass of a spheroid's

cytoplasmic NADH FLIM pixel distribution to the position of purely bound NADH divided by the distance between purely free NADH and purely bound NADH on the phasor plot. These segmentation and phasor analysis methods are described in detail elsewhere [Ranjit et al. (2018)].

#### 5.5.14 Single cell analysis

To analyze the differences in the expression of NME1 between metastases and tumors in these models, we accessed our previously published dataset on these PDX models, which included single cell gene expression profiles of metastatic and primary tumor cells [Shafee et al. (2008)]. The expression matrices were log-transformed into  $\log[\text{transcripts per kilobase million} + 1]$  matrices and loaded into the Seurat analysis package [Butler et al. (2018)].

#### 5.5.15 qPCR analysis

RNA was extracted by using Quick-RNA Microprep Kit (Zymo Research, R1050) following manufacturer's protocol. RNA concentration and purity were measured with a Pearl nanospectrophotometer (Implen). Quantitative real-time PCR was conducted using PowerUp SYBR green master mix (Thermo Fisher Scientific, A25742) and primer sequences were found in Harvard primer bank and designed from Integrated DNA Technologies; GAPDH forward primer 5'- CTCTCTGCTCCTCCTGTTCGAC -3', GAPDH reverse primer 5'- TGAGC-GATGTGGCTCGGCT -3'; NME1 forward primer 5'- AAGGAGATCGGCTTGTGGTTT -3', NME1 reverse primer 5'- CTGAGCACAGCTCGTGTAATC -3'. Gene expression was normalized to the GAPDH housekeeping gene. For relative gene expression  $2^{-\Delta\Delta Ct}$  values were used. The statistical significance of differences between groups was determined by unpaired t-test using Prism 6 (GraphPad Software, Inc).

### 5.5.16 Relapse-free survival analysis

Kaplan-Meier (KM) survival curves were generated to perform relapse-free survival analysis on breast cancer patient primary tumor microarray data (of all breast cancer patients and individual subtypes of breast cancer) from the KM plotter database [[Györfy et al. \(2010\)](#)]. All KM plots are displayed using the “Split patients by median” parameter.

## 5.6 Funding

This study was supported by funds from the National Cancer Institute (K22 CA190511 to D.A.L.), the NIH/NCI (1R01CA234496; 4R00CA181490 to K.K.), the American Cancer Society (132551-RSG-18-194-01-DDC to K.K.), the National Institutes of Health (P41-GM103540 to M.A.D. and A.E.Y.T.L, T32CA009054 to R.T.D through matched university funds), the National Science Foundation (1847005 to M.A.D. and NSF GRFP DGE-1839285 to A.E.Y.T.L) and the V Foundation (V2019-019). H.A. was supported by the University of Hail, Hail, Saudi Arabia for the Ph.D. Fellowship. D.M. was supported by the Canadian Institutes of Health Research Postdoctoral Fellowship.

## 5.7 Competing interests

The authors declare no competing interests.

## 5.8 Author Contributions

D.A.L and K.K. supervised research. D.A.L, K.K., D.M., and G.A.H. designed research. D.M., G.A.H., A.E.Y.T.L., H.A., K.B., K.R.D., M.R., J.W.W., R.T.D, K.T.E., M.Y.G.M., R.L., R.A.E., M.A.D., K.K., and D.A.L. performed research; G.A.H., K.B., and J.W.W. per-

formed bioinformatic analyses; D.M., G.A.H., K.K. and D.A.L. wrote the paper manuscript, and all authors discussed the results and provided comments and feedback.

## 5.9 Acknowledgements

We thank Dr. Zena Werb at the University of California, San Francisco for thoughtful discussions and feedback on project overview and study design. We thank Aaron Longworth, Armani Oganyan, Nathan Ryan James, Anh Thien Phung, Scott Nguyen, Lannhi Nguyen and Jennifer Nguyen for their technical assistance and animal handling. We thank Dr. Alana Welm at the Huntsman Cancer Institute for generously providing PDX models. We thank the Genomics High Throughput Facility at the University of California, Irvine for conducting the bulk RNA sequencing of the PDX samples. We wish to acknowledge the support of the Chao Family Comprehensive Cancer Center Experimental Tissue Resource, supported by the National Cancer Institute of the National Institutes of Health under award number P30CA062203.

## 5.10 Summary

In this chapter, we presented our work to create a 3D breast cancer tumor spheroid culture-transplant system to facilitate the expansion and modulation of PDX cells to run functional metabolic assay. This propagation of PDX cells as tumor spheres in vitro not only maintain their global transcriptome after propagation, but also continue to form spontaneous metastases post-transplantation. Additionally, the spheroid cultures can be genetically engineered, and again transplanted to facilitate experiments of in vivo metastasis post-genetic modification.

Insofar as our data have shown, both the phenotypic and genotypic metabolic traits of invading and metastasizing cells differ greatly from their core and primary tumor sites. A

key functional dysregulation of these invading fronts are their consistent shifts towards an oxidative phosphorylation metabolic phenotype, as shown by NADH FLIM. As described in previous chapters, the cells' mitochondria are the sites of oxidative phosphorylation within cells, and their structure and dynamics have been shown to play a large part in fueling cancer and other diseases, as well as basic biological functions like embryonic development. The next chapter will focus on the creation of a new method for unbiased and automatic segmentation and tracking of mitochondria to combat the current gold standard of manual analysis. We also use the 3D spheroid cultures developed in this chapter to experimentally apply our novel method of segmenting and tracking mitochondria to examine differences in mitochondrial phenotypes in breast cancer models of varying invasiveness.

# Chapter 6

## Automated segmentation and tracking of mitochondria in live-cell time-lapse images

This chapter is again a collaborative effort that would not have been possible without the help of Dr. Devon Lawson and Dr. Kai Kessenbrock’s lab along with post-doctoral researcher Dr. Dennis Ma. This chapter is a slightly modified version of a paper from: Lefebvre et al., Automated segmentation and tracking of mitochondria in live-cell time-lapse images, Nature Methods, published 2021, Springer Nature and has been reproduced here with the permission of the copyright holder.

Mitometer’s manual can be found in [Appendix C](#), and its supplementary materials can be found in [Appendix D](#).

### 6.1 Abstract

Mitochondria display complex morphology and movements, which complicates their segmentation and tracking in time-lapse images. Here, we introduce Mitometer, an algorithm for

fast, unbiased, and automated segmentation and tracking of mitochondria in live-cell two-dimensional and three-dimensional time-lapse images. Mitometer requires only the pixel size and the time between frames to identify mitochondrial motion and morphology, including fusion and fission events. The segmentation algorithm isolates individual mitochondria via a shape- and size-preserving background removal process. The tracking algorithm links mitochondria via differences in morphological features and displacement, followed by a gap-closing scheme. Using Mitometer, we show that mitochondria of triple-negative breast cancer cells are faster, more directional, and more elongated than those in their receptor-positive counterparts. Furthermore, we show that mitochondrial motility and morphology in breast cancer, but not in normal breast epithelia, correlate with metabolic activity. Mitometer is an unbiased and user-friendly tool that will help resolve fundamental questions regarding mitochondrial form and function.

## 6.2 Main

The cell governs our birth, our response to mental and physical wounds, and ultimately our demise. Within these cells, the mitochondrion lies at the intersection of these three physiological states, and understanding its dynamics may help to identify important therapeutic targets for the pharmaceutical treatment of a broad range of diseases, from Alzheimer’s disease to cancer [[Federico et al. \(2012\)](#); [Green and Reed \(1998\)](#); [Iwata et al. \(2020\)](#)].

The roles that structure and function play in healthy mitochondria and the impact that altered mitochondrial morphology, movement, and fission and fusion dynamics have on the regulation of vital biological processes are currently the subjects of active research. For example, recent studies have demonstrated mitochondria-associated actin accumulation before fission events [[Schiavon et al. \(2020\)](#)]. Additionally, their localization in neurons has been found to fuel the bioenergy demands at distal extremities [[Baloh \(2008\)](#)], regulate the turnover of dysfunctional mitochondria [[Westermann \(2010\)](#)], and regulate neurogenesis in

postmitotic cells [Iwata et al. (2020)]. Impairment of these mitochondrial dynamics has also been associated with a wide variety of neurodegenerative diseases, including Alzheimer’s disease [Pigino et al. (2003); Rui et al. (2006)], Huntington’s disease [Trushina et al. (2004)] and Parkinson’s disease [Kapitein and Hoogenraad (2015); Wang et al. (2011); Waterman-Storer (1998)]. It has also been suggested that dysregulation of mitochondrial motion may contribute to the fueling of bioenergy demands in metastatic cancer [Caino et al. (2016,1)]. However, the advancement of both basic and preclinical mitochondria research has been held back by the biased and time-consuming manual analysis methods currently serving as the gold standard in the field. To uncover the peculiarities of these important life-preserving and disease-driving organelles, a novel method for automated and robust mitochondrial segmentation and tracking must first be developed.

Existing segmentation and tracking methods are difficult to tailor to mitochondria because of their dynamics and unique shapes. Several general techniques exist, but they make use of a Gaussian fit to estimate morphology, which works well only for spherical and elliptical particles [Abad et al. (2004); Cheezum et al. (2001); Tang et al. (2015); Tinevez et al. (2017)]. Object-based tracking methods are better suited for mitochondrial morphologies because they allow for variability in size and shape. Importantly, these methods require unbiased segmentation of the objects to be tracked, which is non-trivial. A deep learning model has been constructed for mitochondrial segmentation and it includes transfer learning, to train the model in one’s own system, although manual annotation is required, which may introduce bias [Fischer et al. (2020)]. Other deep learning models tailored broadly to biological segmentation may also be adapted to organellar segmentation, but they are still in their early stages and are not yet consistently used [Falk et al. (2019); Isensee et al. (2021)]. Current methods for tracking mitochondria are also limited, most of which work only for linear axonal transport in neurons, and require extensive user input [Alsina et al. (2017); Miller et al. (2015); Vallmitjana et al. (2017); Winter et al. (2012)]. These methods also ignore fission and fusion events altogether, or else require high temporal resolution to



connect overlapping regions between frames [GIEDT et al. (2012); Kandel et al. (2015)]. We compare several of these open-source techniques (Appendix D.1, Appendix Table D.1, and Appendix Figs. D.2, D.3) [Fischer et al. (2020); Kandel et al. (2015); Klopfenstein and Vale (2004); Lihavainen et al. (2012); Tinevez et al. (2017); Valente et al. (2017); Viana et al. (2015)].

To address the issues in analyzing mitochondrial dynamics, we developed Mitometer, a software package that incorporates a new method in a fast, unbiased and automated approach to segmentation and spatiotemporal tracking of mitochondria in live-cell fluorescence microscopy time-lapse images. Mitometer requires only pixel size and the time between frames to identify changes in mitochondrial morphology, motion, and fission and fusion dynamics. We validate our segmentation and tracking algorithms *in silico* via mitochondria simulations, and *in vitro* on a panel of cell types with differing basal mitochondrial morphologies, and with influencers of mitochondrial motion, fission and fusion. Using Mitometer we analyze heterogeneities between non-cancerous normal breast epithelial mitochondria, receptor-positive breast cancer (estrogen receptor or progesterone receptor positive; ER/PR+) mitochondria, and triple-negative breast cancer (TNBC) mitochondria from patient-derived xenograft (PDX) breast cancer cells, primary breast cells, and various breast cancer cell lines in both two-dimensional (2D) and three-dimensional (3D) environments. These results show TNBC mitochondria to be faster, more directional and more elongated than their ER/PR+ counterparts. We further examined correlations between metabolic heterogeneity and the mitochondrial morphology and motility of mitochondria at the level of the single mitochondrion. We found a positive relationship between fractions of bound nicotinamide adenine dinucleotide in its reduced form (NADH) and features such as speed and displacement, and negative relationships with features such as directionality and branching in both TNBC and ER/PR+ mitochondria, but not in normal breast epithelial mitochondria. Together, the automated segmentation and tracking algorithms and the intuitive user interface make Mitometer a broadly accessible tool that requires only basic fluorescence imaging ca-

pabilities, and which will serve to advance mitochondrial research in basic science and its clinical applications.

## 6.3 Results

### 6.3.1 Object-based segmentation of mitochondria

Mitometer takes a 3D or 2D time series of mitochondrial fluorescence images (Fig. 6.1a). First, we apply a diffuse background removal algorithm to each time frame and z-plane of the series (Fig. 6.2 and Appendix D.2). This diffuse background subtraction algorithm allows for a size- and shape-independent method of keeping well-isolated mitochondria intact, such as perilamellar mitochondria, and of separating mitochondria in crowded environments, such as perinuclear mitochondria (Fig. 6.1b, Fig. 6.2). Next, we convolve a Gaussian kernel with the diffuse background-subtracted image to remove high-frequency noise, which is followed by an intensity threshold to create a mask of the segmented mitochondria (Appendix D.3). To ensure the stability of the mask, we run a parameter exploration algorithm to select the standard deviation of the kernel and the threshold level (Fig. 6.1c). A mismatch between these parameters results in improper connections or separations of mitochondria (Fig. 6.3). The optimal parameters minimize the variation in the number and area of mitochondria between adjacent temporal frames of the image while maximizing the median number of mitochondria detected (Fig. 6.1d and Fig. 6.3). We then remove any detected objects below and above predefined minimum and maximum area thresholds and multiply the mask by the original image (Fig. 6.1e). In 3D images, we conduct the parameter exploration on the frame with the largest mean intensity value and use the parameters for all layers in the stack. Mitometer performs semantic segmentation by assigning all true pixels in the final binary mask to a mitochondrion. This is followed by a connected-component instance segmentation in which all spatially connected true pixels in the final mask belong to an individual mitochondrion, whereas pixels separated by false pixels belong to different

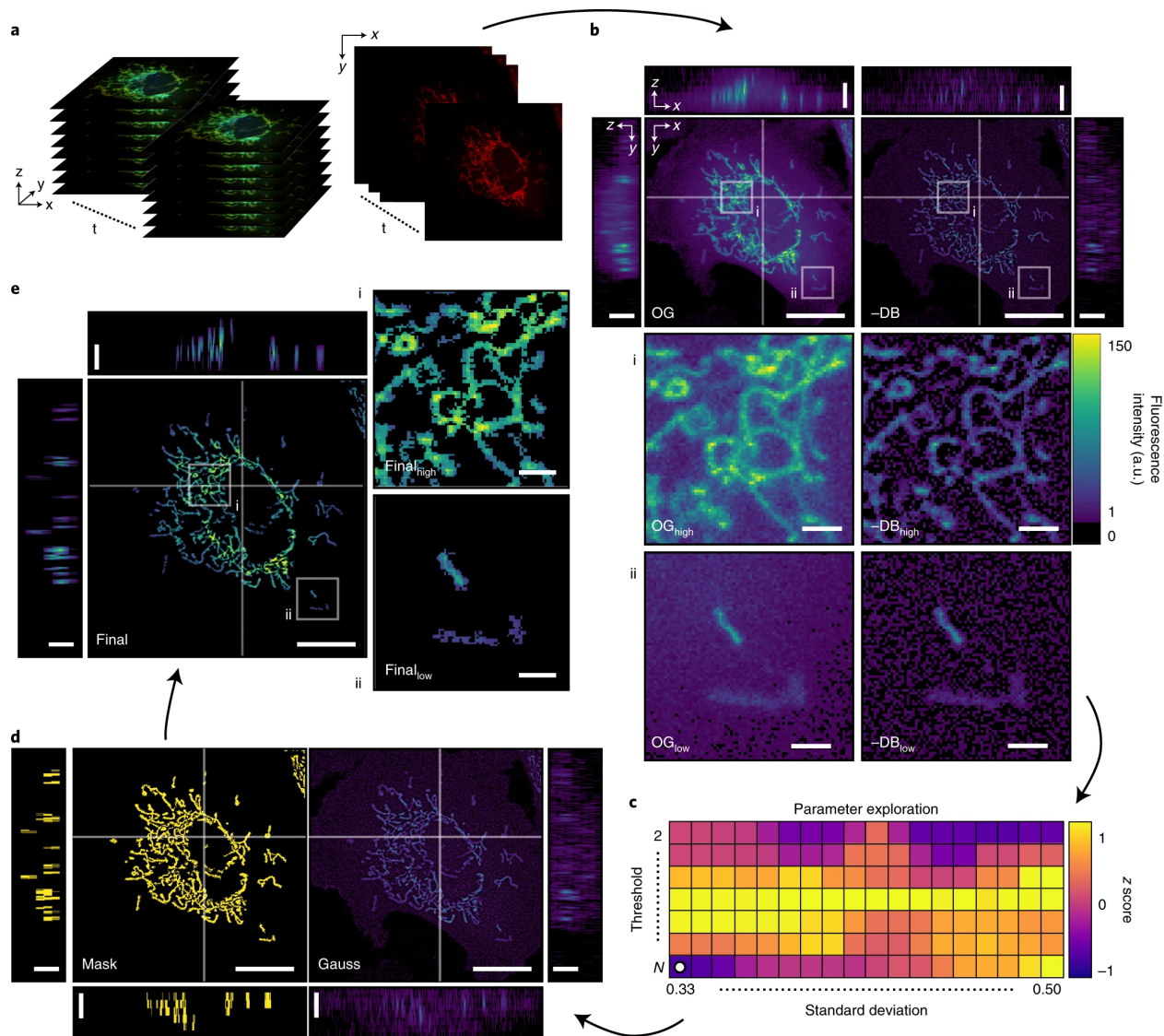


Figure 6.1: Object-based segmentation of individual mitochondria from fluorescence images. **a**, A 3D or 2D time stack of mitochondrial fluorescence images is taken as an input. **b**, The original (OG) stack (left), with orthogonal z projections of white crosshairs is shown. This stack is run through a diffuse background (DB) subtraction algorithm to remove noise between adjacent mitochondria. An example of a perinuclear region with a high DB (i) and a perilamellar region with a low DB (ii) are shown. **c**, A parameter exploration scheme iterates through combinations of Gaussian filter standard deviations and absolute thresholds, and the resulting time stack's connected components are analyzed for variability in number and size throughout the stack. This produces a specific minimum value (white dot) at the optimal parameters. **d**, The optimal Gaussian filter (right) and the intensity and area thresholds are applied to the stack to produce a binary mask (left). **e**, The binary mask is multiplied with the original stack to produce the final stack used for tracking. Scale bars, 20  $\mu\text{m}$  for full images, 2  $\mu\text{m}$  for close-ups. This example is a depiction of a BT-549 cell with mitochondrially targeted mCherry via a lentiviral expression system.

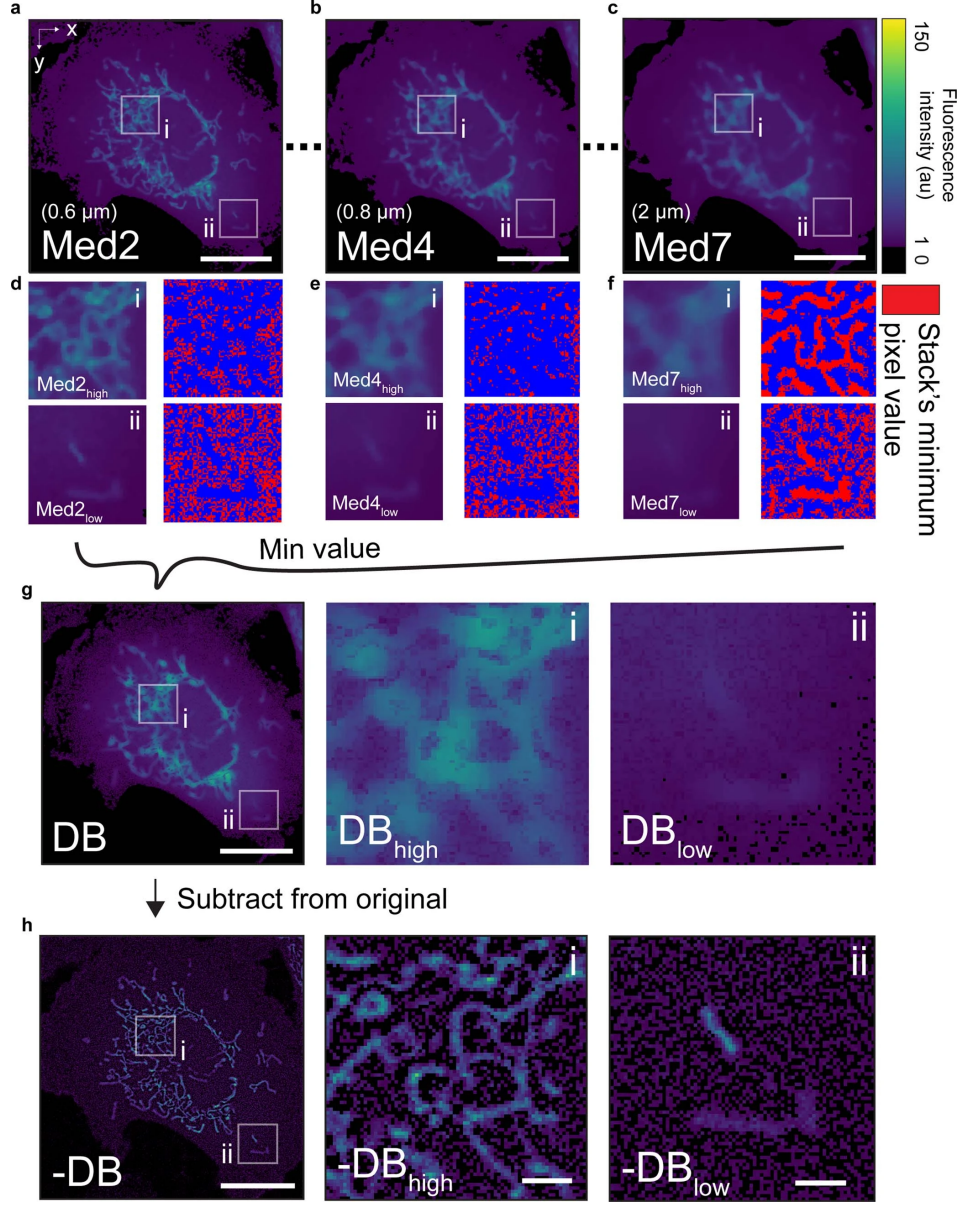


Figure 6.2: Diffuse background removal surrounding objects of complex shapes. Circular median filters of diameters of  $0.6 \mu\text{m}$  (a) to  $2 \mu\text{m}$  (c) (corresponding to the minimum area threshold and a value larger than the minor axis length of mitochondria) in 1-pixel increments (b) are convolved with the original image. Close-ups of regions with high (i) and low (i) diffuse background noise convolved with a small (d) medium (e) and large (f) median filter (left), with corresponding minimum median filter values at each filter size (right). g, The minimum value of each pixel in the stack of median filtered images (which also contains the original image) is used to build the diffuse background image, showing high diffuse noise in the dense regions (i) and minimal diffuse noise in the sparse regions (ii). h, The diffuse background image is then subtracted from the original image to produce a diffuse background subtracted image, separating adjacent mitochondria in dense regions (i) and keeping mitochondria intact in sparse regions (ii).



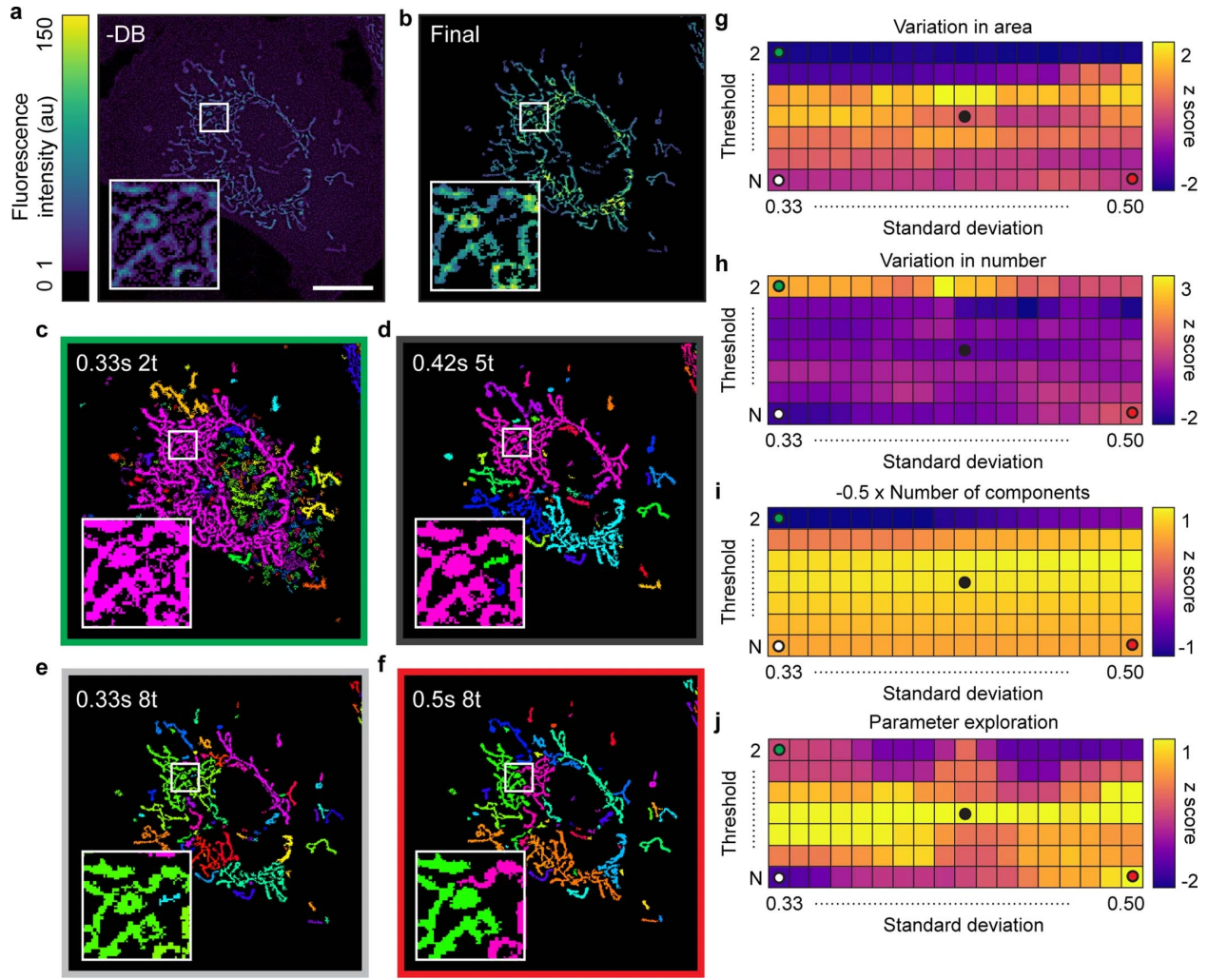


Figure 6.3: Parameter exploration for choosing low-pass filter and threshold parameters. **a**, The diffuse background subtracted (-DB) image is taken as an input. **b**, The output is an image with optimal parameters (**e**) chosen to segment mitochondrial objects and remove noise. A mismatch in parameters results in high noise (**c**), false connections and area over-estimation (**d**), and loose connections (leading to high variability) with area overestimation (**f**). The parameters are chosen based on the z score normalized addition of 3 features: the variability in the median area of the mitochondria between temporal frames (**g**), the variability in the number of mitochondria found between temporal frames (**h**), and  $\frac{1}{2}$  the negative number of mitochondria found between temporal frames (**i**). We give less weight to the number of mitochondria found as many false disconnections biases the parameter selection towards a highly thresholded image, while noise biases the parameter selection towards a non-thresholded image. This addition results in the cost function used for minimization to select optimal parameters, which we run through a symmetrically padded  $3 \times 3$  median filter to ensure selected parameters are in a region of low cost, rather than an outlying point (**j**). Colored dots represent parameters chosen to create images shown in **c-f** with respective border colors. Colors in **c-f** represent randomly pseudocolored connected components.

mitochondria. The mitochondria now having been properly segmented, tracking can be accurately performed.

### 6.3.2 Object-based tracking of mitochondria

Mitochondria are dynamic organelles that undergo translational motion via molecular motors, fission by proteins such as dynamin-related protein 1 (Drp1), fusion by proteins such as mitofusin 1/2 (Mfn1/2) and optic atrophy 1 (Opa1), organic appearance via mitochondrial biogenesis or movement into the plane of focus, and organic disappearance via mitophagy or movement out of the plane of focus [Chang and Blackstone (2010); Pilling et al. (2006); Ploumi et al. (2017)]. For translational motion, a mitochondrion is assigned to its track from the previous frame. In the case of fission, one mitochondrion splits into two or more. In the case of fusion, two or more mitochondria merge into one mitochondrion. Fission and fusion events are differentiated from a mitochondrion's organic appearance and disappearance via a volume (or in two dimensions, area) comparison of new and lost tracks to existing tracks.

Our tracking algorithm uses a frame-by-frame global optimization scheme for track assignment, while allowing new tracks to be made and old tracks to be left unassigned. We first assign each mitochondrion in the first temporal frame to a new track. In each subsequent temporal frame, we assign each mitochondrion to either an existing track or to a new track. Global assignments are determined by a cost minimization scheme of the weighted and z-score-normalized differences in six (or, in three dimensions, seven) morphological parameters, that is, the area (or volume), the major and minor (and z) lengths, the solidity, the perimeter (or surface area), and the mean intensity of each mitochondrion, along with the difference in intensity-weighted centroid positions between frames (Fig. 6.4a, 6.5, and Appendix D.4). If a mitochondrion has a high correspondence in all parameters to a mitochondrion of an existing track, the cost of assignment between them will be low, while two mitochondria that have a low correspondence will have a high cost of assignment (Fig. 6.4b). We also give a cost to assigning a mitochondrion to a new track. Additionally, to ensure the

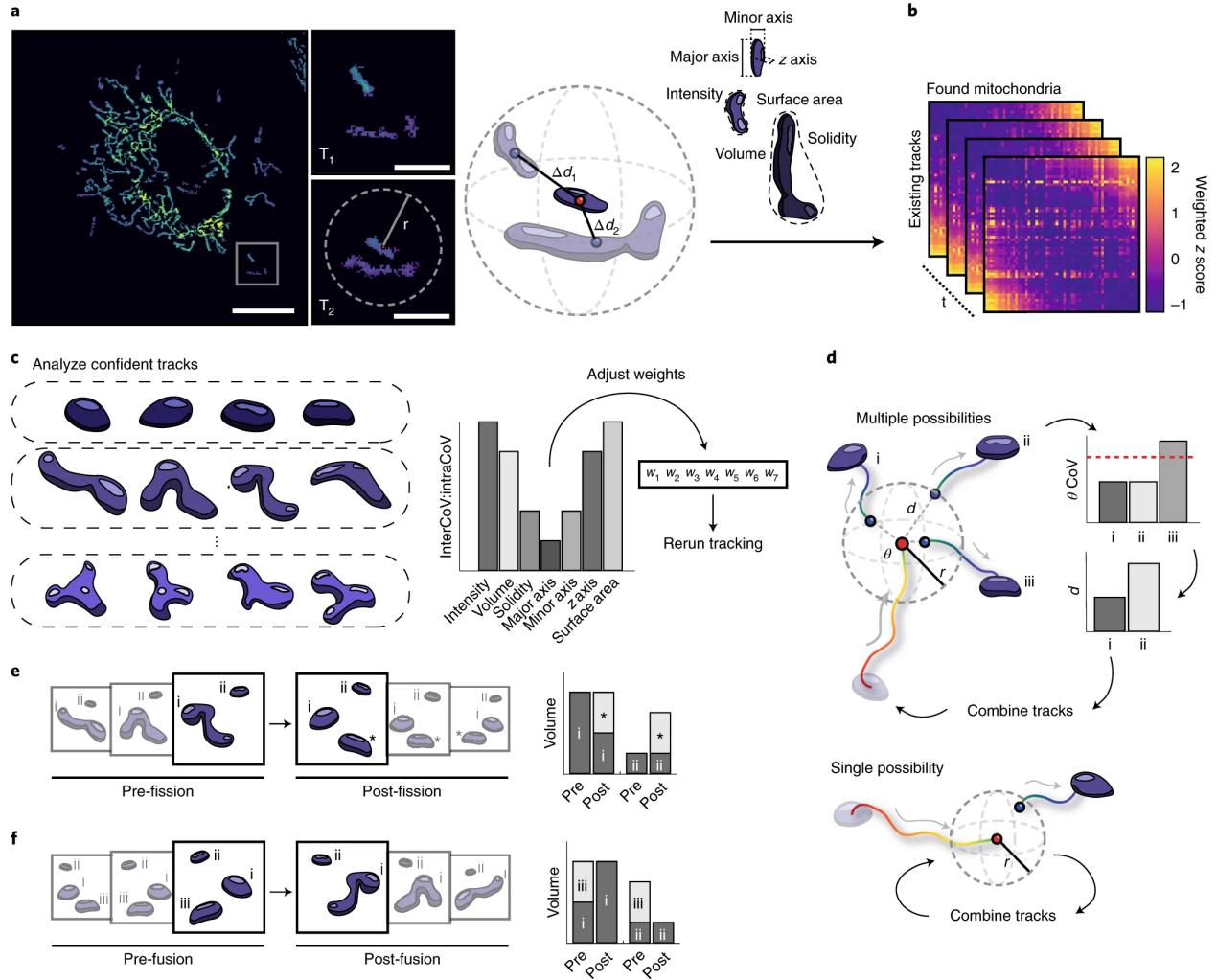


Figure 6.4: Tracking of mitochondria via global minimization of morphological and displacement differences. **a,b**, Mitochondria in the first ( $T_1$ ) and second ( $T_2$ ) temporal frames. Scale bars: left,  $20 \mu\text{m}$ ; right,  $4 \mu\text{m}$ . Center-of-mass distances ( $\Delta d_1$ ,  $\Delta d_2$ ) and differences in morphological features within the maximum velocity threshold ( $r$ ) are used to create a z-score-normalized assignment cost matrix. **c**, Confident mitochondrial tracks and their interCoV : intraCoV ratio for each morphological parameter used for weighting. **d**, In the case of multiple possibilities, gap-closing within  $r$  is done via travel angle ( $\theta$ ) and center-of-mass distance ( $d$ ) of the tracks at the new and lost positions. In the case of a single possible combination, the tracks are combined. **e**, Fission between existing tracks (i,ii) and a newly created track (\*) is determined by comparisons of the volume (or area, in two dimensions) and of the extrema distances of nearby mitochondria before and after fission. **f**, Fusion is handled the same way as fission, but compares the volume (or area) and the extrema distances of nearby mitochondria before (i-iii) and after fusion (i,ii).

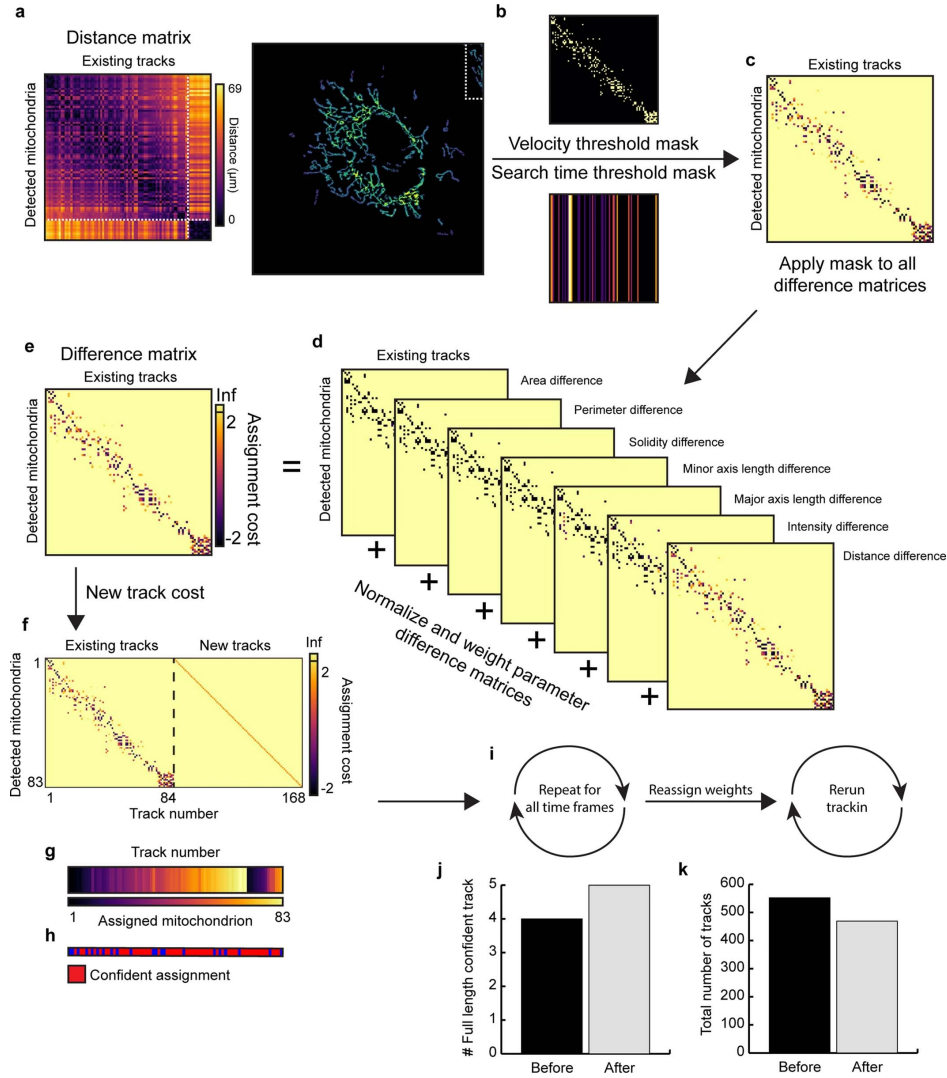


Figure 6.5: Flowchart for morphology and displacement-based global cost minimization tracking. **a**, A matrix of intensity weighted centroid distances is built comprised of existing tracks and mitochondrion found in the current time frame. An adjacent cell can be seen in the dotted white area. **b**, A mask is created to avoid assignments above the maximum search time and velocity thresholds. **c**, The mask is applied to the difference matrices. **d**, The difference matrices are summed to create the final matrix (**e**). **f**, A diagonal matrix of new track costs is appended to the difference matrix to allow newly found mitochondria to be assigned to a new track. **g**, Every mitochondrion (row) in the matrix is assigned to a single track (column) that leads to a globally minimized cost of assignment. **h**, A mitochondrion which is assigned to a track that also corresponds to its own individually minimum cost is labelled as a confident assignment. **i**, This process is repeated for all temporal frames. All confident tracks are then analyzed for interCoV : intraCoV ratios for each mitochondrial morphological feature, and weights are set accordingly. These weights are used to rerun the tracking algorithm, leading to a higher number of mitochondria that are confidently tracked for the full length of the time stack (**j**) and to less total number of tracks overall (**k**).



avoidance of highly improbable assignments and to increase the efficiency of our algorithm, we ignore the costs of assigning mitochondria to tracks that violate two defined thresholds: the maximum velocity threshold and the maximum search time threshold (Fig. 6.5). The maximum velocity threshold is the furthest distance a mitochondrion can be from a potential track between frames, derived both empirically and from existing literature [McCarron et al. (2013)], and the maximum search time threshold is the maximum number of temporal frames between which a mitochondrion can be assigned to an unassigned track (Appendix D.5 and Fig. D.4).

Each mitochondrion has a track that minimizes the assignment cost for that individual mitochondrion, which may be a different track than one that globally minimizes the assignment of all mitochondria in that frame (Fig. 6.5). We define the assignments that both individually and globally minimize the cost as confident assignments. We calculate the 98<sup>th</sup> quantile of the running list of confident assignment costs and designate this adaptive cost as the cost of assigning a mitochondrion to a new track (which we initially set to 1 for the first temporal frame, equivalent to 1 standard deviation above the mean cost of all assignments) (Fig. 6.5). We further define a track consisting entirely of confident assignments at the end of the track assignment process as a confident track. For every confident track, we calculate the coefficient of variation (CoV) of each morphological parameter in the track (intraCoV), and between different tracks (interCoV). We use the numeric interCoV : intraCoV ratio normalized to the number of weighted variables (seven in three dimensions, six in two dimensions) as the weighting for each morphological parameter in our cost matrix; conceptually, parameters differing greatly between different tracks will be given a higher weighting, while parameters differing greatly in the same track will be given a lower weighting (Fig. 6.4c and Appendix D.6). We then rerun the tracking algorithm using these calculated weights to improve assignments (Fig. 6.5).

To account for mistakenly disconnected tracks, we apply a stack-wide gap-closing scheme between new and lost tracks (Fig. 6.4d and D.7). We merge every combination of new

and lost tracks that satisfies the velocity and search time thresholds. We then retain as candidates those combinations with a travel angle CoV below 20 % (Fig. 6.6). Next, we globally minimize the cost of closure based on the intensity-weighted centroid displacement between viable new and lost track candidates. We also merge any new tracks that have only one possible assignment to a lost track based on velocity and search time thresholds. We iterate through this scheme until the number of tracks ceases to change (Fig. 6.6).

Finally, we discriminate between fission events and organic appearance in new tracks, and fusion events and organic disappearance in lost tracks to detect and quantify these mitochondrial dynamics. We build a list of fission and fusion candidates within the search time threshold of those tracks with extrema distances within the velocity threshold of the new or lost track. We use the extrema distance rather than intensity-weighted centroid distance given that fission or fusion events would result in the appearance or disappearance of two adjacent extrema, respectively. In the case of fission, we limit the possible candidates from which a mitochondrion has split by performing a volume (or area, in two dimensions) threshold by calculating the absolute difference of the mean volume of the track before fission and the sum of the mean volumes of the two tracks after fission (Fig. 6.4e). In the case of fusion, we instead calculate the absolute difference of the mean volume of the track after fusion and the sum of the mean volumes of the two tracks before fusion (Fig. 6.4f). To retain the track as a possible fission and fusion candidate, it must meet stringent requirements to ensure a high accuracy while keeping false-positive assignments low (Appendix D.8).

### 6.3.3 In silico validation of segmentation and tracking algorithms

To validate Mitometer, we simulate mitochondrial objects in silico and assign dynamic events to them. This allows us to generate ground truth tracks of mitochondria with varying magnitudes of directed motion, with the ability to appear and disappear, and to undergo fusion and fission events (Appendix D.9). We did not use manually annotated datasets because these are subjective and are known to generate large position estimation errors

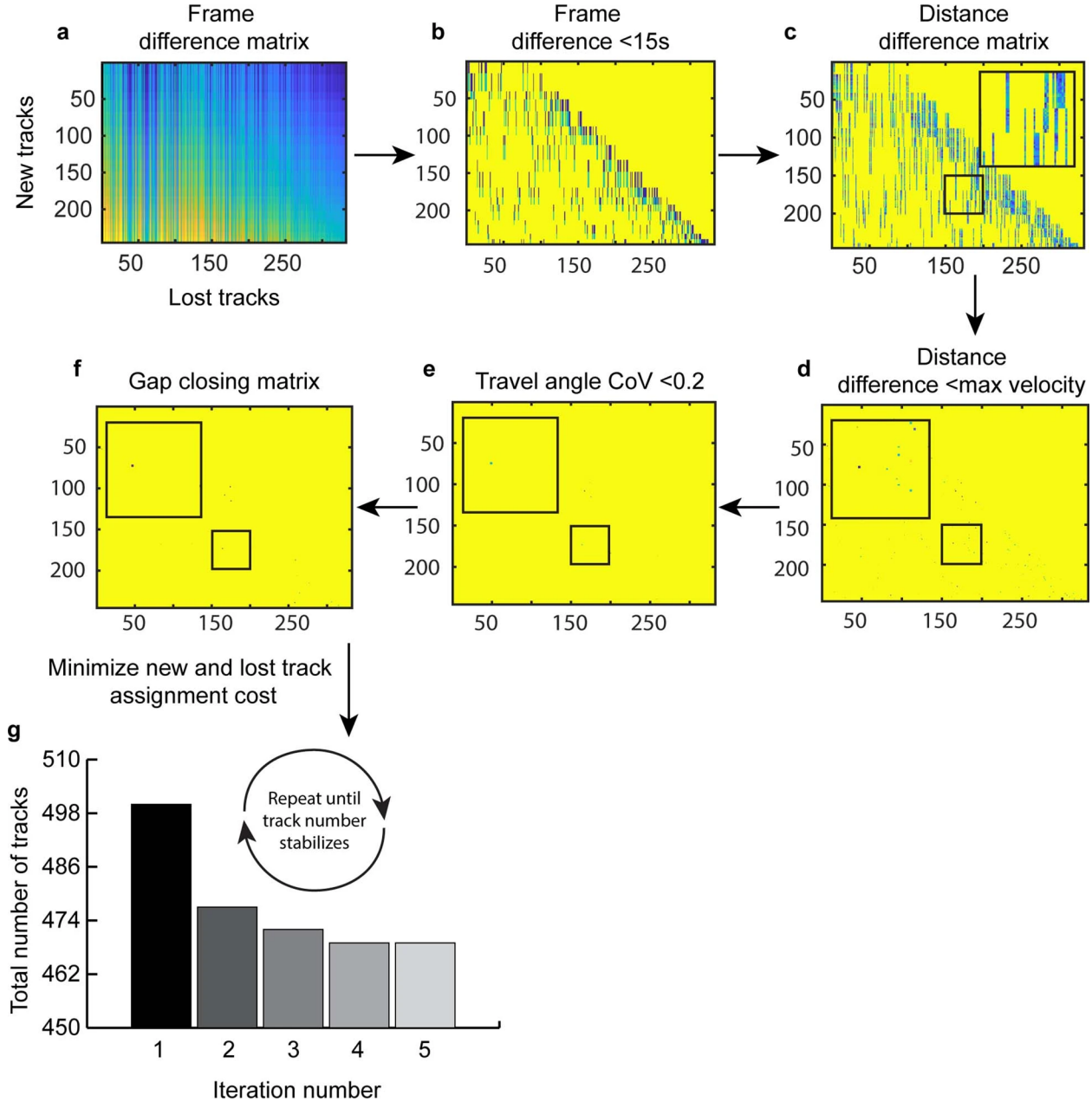


Figure 6.6: Flowchart for gap-closing scheme. **a**, A matrix of differences between all new tracks' first frame number and all lost tracks' last frame number. **b**, The frame difference matrix is thresholded based a maximum search time threshold of 15 seconds to create a mask. **c**, The mask is applied to the matrix of the intensity weighted centroid distances between the new tracks' first centroid position and last tracks' last centroid position. **d**, The distance matrix is thresholded based on the maximum velocity threshold of  $1 \mu\text{m/s}$ . **e**, Any gap closure resulting in a travel angle coefficient of variation under 0.2 is removed. **f**, The final masked gap closing matrix is produced, which is then globally minimized to assign new tracks with possible lost track candidates. **g**, The gap-closing scheme is repeated in its entirety until the total number of tracks stabilizes. In this example, it took 4 iterations to stabilize to 469 tracks.

in general tracking tasks, as compared with computational tracking methods [Dorn et al. (2008); Huth et al. (2010); Smal et al. (2008)].

We test Mitometer’s segmentation robustness with regard to the separation of adjacent mitochondria by simulating two parallel mitochondria with an applied Gaussian blur. We vary both the distance of their nearest pre-blur extrema and the signal-to-noise ratio (SNR), as defined by the mean intensity of the generated mitochondria divided by the standard deviation of the background. We separate out the algorithm’s detection into four categories: 0, 1, 2, and  $>2$  mitochondria found. In 3 independent trials, the segmentation algorithm faithfully recovers both mitochondria, even with low SNRs and separation distances, and performs better than existing segmentation routines (Fig. 6.7a and Appendix D.2).

We test Mitometer’s segmentation robustness with regard to the detection of mitochondria of varying sizes by simulating a  $5 \times 5$  grid of mitochondria while varying both the length of the major axis and the SNR. We separate out the algorithm’s detection into three categories:  $<25$ , 25, and  $>25$  mitochondria found. Mitometer’s segmentation algorithm recovers all 25 mitochondria in most cases of reasonable SNR, again outperforming competing routines (Fig. 6.7b and D.2).

Given that many mitochondrial dyes are sensitive to membrane potential, which may vary widely between mitochondria in a single cell, we also test Mitometer’s segmentation robustness with regard to detecting mitochondria of varying intensities. We simulate a  $5 \times 5$  grid of mitochondria in which each mitochondrion has a different intensity. We vary the range of intensities and the length of the major axis. Mitometer’s segmentation algorithm recovers all 25 mitochondria in most cases and detects at least 18 mitochondria in the most difficult tests, again outperforming almost all competing routines (Fig. 6.7c and D.2).

We validate Mitometer’s tracking robustness by simulating mitochondria under four conditions of increasing densities. We also vary the delay time between each frame, to produce larger and smaller mitochondrial displacements between frames. In all cases, the number of potential track assignments for each mitochondrion is greater than 1 and increases as the

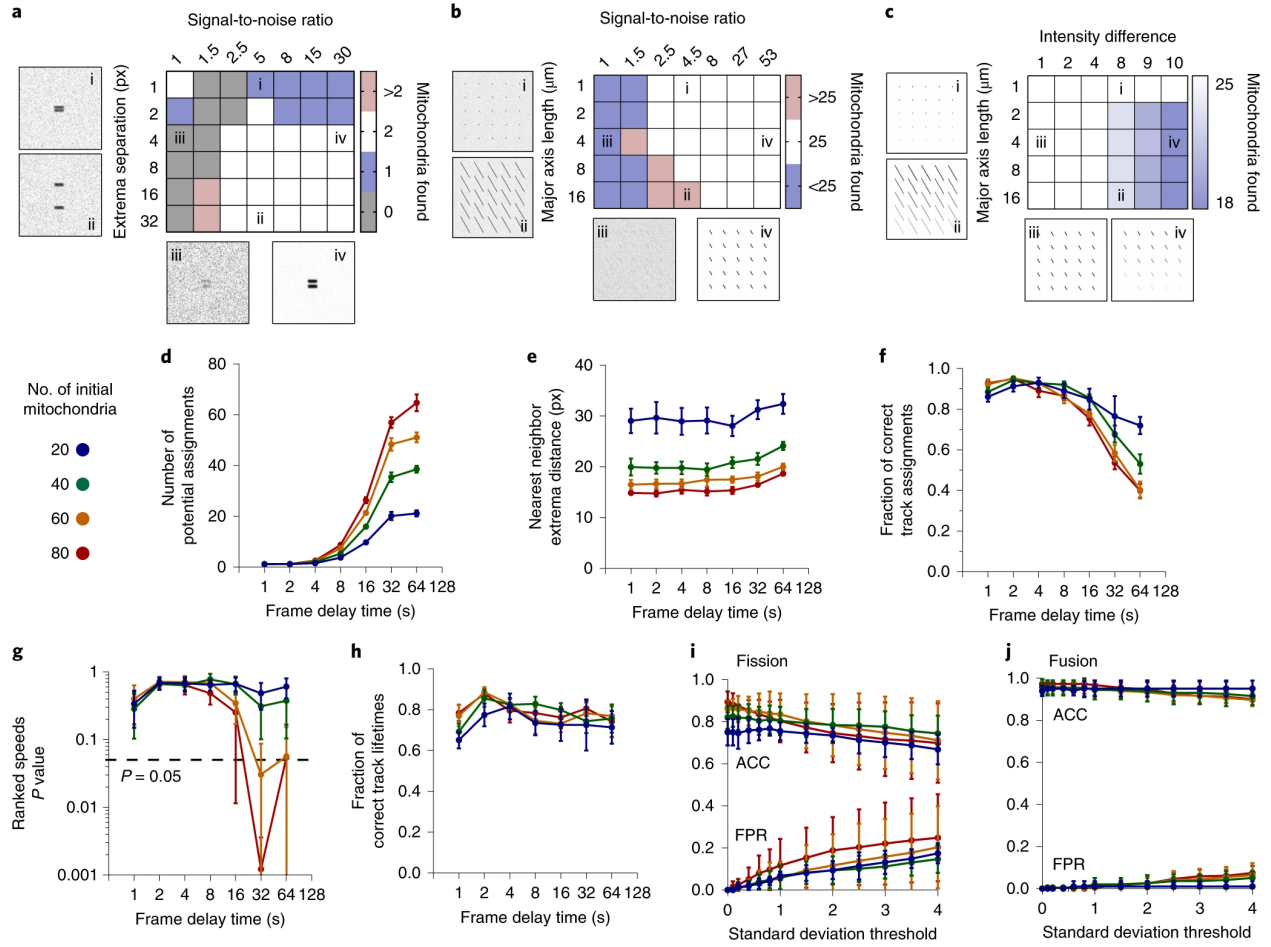


Figure 6.7: In silico validation of mitochondria segmentation and tracking algorithms. **a**, Two adjacent mitochondria are simulated at increasing separations and signal-to-noise ratios. The median number of mitochondria recovered by the segmentation algorithm is shown. **b,c**, A grid of 25 mitochondria is simulated at increasing major axis lengths and signal-to-noise ratios (**b**) or intensity differences (**c**). **d–j**, The mean number of mitochondria recovered by our segmentation algorithm is shown. Twenty (blue), 40 (green), 60 (orange) or 80 (red) mitochondria are simulated in the center quarter of a  $512 \times 512$  image in two dimensions with a pixel size of  $0.138 \mu\text{m}$ . The mean number of potential assignments of individual mitochondria (**d**) and mean distance to their nearest neighbor (**e**) are shown. The performance of the tracking algorithm compared with ground truth values is quantified by its ability to correctly assign tracks (**f**), the rank sum P value of the mitochondrion speeds between the algorithm and the ground truth (two-sided Wilcoxon rank sum test) (**g**), and the fraction of tracks with correct lifetimes (**h**). The mitochondria are then allowed to undergo fission and random appearance (**i**) or fusion and random disappearance (**j**), and the algorithm is quantified in its classification ability according to accuracy (ACC) and false-positive rate (FPR). **d–j**, Data are given as the mean and 95% confidence interval. **a–c**,  $n=3$  independent trials; **d–h**,  $n=10$  independent trials; **i,j**,  $n=5$  independent trials.

frame delay time increases, as expected (Fig. 6.7d). We confirm that the average nearest neighbor distance decreases as we increase the density of mitochondria, and increases only slightly for increasing frame delay times as the mitochondria move out from the center of the field where they are generated (Fig. 6.7e). We quantify Mitometer’s performance based on three important metrics, as compared with ground truth values: the fraction of correct assignments between mitochondria in adjacent frames, the rank sum P value of the mitochondrion speeds between our algorithm and the ground truth, and the fraction of correct lifetimes of the mitochondrial tracks (Fig. 6.7f–h). Mitometer performs well in all three metrics at reasonable frame delay times, and outcompetes existing techniques, but drops steadily at high frame delays (D.3). The increase in nearest neighbor distance probably accounts for the increase in the ranked speeds P value at the longest delay time, which is also seen in other tracking software.

We further validate Mitometer’s ability to correctly identify fission and fusion events. As described previously, Mitometer’s algorithm compares the track areas before and after fission or fusion and adds a track as a candidate if the area difference is below 1 standard deviation. We tested the algorithm’s ability to detect fission and fusion in these simulated conditions with different standard deviation classifications. Mitometer’s algorithm had a high classification accuracy and rarely labeled false-positive events at standard deviations below 1 (Fig. 6.7i,j). As expected, the algorithm performed worse as we increased the standard deviation threshold, and allowed more events to be classified as fission or fusion.

### 6.3.4 In vitro validation of segmentation and tracking algorithms

Although in silico experiments are useful when ground truth data are not available, the full characteristics of a complex system in living cells cannot yet be fully represented in a simulation. Thus, we also validate Mitometer in live mammalian cells.

To validate segmentation robustness in vitro, we compare morphologies of mitochondria in three cell types with differing basal mitochondrial morphologies labeled with tetram-

ethylrhodamine methyl ester perchlorate (TMRM): neoblastic pheochromocytoma 12 cells with circular mitochondria, non-small cell lung carcinoma H1299 cells with intermediately elongated mitochondria, and human foreskin fibroblast (HFF) cells with highly elongated mitochondria (Fig. 6.8a). We compare elongation by quantifying differences in the ratio of the minor axis to the major axis lengths of individual mitochondria. A higher ratio indicates more circular mitochondria, with 1 being a perfect circle. The segmentation algorithm was able to capture the differences in elongation between these three cell types across all tested microscope systems, including an LSM 710 and 880 (Zeiss), Eclipse Ti-E (Nikon), FluoView 1000 (Olympus) and IX83 (Olympus) in total internal reflection fluorescence (TIRF) mode and widefield mode (Fig. 6.8b). We further validate the segmentation efficiency at differing full well depth and read noise root mean square values by adding artificial Poissonian and Gaussian noise to the time lapses in the same three cell lines. We compared area values to the original time lapse and found that the algorithm performs with high precision at typical detector parameters, and only begins to fail for extremely poor-quality detectors (Fig. 6.9a).

To validate the tracking robustness in cultured cells, we use nocodazole to inhibit mitochondrial motion in the same three cell lines [Vasquez et al. (1997)]. Nocodazole is a well-studied drug that destabilizes microtubules and inhibits their polymerization, thereby disrupting the physical structures used for mitochondrial movement [Heggeness et al. (1978)]. As expected, mitochondrial speed in all cell lines dramatically decreased with nocodazole treatment (Fig. 6.8c). We validate the tracking efficiency by adding artificial Poissonian and Gaussian noise. We compared mitochondrial speed with the original time lapse and found that the algorithm again only begins to fail at values of extremely poor-quality detectors (Fig. 6.9b).

Finally, to validate the fission and fusion detection robustness in vitro, we use known inducers of fission and fusion and quantify the dynamic events of the cells before and after treatment in a time-dependent manner. For these experiments, we use 10  $\mu$ M oligomycin to induce fission, and nutrient starvation using Hank’s balanced salt solution (HBSS) to induce



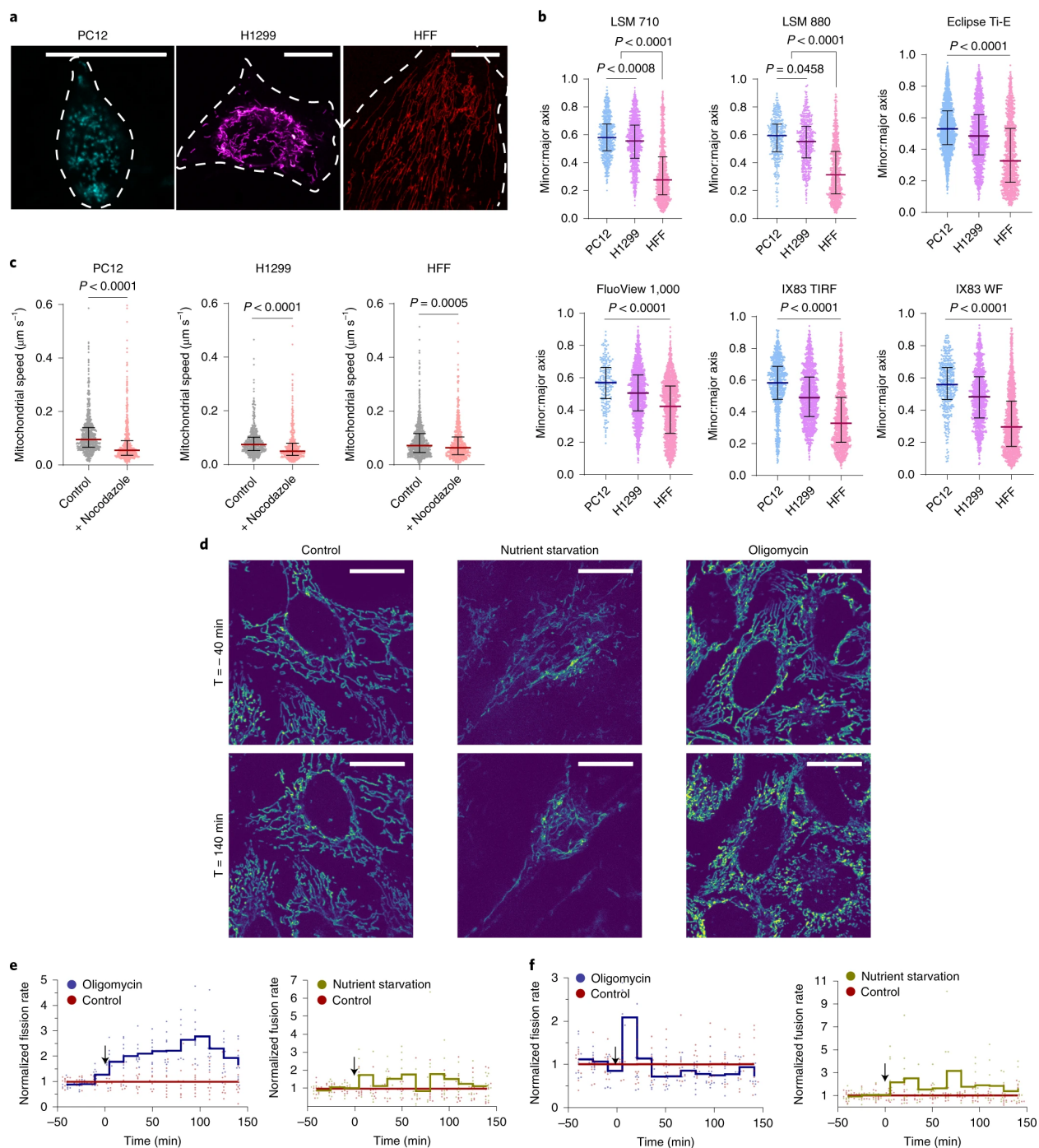


Figure 6.8: In vitro validation of mitochondria segmentation and tracking algorithms. **a**, PC12, H1299 and HFF cells labeled with TMRM. **b**, Minor:major axis ratios of each cell line for various microscopes. **c**, The median mitochondrial speeds of before and after treatment with 10  $\mu$ M nocodazole. **d**, HeLa (control, oligomycin) or MEF (nutrient starvation) cells 40 min before (top row) or 140 min after (bottom row) no treatment (control), nutrient starvation, and treatment with 10  $\mu$ M oligomycin and their corresponding fission and fusion rates **e,f**. Scale bars, 20  $\mu$ m.



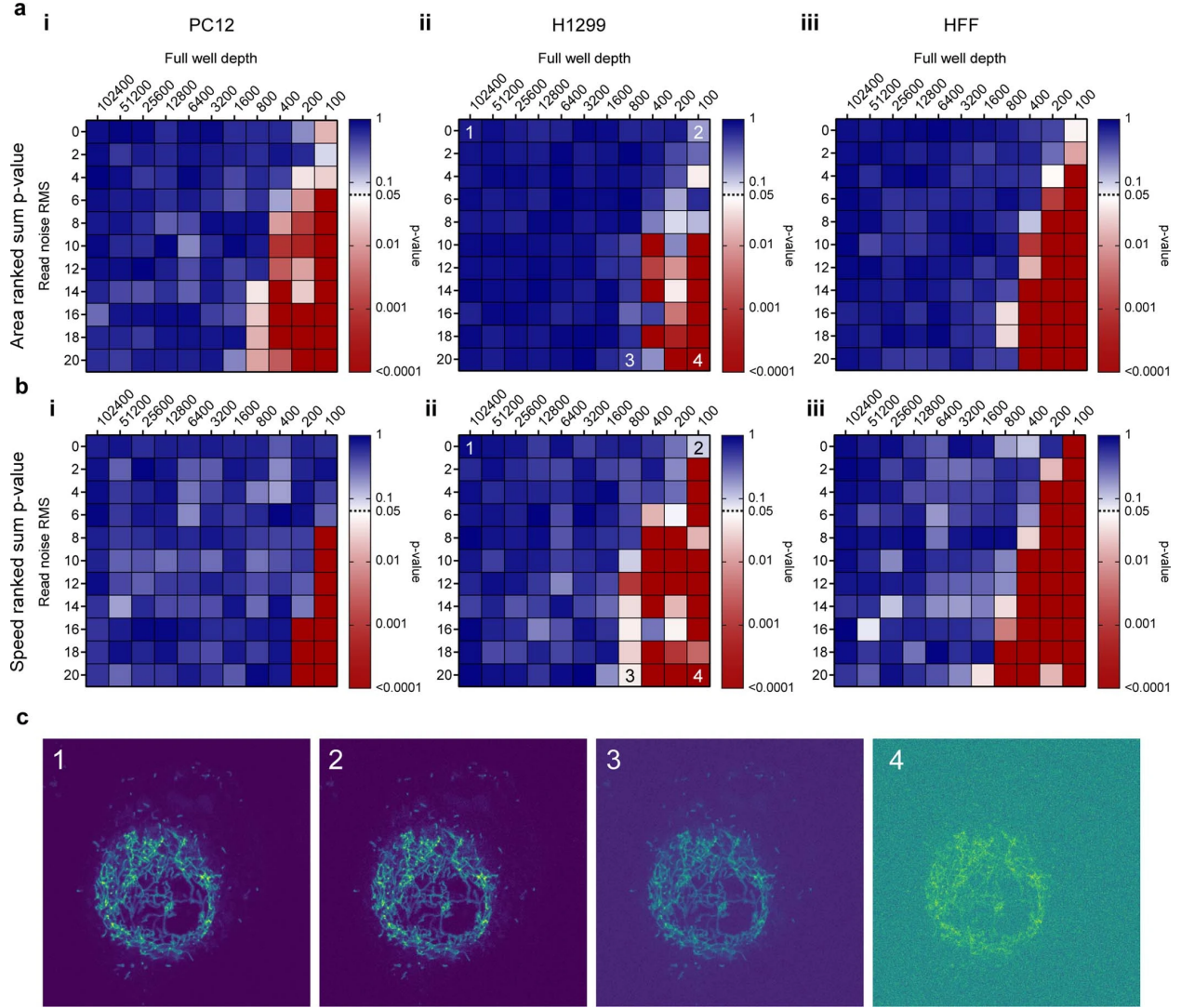


Figure 6.9: Live-cell time lapse images with added noise. The comparison of area (a) and speed (b) of mitochondria in live-cell time lapse images of PC12 (i), H1299 (ii), and HFF (iii) cells between the original image and images with added noise to simulate a lower full well depth (Poissonian noise) and higher read noise root mean square (RMS) value (Gaussian noise). Comparisons are done via a two-sided Wilcoxon rank sum test. c, Representative images of TMRM labelled H1299 cells with simulated noise corresponding to the numbers in panels ii.  $n=3$  time lapse images per cell line.

fusion [Leonard et al. (2015); Rambold et al. (2011)]. We chose to use TMRM-labeled Henrietta Lacks (HeLa) cervical cancer cells and mouse embryonic fibroblast (MEF) cells because both cell lines have been previously validated to respond to nutrient starvation in an expected manner (Fig. 6.8d)[Gomes et al. (2011); Rambold et al. (2011)]. To account for variability in the number of mitochondria in various cells, we normalize each time point’s fission and fusion events to the average number of events in the three time points acquired before treatment. We then compare these events by normalizing to the controls’ events at each time point. We successfully validate in both MEF and HeLa cells an increase in fission and fusion events after treatment with oligomycin or HBSS (Fig. 6.8e,f).

Together, these experiments confirm Mitometer’s robustness and verify the ability of Mitometer’s algorithm to properly segment, track and identify fission and fusion events in mitochondria.

### 6.3.5 Mitochondrial features may predict breast cancer subtype

Mitometer enables us to quantify and compare mitochondrial morphology, motility and dynamics in both 2D and 3D images of mitochondria. We demonstrated these capabilities through a comprehensive analysis of TMRM-labeled mitochondria in a wide panel of breast cells, including five primary normal breast epithelial cell lines from reduction mammaplasties of five different individuals (patients 72, 76, 08, 99, 97), two ER/PR+ breast cancer cell lines (MCF-7, T-47D), three TNBC cell lines (MDA-MB-231, MDA-MB-468, BT-549) and two TNBC PDX cell lines [DeRose et al. (2011)] (HCI-010, HCI-002), all of which are detailed in the supplementary materials (Appendix Table D.6). We cultured all these cell lines in a Matrigel-embedded 3D spheroid environment, as previously established [Ma et al. (2020)], as well as an additional 2D culture environment for the two ER/PR+ lines (MCF-7, T-47D) and three TNBC lines (MDA-MB-231, MDA-MB-468, BT-549) (Fig. 6.10a,b, 6.11).

We compared mitochondria of breast cancer categories (normal epithelia, ER/PR+ and TNBC) in their respective 3D and 2D environments, and also compared mitochondria be-

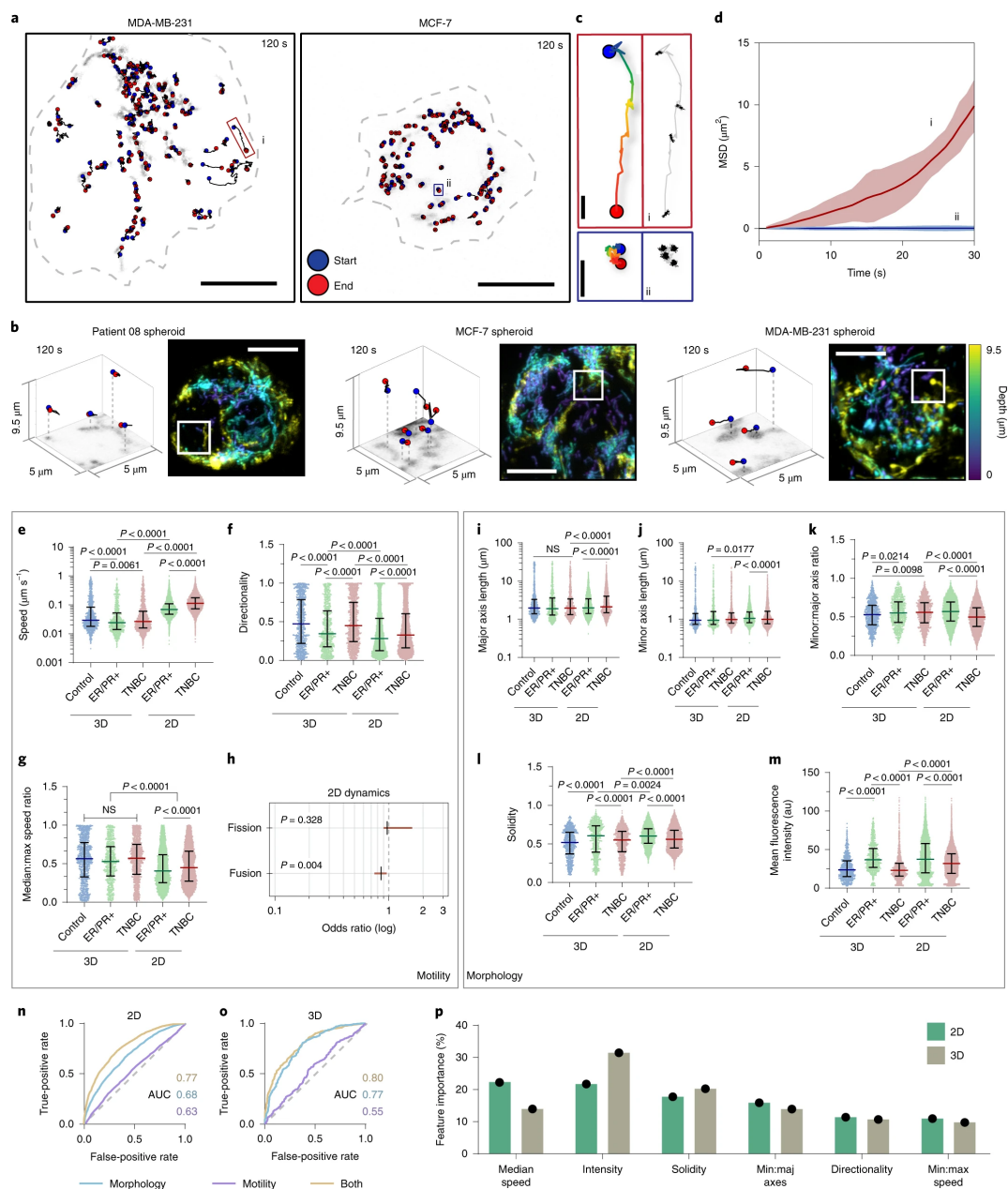


Figure 6.10: Motility and morphology differences in mitochondria of normal breast epithelial cells and breast cancer cells. **a**, Tracks of mitochondria stained with TMRM. **b**, Tracks and corresponding z-stack time-lapse images of TMRM fluorescence in spheroids. **c**, A single mitochondrial track (left) of an MDA-MB-231 (top) and MCF-7 (bottom) cell with morphology shown overlaid, downscaled 10-fold relative to the track length. **d**, A mean-squared displacement (MSD) graph of the tracks (i) and (ii) shown in **a** and **b**. **e–m**, Morphology and motility comparisons of normal primary epithelial cells (control 1–5), ER/PR+ cells (MCF-7, T-47D) and TNBC PDX cells and cell lines (HCI-010, HCI-002, MDA-MB-231, MDA-MB-468, BT-549) in 3D and 2D environments. **n,o**, ROC curves of random forest classifications between mitochondria from ER/PR+ cells and TNBC cells in 2D (**n**) and 3D (**o**) environments. **p**, Feature importances. Scale bars, 20  $\mu\text{m}$  (**a**), 10  $\mu\text{m}$  (**b**) and 1  $\mu\text{m}$  (**c**).

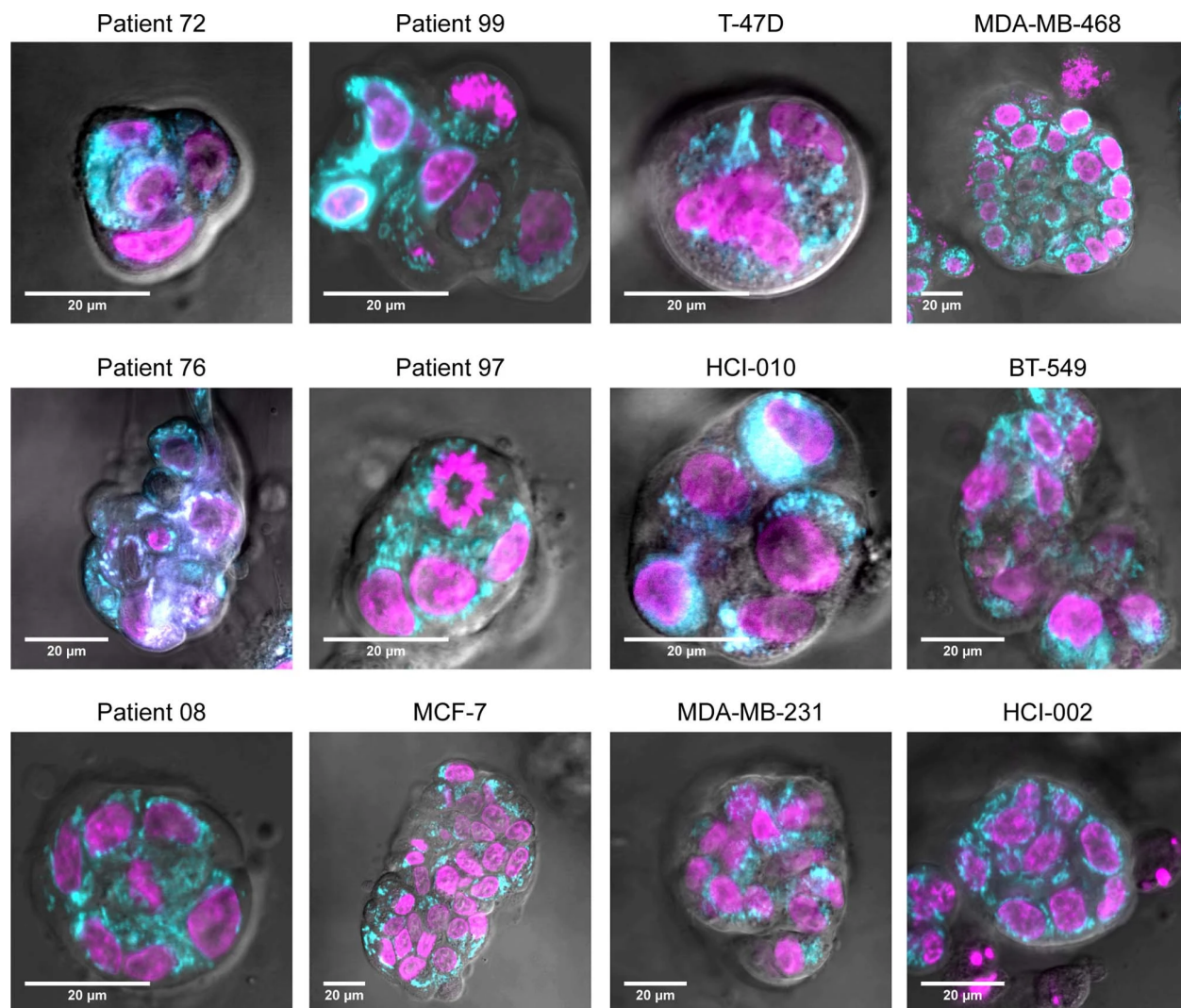


Figure 6.11: Three-dimensional spheroid cultures. **a**, Representative images of human reduction mammoplasty samples (Patient 72, Patient 76, Patient 08, Patient 99, Patient 97), established breast cancer cell lines (MCF-7, T-47D, MDA-MB-231, MDA-MB-468, BT-549), and patient derived xenografts (HCI-010, HCI-002) embedded in Matrigel and grown in three-dimensional spheroid culture. Gray = brightfield, cyan = mitochondria fluorescence (TMRM), pink = nuclear fluorescence (NucBlue).



tween 3D and 2D environments in their respective breast cancer categories, using Mitometer. We construct tracks of 3D and 2D mitochondrial displacement while retaining morphological information of every mitochondrion in each frame (Fig. 6.10c). Simple comparisons of the mean-squared displacement of individual mitochondria show large heterogeneity across cell types (Fig. 6.10d). We analyzed three motility parameters in each individual mitochondrion across all cell lines and environments: their median speed, their directionality (calculated as the maximum displacement divided by the total distance traveled), and the ratio of the median to the maximum speed (suggesting the propensity for mitochondria to have bursts of motion) (Fig. D.7). To remain cell size agnostic when constructing the models, instead of using total displacement or distance traveled, we use our directionality metric by dividing the maximum displacement of a track by its total distance traveled (a value necessarily constrained between 0 and 1). In 3D cultures, mitochondria are slower and more directional, with a lower propensity for bursts of motion than their 2D groups (Fig. 6.10e–g). Interestingly, this phenomenon is consistent at the cellular level during cell migration, in which 3D cultures move slowly but more directionally than their 2D counterparts [Wu et al. (2014)]. Additionally, at the 3D level, mitochondria in breast cancer cells are significantly slower than those of normal breast epithelia, hinting at mitochondrial dysregulation within the cancerous conditions. We also compared the fission and fusion occurrences in 2D cell cultures and noted a lowered odds ratio of fusion, but not fission, in TNBC cells compared with ER/PR+ cells (Fig. 6.10h). Interestingly, the suppression of mitochondrial fusion in TNBC cells has been shown to enhance breast cancer cell migration and invasion [Zhao et al. (2013)]. The results hint at an involvement of mitochondrial dynamics in the increased aggressiveness seen in cases of TNBC compared with cases of ER/PR+ breast cancer. We further analyzed five morphological parameters: the length of mitochondrial minor axes, the length of the major axes, their ratio (which gives the sphericity of the mitochondria), the solidity (calculated as the ratio of the volume of individual mitochondria to their convex hull, which gives information on how branched the mitochondria are), and the mean TMRM fluorescence intensity

in individual mitochondria (which gives information on the membrane potential) (Fig. D.7) [Walker (2013)]. In general, ER/PR+ cells have mitochondria that are less networked and which have higher membrane potentials compared with TNBC mitochondria, but are more rounded only in 2D cultures (Fig. 6.10i–m). However, there seems to be large heterogeneity in mitochondrial membrane potential and solidity between cell lines, even in the same cancer subtypes, necessitating more in-depth analysis, which is beyond the scope of this paper (Fig. D.8). Interestingly, TNBC mitochondria are more similar in all parameters to normal breast epithelial mitochondria than to ER/PR+ mitochondria in 3D cultures. Together, these results reinforce a role for mitochondria in breast cancer aggressiveness through the modulation of specific morphological and motile mechanisms, and reaffirm the importance of culture environment for the study of cellular processes.

We are also able to predict with high accuracy whether a mitochondrion belongs to an ER/PR+ cancer cell or to a TNBC cell in both 2D and 3D environments. We used a random forest classification through Python’s Scikit-learn with a 70:30 train : test split on 8,065 ER/PR+ and 15,022 TNBC mitochondria in the 2D environment, and 670 ER/PR+ and 1,320 TNBC mitochondria in the 3D environment. For classification, we used either morphological characteristics, motility characteristics, or both combined (Tables D.10, D.11, and Fig. D.9) [Pedregosa et al. (2011)]. We achieve an area under the curve (AUC) of the receiver operating characteristic (ROC) curves of above 0.5 in all cases, with the best AUCs of 0.77 and 0.80 for 2D environments and 3D environments, respectively, resulting from the combination of morphological and motility characteristics as an input for predicting mitochondria from ER/PR+ and TNBC subtypes (Fig. 6.10n,o). The random forest classifier also assesses the feature importance, with median speed ranking highest in the case of the 2D environment, and intensity ranking highest in the case of the 3D environment (Fig. 6.10p).

### 6.3.6 Metabolism of single mitochondria

We also used Mitometer to analyze the metabolism of single dynamic mitochondria in live normal breast epithelial, ER/PR+ and TNBC cells. We make use of a well-established technique, the phasor approach to the fluorescence lifetime imaging (FLIM) of intrinsically fluorescent and endogenously expressed NADH, to quantify metabolic alterations [Bird et al. (2005); Digman et al. (2008); Stringari et al. (2011)]. We labeled the mitochondria of the cells with 100 nM TMRM, a concentration lower than those that affect mitochondrial respiration [Scaduto and Grotyohann (1999)]. We collected NADH and TMRM fluorescence in two separate detectors while simultaneously acquiring FLIM data from the NADH emission in the frequency domain (Appendix D.15). We use the rule of linear addition of two components to calculate the fraction of bound NADH (NADH<sub>b</sub>) of each mitochondrion that is tracked for at least 20 frames (Fig. 6.12a). A much more detailed explanation of the use of the rule of linear addition for calculating NADH fractions can be found in our previous work [Stringari et al. (2011)]. We find that mitochondrial NADH<sub>b</sub> in each breast cell subtype follows a normal distribution, but that normal breast epithelial cells have a significantly lowered mean NADH<sub>b</sub> than that of breast cancer cells (Fig. 6.12b,c). We also find that these normal cells have more variation in their NADH<sub>b</sub> compared with cancerous breast cells, as calculated using the CoVs (Fig. 6.12d). We further analyze how mitochondrial motility and morphology parameters correlate with respect to mitochondrial NADH<sub>b</sub> (Fig. 6.12e). Again, to ensure that we remain cell size agnostic when deriving correlations between mitochondrial parameters and bound NADH values, we analyze mitochondria only within the same cell, rather than correlating these values in bulk across all samples. This also allows us to account for natural variations in both TMRM labeling efficiency and basal NADH fractions between different cells. We find few significant correlations in any parameters in normal breast epithelial cells, except for a small positive correlation in perimeter and a negative correlation in solidity. By contrast, mitochondria in both ER/PR+ and TNBC cancer cells had highly significant correlations in a wide array of parameters. Most notably,

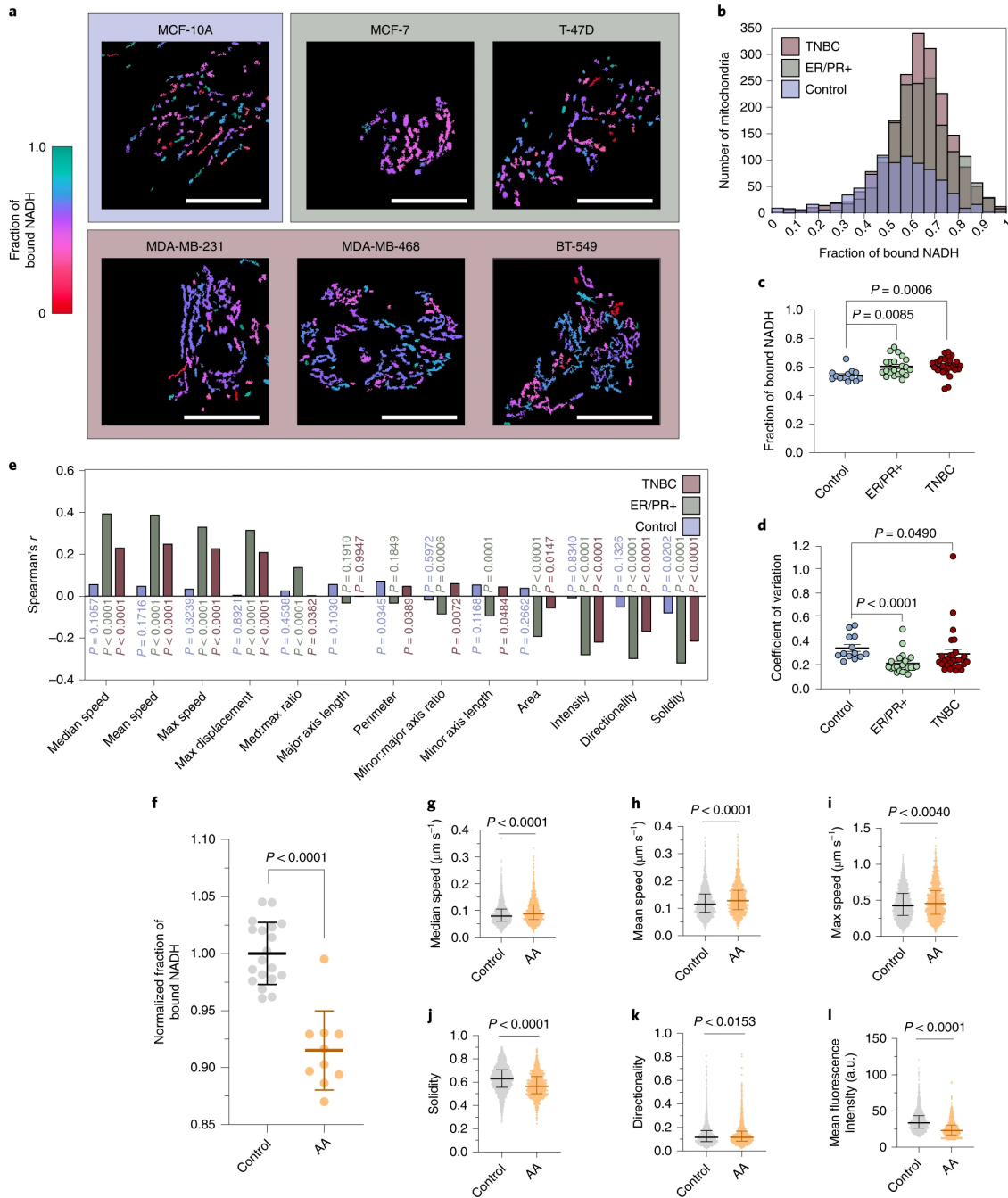


Figure 6.12: Cancer-specific metabolic heterogeneity in single mitochondria. **a**, TMRM-labeled mitochondria. Scale bars, 20  $\mu\text{m}$ . **b**, Histogram distributions of the mitochondrial fraction of bound NADH of normal, ER/PR+ and TNBC cells. **c**, The mean fraction of bound NADH of each cell type's mitochondria. **d**, The coefficients of variation of bound NADH for each cell type. **e**, Spearman's correlation coefficient ( $r$ ) between bound NADH and the mitochondrial parameters of motility and morphology for each cell type. **f-l**, Normalized fraction of NADHb in control (gray) and antimycin A (AA)-treated (orange) cells (**f**), along with morphological and motility features (**g-l**).



mitochondria in breast cancer cells had positive correlations of NADHb with mitochondrial speed and displacement, and negative correlations of NADHb with solidity, directionality and TMRM intensity. Interestingly, mitochondria in ER/PR+ cancer cells had higher correlation coefficients than those in TNBC cells in every tested parameter. These results suggest an association between changes in mitochondrial metabolism and changes in mitochondrial motility and morphology in breast cancer cells, but not in normal breast epithelial cells, and may identify therapeutic vulnerabilities to specifically target breast cancer cells. To determine if these feature differences are brought about due to changes in metabolism, we treated MDA-MB-231 cells with 5  $\mu$ M antimycin A, an inhibitor of mitochondrial electron transport chain complex III. Treatment induced a lowering of cell-wide NADHb as expected (Fig. 6.12f). We then performed an analysis of the three most positively and negatively NADHb-correlated mitochondrial parameters. Surprisingly, antimycin A treatment led to an increase in mitochondrial median, mean and maximum speeds, and decreases in solidity, directionality, and mean fluorescence intensity, all of which are the inverse of the calculated correlations with NADHb (Fig. 6.12g–l). This suggests that mitochondrial motility and morphological features do not directly depend on NADHb and that instead, specific mitochondria in individual cells are modulated to perhaps serve specific metabolic needs. This also represents an analysis of metabolic alterations in relation to mitochondrial motility and morphology at the level of the single mitochondrion in living cells.

## 6.4 Discussion

Mitometer is an efficient resource for quickly and accurately analyzing morphological and motility features of mitochondria that eliminates the need for time-consuming and biased user intervention. We optimize and automate segmentation techniques to maintain the integrity of mitochondrial morphology for object-based tracking. The minimization scheme used for tracking allows for computational efficiency and an accurate and automated track

construction process. Furthermore, the use of an object-based tracking method allows for determination of fission and fusion events via comparison of mitochondrial volumes. Simulations and experiments with cell lines of heterogeneous mitochondria, nocodazole, and fission- and fusion-inducing agents validated the robustness of the algorithms. Validation experiments confirmed the robustness of the algorithms, with cases of failure occurring only at low SNRs (1.5) and low mitochondrial separation (2 pixels), and for simulated parameters of especially poor (800 full well depth) detectors.

We have demonstrated Mitometer’s ability to detect small but important differences in morphology and motility in the mitochondria of TNBC, ER/PR+, and normal breast cells in clinically relevant PDX TNBC models, primary mammary cells, and well-established breast cancer cell lines. These results will have important implications for the understanding of how mitochondria are recruited to the invading edges of cells to fuel invasion and metastasis [Caino et al. (2016)]. Moreover, we were able to integrate Mitometer with other fluorescence-based measurements by combining mitochondrial analysis with FLIM of NADH. Mitometer identified heterogeneity and trends in mitochondrial dynamics and morphology in relation to the bioenergetics of mitochondrial populations in varying metabolic states, which was particularly evident in breast cancer cells compared with non-cancerous mammary epithelial cells. These results suggest that specific subsets of mitochondria serve to regulate tumorigenic metabolism, and will lead to important insights into how these organelles drive tumor progression. This study critically depended on object-based tracking to quantify NADH lifetime values of individual mitochondria instead of individual pixels in an averaged fluorescence image stack. Additionally, Mitometer’s ability to build tracks with accurate track lifetimes allowed sufficient FLIM data to be averaged through the image stack for each mitochondrion to reliably quantify its fraction of bound NADH.

We hope Mitometer will encourage the widespread dissemination of mitochondrial morphological and motility feature datasets, which would allow the use of deep learning techniques to improve unbiased and situation-specific segmentation and tracking. Additionally, Mito-

meter currently requires a time-lapse image for automated segmentation, which presumably can be overcome with data-driven machine learning techniques and would be advantageous for morphology-only analyses.

This pipeline, which features a simple and intuitive user interface and ImageJ compatibility, is accessible to any cell biologist with the ability to acquire fluorescence images. Mitometer may be adapted to a variety of other applications for which segmentation and tracking of variably sized objects in a noisy image is required, including but not limited to other organelles and intracellular structures. The further integration of Mitometer with other mitochondria-localizing probes, such as intracellular oxygen sensors [Will et al. (2006)], temperature sensors [Arai et al. (2015)] and pH sensors [Lee et al. (2014)], opens the door to many additional exciting avenues for the investigation of biologic and, more specifically, metabolic alterations at the level of the single mitochondrion in live cells and animal models.

## 6.5 Methods

### 6.5.1 Primary human mammary tissue dissociation and processing

Human reduction mammoplasty samples were obtained with informed consent through the Cooperative Human Tissue Network (CHTN) under the approved institutional review board protocol UCI 17-05. Tissue samples were processed as previously reported<sup>56</sup>. In brief, human mammary tissues were washed in PBS, mechanically dissociated with scalpels, digested with 2 mg

ml<sup>-1</sup> collagenase type I (Life Technologies, 17100-017) in DMEM with 5 % FBS at 37 °C overnight on a shaker, treated with DNase I (Worthington Biochemical, LS002139) and subjected to three pulse centrifugations to 500×g. Supernatants were then collected and centrifuged for 5 min at 500×g to isolate primary mammary fibroblasts, and pellets contain-

ing mammary epithelial organoids were digested with trypsin (Corning, 25-052-CI) for 10 min at 37 °C to generate single-cell suspensions of primary mammary epithelial cells. Cells were filtered through a 70  $\mu$ m strainer.

### 6.5.2 Collection and processing of PDX tumors

All tissue samples were collected with informed consent from individuals being treated at the Huntsman Cancer Hospital and the University of Utah. Samples were collected and de-identified by the Huntsman Cancer Institute Tissue Resource and Application Core facility before being obtained for implantation under a protocol approved by the University of Utah Institutional Review Board. We were able to obtain human reduction mammoplasty samples under the approved institutional review board protocol UCI 17-05. HCI-010 and HCI-002 PDX tumors [DeRose et al. (2011)] were established and grown in NSG mice purchased from The Jackson Laboratory. Animals were maintained in a pathogen-free facility and animal procedures were approved by the University of California, Irvine, Institutional Animal Care and Use Committee. After 3–6 months of growth, PDX tumors were collected, mechanically dissociated, digested with 2 mg ml<sup>-1</sup> collagenase type IV (Sigma-Aldrich, C5138-1G) in DMEM with 5 % FBS at 37 °C for 45 min on a shaker. Digested tumors were washed with PBS, treated with DNase I (Worthington Biochemical, LS002139) and dissociated to single cells with trypsin (Corning, 25-052-CI). PDX cells were filtered through a 70  $\mu$ m strainer.

### 6.5.3 Primary and PDX cell culture

Primary mammary epithelial cells and HCI-010 and HCI-002 PDX cells were grown in 3D spheroid culture as previously described [Ma et al. (2020)]. In brief, approximately  $7 \times 10^4$ – $1 \times 10^5$  cells were embedded in Corning Matrigel Growth Factor Reduced Matrix (Corning, 354230) and cultured on 35 mm glass-bottom imaging dishes in EpiCult Medium (StemCell Technologies, 05610) supplemented with 5 % FBS, 10 ng ml<sup>-1</sup> human epidermal growth

factor (PeproTech, AF-100-15), 10 ng ml<sup>-1</sup> basic fibroblast growth factor (PeproTech, 100-18B) and 1 % penicillin–streptomycin (Hyclone, SV30010) for 4–7 d at 37 °C at 5 % CO<sub>2</sub> before imaging.

#### **6.5.4 Three-dimensional culture of cell lines**

Cell lines were embedded in Corning Matrigel Growth Factor Reduced Matrix (Corning, 354230) using seeding densities of between  $5 \times 10^4$  and  $1 \times 10^5$  cells. Embedded cells were grown in 3D spheroid culture on 35 mm glass-bottom imaging dishes in DMEM supplemented with 10 % FBS and 1 % penicillin–streptomycin (Hyclone, SV30010) for 4–7 d at 37 °C at 5 % CO<sub>2</sub> before imaging.

#### **6.5.5 Two-dimensional culture of cell lines**

Cell lines were plated on 10  $\mu$ g ml<sup>-1</sup> fibronectin-coated 35 mm glass-bottom imaging dishes in DMEM supplemented with 10 % FBS and 1 % penicillin–streptomycin (Hyclone, SV30010) or, in the case of MCF-10A cells, DMEM/F12 media supplemented with 5 % horse serum, 20 ng  $\mu$ l<sup>-1</sup> epidermal growth factor (PeproTech, AF-100-15), 0.5 mg ml<sup>-1</sup> hydrocortisone (Sigma, H0888), 100 ng ml<sup>-1</sup> cholera toxin (Sigma, C8052), 10  $\mu$ g ml<sup>-1</sup> insulin (Sigma, I1882) and 1 % penicillin–streptomycin (Hyclone, SV30010) at 37 °C at 5 % CO<sub>2</sub> before imaging.

#### **6.5.6 TMRM studies**

For TMRM experiments, 2D and 3D cell cultures in imaging dishes were incubated with 100 nM TMRM for 15 min without washout, immediately followed by imaging.

### 6.5.7 Nocodazole studies

For in vitro nocodazole validation studies, 100 nM TMRM was added to cells for 45 min, followed by the addition of nocodazole at a final concentration of 10  $\mu$ M. The treatment was applied for 1 h without washout, immediately followed by imaging.

### 6.5.8 Fission and fusion studies

Cells were first treated with 100 nM TMRM for 45 min, and immediately imaged for 1 min time lapses at 15 min intervals for 40 min. To induce mitochondrial fission, 10  $\mu$ M oligomycin was added to the medium. To induce mitochondrial fusion, the media was replaced with phenol red-free HBSS with 10 mM HEPES. Cells were then again imaged for 1 min time lapses at 15 min intervals for 140 min.

### 6.5.9 Mitochondria and fluorescence lifetime imaging

For nocodazole and MEF fission and fusion studies we performed experiments on an LSM 880 (Zeiss), and for HeLa fission and fusion studies on an LSM 710 (Zeiss) inverted laser scanning confocal microscope with a 63 $\times$ , numerical aperture 1.4, oil-immersion objective, at a frame size of  $512 \times 512$  pixels, with a pixel size of 138 nm, and at a rate of 1 frame per second for 30 s.

For 2D and 3D TMRM studies we performed experiments on a Zeiss LSM 710 inverted laser scanning confocal microscope with a 40 $\times$ , numerical aperture 1.2 water-immersion objective. In the 2D studies we used a frame size of  $512 \times 512$  with a pixel size of 87.9 nm and at a rate of 1 frame per second for 120 frames. In the 3D studies we used a frame size of  $256 \times 256$  with a pixel size of 105.4 nm and at a rate of 1 stack every 10 s, with 21 z-planes per stack at a distance of 450 nm between planes. In both cases, we used a two-photon titanium : sapphire laser (Spectra-Physics, MaiTai) to excite the TMRM at a wavelength of 820 nm, which was passed through a 690 nm dichroic filter. The fluorescence emission in

the range of 520–700 nm was captured through the microscope’s internal detector. The cells were kept under biological conditions through the imaging. Images were converted to TIFs in ImageJ v1.53c.

For FLIM of NADH studies, we performed experiments on a Zeiss LSM 710 inverted laser scanning confocal microscope with a 63 $\times$ , numerical aperture 1.4, oil-immersion objective at a frame size of 256  $\times$  256 with a pixel size of 180 nm and at a rate of 0.398 frames per second for varying numbers of frames. The cells were excited at approximately 2 mW at the plane of excitation with a two-photon titanium : sapphire laser (Spectra-Physics, MaiTai) at 740 nm, which was passed through a 690 nm dichroic filter. The fluorescence emission was separated through two bandpass filters, a 460/80 nm filter for NADH fluorescence emission and a 641/75 nm filter for TMRM fluorescence emission, and was then detected using two separate photomultiplier tubes (Hamamatsu, H7422P-40). The fluorescence lifetime decays were captured in the frequency domain via an A320 FastFLIM box (ISS) and calibrated using SimFCS v4 developed at the Laboratory for Fluorescence Dynamics at the University of California, Irvine. Coumarin-6 in ethanol, with a known single exponential fluorescence lifetime of 2.5 ns, was imaged on each day of imaging and was used as the calibration sample for the instrument response time. The cells were kept under biological conditions through the imaging.

### **6.5.10 Statistical testing**

Random forest classification was implemented using the scikit-learn package in Python. All other statistical analyses were done using Graphpad Prism v7.

## **6.6 Reporting Summary**

Further information on research design is available in the Nature Research Reporting Summary linked to this article.

## 6.7 Data availability

The authors declare that all data supporting the findings of this study are available in the article and its supplementary information files or from the corresponding author upon reasonable request. Source data are provided with this paper.

## 6.8 Code availability

The Mitometer program is written in MATLAB (MathWorks). The MATLAB GUI Mitometer app and corresponding source code are available as Supplementary Software. The software and updated versions are also freely available online through GitHub at

<https://github.com/aelefebv/Mitometer>

with a direct download link available at

<https://github.com/aelefebv/Mitometer/archive/refs/heads/main.zip>.

## 6.9 Summary

In this chapter, we presented our work to create a new method for unbiased and automatic segmentation and tracking of mitochondria. We used this method to comprehensively compare mitochondrial morphology and motility phenotypes across 10 different breast tissue models and quantify differences between non-cancerous, cancerous but receptor positive, and triple negative breast cancerous tumor cells. From these experiments we found that TNBC mitochondria behave quite similarly to non-cancerous breast mitochondria in 3D spheroid models. Additionally we found that mitochondrial parameters differ very significantly when compared between cells in 2D and 3D cultures, emphasizing the importance of studying clinically relevant models. Finally, we correlated mitochondrial morphology and motility features with NADH FLIM metabolic features and found that breast cancer cells had signif-



icant correlations with mitochondrial phenotypes, whereas non-cancerous cells had little to none.

In the following chapter, we will apply Mitometer in cancer cells in an attempt to connect everything from previous chapters: cellular contractility, metabolism, and mitochondrial phenotypes.

# Chapter 7

## Mitochondrial and metabolic phenotypes as a function of the cellular cytoskeleton

All materials of this chapter consist of unpublished data as of the time of writing this dissertation, and materials, including any text portions taken from Dr. Alireza Sohrabi's dissertation, have been used with permission from co-authors.

### 7.1 Introduction

The cell's internal response to external mechanical stimuli, termed mechanosensation, has recently been shown to modulate cancer cell metabolic shifts, influencing its usage of glycolysis and oxidative phosphorylation [Mah et al. (2018)]. Mechanosensation is also crucial in signaling the cell to rearrange the cytoskeleton, conforming and adapting to the surrounding extracellular matrix or lack thereof. Dysregulated cytoskeletal dynamics help to fuel many diseases such as aiding cancer cells during the invasion process [Machesky (2008)]. This

invasion process requires a contractility mechanism, which allows the cells to pull themselves forward in order to advance.

The main protein responsible for cellular contractility is myosin light chain (MLC). MLC in turn is activated via phosphorylation by two primary kinases, myosin light chain kinase (MLCK) and rhoA associated protein kinase (ROCK). MLCK and ROCK, though similar in function, have very distinct roles during phosphorylation. The inhibition of each separately leads to large diversities in cell shape and function. Specifically, MLCK inhibition has been shown to increase cellular spreading while ROCK inhibition seems to increase cellular polarity [[Totsukawa et al. \(2004\)](#)].

In many types of cancer, these contractility pathways have been found to be dysregulated [[Sahai and Marshall \(2002\)](#)]. Although the connection between mechanosensation and metabolism are starting to become understood, the role that contractility plays on mitochondrial phenotype - morphologic, motile, and metabolic - is still unknown. To uncover this role, and its effect in cancer, we probe mitochondrial phenotypes of three different cell lines, non-cancerous MCF-10A breast epithelial cells, cancerous and receptor positive MCF-7 breast cancer cells, and cancerous and receptor triple-negative MDA-MB-231 breast cancer cells under conditions of inhibited contractility. To inhibit contractility we used ROCK inhibitor Y27632 or MLCK inhibitor ML7. Under these inhibited conditions, we probe the cells metabolic response by phenotypically analyzing the shifts of the reduced form of nicotinamide adenine dinucleotide (NADH) bound and free fractions via the fluorescence lifetime imaging of NADH. We also probe the mitochondrial morphologic and motile response by using Mitometer to analyze mitochondrial shape and movement in an automated and unbiased manner.

To understand closely related pathways of cytoskeletal rearrangements to mitochondrial phenotype, we also probed mitochondrial morphology and motility after inhibition with inhibitors of PI3K, PAK1, LIMK, and microtubule polymerization.

We also investigated the effects of cytoskeletal inhibitors in a 3D model of glioblastoma multiforme (GBM). Specifically, we blocked the cells' ability to interact with the surrounding hyaluronic acid hydrogel by treating cells with either an ezrin inhibitor, a CD44 inhibitor, or a combination of both. We then analyzed the effects of this crosstalk inhibition on mitochondrial motility, morphology, and cellular metabolism as a whole.

## 7.2 Results

### 7.2.1 Contractility inhibition on mitochondrial morphology and motility in breast cells

To investigate the mitochondrial response to changes in the cell's contractility, we use inhibitors Y27632 and ML7 to block the activity of two kinases that phosphorylate myosin light chain, Rho-associated protein kinase (ROCK) and myosin light chain kinase (MLCK), respectively. We use these inhibitors in three different cell types, MCF-10A cells which are non-cancerous breast epithelial cells, MCF-7 cells which are minimally aggressive, receptor positive breast cancer cells, and MDA-MB-231 cells which are highly aggressive, receptor triple-negative breast cancer cells (Fig. 7.1a). To investigate mitochondrial phenotypes, we use Mitometer to automatically segment and track mitochondria, allowing us to quantify motility and morphology in a high-throughput and unbiased manner.

To quantify motility, we compare mitochondrial speed in the three cell lines under a vehicle-control DMSO treatment, a 200  $\mu$ M Y27632 treatment, and a 50  $\mu$ M ML7 treatment. We normalize the values of each treatment to the DMSO control and compare percent differences of speed so as to avoid comparisons of any intercellular differences. We find that in all cell lines, contractility inhibition with both Y27632 and ML7 act to significantly reduce mitochondrial speed (Fig. 7.1b). In MCF-10A cells, Y27632 reduces mitochondrial median speed to 77.78% and ML7 to 49.50% of its original DMSO median speed. In MCF-7 cells,

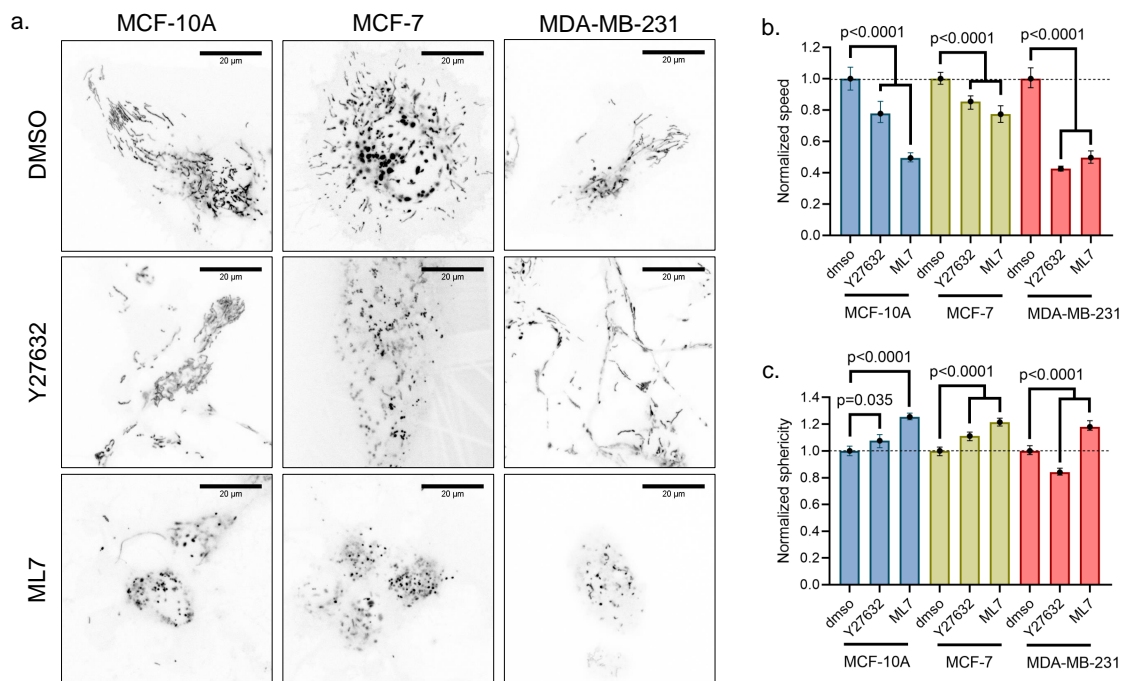


Figure 7.1: Contractility inhibition on mitochondrial morphology and motility. **a**, Representative TMRM fluorescence images of mitochondria in MCF-10A, MCF-7, and MDA-MB-231 treated with DMSO, 200  $\mu$ M Y27632, or 50  $\mu$ M ML7. **b**, Median values of mitochondrial speed following treatments of DMSO or contractility inhibitors. **c**, Median values  $\pm$  95% confidence intervals of mitochondrial sphericity (minor:major axis length) following treatments of DMSO or contractility inhibitors.  $n = 1368, 1156, 665$  for MCF-10A, 1403, 773, 1021 for MCF-7, and 712, 552, 1764 for MDA-MB-231 of individual mitochondrial tracks for DMSO, Y27632, and ML7 treatments, respectively.  $p$ -value derived from a non-parametric Kruskal-Wallis rank test with a Dunn's multiple comparisons test against the DMSO control. Scale bar: 20  $\mu$ m. Error bars represent 95% confidence intervals of the median values.

Y27632 reduces mitochondrial median speed to 85.43% and ML7 to 77.34% of its original DMSO median speed. In MDA-MB-231 cells, Y27632 reduces mitochondrial median speed to 42.59% and ML7 to 49.63% of its original DMSO median speed.

To quantify morphology, we compare mitochondrial sphericity, as calculated by the ratio of the median minor axis length to the median major axis length of an individual mitochondrial track, in the three cell lines under a vehicle-control DMSO treatment, a 200  $\mu$ M Y27632 treatment, and a 50  $\mu$ M ML7 treatment. We again normalize the values of each treatment to the DMSO control and compare percent differences of speed so as to avoid comparisons of any intercellular differences. We find that in the non-cancerous MCF-10A

and the less aggressive MCF-7 breast cell lines, contractility inhibition with both Y27632 and ML7 act to significantly increase mitochondrial sphericity (Fig. 7.1c). In contrast, contractility inhibition with Y27632 acts to significantly reduce mitochondrial sphericity in the TNBC MDA-MB-231 cell line. In MCF-10A cells, Y27632 increases mitochondrial sphericity to 107.6% and ML7 to 125.5% of its original DMSO median sphericity. In MCF-7 cells, Y27632 increases mitochondrial median sphericity to 111.2% and ML7 to 121.5% of its original DMSO median sphericity. In MDA-MB-231 cells, Y27632 reduces mitochondrial median sphericity to 84.02% and ML7 increases mitochondrial median sphericity to 118.0% of its original DMSO median speed.

Together, these data suggest that the contractility inhibitors act to reduce mitochondrial translocation across all examined cell lines, but differentially acts to modulate mitochondrial morphology. This was seen in MDA-MB-231 cells, where blocking contractility via ROCK inhibition with Y27632 decreased mitochondrial sphericity, but via MLCK inhibition via ML7 increased mitochondrial sphericity. This is in contrast to the less aggressive cell lines MCF-10A and MCF-7 where both contractility inhibitors increased mitochondrial sphericity.

## 7.2.2 Cytoskeletal effects on mitochondrial morphology and motility in breast cells

Given the observed differences in mitochondrial response to contractility inhibition, we wanted to investigate upstream and orthogonally cytoskeletal-related pathways to potentially tease out where these differences stemmed from. To do this, we used additional inhibitors of cytoskeletal dynamics. Upstream of cellular actin turnover mechanisms, we inhibited LIM kinase (LIMK) via CRT 0105950, which acts to stabilize actin filaments, and P21 activated kinase 1 (PAK1) via AZ 13705339, which acts to phosphorylate LIMK. Upstream of both contractility and actin turnover pathways, we also inhibited phosphoinositide 3-kinase (PI3K) via Wortmannin, which acts to activate Rac1, among other proteins, upstream of

PAK1. We also wanted to observe the effects of microtubule dysregulation by inhibiting its polymerization via nocodazole.

Again we analyzed mitochondrial speed and sphericity normalized to a DMSO control as phenotypical indicators of mitochondrial motility and morphology. In MCF-10A cells, mitochondria show increased speed to 125% of its original value under PI3K inhibition and 120% under Pak1 inhibition (Fig. 7.2a). In comparison, MCF-7 cells showed no significant

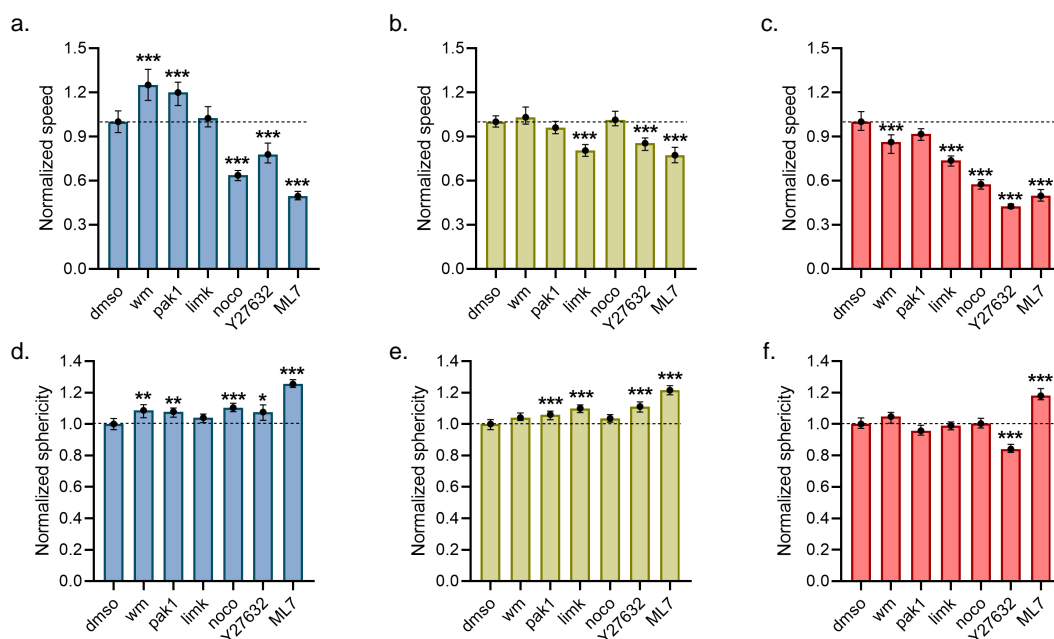


Figure 7.2: Cytoskeletal effects on mitochondrial morphology and motility. **a**, Median values of mitochondrial speed of MCF-10A (**a**), MCF-7 (**b**), and MDA-MB-231 (**c**) cells following treatments with DMSO, 100 nM Wortmannin (wm), 1 nM Pak1 inhibitor AZ 13705339 (pak1), 10  $\mu$ M LIMK inhibitor CRT 0105950 (limk), 100  $\mu$ M Nocodazole (noco), 200  $\mu$ M Y27632, and 50  $\mu$ M ML7. Median values of mitochondrial sphericity of MCF-10A (**d**), MCF-7 (**e**), and MDA-MB-231 (**f**) under the same treatments as **a-c**.  $n = 1368, 655, 846, 954, 1551, 665, 1156$  for MCF-10A,  $1403, 1351, 1177, 1163, 1869, 1021, 773$  for MCF-7, and  $712, 726, 1042, 1105, 1197, 1764, 552$  for MDA-MB-231 of individual mitochondrial tracks for DMSO, wm, pak1, limk, noco, Y27632, and ML7 treatments, respectively. p-value derived from a non-parametric Kruskal-Wallis rank test with a Dunn's multiple comparisons test against the DMSO control. Error bars represent 95% confidence intervals of the median values.

changes under either inhibitor, and MDA-MB-231 showed a significant decrease in mitochondrial speed under PI3K inhibition, dropping to 86.20% of its DMSO speed (Fig. 7.2b,c).

LIMK inhibition showed decreases in mitochondrial speed to 80.44% in MCF-7 and 73.71% in MDA-MB-231 cells, while showing no significant changes in MCF-10A mitochondria. Alternatively, nocodazole significantly slowed MCF-10A and MDA-MB-231 mitochondria to 63.72% and 57.52% of their DMSO speed, but showed no significant changes in MCF-7 cells.

Morphologically, PI3K inhibition increased mitochondrial sphericity only in MCF-10A mitochondria, to 108.7% of its DMSO sphericity (Fig. 7.2d). Pak1 inhibition increased sphericity to 107.9% in MCF-10A and 106.0% in MCF-7 mitochondria, but did not significantly affect MDA-MB-231 mitochondria (Fig. 7.2e,f). LIMK inhibition had only an effect on increasing MCF-7 mitochondrial sphericity to 109.9%. Finally, nocodazole only significantly affected MCF-10A mitochondrial sphericity by increasing it to 110.5%.

It is interesting to note that most of the actin and contractility inhibitors significantly acted to increase mitochondrial sphericity in both MCF-10A and MCF-7 mitochondria, but only the direct contractility inhibitors Y27632 and ML7 modulated sphericity in MDA-MB-231. However, all inhibitors except of the Pak1 inhibitor decreased mitochondrial speed in MDA-MB-231 mitochondria, but had minimal effects on MCF-7, and opposite effects in MCF-10A mitochondria in the case of PI3K inhibition. These data suggest large cell type-dependent heterogeneities in mitochondrial morphology and motility in response to cytoskeletal modulation, and could hint to mechanisms of targeting TNBC-specific mitochondria.

### **7.2.3 Metabolic shifts following contractility inhibition in breast cells**

To understand how these alterations in mitochondrial morphology and motility translate to metabolic changes within the cell, we performed FLIM of NADH on MCF-10A, MCF-7, and MDA-MB-231 cells under inhibition of contractility (Fig. 7.3a). Specifically, we analyzed how fractions of bound NADH changed after treatment of 200  $\mu$ M of ROCK inhibitor Y27632,



or 50  $\mu$ M of MLCK inhibitor ML7, as compared to the vehicle-control condition treated with DMSO.

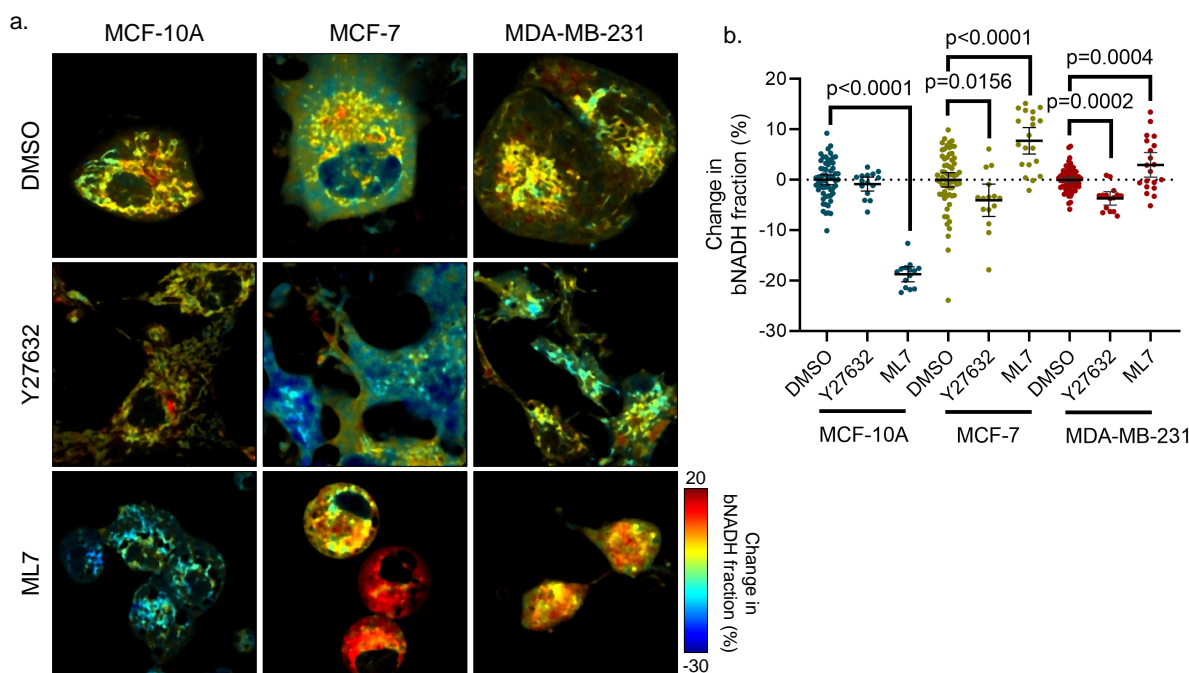


Figure 7.3: Metabolic shifts following contractility inhibition in breast cells. **a**, Representative endogenous NADH fluorescence images, pseudocolored to bNADH fraction change of MCF-10A, MCF-7, and MDA-MB-231 cells treated with DMSO, 200  $\mu$ M Y27632, or 50  $\mu$ M ML7. **b**, Mean values of bNADH fraction change percentage following treatments of DMSO or contractility inhibitors.  $n = 60, 15, 14$  for MCF-10A, 65, 15, 20 for MCF-7, and 65, 15, 20 for MDA-MB-231 of individual intensity thresholded frames of NADH lifetime for DMSO, Y27632, and ML7 treatments, respectively.  $p$ -value derived from an ordinary one-way ANOVA with a Holm-Sidak's multiple comparisons test against the DMSO control. Error bars represent 95% confidence intervals of the mean values.

After treatment with Y27632, both cancer cell lines showed a significant decrease in their bound NADH (bNADH) fraction. MCF-7 cells decreased their fraction by 3.644%, while MDA-MB-231 cells decreased their fraction by 3.171%, indicating a shift towards a more glycolytic phenotype following high concentrations of ROCK inhibition (Fig. 7.3b). MCF-10A, however, showed no significant changes following treatment. Conversely, after treatment with ML7, again both cancer cell lines showed corresponding effects, increasing significantly in their bNADH fractions. MCF-7 cells increased their bNADH fraction by 7.895%, and

MDA-MB-231 cells by 2.268%. Surprisingly, MCF-10A cells showed a strong and opposing bNADH shift, decreasing their fraction by 18.18%(Fig 7.3b).

Together, these results indicate a highly heterogeneous metabolic response to contractility inhibition, and show differential effects between the two kinases. Y27632 inhibition led to small shifts, though significant in cancer cells, towards a glycolytic metabolic phenotype. ML7 inhibition instead lead to opposite shifts towards a more oxidative phosphorylation metabolic phenotype in cancer cells, while leading to a strong shift towards a glycolytic phenotype in the non-cancerous MCF-10A breast epithelial cell line.

#### **7.2.4 Integrins and CD44 directly mediate the metabolic switch in GBM cells**

In addition to breast normal epithelial and cancerous cells, we wanted to understand how GBM cell-ECM interactions affected metabolic and mitochondrial phenotypic shifts in soft and stiff hydrogels. Interactions between GBM cells and its surrounding substrate occur predominantly through two proteins, integrins with RGD peptides, and CD44 with the hyaluronic acid. To understand these metabolic and mitochondrial shifts, we used inhibitors of both of these proteins.

To inhibit integrin interactions with the hydrogel, we treated GBM spheroids with cilengitide (CRGD). Cilengitide is a cyclic RGD pentapeptide that specifically inhibits the integrin  $\alpha V$  family interactions with the RGD motif in ECM proteins [Mas-Moruno et al. (2010)].

We also inhibited the Ezrin/CD44 interaction that helps bridge the CD44 receptors to the actin cytoskeleton to relay signals of the surrounding ECM [Vaheri et al. (1997)]. To do this, we inhibited ezrin using a small molecule drug that has been shown to downregulate invasiveness in other cancers in vitro [Bulut et al. (2012)].

In GBM spheroids treated with CRGD, we found a shift in metabolism towards oxidative phosphorylation in both soft and stiff hydrogels (Fig. 7.4). GBM spheres in soft hydrogels

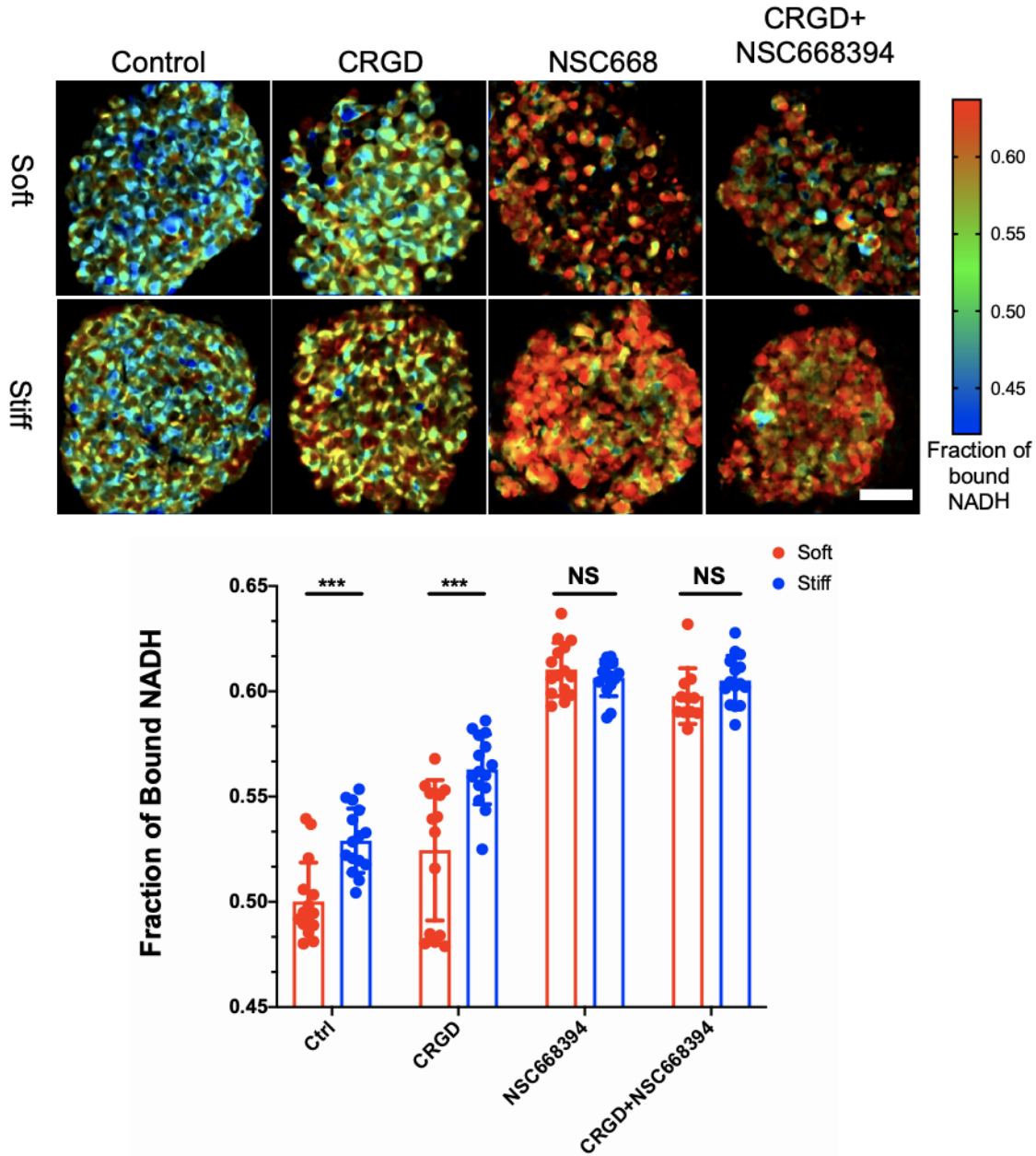


Figure 7.4: Integrins and CD44 directly mediate the metabolic switch in GBM cells. **Top:** Representative fraction of bound NADH colormapped images of GBM cells in control conditions, or following treatments of 25  $\mu\text{M}$  integrin-interaction inhibitor Cilengitide (CRGD) or 10  $\mu\text{M}$  of Ezrin inhibitor NSC668394, or both combined (CRGD+NSC668394) in both soft and stiff HA hydrogels. **Bottom:** Mean fractions of bound NADH for each condition in both soft and stiff HA hydrogels.  $n = 15$  individual intensity thresholded frames of NADH lifetime for each condition. Significance was derived from a one-way ANOVA followed by t-tests within the groups. \*\*\* $p < 0.001$ . Error bars represent standard deviations of the mean values. Scale bar = 50  $\mu\text{M}$

showed an increase in bound NADH from  $0.5\pm0.01$  in control samples to  $0.52\pm0.03$  in CRGD treated conditions ( $p=0.0216$ ). Alternatively, in stiff hydrogels, the CRGD treatment led to a larger increase in bound NADH, from  $0.53\pm0.02$  in control samples to  $0.56\pm0.02$  in CRGD treated conditions ( $p<0.0001$ ). However, GBM spheres in soft condition continued to show a lower fraction of bound NADH, even in CRGD-treated conditions, when compared to GBM spheres in stiff condition. In the CRGD treated conditions, soft-hydrogel cultured GBM spheres had a fraction of bound NADH of  $0.52\pm0.03$  compared to  $0.56\pm0.02$  in stiff-hydrogel cultured conditions ( $p<0.01$ ).

Alternatively, in Ezrin-inhibited conditions, there was a strong increase of bound NADH in both soft and stiff GBM-cultured conditions. Specifically, in soft hydrogels, GBM spheroids showed an increase in their fraction of bound NADH from  $0.5\pm0.01$  in control samples to  $0.61\pm0.01$  in treated group ( $p<0.0001$ ). In stiff hydrogels, GBM spheroids showed an increase in their fraction of bound NADH from  $0.53\pm0.02$  in control samples to  $0.6\pm0.008$  in treated group ( $p<0.0001$ ). Interestingly, there were no statistical differences between GBM spheroid NADH fractions between soft and stiff hydrogels after ezrin inhibition ( $p=0.32$ ). Combinatory treatment of CRGD and NSC668394, worked similarly to ezrin inhibition alone.

These results suggest that a specific CD44 inhibition may act as a mechanosensitive transducer to modulate GBM spheroid metabolism in HA gels. Indeed, we saw its inhibition to, first, increase oxidative phosphorylation within cells in both stiff and soft conditions, and second, remove differences in fractions of bound NADH between soft and stiff conditions.

### **7.2.5 ECM stiffness and CD44 alter mitochondrial morphology and motility**

Following these stark metabolic differences found after ezrin inhibition, and from the studies conducted in soft and stiff HA hydrogels, we hypothesized to see equally interesting dif-

ferences in mitochondrial morphology and motility, considering our results of cytoskeletal inhibitors in breast cells.

Analysis of mitochondrial motility in stiff and soft conditions, in control and ezrin inhibited conditions showed a very significant decrease in mitochondrial speed in soft HA-hydrogels, from  $0.077 \mu\text{m/s}$  in stiff HA gels to  $0.059 \mu\text{m/s}$  in soft HA gels (Fig. 7.5a,b). Ezrin inhibition

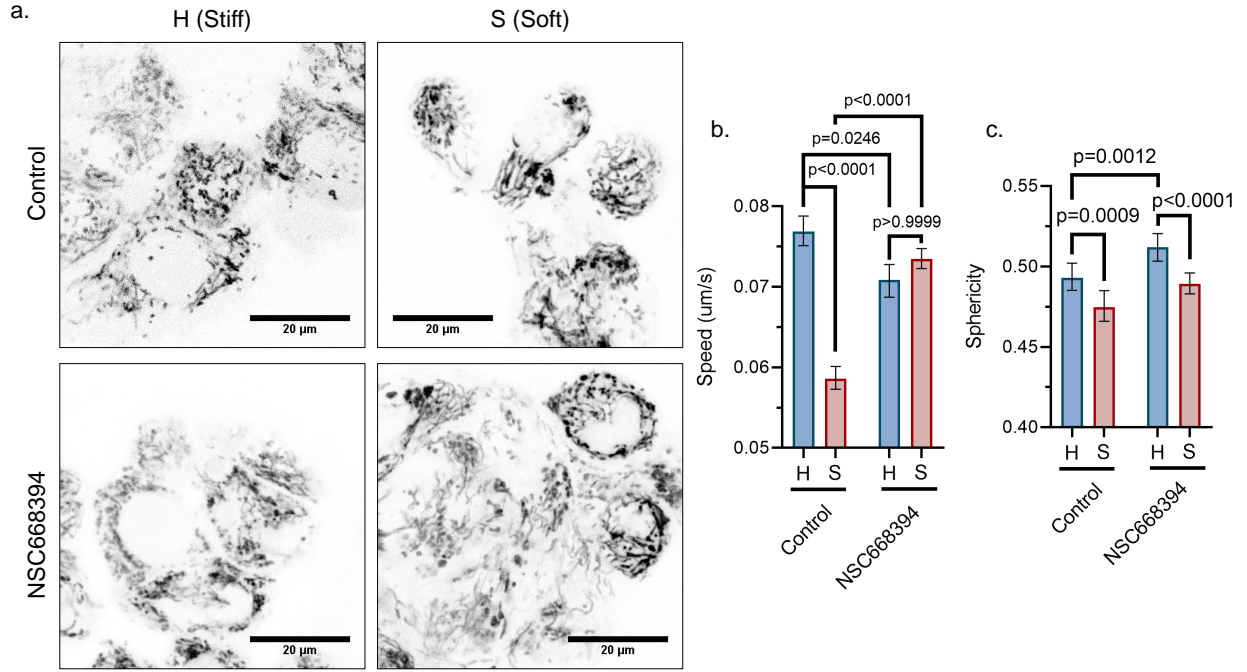


Figure 7.5: ECM stiffness and CD44 alter mitochondrial morphology and motility. **a**, Representative images of GBM mitochondria in stiff (H) and soft (S) HA hydrogels in control conditions, or following treatments  $10 \mu\text{M}$  of ezrin inhibitor NSC668394. **b**, Median mitochondrial speed and sphericity of GBM cells in the same conditions as **a**.  $n = 2596, 2366$  for control, and  $n = 2198, 3221$  individual mitochondrial tracks for Ezrin-inhibited cells, in stiff and soft HA-hydrogels, respectively. P-values were derived from a non-parametric Kruskal-Wallis test followed by a Dunn's multiple comparisons test. Error bars represent 95% confidence intervals of the median values. Scale bar =  $20 \mu\text{M}$ . H = stiff HA gel, S = soft HA gel.

caused a slight decrease in mitochondrial speed in stiff gels, reducing it to  $0.071 \mu\text{m/s}$ . Interestingly, ezrin inhibition also abrogated the decrease in mitochondrial speed caused by the soft HA gel, raising it to the same speed as the ezrin inhibited cells in the stiff HA gel.

Analysis of mitochondrial morphology shows a decrease in mitochondrial sphericity in soft HA gels (0.4746) as compared to stiff HA gels (0.4930) (Fig. 7.5c). Ezrin inhibited cells also showed this decrease in soft gels (0.4891) as compared to stiff gels (0.5121), and increased mitochondrial sphericity significantly in stiff conditions, but not in soft conditions, as compared to the control condition.

## 7.3 Discussion

In these experiments, we explored the connection between three highly dynamic cellular processes: mitochondrial function, metabolic phenotype, and cellular contractility. We used inhibitors of contractility, to show that cellular contractility in breast cells acts to reduce intracellular mitochondrial movement. However, these inhibitors act differentially in TNBC cells as compared to non-TNBC and non-cancerous breast cells, suggesting a possible mechanistic link to mitochondrial phenotypic differences in these aggressive cancers.

To understand the mechanisms upstream of contractility, and its related, but orthogonal mechanisms of actin turnover and microtubule polymerization, we used inhibitors of LIMK, PAK1, PI3K, and Nocodazole, which inhibits microtubule polymerization. We found large cell type-dependent heterogeneities in both mitochondrial morphology and motility in response to these inhibitors, with the largest effects surrounding TNBC phenotypic mitochondrial changes.

To connect these contractility-dependent mitochondrial phenotypic changes to the cells' metabolic landscape, we used FLIM of NADH to quantify phenotypic changes in metabolism under conditions of inhibited contractility. We found that cancer cells shifted to a more glycolytic metabolism under ROCK-based contractility inhibition, but to a more oxidative phosphorylation metabolism under MLCK-based contractility inhibition. This was in contrast to non-cancerous cells, where ROCK-based contractility inhibition showed no significant changes in metabolic phenotype, but under MLCK-based contractility inhibition, a large

shift towards a glycolytic metabolism was found. Together, these results indicate a potential mechanistic connection between contractility and metabolism, and how this connection may be dysregulated in breast cancer.

Additionally, we used GBM spheroids cultured in soft and stiff hyaluronic-acid hydrogels to explore the mechanosensitive pathways contributing to metabolic changes of the spheroids within these gels. Ezrin inhibition produced a large increase in fractions of bound NADH in both soft and stiff hydrogel-cultured GBM spheroids, and an increase in mitochondrial speed in soft hydrogel-cultured GBM spheroids, but no noticeable mitochondrial morphological changes. Interestingly, mitochondria were also much slower in conditions of increased invasion, of which the opposite was found in breast cancer cells in the previous chapter. These results could provide indications at mechanistic connections of the mechanosensation pathways that influence metabolism in cancer cells, and how these pathways are dysregulated during the invasion process.

## 7.4 Materials and Methods

### 7.4.1 Cell culture

MCF-7 and MDA-MB-231 cells were cultured 25 cm<sup>2</sup> dishes with DMEM, 5% heat inactivated fetal bovine serum, and 1% penicillin–streptomycin 100× solution. MCF-10A cells were cultured in DMEM/F12 media supplemented with 5% horse serum, 20 ng\*μL<sup>-1</sup> epidermal growth factor, 0.5 mg\*mL<sup>-1</sup> hydrocortisone, 100 ng\*mL<sup>-1</sup> cholera toxin, 10 μg\*mL<sup>-1</sup> insulin and 1% penicillin–streptomycin. Cells were kept at 37°C at 5% CO<sub>2</sub>.

The cells were passaged with 0.05% trypsin after reaching 70% confluency. The cells were plated with 400 μL of complete media at a confluency of 1×10<sup>4</sup> cells\*cm<sup>-2</sup> in 8-well glass-bottomed fibronectin-coated imaging dishes approximately 24h before drug treatment and left to adhere. The following day, half the media was taken out, mixed with TMRM to a

working concentration of 100 nM, along with the specified inhibitor or DMSO at the specified concentrations, and placed back into the well with the cells.

### **7.4.2 Fluorescence imaging of mitochondria**

For breast cell experiments, mitochondrial imaging was performed on a Zeiss LSM 880 inverted laser scanning confocal microscope with a 63 $\times$ , numerical aperture 1.4, oil-immersion objective. We used a frame size of 512 $\times$ 512 with a pixel size of 132 nm and at a rate of 1 frame per second for 60 frames. In the GBM studies we used a frame size of 256 $\times$ 256 with a pixel size of 118 nm and at a rate of 1 frame per second for 60 seconds. In both cases, we used a two-photon titanium:sapphire laser (Spectra-Physics, MaiTai) to excite the TMRM at a wavelength of 820 nm, which was passed through a 690 nm dichroic filter. The fluorescence emission in the range of 520–700 nm was captured through the microscope’s internal detector. The cells were kept under biological conditions through the imaging. Images were converted to TIFs in ImageJ v1.53c.

### **7.4.3 FLIM of NADH**

Fluorescence lifetime images were acquired on a Zeiss LSM 880 inverted laser scanning confocal microscope. For breast cells, a 63 $\times$ , numerical aperture 1.4, oil-immersion objective was used, with cells kept under biological conditions throughout imaging. For GBM cells, a  $\times$ 40/1.2 numerical aperture water-immersion objective was used, with cells kept under biological conditions throughout. All cells were excited at approximately 2 mW with a two-photon Ti:Sapphire laser (Spectra-Physics, MaiTai) at 740 nm, which was passed through a 690 nm dichroic filter. The fluorescence emission was separated through a bandpass filter (460/80 nm) to capture the cell auto-fluorescence in the NADH range, and exclude any other emission, followed by detection using a photomultiplier tube (Hamamatsu, cat. no. H7422P-40). The fluorescence lifetime decays were captured via an A320 FastFLIM box



(ISS) and subsequently mapped onto the phasor plot using the SimFCS software—developed at the Laboratory for Fluorescence Dynamics at the University of California, Irvine—for quantitative NADH lifetime analysis.

Coumarin-6 in ethanol, with a known single exponential fluorescence lifetime of 2.5 ns, was imaged before each experiment and used as a calibration sample for the instrument response time. Analysis was performed as described in Chapter 2.

#### **7.4.4 GBM receptor inhibition**

To interfere GBM cell interaction with RGD and HA, Cilengitide (CRGD) and ezrin inhibitor was used respectively. Post-encapsulation, spheroids were treated with Cilengitide (Sigma Aldrich) and NSC668394 (Ezrin inhibitor, Sigma Aldrich). Cilengitide stock solution was prepared at 5 mM in PBS. NSC668394 stock solution was prepared at 10 mM in DMSO. For inhibition experiments, final concentration of 25  $\mu$ M Cilengitide and 10  $\mu$ M NSC668394 were used.

#### **7.4.5 Statistical analysis**

For the breast metabolic studies, a one-way ANOVA test followed by a Holm-Sidak's multiple comparisons test with a single pooled variance was performed to determine statistical significance. For mitochondrial breast studies, a non-parametric Kruskal-Wallis test was used, followed by a Dunn's multiple comparisons test.

For the metabolic GBM studies, normality of each data set was analyzed using D'Agostino & Pearson omnibus normality test. For normally distributed population, one-way ANOVA and then t-test were used to determine the statistical differences among the groups. For non-normal distributions, Mann-Whitney non-parametric test was used. For mitochondrial GBM studies, a non-parametric Kruskal-Wallis test was used, followed by a Dunn's multiple comparisons test.

All statistical analyses were done in Prism 8 software.

## 7.5 Summary

In this chapter, we have used Mitometer in cancer cells to connect everything from previous chapters: cellular contractility, metabolism, and mitochondrial phenotypes. We found interesting differences between non-cancerous breast cells, cancerous and receptor-positive breast cancer cells, and aggressive and receptor triple-negative breast cancer cells when treated with two different inhibitors of orthogonal pathways of contractility. We expanded these results to a GBM spheroid model in soft and stiff substrates to find different results between cancer models.

# Chapter 8

## Conclusions

### 8.1 Solving problems

As a bioengineering graduate student, it is often difficult to determine how much of one's time to allocate towards the bio- portion, and how much to allocate towards the -engineering portion. I began my time in graduate school attempting to solve a purely biological problem - one of understanding mitochondrial translocation in response to cellular motion in cancer cells - by applying an arsenal of pre-existing tools.

I think it's important to begin with the biology side. Similar to the motto of a few business classes and workshops I attended, I have learned that often times (though not always) a new tool is useless if it doesn't have a pre-existing question to solve. For me, it was this mitochondrial tracking and morphological quantification that struck me as lacking in tools. Thus, the engineering aspect revealed itself.

As an engineer, one finds themselves constantly iterating to improve on one aspect or another of one's project. One learns to use their mathematical skills, programming skills, mechanical skills, or any other skills that one has at their disposal to create a solution to these biological problems. In the process, one publishes these solutions, and helps others with similar problems along the way.

In this sense, a bioengineer encapsulates the definition of a scientist, where they make solutions to solve their biological problems, and use the answers to these problems to create increasingly complex but important new problems.

In chapter 3, I begin my dissertation by connecting the metabolism of invasive triple-negative breast cancer cells with its mechanosensation of surrounding collagen extracellular matrix. This data, however, was on a single-cell level in collagen, which is a step in the right direction to mimic physiological conditions, but is lacking in the cell-cell interactivity and culture complexity that can be found in organoid models.

In chapter 4, I move to two more clinically relevant models. The first model is that of patient-derived glioblastoma multiforme (GBM) tumor spheroids within a 3D hyaluronic acid (HA) hydrogel culture, in collaboration with Dr. Stephanie Seidlits and her post-doctoral student Dr. Alireza Sohrabi, who designed the culture system and have grown multiple GBM cell lines within these HA gels for us to image and analyze. The second model is that of patient-derived xenograft breast tumors displaying spontaneous metastases to various organs within in vivo mouse models in collaboration with Dr. Devon Lawson's and Dr. Kai Kessenbrock's lab at UC Irvine. Using these models, I present results that showed large metabolic diversities, both transcriptionally and phenotypically, between the GBM cell cultures in soft and stiff hyaluronic acid hydrogels, and between breast cancer tumor primary sites and secondary sites. We used the information gleaned from the breast cancer data to reduce metastatic dissemination in mouse models by inhibiting oxidative phosphorylation mechanisms. Though this model is extremely powerful, its flexibility for phenotypic assays in live cells is limited, and an alternative method for higher throughput studies must be created.

In chapter 5, I present our work to create a 3D breast cancer tumor spheroid culture-transplant system to facilitate the expansion and modulation of PDX cells to run functional metabolic assay. This method of PDX propagation as tumor spheres in vitro maintains their global transcriptome after propagation and continues to form spontaneous metastases post-

transplantation. The spheroid cultures can also be genetically engineered and retransplanted to facilitate experiments of in vivo metastasis post-genetic modification.

The cells' mitochondria are one of the primary sites carrying out metabolic processes, and their structure and function have been shown to be highly dysregulated in different diseases. In chapter 6, I present my work to create a new method for unbiased and automated segmentation and tracking of mitochondria. I use this method to phenotypically compare mitochondrial morphology and motility across 10 different breast tissue models and quantify differences between non-cancerous, cancerous but receptor positive, and triple negative breast cancerous tumor cells. These experiments show that TNBC mitochondria behave similar to non-cancerous breast mitochondria in 3D spheroid models as compared to receptor-positive breast cancer cells. Additionally 2D and 3D cultured cells of the same line differ very significantly when compared by mitochondrial morphology and motility, emphasizing the importance of studying clinically relevant models. I then correlate mitochondrial morphology and motility features with the NADH FLIM signature of individual mitochondria, connecting metabolic features with mitochondrial phenotype.

Finally, in chapter 7, I present results of using Mitometer in cancer cells to connect everything from previous chapters: cellular contractility, metabolism, and mitochondrial phenotypes. I found interesting differences between non-cancerous breast cells, cancerous and receptor-positive breast cancer cells, and aggressive and receptor triple-negative breast cancer cells when treated with two different inhibitors of orthogonal pathways of contractility. I expand on these results by investigating the same GBM spheroid model as in previous chapters in soft and stiff substrates under conditions of inhibited cell-ECM interactions to understand their invasive abilities.

## 8.2 Making new ones

As with any engineered tool or technique, its final version does not exist, it is only improved upon. Similarly, a biological question is never truly solved, just further understood. Their questions become deeper, and their answers harder to find, and thus, the engineered solutions become harder to develop.

The questions answered in this dissertation and their corresponding publications advance the field in helpful ways, but their results bring up many other questions. Likewise, the engineered tools developed in this dissertation have helped to answer many questions, but their possibilities for use and for improvement are vast.

On the topic of mitochondrial phenotyping, I believe the next step towards proper contextual understanding is to be able to investigate these organelles without the use of fluorescent probes. Within this dissertation, we use TMRM for mitochondrial fluorescence staining, allowing us to segment and track these mitochondria in live cells. However, bound NADH, which has a relatively high quantum yield compared to its free state, lies predominantly in the mitochondria, and can be used to visualize these organelles without any staining. Though useful, the current excitation and detection tools available remain lacking when attempting to image cellular, let alone mitochondrial autofluorescence. Developments in the proper understanding of mitochondria-related autofluorescence, and the advancements in photon detectors will help to capture mitochondrial signal using only autofluorescence, and keep their physiological states unaltered by external influences.

In each section, I present data collected on a relatively very limited breadth of cancer cells. Indeed, this work focuses on a collection of almost exclusively breast cells, with some work on melanoma and glioblastoma. Though these results will hopefully prove useful to the cancer community as a whole, similar experiments should be carried out on a large and diverse panel of breast cancer models to truly validate its translatability across the field.

Similarly, the more complex microphysiological culture systems introduced in chapters 3, 4, and 5, though an important stride in the direction of contextual validity, remains lacking in its full potential. To understand the complexities of metabolism and mitochondria, and how their dysregulation expedites disease progression, we must first observe them in their proper context. Indeed, already protocols exist to create co-culture systems, incorporating important stromal and tumor-associated cells to the culture system, replicating in vivo cellular scenarios in an engineered system. Multi-organ systems and systems with vasculature are also being refined, and consistently becoming easier to incorporate into a cell biologist's workflow. Even fluorescence methodologies in living animal models are becoming more commonplace. It is with little doubt that applying the live-cell and single-organellar phenotyping methods expanded upon and developed in this dissertation to these advanced culture systems will unveil even further complexities of the metabolic and mitochondrial landscapes of cells.

Furthermore, the discovery of this large phenotypic diversity of mitochondria in various types of breast cancer should give inspiration to those interested in phenotypic drug discovery. These high-throughput, quantitative correlations associated with phenotypic changes of mitochondria following drug treatments can be a powerful tool to add to the list of quantifiable metrics to determine a drug's translational potential.

My wish is that the dissertation presented here gives inspiration to other scientists for creating new assays and techniques for single-organellar characterization, and to create them with the importance of context and translatability in mind. Often times with seminal biological discoveries, a phenotypic change is first noticed within the system. It is this observation of phenotypic changes that pushes the field to develop better questions and novel methods to probe those questions with a fine-toothed comb leading to their mechanistic understanding.

It is with great hope that in the future, my research during these years in graduate school will prove to fill the two roles of a bioengineer: solving problems and making new ones.

# References

- Abad, M. F. C., Di Benedetto, G., Magalhães, P. J., Filippin, L., and Pozzan, T. (2004). Mitochondrial pH monitored by a new engineered green fluorescent protein mutant. *The Journal of Biological Chemistry*, 279(12):11521–11529.
- Aguilar-Arnal, L., Ranjit, S., Stringari, C., Orozco-Solis, R., Gratton, E., and Sassone-Corsi, P. (2016). Spatial dynamics of SIRT1 and the subnuclear distribution of NADH species. *Proceedings of the National Academy of Sciences*, 113(45):12715–12720.
- Albrecht, J., Sidoryk-Wegrzynowicz, M., Zielinska, M., and Aschner, M. (2010). Roles of glutamine in neurotransmission. *Neuron Glia Biology*, 6(4):263–276.
- Alexander, N. R., Branch, K. M., Parekh, A., Clark, E. S., Iwueke, I. C., Guelcher, S. A., and Weaver, A. M. (2008). Extracellular Matrix Rigidity Promotes Invadopodia Activity. *Current Biology*, 18(17):1295–1299.
- Alonso, A., Marsal, S., and Julià, A. (2015). Analytical Methods in Untargeted Metabolomics: State of the Art in 2015. *Frontiers in Bioengineering and Biotechnology*, 3.
- Alsina, A., Lai, W. M., Wong, W. K., Qin, X., Zhang, M., and Park, H. (2017). Real-time subpixel-accuracy tracking of single mitochondria in neurons reveals heterogeneous mitochondrial motion. *Biochemical and Biophysical Research Communications*, 493(1):776–782.
- Andrzejewski, S., Klimcakova, E., Johnson, R. M., Tabariès, S., Annis, M. G., McGuirk, S., Northey, J. J., Chénard, V., Sriram, U., Papadopoli, D. J., Siegel, P. M., and St-Pierre, J. (2017). PGC-1 $\alpha$  Promotes Breast Cancer Metastasis and Confers Bioenergetic Flexibility against Metabolic Drugs. *Cell Metabolism*, 26(5):778–787.e5.
- Antalis, C. J., Uchida, A., Buhman, K. K., and Siddiqui, R. A. (2011). Migration of MDA-MB-231 breast cancer cells depends on the availability of exogenous lipids and cholesterol esterification. *Clinical & Experimental Metastasis*, 28(8):733–741.
- Antoniewicz, M. R. (2015). Methods and advances in metabolic flux analysis: a mini-review. *Journal of Industrial Microbiology & Biotechnology*, 42(3):317–325.
- Arai, S., Suzuki, M., Park, S.-J., Yoo, J. S., Wang, L., Kang, N.-Y., Ha, H.-H., and Chang, Y.-T. (2015). Mitochondria-targeted fluorescent thermometer monitors intracellular temperature gradient. *Chemical Communications*, 51(38):8044–8047.
- Artym, V. V., Swatkoski, S., Matsumoto, K., Campbell, C. B., Petrie, R. J., Dimitriadis, E. K., Li, X., Mueller, S. C., Bugge, T. H., Gucsek, M., and Yamada, K. M. (2015). Dense fibrillar collagen is a potent inducer of invadopodia via a specific signaling network. *Journal of Cell Biology*, 208(3):331–350.



- Ata, R. and Antonescu, C. N. (2017). Integrins and Cell Metabolism: An Intimate Relationship Impacting Cancer. *International Journal of Molecular Sciences*, 18(1):189.
- Baloh, R. H. (2008). Mitochondrial Dynamics and Peripheral Neuropathy. *The Neuroscientist*, 14(1):12–18.
- Basnet, H., Tian, L., Ganesh, K., Huang, Y.-H., Macalinao, D. G., Brogi, E., Finley, L. W., and Massagué, J. (2019). Flura-seq identifies organ-specific metabolic adaptations during early metastatic colonization. *eLife*, 8:e43627.
- Basu, H. and Schwarz, T. L. (2020). QuoVadoPro, an Autonomous Tool for Measuring Intracellular Dynamics Using Temporal Variance. *Current Protocols in Cell Biology*, 87(1):e108.
- Bays, J. L., Campbell, H. K., Heidema, C., Sebbagh, M., and DeMali, K. A. (2017). Linking E-cadherin mechanotransduction to cell metabolism through force-mediated activation of AMPK. *Nature Cell Biology*, 19(6):724–731.
- Beaty, B. T., Sharma, V. P., Bravo-Cordero, J. J., Simpson, M. A., Eddy, R. J., Koleske, A. J., and Condeelis, J. (2013).  $\beta 1$  integrin regulates Arg to promote invadopodial maturation and matrix degradation. *Molecular Biology of the Cell*, 24(11):1661–1675.
- Bianchini, G., Balko, J. M., Mayer, I. A., Sanders, M. E., and Gianni, L. (2016). Triple-negative breast cancer: challenges and opportunities of a heterogeneous disease. *Nature Reviews. Clinical Oncology*, 13(11):674–690.
- Bieling, P., Li, T.-D., Weichsel, J., McGorty, R., Jreij, P., Huang, B., Fletcher, D. A., and Mullins, R. D. (2016). Force Feedback Controls Motor Activity and Mechanical Properties of Self-Assembling Branched Actin Networks. *Cell*, 164(1):115–127.
- Bird, D. K., Yan, L., Vrotsos, K. M., Eliceiri, K. W., Vaughan, E. M., Keely, P. J., White, J. G., and Ramanujam, N. (2005). Metabolic Mapping of MCF10A Human Breast Cells via Multiphoton Fluorescence Lifetime Imaging of the Coenzyme NADH. *Cancer Research*, 65(19):8766–8773.
- Blacker, T. S., Mann, Z. F., Gale, J. E., Ziegler, M., Bain, A. J., Szabadkai, G., and Duchen, M. R. (2014). Separating NADH and NADPH fluorescence in live cells and tissues using FLIM. *Nature Communications*, 5(1):3936.
- Bodmer, M., Becker, C., Meier, C., Jick, S. S., and Meier, C. R. (2011). Use of metformin and the risk of ovarian cancer: a case-control analysis. *Gynecologic Oncology*, 123(2):200–204.
- Boissan, M., Schlattner, U., and Lacombe, M.-L. (2018). The NDPK/NME superfamily: state of the art. *Laboratory Investigation*, 98(2):164–174.
- Bond, S. T., McEwen, K. A., Yoganantharajah, P., and Gibert, Y. (2018). Live Metabolic Profile Analysis of Zebrafish Embryos Using a Seahorse XF 24 Extracellular Flux Analyzer. In Félix, L., editor, *Teratogenicity Testing: Methods and Protocols*, Methods in Molecular Biology, pages 393–401. Springer, New York, NY.
- Bos, P. D., Zhang, X. H.-F., Nadal, C., Shu, W., Gomis, R. R., Nguyen, D. X., Minn, A. J., van de Vijver, M. J., Gerald, W. L., Foekens, J. A., and Massagué, J. (2009). Genes that mediate breast cancer metastasis to the brain. *Nature*, 459(7249):1005–1009.
- Boyer, P. D., Theorell, H., Pokras, L., Sillén, L. G., and Thorell, B. (1956). The Change in Reduced Diphosphopyridine Nucleotide (DPNH) Fluorescence upon Combination with Liver Alcohol Dehydrogenase (ADH). *Acta Chemica Scandinavica*, 10:447–450.

- Bruna, A., Rueda, O., Greenwood, W., Batra, A., Callari, M., Batra, R., Pogrebniak, K., Sandoval, J., Cassidy, J., Tufegdizic-Vidakovic, A., Sammut, S.-J., Jones, L., Provenzano, E., Baird, R., Eirew, P., Hadfield, J., Eldridge, M., McLaren-Douglas, A., Barthorpe, A., Lightfoot, H., O'Connor, M., Gray, J., Cortes, J., Baselga, J., Marangoni, E., Welm, A., Aparicio, S., Serra, V., Garnett, M., and Caldas, C. (2016). A Biobank of Breast Cancer Explants with Preserved Intra-tumor Heterogeneity to Screen Anticancer Compounds. *Cell*, 167(1):260–274.e22.
- Bugyi, B. and Carlier, M.-F. (2010). Control of Actin Filament Treadmilling in Cell Motility. *Annual Review of Biophysics*, 39(1):449–470.
- Bulut, G., Hong, S.-H., Chen, K., Beauchamp, E. M., Rahim, S., Kosturko, G. W., Glasgow, E., Dakshanamurthy, S., Lee, H.-S., Daar, I., Toretsky, J. A., Khanna, C., and Üren, A. (2012). Small molecule inhibitors of ezrin inhibit the invasive phenotype of osteosarcoma cells. *Oncogene*, 31(3):269–281.
- Butler, A., Hoffman, P., Smibert, P., Papalexi, E., and Satija, R. (2018). Integrating single-cell transcriptomic data across different conditions, technologies, and species. *Nature Biotechnology*, 36(5):411–420.
- Byun, Y.-S., Tibrewal, S., Kim, E., Yco, L., Sarkar, J., Ivanir, Y., Liu, C.-Y., Sano, C. M., and Jain, S. (2014). Keratocytes Derived from Spheroid Culture of Corneal Stromal Cells Resemble Tissue Resident Keratocytes. *PLOS ONE*, 9(11):e112781.
- Caino, M. C. and Altieri, D. C. (2015). Disabling mitochondrial reprogramming in cancer. *Pharmacological research*, 102:42–45.
- Caino, M. C., Seo, J. H., Aguinaldo, A., Wait, E., Bryant, K. G., Kossenkova, A. V., Hayden, J. E., Vaira, V., Morotti, A., Ferrero, S., Bosari, S., Gabrilovich, D. I., Languino, L. R., Cohen, A. R., and Altieri, D. C. (2016). A neuronal network of mitochondrial dynamics regulates metastasis. *Nature Communications*, 7.
- Caino, M. C., Seo, J. H., Wang, Y., Rivadeneira, D. B., Gabrilovich, D. I., Kim, E. T., Weeraratna, A. T., Languino, L. R., and Altieri, D. C. (2017). Syntaphilin controls a mitochondrial rheostat for proliferation-motility decisions in cancer. *The Journal of Clinical Investigation*, 127(10):3755–3769.
- Calderwood, D. A., Campbell, I. D., and Critchley, D. R. (2013). Talins and kindlins: partners in integrin-mediated adhesion. *Nature Reviews Molecular Cell Biology*, 14(8):503–517.
- Calvert, A. E., Chalastanis, A., Wu, Y., Hurley, L. A., Kouri, F. M., Bi, Y., Kachman, M., May, J. L., Bartom, E., Hua, Y., Mishra, R. K., Schiltz, G. E., Dubrovskyi, O., Mazar, A. P., Peter, M. E., Zheng, H., James, C. D., Burant, C. F., Chandel, N. S., Davuluri, R. V., Horbinski, C., and Stegh, A. H. (2017). Cancer-Associated IDH1 Promotes Growth and Resistance to Targeted Therapies in the Absence of Mutation. *Cell Reports*, 19(9):1858–1873.
- Camarda, R., Zhou, A. Y., Kohnz, R. A., Balakrishnan, S., Mahieu, C., Anderton, B., Eyob, H., Kajimura, S., Tward, A., Krings, G., Nomura, D. K., and Goga, A. (2016). Inhibition of fatty acid oxidation as a therapy for MYC-overexpressing triple-negative breast cancer. *Nature Medicine*, 22(4):427–432.
- Cancer Genome Atlas Research Network (2008). Comprehensive genomic characterization defines human glioblastoma genes and core pathways. *Nature*, 455(7216):1061–1068.

- Cantó, C., Menzies, K., and Auwerx, J. (2015). NAD<sup>+</sup> metabolism and the control of energy homeostasis - a balancing act between mitochondria and the nucleus. *Cell metabolism*, 22(1):31–53.
- Cavalcanti-Adam, E. A., Volberg, T., Micoulet, A., Kessler, H., Geiger, B., and Spatz, J. P. (2007). Cell Spreading and Focal Adhesion Dynamics Are Regulated by Spacing of Integrin Ligands. *Biophysical Journal*, 92(8):2964–2974.
- Chaicharoenaudomrung, N., Kunhorm, P., and Noisa, P. (2019). Three-dimensional cell culture systems as an in vitro platform for cancer and stem cell modeling. *World Journal of Stem Cells*, 11(12):1065–1083.
- Chance, B. (2004). Mitochondrial NADH redox state, monitoring discovery and deployment in tissue. *Methods in Enzymology*, 385:361–370.
- Chance, B. and Baltscheffsky, H. (1958). Respiratory Enzymes in Oxidative Phosphorylation. *Journal of Biological Chemistry*, 233(3):736–739.
- Chance, B., Cohen, P., Jobsis, F., and Schoener, B. (1962). Intracellular Oxidation-Reduction States in Vivo: The microfluorometry of pyridine nucleotide gives a continuous measurement of the oxidation state. *Science*, 137(3529):499–508.
- Chance, B. and Lieberman, M. (1978). Intrinsic fluorescence emission from the cornea at low temperatures: Evidence of mitochondrial signals and their differing redox states in epithelial and endothelial sides. *Experimental Eye Research*, 26(1):111–117.
- Chance, B., Schoener, B., Oshino, R., Itshak, F., and Nakase, Y. (1979). Oxidation-reduction ratio studies of mitochondria in freeze-trapped samples. NADH and flavoprotein fluorescence signals. *The Journal of Biological Chemistry*, 254(11):4764–4771.
- Chang, C.-R. and Blackstone, C. (2010). Dynamic regulation of mitochondrial fission through modification of the dynamin-related protein Drp1. *Annals of the New York Academy of Sciences*, 1201:34–39.
- Cheezum, M. K., Walker, W. F., and Guilford, W. H. (2001). Quantitative Comparison of Algorithms for Tracking Single Fluorescent Particles. *Biophysical Journal*, 81(4):2378–2388.
- Chen, J., Lee, H.-J., Wu, X., Huo, L., Kim, S.-J., Xu, L., Wang, Y., He, J., Bollu, L. R., Gao, G., Su, F., Briggs, J., Liu, X., Melman, T., Asara, J. M., Fidler, I. J., Cantley, L. C., Locasale, J. W., and Weihua, Z. (2015). Gain of glucose-independent growth upon metastasis of breast cancer cells to the brain. *Cancer Research*, 75(3):554–565.
- Chiu, C.-L., Digman, M. A., and Gratton, E. (2013). Cell matrix remodeling ability shown by image spatial correlation. *Journal of Biophysics (Hindawi Publishing Corporation: Online)*, 2013:532030.
- Choe, S. S., Huh, J. Y., Hwang, I. J., Kim, J. I., and Kim, J. B. (2016). Adipose Tissue Remodeling: Its Role in Energy Metabolism and Metabolic Disorders. *Frontiers in Endocrinology*, 7:30.
- Choi, S. W., Gerencser, A. A., and Nicholls, D. G. (2009). Bioenergetic analysis of isolated cerebrocortical nerve terminals on a microgram scale: spare respiratory capacity and stochastic mitochondrial failure. *Journal of Neurochemistry*, 109(4):1179–1191.
- Christen, S., Lorendeau, D., Schmieder, R., Broekaert, D., Metzger, K., Veys, K., Elia, I., Buescher, J. M., Orth, M. F., Davidson, S. M., Grünewald, T. G. P., De Bock, K., and Fendt, S.-M. (2016). Breast Cancer-Derived Lung Metastases Show Increased Pyruvate Carboxylase-Dependent Anaplerosis. *Cell Reports*, 17(3):837–848.

- Cinco, R., Digman, M. A., Gratton, E., and Luderer, U. (2016). Spatial Characterization of Bioenergetics and Metabolism of Primordial to Preovulatory Follicles in Whole Ex Vivo Murine Ovary. *Biology of Reproduction*, 95(6).
- Ciobanasiu, C., Faivre, B., and Le Clainche, C. (2013). Integrating actin dynamics, mechanotransduction and integrin activation: The multiple functions of actin binding proteins in focal adhesions. *European Journal of Cell Biology*, 92(10):339–348.
- Claes, A., Idema, A. J., and Wesseling, P. (2007). Diffuse glioma growth: a guerilla war. *Acta Neuropathologica*, 114(5):443–458.
- Col, N. F., Ochs, L., Springmann, V., Aragaki, A. K., and Chlebowski, R. T. (2012). Metformin and breast cancer risk: a meta-analysis and critical literature review. *Breast Cancer Research and Treatment*, 135(3):639–646.
- Covarrubias, A. J., Perrone, R., Grozio, A., and Verdin, E. (2021). NAD<sup>+</sup> metabolism and its roles in cellular processes during ageing. *Nature Reviews. Molecular Cell Biology*, 22(2):119–141.
- Creagh, E. M., Sheehan, D., and Cotter, T. G. (2000). Heat shock proteins—modulators of apoptosis in tumour cells. *Leukemia*, 14(7):1161–1173.
- Cuddapah, V. A., Robel, S., Watkins, S., and Sontheimer, H. (2014). A neurocentric perspective on glioma invasion. *Nature Reviews. Neuroscience*, 15(7):455–465.
- Cunniff, B., McKenzie, A. J., Heintz, N. H., and Howe, A. K. (2016). AMPK activity regulates trafficking of mitochondria to the leading edge during cell migration and matrix invasion. *Molecular Biology of the Cell*, 27(17):2662–2674.
- Dai, X., Li, T., Bai, Z., Yang, Y., Liu, X., Zhan, J., and Shi, B. (2015). Breast cancer intrinsic subtype classification, clinical use and future trends. *American Journal of Cancer Research*, 5(10):2929–2943.
- Daniel, V. C., Marchionni, L., Hierman, J. S., Rhodes, J. T., Devereux, W. L., Rudin, C. M., Yung, R., Parmigiani, G., Dorsch, M., Peacock, C. D., and Watkins, D. N. (2009). A Primary Xenograft Model of Small-Cell Lung Cancer Reveals Irreversible Changes in Gene Expression Imposed by Culture In vitro. *Cancer Research*, 69(8):3364–3373.
- Datta, R., Alfonso-Garcia, A., Cinco, R., and Gratton, E. (2015). Fluorescence lifetime imaging of endogenous biomarker of oxidative stress. *Scientific Reports*, 5:9848.
- Datta, R., Heaster, T. M., Sharick, J. T., Gillette, A. A., and Skala, M. C. (2020). Fluorescence lifetime imaging microscopy: fundamentals and advances in instrumentation, analysis, and applications. *Journal of Biomedical Optics*, 25(7):071203.
- Davis, R. T., Blake, K., Ma, D., Gabra, M. B. I., Hernandez, G. A., Phung, A. T., Yang, Y., Maurer, D., Lefebvre, A. E. Y. T., Alshetaiwi, H., Xiao, Z., Liu, J., Locasale, J. W., Digman, M. A., Mjolsness, E., Kong, M., Werb, Z., and Lawson, D. A. (2020). Transcriptional diversity and bioenergetic shift in human breast cancer metastasis revealed by single-cell RNA sequencing. *Nature Cell Biology*, 22(3):310–320.
- Dayan, F., Bilton, R. L., Laferrière, J., Trottier, E., Roux, D., Pouyssegur, J., and Mazure, N. M. (2009). Activation of HIF-1 $\alpha$  in exponentially growing cells via hypoxic stimulation is independent of the Akt/mTOR pathway. *Journal of Cellular Physiology*, 218(1):167–174.
- DeBerardinis, R. J., Lum, J. J., Hatzivassiliou, G., and Thompson, C. B. (2008). The Biology of Cancer: Metabolic Reprogramming Fuels Cell Growth and Proliferation. *Cell Metabolism*, 7(1):11–20.

- DeCamp, S. J., Tsuda, V. M. K., Ferruzzi, J., Koehler, S. A., Giblin, J. T., Roblyer, D., Zaman, M. H., Weiss, S. T., Kılıç, A., De Marzio, M., Park, C. Y., Ogassavara, N. C., Mitchel, J. A., Butler, J. P., and Fredberg, J. J. (2020). Epithelial layer unjamming shifts energy metabolism toward glycolysis. *Scientific Reports*, 10(1):18302.
- DeRose, Y. S., Gligorich, K. M., Wang, G., Georgelas, A., Bowman, P., Courdy, S. J., Welm, A. L., and Welm, B. E. (2013). Patient-Derived Models of Human Breast Cancer: Protocols for In Vitro and In Vivo Applications in Tumor Biology and Translational Medicine. *Current Protocols in Pharmacology*, 60(1):14.23.1–14.23.43.
- DeRose, Y. S., Wang, G., Lin, Y.-C., Bernard, P. S., Buys, S. S., Ebbert, M. T. W., Factor, R., Matsen, C., Milash, B. A., Nelson, E., Neumayer, L., Randall, R. L., Stijleman, I. J., Welm, B. E., and Welm, A. L. (2011). Tumor grafts derived from women with breast cancer authentically reflect tumor pathology, growth, metastasis and disease outcomes. *Nature Medicine*, 17(11):1514–1520.
- Desai, S. P., Bhatia, S. N., Toner, M., and Irimia, D. (2013). Mitochondrial Localization and the Persistent Migration of Epithelial Cancer cells. *Biophysical Journal*, 104(9):2077–2088.
- DeSantis, C. E., Fedewa, S. A., Goding Sauer, A., Kramer, J. L., Smith, R. A., and Jemal, A. (2016). Breast cancer statistics, 2015: Convergence of incidence rates between black and white women. *CA: a cancer journal for clinicians*, 66(1):31–42.
- Digman, M. A., Caiolfa, V. R., Zamai, M., and Gratton, E. (2008). The phasor approach to fluorescence lifetime imaging analysis. *Biophysical Journal*, 94(2):L14–16.
- Dillekås, H., Rogers, M. S., and Straume, O. (2019). Are 90% of deaths from cancer caused by metastases? *Cancer Medicine*, 8(12):5574–5576.
- Divakaruni, A. S., Rogers, G. W., and Murphy, A. N. (2014). Measuring Mitochondrial Function in Permeabilized Cells Using the Seahorse XF Analyzer or a Clark-Type Oxygen Electrode. *Current Protocols in Toxicology*, 60(1):25.2.1–25.2.16.
- Dobin, A., Davis, C. A., Schlesinger, F., Drenkow, J., Zaleski, C., Jha, S., Batut, P., Chaisson, M., and Gingeras, T. R. (2013). STAR: ultrafast universal RNA-seq aligner. *Bioinformatics*, 29(1):15–21.
- Dong, C., Yuan, T., Wu, Y., Wang, Y., Fan, T. W. M., Miriyala, S., Lin, Y., Yao, J., Shi, J., Kang, T., Lorkiewicz, P., St Clair, D., Hung, M.-C., Evers, B. M., and Zhou, B. P. (2013). Loss of FBP1 by Snail-mediated repression provides metabolic advantages in basal-like breast cancer. *Cancer Cell*, 23(3):316–331.
- Dorn, J. F., Danuser, G., and Yang, G. (2008). Computational Processing and Analysis of Dynamic Fluorescence Image Data. In *Methods in Cell Biology*, volume 85 of *Fluorescent Proteins*, pages 497–538. Academic Press.
- Dornier, E., Rabas, N., Mitchell, L., Novo, D., Dhayade, S., Marco, S., Mackay, G., Sumpton, D., Pallares, M., Nixon, C., Blyth, K., Macpherson, I. R., Rainero, E., and Norman, J. C. (2017). Glutaminolysis drives membrane trafficking to promote invasiveness of breast cancer cells. *Nature Communications*, 8(1):2255.
- Dupuy, F., Tabariès, S., Andrzejewski, S., Dong, Z., Blagih, J., Annis, M. G., Omeroglu, A., Gao, D., Leung, S., Amir, E., Clemons, M., Aguilar-Mahecha, A., Basik, M., Vincent, E. E., St-Pierre, J., Jones, R. G., and Siegel, P. M. (2015). PDK1-Dependent Metabolic Reprogramming Dictates Metastatic Potential in Breast Cancer. *Cell Metabolism*, 22(4):577–589.

- Ebert, D., Haller, R. G., and Walton, M. E. (2003). Energy contribution of octanoate to intact rat brain metabolism measured by  $^{13}\text{C}$  nuclear magnetic resonance spectroscopy. *The Journal of Neuroscience: The Official Journal of the Society for Neuroscience*, 23(13):5928–5935.
- Edmondson, R., Broglie, J. J., Adcock, A. F., and Yang, L. (2014). Three-dimensional cell culture systems and their applications in drug discovery and cell-based biosensors. *Assay and Drug Development Technologies*, 12(4):207–218.
- Elia, I., Broekaert, D., Christen, S., Boon, R., Radaelli, E., Orth, M. F., Verfaillie, C., Grünewald, T. G. P., and Fendt, S.-M. (2017). Proline metabolism supports metastasis formation and could be inhibited to selectively target metastasizing cancer cells. *Nature Communications*, 8:15267.
- Elia, I., Doglioni, G., and Fendt, S.-M. (2018). Metabolic Hallmarks of Metastasis Formation. *Trends in Cell Biology*, 28(8):673–684.
- Elodi, P. and Szabolcsi, G. (1959). Role of the Coenzyme in the Stabilization of Glyceraldehyde-3-phosphate Dehydrogenase. *Nature*, 184(4679):56–56.
- Estrella, V., Chen, T., Lloyd, M., Wojtkowiak, J., Cornnell, H. H., Ibrahim-Hashim, A., Bailey, K., Balagurunathan, Y., Rothberg, J. M., Sloane, B. F., Johnson, J., Gatenby, R. A., and Gillies, R. J. (2013). Acidity Generated by the Tumor Microenvironment Drives Local Invasion. *Cancer Research*, 73(5):1524–1535.
- Falk, T., Mai, D., Bensch, R., Cicek, O., Abdulkadir, A., Marrakchi, Y., Böhm, A., Deubner, J., Jäckel, Z., Seiwald, K., Dovzhenko, A., Tietz, O., Dal Bosco, C., Walsh, S., Saltukoglu, D., Tay, T. L., Prinz, M., Palme, K., Simons, M., Diester, I., Brox, T., and Ronneberger, O. (2019). U-Net: deep learning for cell counting, detection, and morphometry. *Nature Methods*, 16(1):67–70.
- Federico, A., Cardaioli, E., Da Pozzo, P., Formichi, P., Gallus, G. N., and Radi, E. (2012). Mitochondria, oxidative stress and neurodegeneration. *Journal of the Neurological Sciences*, 322(1):254–262.
- Fernyhough, P. and McGavock, J. (2014). Chapter 25 - Mechanisms of disease: Mitochondrial dysfunction in sensory neuropathy and other complications in diabetes. In Zochodne, D. W. and Malik, R. A., editors, *Handbook of Clinical Neurology*, volume 126 of *Diabetes and the Nervous System*, pages 353–377. Elsevier.
- Ferri, G., Tesi, M., Massarelli, F., Marselli, L., Marchetti, P., and Cardarelli, F. (2020). Metabolic response of Insulinoma 1E cells to glucose stimulation studied by fluorescence lifetime imaging. *FASEB BioAdvances*, 2(7):409–418.
- Fidler, I. J. (1970). Metastasis: quantitative analysis of distribution and fate of tumor emboli labeled with  $^{125}\text{I}$ -5-iodo-2'-deoxyuridine. *Journal of the National Cancer Institute*, 45(4):773–782.
- Fiorillo, M., Lamb, R., Tanowitz, H. B., Mutti, L., Krstic-Demonacos, M., Cappello, A. R., Martinez-Outschoorn, U. E., Sotgia, F., and Lisanti, M. P. (2016). Repurposing atovaquone: targeting mitochondrial complex III and OXPHOS to eradicate cancer stem cells. *Oncotarget*, 7(23):34084–34099.
- Fischer, C. A., Besora-Casals, L., Rolland, S. G., Haeussler, S., Singh, K., Duchon, M., Conradt, B., and Marr, C. (2020). MitoSegNet: Easy-to-use Deep Learning Segmentation for Analyzing Mitochondrial Morphology. *iScience*, 23(10):101601.

- Frese, K. K. and Tuveson, D. A. (2007). Maximizing mouse cancer models. *Nature Reviews Cancer*, 7(9):654–658.
- Friedl, P. and Wolf, K. (2003). Tumour-cell invasion and migration: diversity and escape mechanisms. *Nature Reviews. Cancer*, 3(5):362–374.
- Gafni, A. and Brand, L. (1976). Fluorescence decay studies of reduced nicotinamide adenine dinucleotide in solution and bound to liver alcohol dehydrogenase. *Biochemistry*, 15(15):3165–3171.
- Gardel, M. L., Schneider, I. C., Aratyn-Schaus, Y., and Waterman, C. M. (2010). Mechanical Integration of Actin and Adhesion Dynamics in Cell Migration. *Annual Review of Cell and Developmental Biology*, 26(1):315–333.
- Gaviola, E. (1926). Die Abklingungszeiten der Fluoreszenz von Farbstofflösungen. *Zeitschrift für Physik*, 35(10):748–756.
- Giannoni, E., Buricchi, F., Grimaldi, G., Parri, M., Cialdai, F., Taddei, M. L., Raugei, G., Ramponi, G., and Chiarugi, P. (2008). Redox regulation of anoikis: reactive oxygen species as essential mediators of cell survival. *Cell Death and Differentiation*, 15(5):867–878.
- GIEDT, R. J., PFEIFFER, D. R., MATZAVINOS, A., KAO, C.-Y., and ALEVRIADOU, B. R. (2012). Mitochondrial Dynamics and Motility Inside Living Vascular Endothelial Cells: Role of Bioenergetics. *Annals of biomedical engineering*, 40(9):1903–1916.
- Gomes, L. C., Di Benedetto, G., and Scorrano, L. (2011). During autophagy mitochondria elongate, are spared from degradation and sustain cell viability. *Nature cell biology*, 13(5):589–598.
- Gottling, P. F. (1923). The Determination of the Time between Excitation and Emission for certain Fluorescent Solids. *Physical Review*, 22(6):566–573.
- Gould, C. M. and Courtneidge, S. A. (2014). Regulation of invadopodia by the tumor microenvironment. *Cell Adhesion & Migration*, 8(3):226–235.
- Green, D. R. and Reed, J. C. (1998). Mitochondria and Apoptosis. *Science*, 281(5381):1309–1312.
- Guppy, M., Greiner, E., and Brand, K. (1993). The role of the Crabtree effect and an endogenous fuel in the energy metabolism of resting and proliferating thymocytes. *European Journal of Biochemistry*, 212(1):95–99.
- Györfy, B., Lanczky, A., Eklund, A. C., Denkert, C., Budczies, J., Li, Q., and Szallasi, Z. (2010). An online survival analysis tool to rapidly assess the effect of 22,277 genes on breast cancer prognosis using microarray data of 1,809 patients. *Breast Cancer Research and Treatment*, 123(3):725–731.
- Gómez-Cuadrado, L., Tracey, N., Ma, R., Qian, B., and Brunton, V. G. (2017). Mouse models of metastasis: progress and prospects. *Disease Models & Mechanisms*, 10(9):1061–1074.
- Haage, A. and Schneider, I. C. (2014). Cellular contractility and extracellular matrix stiffness regulate matrix metalloproteinase activity in pancreatic cancer cells. *The FASEB Journal*, 28(8):3589–3599.
- Hafeez, B. B., Fischer, J. W., Singh, A., Zhong, W., Mustafa, A., Meske, L., Sheikhan, M. O., and Verma, A. K. (2015). Plumbagin Inhibits Prostate Carcinogenesis in Intact and Castrated PTEN Knockout Mice via Targeting PKC $\epsilon$ , Stat3, and Epithelial-to-Mesenchymal Transition Markers. *Cancer Prevention Research*, 8(5):375–386.

- Hafeez, B. B., Zhong, W., Mustafa, A., Fischer, J. W., Witkowski, O., and Verma, A. K. (2012). Plumbagin inhibits prostate cancer development in TRAMP mice via targeting PKC $\epsilon$ , Stat3 and neuroendocrine markers. *Carcinogenesis*, 33(12):2586–2592.
- Hanahan, D. and Weinberg, R. A. (2011). Hallmarks of Cancer: The Next Generation. *Cell*, 144(5):646–674.
- Hao, W., Chang, C.-P. B., Tsao, C.-C., and Xu, J. (2010). Oligomycin-induced Bioenergetic Adaptation in Cancer Cells with Heterogeneous Bioenergetic Organization. *Journal of Biological Chemistry*, 285(17):12647–12654.
- Hayashi, T., Hirshman, M. F., Kurth, E. J., Winder, W. W., and Goodyear, L. J. (1998). Evidence for 5' AMP-activated protein kinase mediation of the effect of muscle contraction on glucose transport. *Diabetes*, 47(8):1369–1373.
- Heggeness, M. H., Simon, M., and Singer, S. J. (1978). Association of mitochondria with microtubules in cultured cells. *Proceedings of the National Academy of Sciences*, 75(8):3863–3866.
- Heiden, M. G. V., Cantley, L. C., and Thompson, C. B. (2009). Understanding the Warburg Effect: The Metabolic Requirements of Cell Proliferation. *Science*, 324(5930):1029–1033.
- Held, P. (2018). Using Phenol Red to Assess pH in Tissue Culture Media.
- Hermann, P. C., Huber, S. L., Herrler, T., Aicher, A., Ellwart, J. W., Guba, M., Bruns, C. J., and Heeschen, C. (2007). Distinct populations of cancer stem cells determine tumor growth and metastatic activity in human pancreatic cancer. *Cell Stem Cell*, 1(3):313–323.
- Hidalgo, M., Amant, F., Biankin, A. V., Budinska, E., Byrne, A. T., Caldas, C., Clarke, R. B., Jong, S. d., Jonkers, J., Mælandsmo, G. M., Roman-Roman, S., Seoane, J., Trusolino, L., and Villanueva, A. (2014). Patient-Derived Xenograft Models: An Emerging Platform for Translational Cancer Research. *Cancer Discovery*, 4(9):998–1013.
- Hirata, H., Tatsumi, H., Lim, C. T., and Sokabe, M. (2014). Force-dependent vinculin binding to talin in live cells: a crucial step in anchoring the actin cytoskeleton to focal adhesions. *American Journal of Physiology-Cell Physiology*, 306(6):C607–C620.
- Hochhauser, D. and Caldas, C. (2017). Of mice and men: patient-derived xenografts in cancer medicine. *Annals of Oncology: Official Journal of the European Society for Medical Oncology*, 28(10):2330–2331.
- Hull, R. V., Conger, P. S., and Hoobler, R. J. (2001). Conformation of NADH studied by fluorescence excitation transfer spectroscopy. *Biophysical Chemistry*, 90(1):9–16.
- Huth, J., Buchholz, M., Kraus, J. M., Schmucker, M., von Wichert, G., Krndija, D., Seufferlein, T., Gress, T. M., and Kestler, H. A. (2010). Significantly improved precision of cell migration analysis in time-lapse video microscopy through use of a fully automated tracking system. *BMC Cell Biology*, 11(1):24.
- Höpf, G., Gassmann, M., and Desbaillets, I. (2004). Differentiating embryonic stem cells into embryoid bodies. *Methods in Molecular Biology (Clifton, N.J.)*, 254:79–98.
- Ikwegbue, P. C., Masamba, P., Oyinloye, B. E., and Kappo, A. P. (2018). Roles of Heat Shock Proteins in Apoptosis, Oxidative Stress, Human Inflammatory Diseases, and Cancer. *Pharmaceutics*, 11(1):2.
- Indra, I. and Beningo, K. A. (2011). An in vitro correlation of metastatic capacity, substrate rigidity, and ECM composition. *Journal of Cellular Biochemistry*, 112(11):3151–3158.



- Isensee, F., Jaeger, P. F., Kohl, S. A. A., Petersen, J., and Maier-Hein, K. H. (2021). nnU-Net: a self-configuring method for deep learning-based biomedical image segmentation. *Nature Methods*, 18(2):203–211.
- Iwata, R., Casimir, P., and Vanderhaeghen, P. (2020). Mitochondrial dynamics in postmitotic cells regulate neurogenesis. *Science*, 369(6505):858–862.
- Izumchenko, E., Paz, K., Ciznadija, D., Sloma, I., Katz, A., Vasquez-Dunddel, D., Ben-Zvi, I., Stebbing, J., McGuire, W., Harris, W., Maki, R., Gaya, A., Bedi, A., Zacharoulis, S., Ravi, R., Wexler, L. H., Hoque, M. O., Rodriguez-Galindo, C., Pass, H., Peled, N., Davies, A., Morris, R., Hidalgo, M., and Sidransky, D. (2017). Patient-derived xenografts effectively capture responses to oncology therapy in a heterogeneous cohort of patients with solid tumors. *Annals of Oncology: Official Journal of the European Society for Medical Oncology*, 28(10):2595–2605.
- Jabłoński, A. (1935). Über den Mechanismus der Photolumineszenz von Farbstoffphosphoren. *Zeitschrift für Physik*, 94(1):38–46.
- Jameson, D. M., Gratton, E., and Hall, R. D. (1984). The Measurement and Analysis of Heterogeneous Emissions by Multifrequency Phase and Modulation Fluorometry. *Applied Spectroscopy Reviews*, 20(1):55–106.
- Jameson, D. M., Thomas, V., and Zhou, D. (1989). Time-resolved fluorescence studies on NADH bound to mitochondrial malate dehydrogenase. *Biochimica et Biophysica Acta (BBA) - Protein Structure and Molecular Enzymology*, 994(2):187–190.
- Jarrett, S. G., Novak, M., Harris, N., Merlino, G., Slominski, A., and Kaetzel, D. M. (2013). NM23 deficiency promotes metastasis in a UV radiation-induced mouse model of human melanoma. *Clinical & Experimental Metastasis*, 30(1):25–36.
- Kamarajugadda, S., Stemboroski, L., Cai, Q., Simpson, N. E., Nayak, S., Tan, M., and Lu, J. (2012). Glucose oxidation modulates anoikis and tumor metastasis. *Molecular and Cellular Biology*, 32(10):1893–1907.
- Kanchanawong, P., Shtengel, G., Pasapera, A. M., Ramko, E. B., Davidson, M. W., Hess, H. F., and Waterman, C. M. (2010). Nanoscale architecture of integrin-based cell adhesions. *Nature*, 468(7323):580–584.
- Kandel, J., Chou, P., and Eckmann, D. M. (2015). Automated detection of whole-cell mitochondrial motility and its dependence on cytoarchitectural integrity. *Biotechnology and bioengineering*, 112(7):1395–1405.
- Kapitein, L. and Hoogenraad, C. (2015). Building the Neuronal Microtubule Cytoskeleton. *Neuron*, 87(3):492–506.
- Keller, G. M. (1995). In vitro differentiation of embryonic stem cells. *Current Opinion in Cell Biology*, 7(6):862–869.
- Kessenbrock, K., Plaks, V., and Werb, Z. (2010). Matrix Metalloproteinases: Regulators of the Tumor Microenvironment. *Cell*, 141(1):52–67.
- Kim, D.-H. and Wirtz, D. (2013). Focal adhesion size uniquely predicts cell migration. *The FASEB Journal*, 27(4):1351–1361.
- Klopfenstein, D. R. and Vale, R. D. (2004). The Lipid Binding Pleckstrin Homology Domain in UNC-104 Kinesin is Necessary for Synaptic Vesicle Transport in *Caenorhabditis elegans*. *Molecular Biology of the Cell*, 15(8):3729–3739.
- Kolb, D. A. and Weber, G. (1975). Quantitative demonstration of the reciprocity of ligand effects in the ternary complex of chicken heart lactate dehydrogenase with nicotinamide

- adenine dinucleotide oxalate. *Biochemistry*, 14(20):4471–4476.
- Koppenol, W. H., Bounds, P. L., and Dang, C. V. (2011). Otto Warburg’s contributions to current concepts of cancer metabolism. *Nature Reviews. Cancer*, 11(5):325–337.
- Krämer, A., Green, J., Pollard, J., and Tugendreich, S. (2014). Causal analysis approaches in Ingenuity Pathway Analysis. *Bioinformatics (Oxford, England)*, 30(4):523–530.
- Kumar, S., Meuter, A., Thapa, P., Langstraat, C., Giri, S., Chien, J., Rattan, R., Cliby, W., and Shridhar, V. (2013). Metformin intake is associated with better survival in ovarian cancer: a case-control study. *Cancer*, 119(3):555–562.
- König, K., So, P. T., Mantulin, W. W., Tromberg, B. J., and Gratton, E. (1996). Two-photon excited lifetime imaging of autofluorescence in cells during UVA and NIR photostress. *Journal of microscopy*, 183(Pt 3):197–204.
- Lakowicz, J. R., Szmajda, H., Nowaczyk, K., Berndt, K. W., and Johnson, M. (1992). Fluorescence lifetime imaging. *Analytical Biochemistry*, 202(2):316–330.
- Lambert, A. W., Pattabiraman, D. R., and Weinberg, R. A. (2017). Emerging Biological Principles of Metastasis. *Cell*, 168(4):670–691.
- Lawson, D. A., Bhakta, N. R., Kessenbrock, K., Prummel, K. D., Yu, Y., Takai, K., Zhou, A., Eyob, H., Balakrishnan, S., Wang, C.-Y., Yaswen, P., Goga, A., and Werb, Z. (2015). Single-cell analysis reveals a stem-cell program in human metastatic breast cancer cells. *Nature*, 526(7571):131–135.
- Lawson, D. A., Kessenbrock, K., Davis, R. T., Pervolarakis, N., and Werb, Z. (2018). Tumour heterogeneity and metastasis at single-cell resolution. *Nature Cell Biology*, 20(12):1349–1360.
- LeBleu, V. S., O’Connell, J. T., Gonzalez Herrera, K. N., Wikman, H., Pantel, K., Haigis, M. C., de Carvalho, F. M., Damascena, A., Domingos Chinen, L. T., Rocha, R. M., Asara, J. M., and Kalluri, R. (2014). PGC-1 $\alpha$  mediates mitochondrial biogenesis and oxidative phosphorylation in cancer cells to promote metastasis. *Nature Cell Biology*, 16(10):992–1003, 1–15.
- Lee, M. H., Park, N., Yi, C., Han, J. H., Hong, J. H., Kim, K. P., Kang, D. H., Sessler, J. L., Kang, C., and Kim, J. S. (2014). Mitochondria-Immobilized pH-Sensitive Off-On Fluorescent Probe. *Journal of the American Chemical Society*, 136(40):14136–14142.
- Lefebvre, A. E. Y. T., Ma, D., Kessenbrock, K., Lawson, D. A., and Digman, M. A. (2021). Automated segmentation and tracking of mitochondria in live-cell time-lapse images. *Nature Methods*, pages 1–12.
- Lehuédé, C., Dupuy, F., Rabinovitch, R., Jones, R. G., and Siegel, P. M. (2016). Metabolic Plasticity as a Determinant of Tumor Growth and Metastasis. *Cancer Research*, 76(18):5201–5208.
- Lemma, S., Di Pompo, G., Porporato, P. E., Sboarina, M., Russell, S., Gillies, R. J., Baldini, N., Sonveaux, P., and Avnet, S. (2017). MDA-MB-231 breast cancer cells fuel osteoclast metabolism and activity: A new rationale for the pathogenesis of osteolytic bone metastases. *Biochimica Et Biophysica Acta. Molecular Basis of Disease*, 1863(12):3254–3264.
- Leonard, A. P., Cameron, R. B., Speiser, J. L., Wolf, B. J., Peterson, Y. K., Schnellmann, R. G., Beeson, C. C., and Rohrer, B. (2015). Quantitative analysis of mitochondrial morphology and membrane potential in living cells using high-content imaging, machine learning, and morphological binning. *Biochimica et Biophysica Acta (BBA) -*

- Molecular Cell Research*, 1853(2):348–360.
- Levental, K. R., Yu, H., Kass, L., Lakins, J. N., Egeblad, M., Erler, J. T., Fong, S. F. T., Csiszar, K., Giaccia, A., Weninger, W., Yamauchi, M., Gasser, D. L., and Weaver, V. M. (2009). Matrix Crosslinking Forces Tumor Progression by Enhancing Integrin Signaling. *Cell*, 139(5):891–906.
- Li, X.-X., Wang, Z.-J., Zheng, Y., Guan, Y.-F., Yang, P.-B., Chen, X., Peng, C., He, J.-P., Ai, Y.-L., Wu, S.-F., Chien, K.-Y., Wu, Q., and Chen, H.-Z. (2018). Nuclear Receptor Nur77 Facilitates Melanoma Cell Survival under Metabolic Stress by Protecting Fatty Acid Oxidation. *Molecular Cell*, 69(3):480–492.e7.
- Liberti, M. V. and Locasale, J. W. (2016). The Warburg Effect: How Does it Benefit Cancer Cells? *Trends in Biochemical Sciences*, 41(3):211–218.
- Lien, E. C., Lyssiotis, C. A., and Cantley, L. C. (2016). Metabolic Reprogramming by the PI3K-Akt-mTOR Pathway in Cancer. *Recent Results in Cancer Research. Fortschritte Der Krebsforschung. Progres Dans Les Recherches Sur Le Cancer*, 207:39–72.
- Lihavainen, E., Mäkelä, J., Spelbrink, J. N., and Ribeiro, A. S. (2012). Mytoe: automatic analysis of mitochondrial dynamics. *Bioinformatics*, 28(7):1050–1051.
- Liu, M., Quek, L.-E., Sultani, G., and Turner, N. (2016). Epithelial-mesenchymal transition induction is associated with augmented glucose uptake and lactate production in pancreatic ductal adenocarcinoma. *Cancer & Metabolism*, 4:19.
- Liu, R., Zhao, Z., Zou, L., Fang, Q., Chen, L., Argento, A., and Lo, J. F. (2015). Compact, non-invasive frequency domain lifetime differentiation of collagens and elastin. *Sensors and Actuators B: Chemical*, 219:283–293.
- Lodhia, K. A., Hadley, A. M., Haluska, P., and Scott, C. L. (2015). Prioritizing therapeutic targets using patient-derived xenograft models. *Biochimica Et Biophysica Acta*, 1855(2):223–234.
- Loo, J. M., Scherl, A., Nguyen, A., Man, F. Y., Weinberg, E., Zeng, Z., Saltz, L., Paty, P. B., and Tavazoie, S. F. (2015). Extracellular metabolic energetics can promote cancer progression. *Cell*, 160(3):393–406.
- Love, M. I., Huber, W., and Anders, S. (2014). Moderated estimation of fold change and dispersion for RNA-seq data with DESeq2. *Genome Biology*, 15(12):550.
- Lu, J., Tan, M., and Cai, Q. (2015). The Warburg effect in tumor progression: mitochondrial oxidative metabolism as an anti-metastasis mechanism. *Cancer Letters*, 356(2 Pt A):156–164.
- Luz, A. L., Smith, L. L., Rooney, J. P., and Meyer, J. N. (2015). Seahorse Xfe24 Extracellular Flux Analyzer-Based Analysis of Cellular Respiration in *Caenorhabditis elegans*. *Current Protocols in Toxicology*, 66(1):25.7.1–25.7.15.
- Lv, Z., Yan, X., Lu, L., Su, C., and He, Y. (2018). Atovaquone enhances doxorubicin’s efficacy via inhibiting mitochondrial respiration and STAT3 in aggressive thyroid cancer. *Journal of Bioenergetics and Biomembranes*, 50(4):263–270.
- López-Soto, A., Gonzalez, S., Smyth, M. J., and Galluzzi, L. (2017). Control of Metastasis by NK Cells. *Cancer Cell*, 32(2):135–154.
- Ma, D., Hernandez, G. A., Lefebvre, A. E. Y. T., Alshetaiwi, H., Blake, K., Dave, K. R., Rauf, M., Williams, J. W., Davis, R. T., Evans, K. T., Masoud, M. Y. G., Lee, R., Edwards, R. A., Digman, M. A., Kessenbrock, K., and Lawson, D. A. (2020). Patient-derived xenograft culture-transplant system for investigation of human breast cancer

- metastasis. *bioRxiv*, page 2020.06.25.172056.
- Ma, D., Pignanelli, C., Tarade, D., Gilbert, T., Noel, M., Mansour, F., Adams, S., Dowhayko, A., Stokes, K., Vshyvenko, S., Collins, J., Hudlicky, T., McNulty, J., and Pandey, S. (2017). Cancer Cell Mitochondria Targeting by Pancreatistatin Analogs is Dependent on Functional Complex II and III. *Scientific Reports*, 7(1):42957.
- Ma, N., Digman, M. A., Malacrida, L., and Gratton, E. (2016). Measurements of absolute concentrations of NADH in cells using the phasor FLIM method. *Biomedical Optics Express*, 7(7):2441–2452.
- Machesky, L. M. (2008). Lamellipodia and filopodia in metastasis and invasion. *FEBS Letters*, 582(14):2102–2111.
- Mah, E. J., Lefebvre, A. E. Y. T., McGahey, G. E., Yee, A. F., and Digman, M. A. (2018). Collagen density modulates triple-negative breast cancer cell metabolism through adhesion-mediated contractility. *Scientific Reports*, 8(1):17094.
- Maldonado, M. d. M., Medina, J. I., Velazquez, L., and Dharmawardhane, S. (2020). Targeting Rac and Cdc42 GEFs in Metastatic Cancer. *Frontiers in Cell and Developmental Biology*, 8:201.
- Malmström, A., Grønberg, B. H., Marosi, C., Stupp, R., Frappaz, D., Schultz, H., Abacioglu, U., Tavelin, B., Lhermitte, B., Hegi, M. E., Rosell, J., Henriksson, R., and Nordic Clinical Brain Tumour Study Group (NCBTSG) (2012). Temozolomide versus standard 6-week radiotherapy versus hypofractionated radiotherapy in patients older than 60 years with glioblastoma: the Nordic randomised, phase 3 trial. *The Lancet. Oncology*, 13(9):916–926.
- Mani, S. A., Guo, W., Liao, M.-J., Eaton, E. N., Ayyanan, A., Zhou, A. Y., Brooks, M., Reinhard, F., Zhang, C. C., Shipitsin, M., Campbell, L. L., Polyak, K., Briskin, C., Yang, J., and Weinberg, R. A. (2008). The epithelial-mesenchymal transition generates cells with properties of stem cells. *Cell*, 133(4):704–715.
- Marbaniang, C. and Kma, L. (2018). Dysregulation of Glucose Metabolism by Oncogenes and Tumor Suppressors in Cancer Cells. *Asian Pacific journal of cancer prevention: APJCP*, 19(9):2377–2390.
- Martin, G. R. (1981). Isolation of a pluripotent cell line from early mouse embryos cultured in medium conditioned by teratocarcinoma stem cells. *Proceedings of the National Academy of Sciences*, 78(12):7634–7638.
- Martin, K., Reimann, A., Fritz, R. D., Ryu, H., Jeon, N. L., and Pertz, O. (2016). Spatio-temporal co-ordination of RhoA, Rac1 and Cdc42 activation during prototypical edge protrusion and retraction dynamics. *Scientific Reports*, 6(1):21901.
- Mas-Moruno, C., Rechenmacher, F., and Kessler, H. (2010). Cilengitide: the first anti-angiogenic small molecule drug candidate design, synthesis and clinical evaluation. *Anti-Cancer Agents in Medicinal Chemistry*, 10(10):753–768.
- Massia, S. P. and Hubbell, J. A. (1991). Human endothelial cell interactions with surface-coupled adhesion peptides on a nonadhesive glass substrate and two polymeric biomaterials. *Journal of Biomedical Materials Research*, 25(2):223–242.
- Masui, K., Tanaka, K., Akhavan, D., Babic, I., Gini, B., Matsutani, T., Iwanami, A., Liu, F., Villa, G. R., Gu, Y., Campos, C., Zhu, S., Yang, H., Yong, W. H., Cloughesy, T. F., Mellinghoff, I. K., Cavenee, W. K., Shaw, R. J., and Mischel, P. S. (2013). mTOR complex 2 controls glycolytic metabolism in glioblastoma through FoxO acetylation

- and upregulation of c-Myc. *Cell Metabolism*, 18(5):726–739.
- Maus, M., Cotlet, M., Hofkens, J., Gensch, T., De Schryver, F. C., Schaffer, J., and Seidel, C. A. M. (2001). An Experimental Comparison of the Maximum Likelihood Estimation and Nonlinear Least-Squares Fluorescence Lifetime Analysis of Single Molecules. *Analytical Chemistry*, 73(9):2078–2086.
- McCarron, J. G., Wilson, C., Sandison, M. E., Olson, M. L., Girkin, J. M., Saunter, C., and Chalmers, S. (2013). From Structure to Function: Mitochondrial Morphology, Motion and Shaping in Vascular Smooth Muscle. *Journal of Vascular Research*, 50(5):357–371.
- Miller, K. E., Liu, X.-A., and Puthanveetil, S. V. (2015). Automated measurement of fast mitochondrial transport in neurons. *Frontiers in Cellular Neuroscience*, 9.
- Moon, H.-G., Oh, K., Lee, J., Lee, M., Kim, J.-Y., Yoo, T.-K., Seo, M. W., Park, A. K., Ryu, H. S., Jung, E.-J., Kim, N., Jeong, S., Han, W., Lee, D.-S., and Noh, D.-Y. (2015). Prognostic and functional importance of the engraftment-associated genes in the patient-derived xenograft models of triple-negative breast cancers. *Breast Cancer Research and Treatment*, 154(1):13–22.
- Moreno-Sanchez, R., Rodriguez-Enriquez, S., Marin-Hernandez, A., and Saavedra, E. (2007). Energy metabolism in tumor cells. *The FEBS journal*, 274(6):1393–1418.
- Morris, B. A., Burkel, B., Ponik, S. M., Fan, J., Condeelis, J. S., Aguirre-Ghiso, J. A., Castracane, J., Denu, J. M., and Keely, P. J. (2016). Collagen Matrix Density Drives the Metabolic Shift in Breast Cancer Cells. *EBioMedicine*, 13:146–156.
- Muller, F. L., Colla, S., Aquilanti, E., Manzo, V. E., Genovese, G., Lee, J., Eisenson, D., Narurkar, R., Deng, P., Nezi, L., Lee, M. A., Hu, B., Hu, J., Sahin, E., Ong, D., Fletcher-Sananikone, E., Ho, D., Kwong, L., Brennan, C., Wang, Y. A., Chin, L., and DePinho, R. A. (2012). Passenger deletions generate therapeutic vulnerabilities in cancer. *Nature*, 488(7411):337–342.
- Murata, M. M., Kong, X., Moncada, E., Chen, Y., Imamura, H., Wang, P., Berns, M. W., Yokomori, K., and Digman, M. A. (2019). NAD<sup>+</sup> consumption by PARP1 in response to DNA damage triggers metabolic shift critical for damaged cell survival. *Molecular Biology of the Cell*, pages mbc.E18–10–0650.
- Nagy, A., Lanczky, A., Menyhart, O., and Gyorffy, B. (2018). Validation of miRNA prognostic power in hepatocellular carcinoma using expression data of independent datasets. *Scientific Reports*, 8(1):9227.
- Nathanson, S. D. (2003). Insights into the mechanisms of lymph node metastasis. *Cancer*, 98(2):413–423.
- Neve, R. M., Chin, K., Fridlyand, J., Yeh, J., Baehner, F. L., Fevr, T., Clark, L., Bayani, N., Coppe, J.-P., Tong, F., Speed, T., Spellman, P. T., DeVries, S., Lapuk, A., Wang, N. J., Kuo, W.-L., Stilwell, J. L., Pinkel, D., Albertson, D. G., Waldman, F. M., McCormick, F., Dickson, R. B., Johnson, M. D., Lippman, M., Ethier, S., Gazdar, A., and Gray, J. W. (2006). A collection of breast cancer cell lines for the study of functionally distinct cancer subtypes. *Cancer Cell*, 10(6):515–527.
- Ng, M. R. and Brugge, J. S. (2009). A Stiff Blow from the Stroma: Collagen Crosslinking Drives Tumor Progression. *Cancer Cell*, 16(6):455–457.
- Nieman, K. M., Kenny, H. A., Penicka, C. V., Ladanyi, A., Buell-Gutbrod, R., Zillhardt, M. R., Romero, I. L., Carey, M. S., Mills, G. B., Hotamisligil, G. S., Yamada, S. D., Peter, M. E., Gwin, K., and Lengyel, E. (2011). Adipocytes promote ovarian cancer

- metastasis and provide energy for rapid tumor growth. *Nature Medicine*, 17(11):1498–1503.
- Nieto, M. A. (2013). Epithelial plasticity: a common theme in embryonic and cancer cells. *Science (New York, N.Y.)*, 342(6159):1234850.
- Nowell, P. (1976). The clonal evolution of tumor cell populations. *Science*, 194(4260):23–28.
- Obenauf, A. C. and Massagué, J. (2015). Surviving at a Distance: Organ-Specific Metastasis. *Trends in Cancer*, 1(1):76–91.
- Ochsner, M., Textor, M., Vogel, V., and Smith, M. L. (2010). Dimensionality Controls Cytoskeleton Assembly and Metabolism of Fibroblast Cells in Response to Rigidity and Shape. *PLOS ONE*, 5(3):e9445.
- Ogura, M., Yamaki, J., Homma, M. K., and Homma, Y. (2012). Mitochondrial c-Src regulates cell survival through phosphorylation of respiratory chain components. *The Biochemical Journal*, 447(2):281–289.
- Okabe, K., Yaku, K., Tobe, K., and Nakagawa, T. (2019). Implications of altered NAD metabolism in metabolic disorders. *Journal of Biomedical Science*, 26(1):34.
- Oskarsson, T., Batlle, E., and Massagué, J. (2014). Metastatic stem cells: sources, niches, and vital pathways. *Cell Stem Cell*, 14(3):306–321.
- Palorini, R., Simonetto, T., Cirulli, C., and Chiaradonna, F. (2013). Mitochondrial Complex I Inhibitors and Forced Oxidative Phosphorylation Synergize in Inducing Cancer Cell Death. *International Journal of Cell Biology*, 2013:e243876.
- Paszek, M. J., Zahir, N., Johnson, K. R., Lakins, J. N., Rozenberg, G. I., Gefen, A., Reinhart-King, C. A., Margulies, S. S., Dembo, M., Boettiger, D., Hammer, D. A., and Weaver, V. M. (2005). Tensional homeostasis and the malignant phenotype. *Cancer Cell*, 8(3):241–254.
- Pattabiraman, D. R. and Weinberg, R. A. (2014). Tackling the cancer stem cells - what challenges do they pose? *Nature Reviews. Drug Discovery*, 13(7):497–512.
- Pavlidis, S., Whitaker-Menezes, D., Castelló-Cros, R., Flomenberg, N., Witkiewicz, A. K., Frank, P. G., Casimiro, M. C., Wang, C., Fortina, P., Addya, S., Pestell, R. G., Martinez-outschoorn, U. e., Sotgia, F., and Lisanti, M. p. (2009). The reverse Warburg effect: aerobic glycolysis in cancer associated fibroblasts and the tumor stroma. *Cell cycle*, 8(23):3984–4001.
- Pavlova, N. N. and Thompson, C. B. (2016). THE EMERGING HALLMARKS OF CANCER METABOLISM. *Cell metabolism*, 23(1):27–47.
- Pedregosa, F., Varoquaux, G., Gramfort, A., Michel, V., Thirion, B., Grisel, O., Blondel, M., Prettenhofer, P., Weiss, R., Dubourg, V., Vanderplas, J., Passos, A., and Cournapeau, D. (2011). Scikit-learn: Machine Learning in Python. *Journal of Machine Learning Research*, 12:2825–2830.
- Petit, V. and Thiery, J.-P. (2000). Focal adhesions: Structure and dynamics. *Biology of the Cell*, 92(7):477–494.
- Pfeiffer, T., Schuster, S., and Bonhoeffer, S. (2001). Cooperation and Competition in the Evolution of ATP-Producing Pathways. *Science*, 292(5516):504–507.
- Pigino, G., Morfini, G., Pelsman, A., Mattson, M. P., Brady, S. T., and Busciglio, J. (2003). Alzheimer’s Presenilin 1 Mutations Impair Kinesin-Based Axonal Transport. *Journal of Neuroscience*, 23(11):4499–4508.

- Pilling, A. D., Horiuchi, D., Lively, C. M., and Saxton, W. M. (2006). Kinesin-1 and Dynein Are the Primary Motors for Fast Transport of Mitochondria in *Drosophila* Motor Axons. *Molecular Biology of the Cell*, 17(4):2057–2068.
- Piskounova, E., Agathocleous, M., Murphy, M. M., Hu, Z., Huddlestun, S. E., Zhao, Z., Leitch, A. M., Johnson, T. M., DeBerardinis, R. J., and Morrison, S. J. (2015). Oxidative stress inhibits distant metastasis by human melanoma cells. *Nature*, 527(7577):186–191.
- Piston, D. W., Sandison, D. R., and Webb, W. W. (1992). Time-resolved fluorescence imaging and background rejection by two-photon excitation in laser-scanning microscopy. In *Time-Resolved Laser Spectroscopy in Biochemistry III*, volume 1640, pages 379–389. International Society for Optics and Photonics.
- Ploumi, C., Daskalaki, I., and Tavernarakis, N. (2017). Mitochondrial biogenesis and clearance: a balancing act. *The FEBS Journal*, 284(2):183–195.
- Pollari, S., Käkönen, S.-M., Edgren, H., Wolf, M., Kohonen, P., Sara, H., Guise, T., Nees, M., and Kallioniemi, O. (2011). Enhanced serine production by bone metastatic breast cancer cells stimulates osteoclastogenesis. *Breast Cancer Research and Treatment*, 125(2):421–430.
- Ponti, A., Machacek, M., Gupton, S. L., Waterman-Storer, C. M., and Danuser, G. (2004). Two Distinct Actin Networks Drive the Protrusion of Migrating Cells. *Science*, 305(5691):1782–1786.
- Porporato, P., Payen, V., Pérez-Escuredo, J., De Saedeleer, C., Danhier, P., Copetti, T., Dhup, S., Tardy, M., Vazeille, T., Bouzin, C., Feron, O., Michiels, C., Gallez, B., and Sonveaux, P. (2014). A Mitochondrial Switch Promotes Tumor Metastasis. *Cell Reports*, 8(3):754–766.
- Provenzano, P. P., Eliceiri, K. W., and Keely, P. J. (2009). Multiphoton microscopy and fluorescence lifetime imaging microscopy (FLIM) to monitor metastasis and the tumor microenvironment. *Clinical & Experimental Metastasis*, 26(4):357–370.
- Provenzano, P. P., Inman, D. R., Eliceiri, K. W., Knittel, J. G., Yan, L., Rueden, C. T., White, J. G., and Keely, P. J. (2008). Collagen density promotes mammary tumor initiation and progression. *BMC Medicine*, 6(1):11.
- Rambold, A. S., Kostecky, B., Elia, N., and Lippincott-Schwartz, J. (2011). Tubular network formation protects mitochondria from autophagosomal degradation during nutrient starvation. *Proceedings of the National Academy of Sciences*, 108(25):10190–10195.
- Ranjit, S., Malacrida, L., Jameson, D. M., and Gratton, E. (2018). Fit-free analysis of fluorescence lifetime imaging data using the phasor approach. *Nature Protocols*, 13(9):1979–2004.
- Ranjit, S., Malacrida, L., Stakic, M., and Gratton, E. (2019). Determination of the metabolic index using the fluorescence lifetime of free and bound nicotinamide adenine dinucleotide using the phasor approach. *Journal of Biophotonics*, 12(11):e201900156.
- Raub, C. B., Suresh, V., Krasieva, T., Lyubovitsky, J., Mih, J. D., Putnam, A. J., Tromberg, B. J., and George, S. C. (2007). Noninvasive Assessment of Collagen Gel Microstructure and Mechanics Using Multiphoton Microscopy. *Biophysical Journal*, 92(6):2212–2222.
- Raub, C. B., Unruh, J., Suresh, V., Krasieva, T., Lindmo, T., Gratton, E., Tromberg, B. J., and George, S. C. (2008). Image Correlation Spectroscopy of Multiphoton Images

- Correlates with Collagen Mechanical Properties. *Biophysical Journal*, 94(6):2361–2373.
- Richert, M. M., Phadke, P. A., Matters, G., DiGirolamo, D. J., Washington, S., Demers, L. M., Bond, J. S., Manni, A., and Welch, D. R. (2005). Metastasis of hormone-independent breast cancer to lung and bone is decreased by alpha-difluoromethylornithine treatment. *Breast cancer research: BCR*, 7(5):R819–827.
- Rodimova, S., Rodimova, S., Kuznetsova, D., Bobrov, N., Bobrov, N., Elagin, V., Shcheslavskiy, V., Shcheslavskiy, V., Zagainov, V., Zagainov, V., Zagaynova, E., and Zagaynova, E. (2020). Mapping metabolism of liver tissue using two-photon FLIM. *Biomedical Optics Express*, 11(8):4458–4470.
- Rodrigues, M. F., Obre, E., de Melo, F. H. M., Santos, G. C., Galina, A., Jasiulionis, M. G., Rossignol, R., Rumjanek, F. D., and Amoêdo, N. D. (2016). Enhanced OXPHOS, glutaminolysis and  $\beta$ -oxidation constitute the metastatic phenotype of melanoma cells. *The Biochemical Journal*, 473(6):703–715.
- Rogers, G. W., Brand, M. D., Petrosyan, S., Ashok, D., Elorza, A. A., Ferrick, D. A., and Murphy, A. N. (2011). High Throughput Microplate Respiratory Measurements Using Minimal Quantities Of Isolated Mitochondria. *PLOS ONE*, 6(7):e21746.
- Romero, I. L., McCormick, A., McEwen, K. A., Park, S., Karrison, T., Yamada, S. D., Pannain, S., and Lengyel, E. (2012). Relationship of type II diabetes and metformin use to ovarian cancer progression, survival, and chemosensitivity. *Obstetrics and Gynecology*, 119(1):61–67.
- Rui, Y., Tiwari, P., Xie, Z., and Zheng, J. Q. (2006). Acute Impairment of Mitochondrial Trafficking by  $\beta$ -Amyloid Peptides in Hippocampal Neurons. *Journal of Neuroscience*, 26(41):10480–10487.
- Sachs, N., de Lig, J., Kopper, O., Gogola, E., Bounova, G., Weeber, F., Balgobind, A. V., Wind, K., Gracanin, A., Begthel, H., Korving, J., van Boxtel, R., Duarte, A. A., Lelieveld, D., van Hoeck, A., Ernst, R. F., Blokzijl, F., Nijman, I. J., Hoogstraat, M., van de Ven, M., Egan, D. A., Zinzalla, V., Moll, J., Boj, S. F., Voest, E. E., Wessels, L., van Diest, P. J., Rottenberg, S., Vries, R. G. J., Cuppen, E., and Clevers, H. (2018). A Living Biobank of Breast Cancer Organoids Captures Disease Heterogeneity. *Cell*, 172(1-2):373–386.e10.
- Sahai, E. and Marshall, C. J. (2002). RHO-GTPases and cancer. *Nature Reviews. Cancer*, 2(2):133–142.
- Sameni, S., Syed, A., Marsh, J. L., and Digman, M. A. (2016). The phasor-FLIM fingerprints reveal shifts from OXPHOS to enhanced glycolysis in Huntington Disease. *Scientific Reports*, 6.
- Sanzey, M., Abdul Rahim, S. A., Oudin, A., Dirkse, A., Kaoma, T., Vallar, L., Herold-Mende, C., Bjerkvig, R., Golebiewska, A., and Niclou, S. P. (2015). Comprehensive analysis of glycolytic enzymes as therapeutic targets in the treatment of glioblastoma. *PloS One*, 10(5):e0123544.
- Satija, R., Farrell, J. A., Gennert, D., Schier, A. F., and Regev, A. (2015). Spatial reconstruction of single-cell gene expression data. *Nature Biotechnology*, 33(5):495–502.
- Scaduto, R. C. and Grotyohann, L. W. (1999). Measurement of mitochondrial membrane potential using fluorescent rhodamine derivatives. *Biophysical Journal*, 76(1 Pt 1):469–477.



- Schafer, Z. T., Grassian, A. R., Song, L., Jiang, Z., Gerhart-Hines, Z., Irie, H. Y., Gao, S., Puigserver, P., and Brugge, J. S. (2009). Antioxidant and oncogene rescue of metabolic defects caused by loss of matrix attachment. *Nature*, 461(7260):109–113.
- Schiavon, C. R., Zhang, T., Zhao, B., Moore, A. S., Wales, P., Andrade, L. R., Wu, M., Sung, T.-C., Dayn, Y., Feng, J. W., Quintero, O. A., Shadel, G. S., Grosse, R., and Manor, U. (2020). Actin chromobody imaging reveals sub-organellar actin dynamics. *Nature Methods*, 17(9):917–921.
- Schild, T., Low, V., Blenis, J., and Gomes, A. P. (2018). Unique Metabolic Adaptations Dictate Distal Organ-Specific Metastatic Colonization. *Cancer cell*, 33(3):347–354.
- Schweitzer, D., Schenke, S., Hammer, M., Schweitzer, F., Jentsch, S., Birckner, E., Becker, W., and Bergmann, A. (2007). Towards metabolic mapping of the human retina. *Microscopy Research and Technique*, 70(5):410–419.
- Scipioni, L., Rossetta, A., Tedeschi, G., and Gratton, E. (2021). Phasor S-FLIM: a new paradigm for fast and robust spectral fluorescence lifetime imaging. *Nature Methods*, 18(5):542–550.
- Scott, K. E. N., Wheeler, F. B., Davis, A. L., Thomas, M. J., Ntambi, J. M., Seals, D. F., and Kridel, S. J. (2012). Metabolic Regulation of Invadopodia and Invasion by Acetyl-CoA Carboxylase 1 and De novo Lipogenesis. *PLOS ONE*, 7(1):e29761.
- Scott, T. G., Spencer, R. D., Leonard, N. J., and Weber, G. (1970). Synthetic spectroscopic models related to coenzymes and base pairs. V. Emission properties of NADH. Studies of fluorescence lifetimes and quantum efficiencies of NADH, AcPyADH, [reduced acetylpyridineadenine dinucleotide] and simplified synthetic models. *Journal of the American Chemical Society*, 92(3):687–695.
- Seewaldt, V. (2014). ECM stiffness paves the way for tumor cells. *Nature Medicine*, 20(4):332–333.
- Senft, D. and Ronai, Z. A. (2016). Regulators of mitochondrial dynamics in cancer. *Current Opinion in Cell Biology*, 39:43–52.
- Shafee, N., Smith, C. R., Wei, S., Kim, Y., Mills, G. B., Hortobagyi, G. N., Stanbridge, E. J., and Lee, E. Y.-H. P. (2008). Cancer Stem Cells Contribute to Cisplatin Resistance in Brca1/p53-Mediated Mouse Mammary Tumors. *Cancer Research*, 68(9):3243–3250.
- Shifrin, S. and Kaplan, N. O. (1959). Structure of Dihydrodiphosphopyridine Nucleotide. *Nature*, 183(4674):1529–1529.
- Shimono, Y., Zabala, M., Cho, R. W., Lobo, N., Dalerba, P., Qian, D., Diehn, M., Liu, H., Panula, S. P., Chiao, E., Dirbas, F. M., Somlo, G., Pera, R. A. R., Lao, K., and Clarke, M. F. (2009). Downregulation of miRNA-200c links breast cancer stem cells with normal stem cells. *Cell*, 138(3):592–603.
- Skala, M. C., Riching, K. M., Gendron-Fitzpatrick, A., Eickhoff, J., Eliceiri, K. W., White, J. G., and Ramanujam, N. (2007). In vivo multiphoton microscopy of NADH and FAD redox states, fluorescence lifetimes, and cellular morphology in precancerous epithelia. *Proceedings of the National Academy of Sciences*, 104(49):19494–19499.
- Smal, I., Draegestein, K., Galjart, N., Niessen, W., and Meijering, E. (2008). Particle Filtering for Multiple Object Tracking in Dynamic Fluorescence Microscopy Images: Application to Microtubule Growth Analysis. *IEEE Transactions on Medical Imaging*, 27(6):789–804.

- Sohrabi, A. (2021). *Brain-Mimetic, Three-Dimensional Hyaluronic Acid-Based Hydrogels to Investigate Effects of the Tumor Microenvironment on Glioblastoma Progression*. PhD thesis, UCLA.
- Sotgia, F., Whitaker-Menezes, D., Martinez-Outschoorn, U. E., Salem, A. F., Tsirigos, A., Lamb, R., Sneddon, S., Hulit, J., Howell, A., and Lisanti, M. P. (2012). Mitochondria “fuel” breast cancer metabolism: Fifteen markers of mitochondrial biogenesis label epithelial cancer cells, but are excluded from adjacent stromal cells. *Cell Cycle*, 11(23):4390–4401.
- Spencer, R. D. and Weber, G. (1969). Measurements of Subnanosecond Fluorescence Lifetimes with a Cross-Correlation Phase Fluorometer\*. *Annals of the New York Academy of Sciences*, 158(1):361–376.
- St-Pierre, J., Drori, S., Uldry, M., Silvaggi, J. M., Rhee, J., Jäger, S., Handschin, C., Zheng, K., Lin, J., Yang, W., Simon, D. K., Bachoo, R., and Spiegelman, B. M. (2006). Suppression of reactive oxygen species and neurodegeneration by the PGC-1 transcriptional coactivators. *Cell*, 127(2):397–408.
- Steeg, P. S., Bevilacqua, G., Kopper, L., Thorgeirsson, U. P., Talmadge, J. E., Liotta, L. A., and Sobel, M. E. (1988). Evidence for a novel gene associated with low tumor metastatic potential. *Journal of the National Cancer Institute*, 80(3):200–204.
- STERN, O. (1919). Über die abklingungszeit der fluoreszenz. *Phys. Z.*, 20:183–188.
- Stokes, G. G. (1852). XXX. On the change of refrangibility of light. *Philosophical Transactions of the Royal Society of London*, 142:463–562.
- Stringari, C., Cinquin, A., Cinquin, O., Digman, M. A., Donovan, P. J., and Gratton, E. (2011). Phasor approach to fluorescence lifetime microscopy distinguishes different metabolic states of germ cells in a live tissue. *Proceedings of the National Academy of Sciences*, 108(33):13582–13587.
- Stringari, C., Edwards, R. A., Pate, K. T., Waterman, M. L., Donovan, P. J., and Gratton, E. (2012a). Metabolic trajectory of cellular differentiation in small intestine by Phasor Fluorescence Lifetime Microscopy of NADH. *Scientific Reports*, 2:568.
- Stringari, C., Nourse, J. L., Flanagan, L. A., and Gratton, E. (2012b). Phasor fluorescence lifetime microscopy of free and protein-bound NADH reveals neural stem cell differentiation potential. *PloS One*, 7(11):e48014.
- Stupp, R., Taillibert, S., Kanner, A., Read, W., Steinberg, D., Lhermitte, B., Toms, S., Idbaih, A., Ahluwalia, M. S., Fink, K., Di Meco, F., Lieberman, F., Zhu, J.-J., Stragliotto, G., Tran, D., Brem, S., Hottinger, A., Kirson, E. D., Lavy-Shahaf, G., Weinberg, U., Kim, C.-Y., Paek, S.-H., Nicholas, G., Bruna, J., Hirte, H., Weller, M., Palti, Y., Hegi, M. E., and Ram, Z. (2017). Effect of Tumor-Treating Fields Plus Maintenance Temozolomide vs Maintenance Temozolomide Alone on Survival in Patients With Glioblastoma: A Randomized Clinical Trial. *JAMA*, 318(23):2306–2316.
- Sun, Y., Day, R. N., and Periasamy, A. (2011). Investigating protein-protein interactions in living cells using fluorescence lifetime imaging microscopy. *Nature Protocols*, 6(9):1324–1340.
- Tachibana, C. Y. (2018). Stem-cell culture moves to the third dimension. *Nature*, 558(7709):329–332.
- Tang, S., Wang, X., Shen, Q., Yang, X., Yu, C., Cai, C., Cai, G., Meng, X., and Zou, F. (2015). Mitochondrial Ca<sup>2+</sup> uniporter is critical for store-operated Ca<sup>2+</sup> entry-

- dependent breast cancer cell migration. *Biochemical and Biophysical Research Communications*, 458(1):186–193.
- Tateishi, K., Iafrate, A. J., Ho, Q., Curry, W. T., Batchelor, T. T., Flaherty, K. T., Onozato, M. L., Lelic, N., Sundaram, S., Cahill, D. P., Chi, A. S., and Wakimoto, H. (2016). Myc-Driven Glycolysis Is a Therapeutic Target in Glioblastoma. *Clinical Cancer Research: An Official Journal of the American Association for Cancer Research*, 22(17):4452–4465.
- Tentler, J. J., Tan, A. C., Weekes, C. D., Jimeno, A., Leong, S., Pitts, T. M., Arcaroli, J. J., Messersmith, W. A., and Eckhardt, S. G. (2012). Patient-derived tumour xenografts as models for oncology drug development. *Nature Reviews Clinical Oncology*, 9(6):338–350.
- Teoh, S. T. and Lunt, S. Y. (2018). Metabolism in cancer metastasis: bioenergetics, biosynthesis, and beyond. *WIREs Systems Biology and Medicine*, 10(2):e1406.
- Tiede, L. M., Rocha-Sanchez, S. M., Hallworth, R., Nichols, M. G., and Beisel, K. (2007). Determination of hair cell metabolic state in isolated cochlear preparations by two-photon microscopy. *Journal of Biomedical Optics*, 12(2):021004.
- Tilghman, R. W., Blais, E. M., Cowan, C. R., Sherman, N. E., Grigera, P. R., Jeffery, E. D., Fox, J. W., Blackman, B. R., Tschumperlin, D. J., Papin, J. A., and Parsons, J. T. (2012). Matrix Rigidity Regulates Cancer Cell Growth by Modulating Cellular Metabolism and Protein Synthesis. *PLOS ONE*, 7(5):e37231.
- Tinevez, J.-Y., Perry, N., Schindelin, J., Hoopes, G. M., Reynolds, G. D., Laplantine, E., Bednarek, S. Y., Shorte, S. L., and Eliceiri, K. W. (2017). TrackMate: An open and extensible platform for single-particle tracking. *Methods*, 115:80–90.
- Totsukawa, G., Wu, Y., Sasaki, Y., Hartshorne, D. J., Yamakita, Y., Yamashiro, S., and Matsumura, F. (2004). Distinct roles of MLCK and ROCK in the regulation of membrane protrusions and focal adhesion dynamics during cell migration of fibroblasts. *The Journal of Cell Biology*, 164(3):427–439.
- Trinh, A. L., Chen, H., Chen, Y., Hu, Y., Li, Z., Siegel, E. R., Linskey, M. E., Wang, P. H., Digman, M. A., and Zhou, Y.-H. (2017). Tracking Functional Tumor Cell Subpopulations of Malignant Glioma by Phasor Fluorescence Lifetime Imaging Microscopy of NADH. *Cancers*, 9(12).
- Trushina, E., Dyer, R., Badger II, J., Ure, D., Eide, L., Tran, D., Vrieze, B., Legendre-Guillemain, V., McPherson, P., Mandavilli, B., Van Houten, B., Zeitlin, S., McNiven, M., Aebersold, R., Hayden, M., Parisi, J., Seeberg, E., Dragatsis, I., Doyle, K., Bender, A., Chacko, C., and McMurray, C. (2004). Mutant huntingtin impairs axonal trafficking in mammalian neurons in vivo and in vitro. *Molecular and Cellular Biology*, 24(18):8195–8209.
- Tunster, S. J., Creeth, H. D. J., and John, R. M. (2016). The imprinted Phlda2 gene modulates a major endocrine compartment of the placenta to regulate placental demands for maternal resources. *Developmental Biology*, 409(1):251–260.
- Vaheri, A., Carpén, O., Heiska, L., Helander, T. S., Jääskeläinen, J., Majander-Nordenswan, P., Sainio, M., Timonen, T., and Turunen, O. (1997). The ezrin protein family: membrane-cytoskeleton interactions and disease associations. *Current Opinion in Cell Biology*, 9(5):659–666.

- Valente, A. J., Maddalena, L. A., Robb, E. L., Moradi, F., and Stuart, J. A. (2017). A simple ImageJ macro tool for analyzing mitochondrial network morphology in mammalian cell culture. *Acta Histochemica*, 119(3):315–326.
- Vallmitjana, A., Civera-Tregon, A., Hoenicka, J., Palau, F., and Benitez, R. (2017). Motion estimation of subcellular structures from fluorescence microscopy images. *Conference proceedings: ... Annual International Conference of the IEEE Engineering in Medicine and Biology Society. IEEE Engineering in Medicine and Biology Society. Annual Conference*, 2017:4419–4422.
- van Horssen, R., Buccione, R., Willemse, M., Cingir, S., Wieringa, B., and Attanasio, F. (2013). Cancer cell metabolism regulates extracellular matrix degradation by invadopodia. *European Journal of Cell Biology*, 92(3):113–121.
- Vander Heiden, M. G., Cantley, L. C., and Thompson, C. B. (2009). Understanding the Warburg effect: the metabolic requirements of cell proliferation. *Science (New York, N. Y.)*, 324(5930):1029–1033.
- Vasquez, R. J., Howell, B., Yvon, A. M., Wadsworth, P., and Cassimeris, L. (1997). Nanomolar concentrations of nocodazole alter microtubule dynamic instability in vivo and in vitro. *Molecular Biology of the Cell*, 8(6):973–985.
- Verveer, P. J., Squire, A., and Bastiaens, P. I. H. (2000). Global Analysis of Fluorescence Lifetime Imaging Microscopy Data. *Biophysical Journal*, 78(4):2127–2137.
- Viana, M. P., Lim, S., and Rafelski, S. M. (2015). Quantifying mitochondrial content in living cells. *Methods in Cell Biology*, 125:77–93.
- Visvader, J. E. and Lindeman, G. J. (2012). Cancer stem cells: current status and evolving complexities. *Cell Stem Cell*, 10(6):717–728.
- Wakita, M., Nishimura, G., and Tamura, M. (1995). Some Characteristics of the Fluorescence Lifetime of Reduced Pyridine Nucleotides in Isolated Mitochondria, Isolated Hepatocytes, and Perfused Rat Liver In Situ. *The Journal of Biochemistry*, 118(6):1151–1160.
- Walker, J. E. (2013). The ATP synthase: the understood, the uncertain and the unknown. *Biochemical Society Transactions*, 41(1):1–16.
- Walsh, A., Cook, R. S., Rexer, B., Arteaga, C. L., and Skala, M. C. (2012). Optical imaging of metabolism in HER2 overexpressing breast cancer cells. *Biomedical Optics Express*, 3(1):75–85.
- Wang, S., Wang, S., Chacko, J. V., Sagar, A. K., Eliceiri, K. W., Eliceiri, K. W., Yuan, M., and Yuan, M. (2019). Nonparametric empirical Bayesian framework for fluorescence-lifetime imaging microscopy. *Biomedical Optics Express*, 10(11):5497–5517.
- Wang, X., Winter, D., Ashrafi, G., Schlehe, J., Wong, Y., Selkoe, D., Rice, S., Steen, J., LaVoie, M., and Schwarz, T. (2011). PINK1 and Parkin Target Miro for Phosphorylation and Degradation to Arrest Mitochondrial Motility. *Cell*, 147(4):893–906.
- Warburg, O. (1925). The Metabolism of Carcinoma Cells. *The Journal of Cancer Research*, 9(1):148–163.
- Warburg, O. (1956). On the Origin of Cancer Cells. *Science*, 123(3191):309–314.
- Warburg, O., Wind, F., and Negelein, E. (1927). THE METABOLISM OF TUMORS IN THE BODY. *Journal of General Physiology*, 8(6):519–530.
- Ward, M. W., Rego, A. C., Frenguelli, B. G., and Nicholls, D. G. (2000). Mitochondrial membrane potential and glutamate excitotoxicity in cultured cerebellar granule cells. *The Journal of Neuroscience: The Official Journal of the Society for Neuroscience*,

- 20(19):7208–7219.
- Ward, P. S. and Thompson, C. B. (2012). Metabolic Reprogramming: A Cancer Hallmark Even Warburg Did Not Anticipate. *Cancer Cell*, 21(3):297–308.
- Waterman-Storer, C. M. (1998). Microtubules and Microscopes: How the Development of Light Microscopic Imaging Technologies Has Contributed to Discoveries about Microtubule Dynamics in Living Cells. *Molecular Biology of the Cell*, 9(12):3263–3271.
- Weber, G. (1950). Fluorescence of riboflavin and flavin-adenine dinucleotide. *Biochemical Journal*, 47(1):114–121.
- Weber, G. (1957). Intramolecular Transfer of Electronic Energy in Dihydro Diphosphopyridine Nucleotide. *Nature*, 180(4599):1409–1409.
- Weber, G. (1958). Transfert d’énergie dans la dihydro-diphosphopyridine nucléotide. *Journal Chimie Physique*, 55:875–886.
- Weber, G. (1981). Resolution of the fluorescence lifetimes in a heterogeneous system by phase and modulation measurements. *The Journal of Physical Chemistry*, 85(8):949–953.
- Weiss, S., Dunne, C., Hewson, J., Wohl, C., Wheatley, M., Peterson, A. C., and Reynolds, B. A. (1996). Multipotent CNS Stem Cells Are Present in the Adult Mammalian Spinal Cord and Ventricular Neuroaxis. *Journal of Neuroscience*, 16(23):7599–7609.
- Wells, R. G. (2008). The role of matrix stiffness in regulating cell behavior. *Hepatology*, 47(4):1394–1400.
- Westermann, B. (2010). Mitochondrial fusion and fission in cell life and death. *Nature Reviews Molecular Cell Biology*, 11(12):872–884.
- Whittle, J. R., Lewis, M. T., Lindeman, G. J., and Visvader, J. E. (2015). Patient-derived xenograft models of breast cancer and their predictive power. *Breast cancer research: BCR*, 17:17.
- Will, Y., Hynes, J., Ogurtsov, V. I., and Papkovsky, D. B. (2006). Analysis of mitochondrial function using phosphorescent oxygen-sensitive probes. *Nature Protocols*, 1(6):2563–2572.
- Winter, M. R., Fang, C., Banker, G., Roysam, B., and Cohen, A. R. (2012). Axonal transport analysis using Multitemporal Association Tracking. *International Journal of Computational Biology and Drug Design*, 5(1):35–48.
- Wolf, A., Agnihotri, S., Micallef, J., Mukherjee, J., Sabha, N., Cairns, R., Hawkins, C., and Guha, A. (2011). Hexokinase 2 is a key mediator of aerobic glycolysis and promotes tumor growth in human glioblastoma multiforme. *The Journal of Experimental Medicine*, 208(2):313–326.
- Wouters, F. S. and Esposito, A. (2008). Quantitative analysis of fluorescence lifetime imaging made easy. *HFSP Journal*, 2(1):7–11.
- Wright, B. K., Andrews, L. M., Jones, M. R., Stringari, C., Digman, M. A., and Gratton, E. (2012). Phasor-flim analysis of NADH distribution and localization in the nucleus of live progenitor myoblast cells. *Microscopy Research and Technique*, 75(12):1717–1722.
- Wu, J., Kent, I., Shekhar, N., Chancellor, T., Mendonca, A., Dickinson, R., and Lele, T. (2014). Actomyosin Pulls to Advance the Nucleus in a Migrating Tissue Cell. *Biophysical Journal*, 106(1):7–15.
- Wu, M., Neilson, A., Swift, A. L., Moran, R., Tamagnine, J., Parslow, D., Armistead, S., Lemire, K., Orrell, J., Teich, J., Chomicz, S., and Ferrick, D. A. (2007). Multiparameter metabolic analysis reveals a close link between attenuated mitochondrial bioenergetic

- function and enhanced glycolysis dependency in human tumor cells. *American Journal of Physiology-Cell Physiology*, 292(1):C125–C136.
- Wyckoff, J. B., Jones, J. G., Condeelis, J. S., and Segall, J. E. (2000). A critical step in metastasis: in vivo analysis of intravasation at the primary tumor. *Cancer Research*, 60(9):2504–2511.
- Xiao, W., Ehsanipour, A., Sohrabi, A., and Seidlits, S. K. (2018a). Hyaluronic-Acid Based Hydrogels for 3-Dimensional Culture of Patient-Derived Glioblastoma Cells. *JoVE (Journal of Visualized Experiments)*, 138:e58176.
- Xiao, W., Wang, R.-S., Handy, D. E., and Loscalzo, J. (2018b). NAD(H) and NADP(H) Redox Couples and Cellular Energy Metabolism. *Antioxidants & Redox Signaling*, 28(3):251–272.
- Yaku, K., Okabe, K., and Nakagawa, T. (2018). NAD metabolism: Implications in aging and longevity. *Ageing Research Reviews*, 47:1–17.
- Yang, L., Hou, Y., Yuan, J., Tang, S., Zhang, H., Zhu, Q., Du, Y.-e., Zhou, M., Wen, S., Xu, L., Tang, X., Cui, X., and Liu, M. (2015). Twist promotes reprogramming of glucose metabolism in breast cancer cells through PI3K/AKT and p53 signaling pathways. *Oncotarget*, 6(28):25755–25769.
- Yang, L., Moss, T., Mangala, L. S., Marini, J., Zhao, H., Wahlig, S., Armaiz-Pena, G., Jiang, D., Achreja, A., Win, J., Roopaimoole, R., Rodriguez-Aguayo, C., Mercado-Urbe, I., Lopez-Berestein, G., Liu, J., Tsukamoto, T., Sood, A. K., Ram, P. T., and Nagrath, D. (2014). Metabolic shifts toward glutamine regulate tumor growth, invasion and bioenergetics in ovarian cancer. *Molecular Systems Biology*, 10:728.
- Yang, Y. and Sauve, A. A. (2016). NAD(+) metabolism: Bioenergetics, signaling and manipulation for therapy. *Biochimica Et Biophysica Acta*, 1864(12):1787–1800.
- Yap, T. A., Rodon Ahnert, J., Piha-Paul, S. A., Fu, S., Janku, F., Karp, D. D., Naing, A., Ileana Dumbrava, E. E., Pant, S., Subbiah, V., Tsimberidou, A. M., Hong, D. S., Rose, K. M., Xu, Q., Vellano, C. P., Mahendra, M., Jones, P., Di Francesco, M. E., Marszalek, J. R., and Meric-Bernstam, F. (2019). Phase I trial of IACS-010759 (IACS), a potent, selective inhibitor of complex I of the mitochondrial electron transport chain, in patients (pts) with advanced solid tumors. *Journal of Clinical Oncology*, 37(15\_suppl):3014–3014.
- Yu, M., Bardia, A., Aceto, N., Bersani, F., Madden, M. W., Donaldson, M. C., Desai, R., Zhu, H., Comaills, V., Zheng, Z., Wittner, B. S., Stojanov, P., Brachtel, E., Sgroi, D., Kapur, R., Shioda, T., Ting, D. T., Ramaswamy, S., Getz, G., Iafrate, A. J., Benes, C., Toner, M., Maheswaran, S., and Haber, D. A. (2014). Ex vivo culture of circulating breast tumor cells for individualized testing of drug susceptibility. *Science*, 345(6193):216–220.
- Yu, Q. and Heikal, A. A. (2009). Two-photon autofluorescence dynamics imaging reveals sensitivity of intracellular NADH concentration and conformation to cell physiology at the single-cell level. *Journal of Photochemistry and Photobiology. B, Biology*, 95(1):46–57.
- Zenobi, R. (2013). Single-Cell Metabolomics: Analytical and Biological Perspectives. *Science*, 342(6163).
- Zhang, Q., McCorkle, J. R., Novak, M., Yang, M., and Kaetzel, D. M. (2011). Metastasis suppressor function of NM23-H1 requires its 3′-5′ exonuclease activity. *International*

- Journal of Cancer*, 128(1):40–50.
- Zhao, J., Zhang, J., Yu, M., Xie, Y., Huang, Y., Wolff, D. W., Abel, P. W., and Tu, Y. (2013). Mitochondrial dynamics regulates migration and invasion of breast cancer cells. *Oncogene*, 32(40):4814–4824.
- Zhao, R.-Z., Jiang, S., Zhang, L., and Yu, Z.-B. (2019). Mitochondrial electron transport chain, ROS generation and uncoupling (Review). *International Journal of Molecular Medicine*, 44(1):3–15.
- Zielonka, J. and Kalyanaraman, B. (2008). "ROS-generating mitochondrial DNA mutations can regulate tumor cell metastasis"—a critical commentary. *Free Radical Biology & Medicine*, 45(9):1217–1219.

# Appendix A

## NADH fraction calculation code

---

```
function [fraction1,fraction2,fraction3] =  
    fractionCalc(s,g,freeTau,boundTau,frequency,bg)  
    omega = 2*pi*frequency;  
  
    g1 = 1/(1+(omega*freeTau)^2);  
    s1 = (omega*freeTau)/(1+(omega*freeTau)^2);  
  
    g2 = 1/(1+(omega*boundTau)^2);  
    s2 = (omega*boundTau)/(1+(omega*boundTau)^2);  
  
    if nargin==6  
        A = [g1 g2 bg.g;  
             s1 s2 bg.s;  
             1 1 1];  
    else  
        A = [g1 g2 0;  
             s1 s2 0];
```



```

        1   1   1];

end

x = [];

for pixel = 1:numel(g)
    y = [g(pixel);s(pixel);1];
    x(:,pixel) = A\y;
end

pixelNum = 1;
for j = 1:numel(g)
    fraction1(j) = x(1,pixelNum);
    fraction2(j) = x(2,pixelNum);
    fraction3(j) = x(3,pixelNum);
    pixelNum = pixelNum+1;
end

if ~numel(g)
    fraction1 = nan;
    fraction2 = nan;
    fraction3 = nan;
end

end
end

```

---

## Appendix B

Collagen density modulates  
triple-negative breast cancer cell  
metabolism through  
adhesion-mediated contractility:  
Supplementary materials

## B.1 Percent change of bound NADH in all tested cell lines

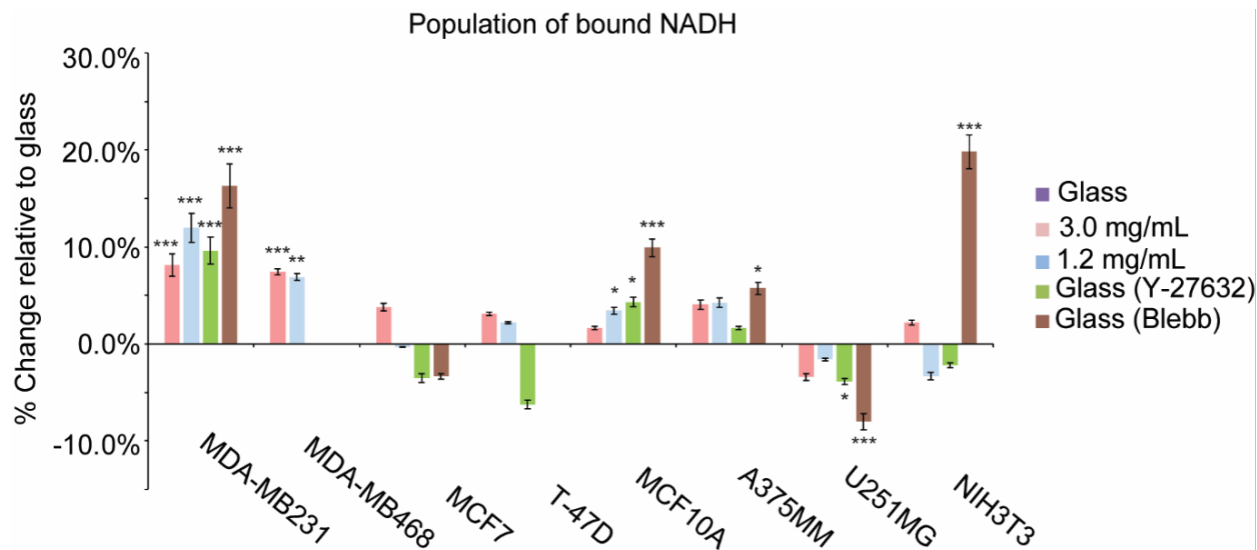


Figure B.1: Percent change in the population of bound NADH of MDA-MB-231 (3.0 mg/mL: n=71; 1.2 mg/mL: n=53; Glass: n=77; Glass (Y-27632): n=33; Glass (Blebb): n=33), MDA-MB-468 (3.0 mg/mL: n=5; 1.2 mg/mL: n=5; Glass: n=5; Glass (Y-27632): n=5), MCF-7 (3.0 mg/mL: n=20; 1.2 mg/mL: n=21; Glass: n=20; Glass (Y-27632): n=21; Glass (Blebb): n=5), T-47D (3.0 mg/mL: n=5; 1.2 mg/mL: n=5; Glass: n=5; Glass (Y-27632): n=5), MCF-10A (3.0 mg/mL: n=64; 1.2 mg/mL: n=59; Glass: n=63; Glass (Y-27632): n=26; Glass (Blebb): n=29), A-375 MM (3.0 mg/mL: n=24; 1.2 mg/mL: n=23; Glass: n=24; Glass (Y-27632): n=28; Glass (Blebb): n=31) and U-251 MG (3.0 mg/mL: n=28; 1.2 mg/mL: n=30; Glass: n=26; Glass (Y-27632): n=22; Glass (Blebb): n=31) and NIH-3T3 (3.0 mg/mL: n=21; 1.2 mg/mL: n=15; Glass: n=20; Glass (Y-27632): n=19; Glass (Blebb): n=11) cells on collagen substrates and glass (treated with Y-27632 or blebbistatin, blebb) with respect to their glass conditions. n=total number of cells measured. \*p<0.05, \*\*p<0.01, and \*\*\*p<1e-3 or less by Student's t-test. Error bars are based off of standard deviation.

## B.2 Metabolic indexes when treated with contractility inhibitors

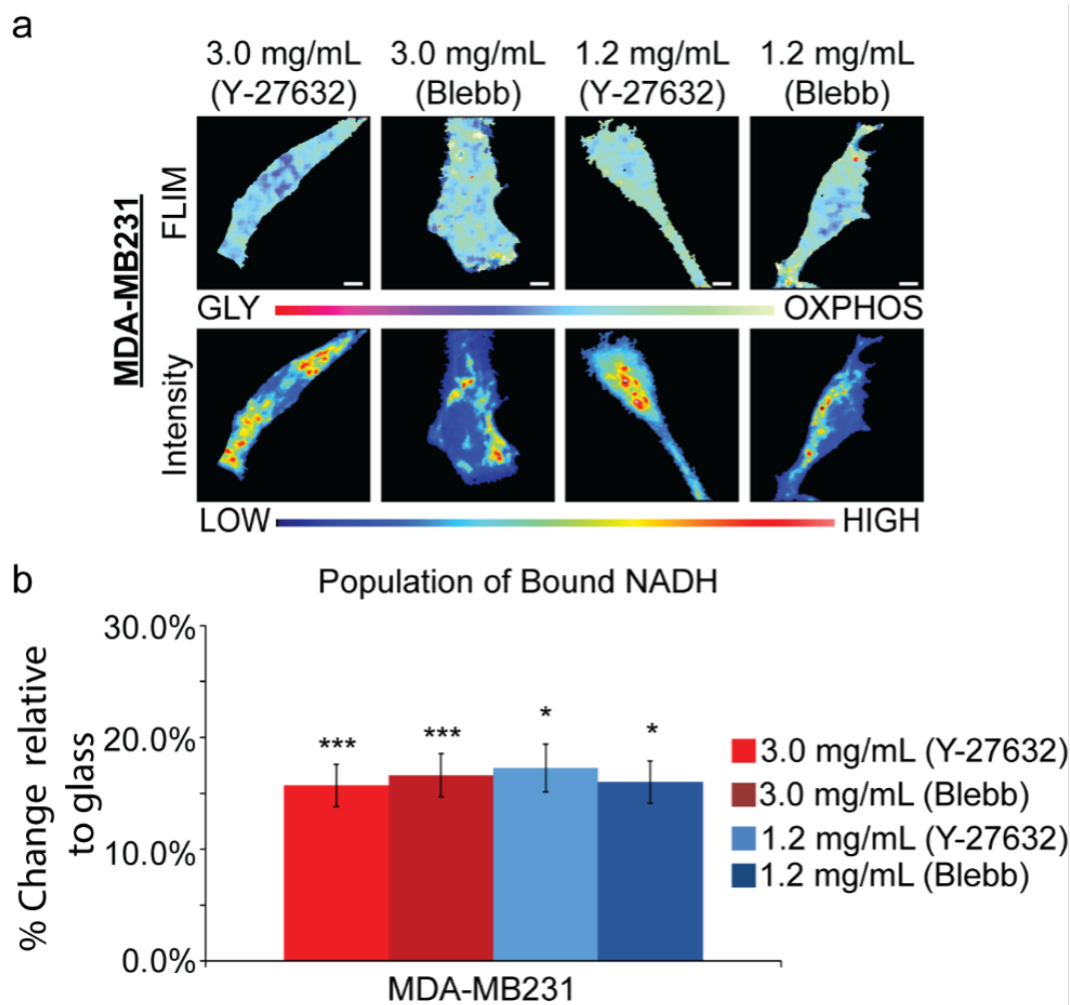


Figure B.2: MDA-MB-231 metabolic indexes when treated with contractility inhibitors. (a) MDA-MB-231 cells on 3.0 mg/mL and 1.2 mg/mL collagen treated with ROCK inhibitor Y-27632 or myosin-II inhibitor blebbistatin to prevent cell contractility. (b) Quantification of the percent change of the population of bound NADH in MDA-MB-231 cells when treated with Y-27632 (3.0 mg/mL:  $n=7$ ; 1.2 mg/mL:  $n=8$ ) or blebbistatin (3.0 mg/mL:  $n=3$ ; 1.2 mg/mL:  $n=4$ ) relative to untreated conditions.  $n$ =total number of cells measured. \* $p<0.05$  and \*\* $p<0.01$  by Student's t-test. Scale bar: 5  $\mu$ m. Error bars are based off of standard deviation.

### B.3 NADH FLIM in cytoplasm vs. nucleus

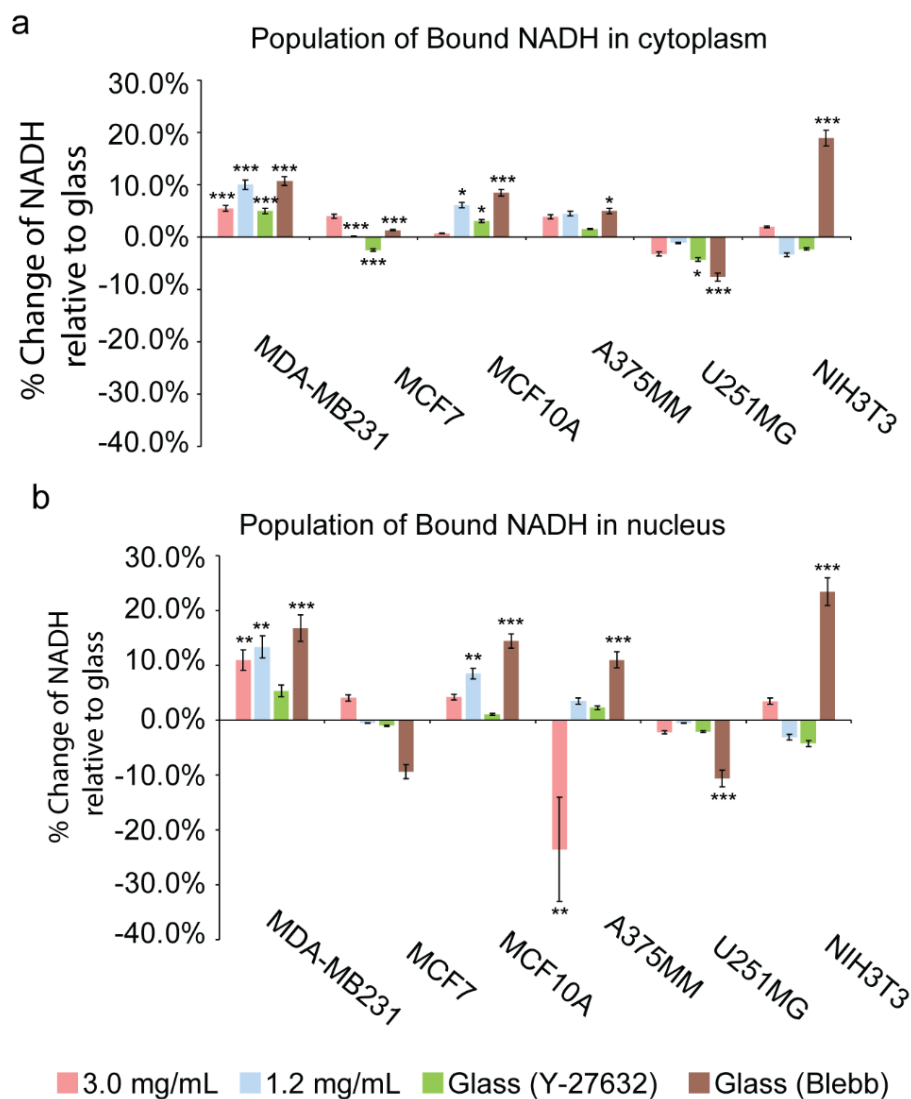


Figure B.3: NADH FLIM signatures of (a) cytoplasmic and (b) nuclear compartments within MDA-MB-231, MCF-7, MCF-10A, A-375 MM and U-251 MG cells on varying substrates. \* $p < 0.05$ , \*\* $p < 0.01$ , \*\*\* $p < 0.001$  by Student's t-test. Error bars are based off of standard deviation.

## B.4 Metabolic indexes of NIH-3T3 cells

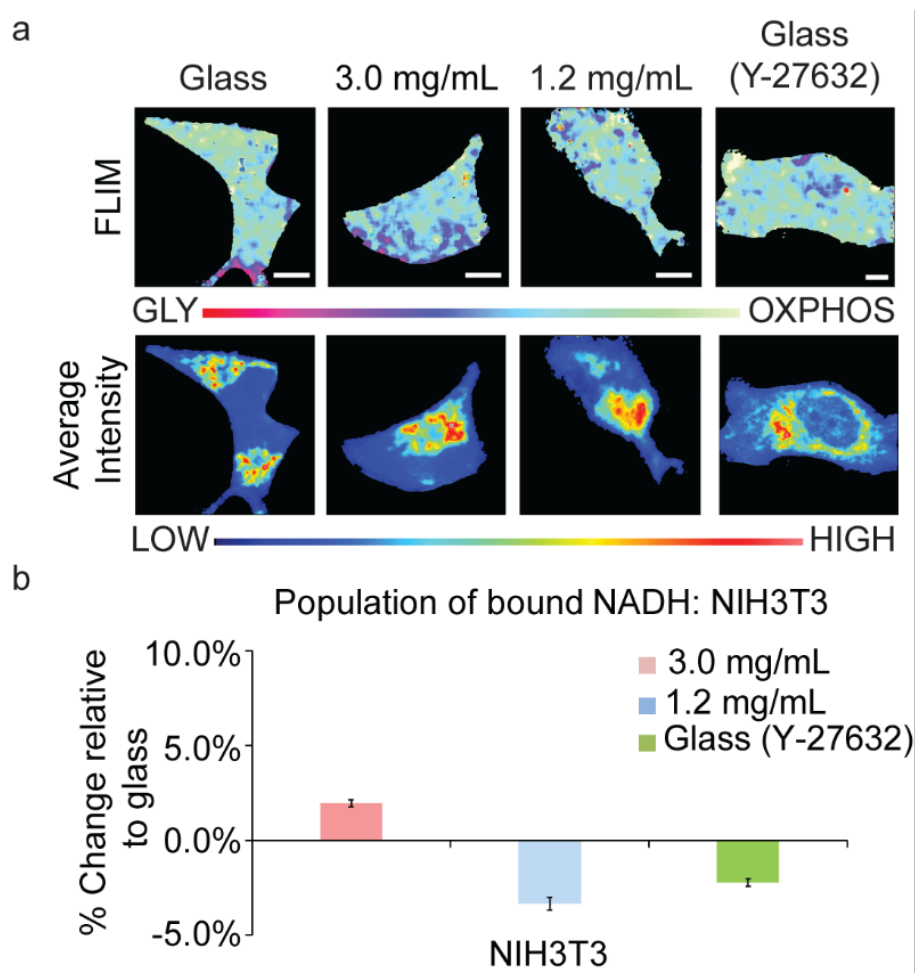


Figure B.4: Metabolic indexes of NIH-3T3 cells (3.0 mg/mL:  $n=21$ ; 1.2 mg/mL:  $n=15$ ; Glass:  $n=20$ ; Glass (Y-27632):  $n=10$ ).  $n$ =total number of cells measured. **(a)** FLIM and average intensity images of NADH within NIH-3T3 fibroblast cell lines. **(b)** Quantification of the percent change of NADH within NIH-3T3 cell on various substrates relative to those on glass.

## B.5 Raw NADH bound percentages

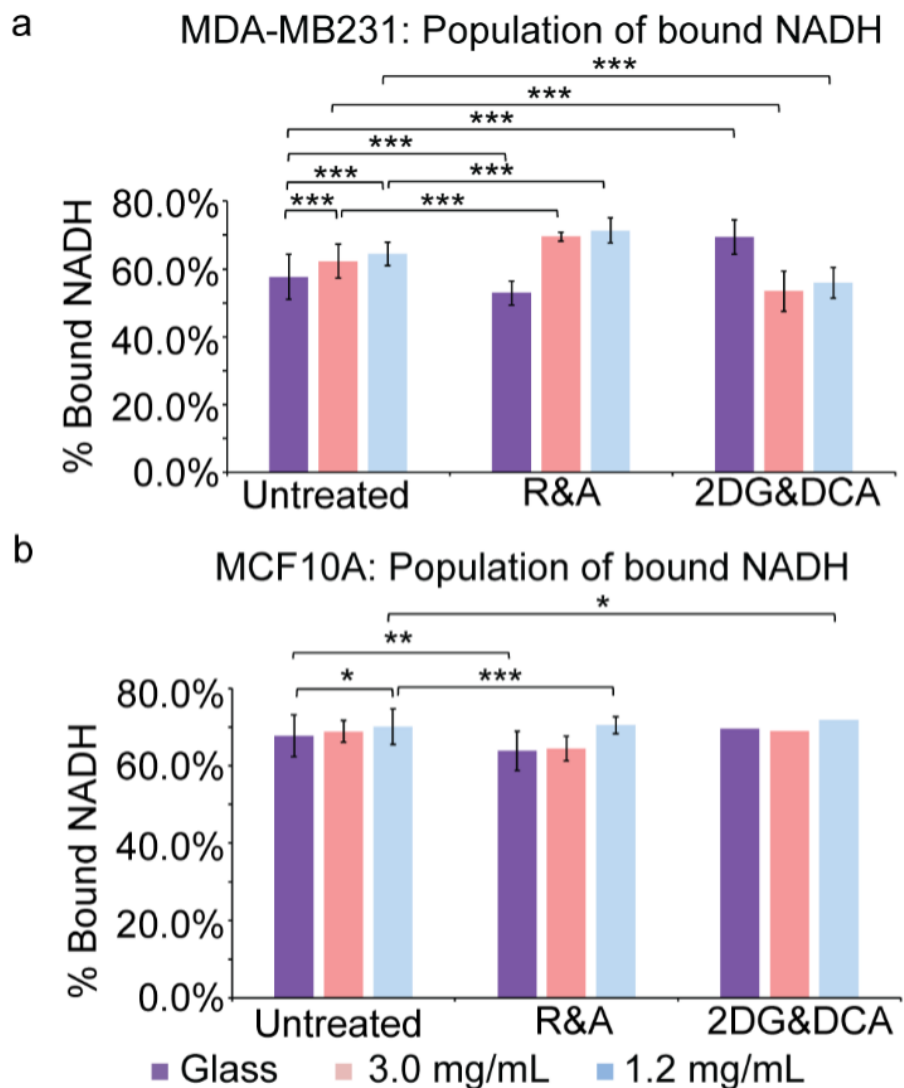


Figure B.5: (a) Raw percent bound of NADH of MDA-MB-231 and (Phasor plots of all cells. (a) Breast cells' average whole cell phasor plots of their metabolic indexes when seeded on glass, 1.2 mg/mL, and 3.0 mg/mL collagen substrates. Untreated and treated conditions with blebbistatin or Y-27632 are shown. (b) Non-breast cells' average whole cell phasors of their metabolic indexes when seeded on glass (untreated and treated with blebbistatin or Y-27632), 1.2 mg/mL, and 3.0 mg/mL collagen substrates. (c) Combined average whole cell phasors from (a) and (b). Error bars are based off of standard deviation.) MCF-10A cells on glass, 1.2 and 3.0 mg/mL collagen substrates when treated with R&A, 2DG&DCA and untreated. \* $p < 0.05$  and \*\* $p < 0.01$ , \*\*\* $p < 0.001$  by Student's t-test.

## B.6 Phasor plots of all tested cells

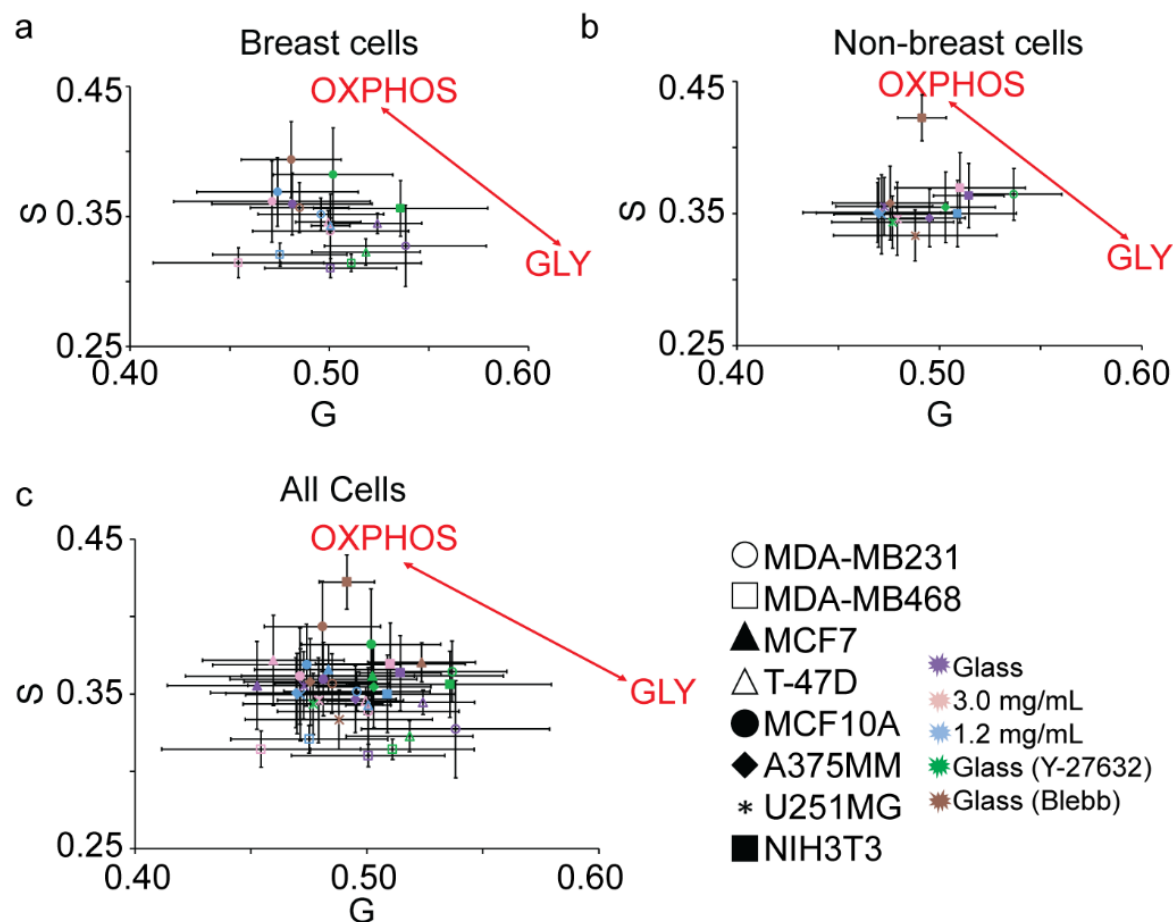


Figure B.6: Phasor plots of all cells. (a) Breast cells' average whole cell phasor plots of their metabolic indexes when seeded on glass, 1.2 mg/mL, and 3.0 mg/mL collagen substrates. Untreated and treated conditions with blebbistatin or Y-27632 are shown. (b) Non-breast cells' average whole cell phasors of their metabolic indexes when seeded on glass (untreated and treated with blebbistatin or Y-27632), 1.2 mg/mL, and 3.0 mg/mL collagen substrates. (c) Combined average whole cell phasors from (a) and (b). Error bars are based off of standard deviation.



# Appendix C

## Mitometer manual

### C.1 Installation

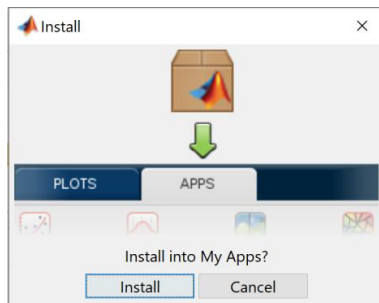
#### C.1.1 Download

The Mitometer program is written in MATLAB (MathWorks). The MATLAB GUI Mitometer app and corresponding source code is freely available online at <https://github.com/aelefebv/Mitometer>.

#### C.1.2 App execution

1. Open the MATLAB App Installer file titled “Mitometer”.
2. Once MATLAB opens, click “Install”.
3. Click the “Mitometer” app in the Apps menu.

**Note:** Installation typically takes no more than 1 minute.



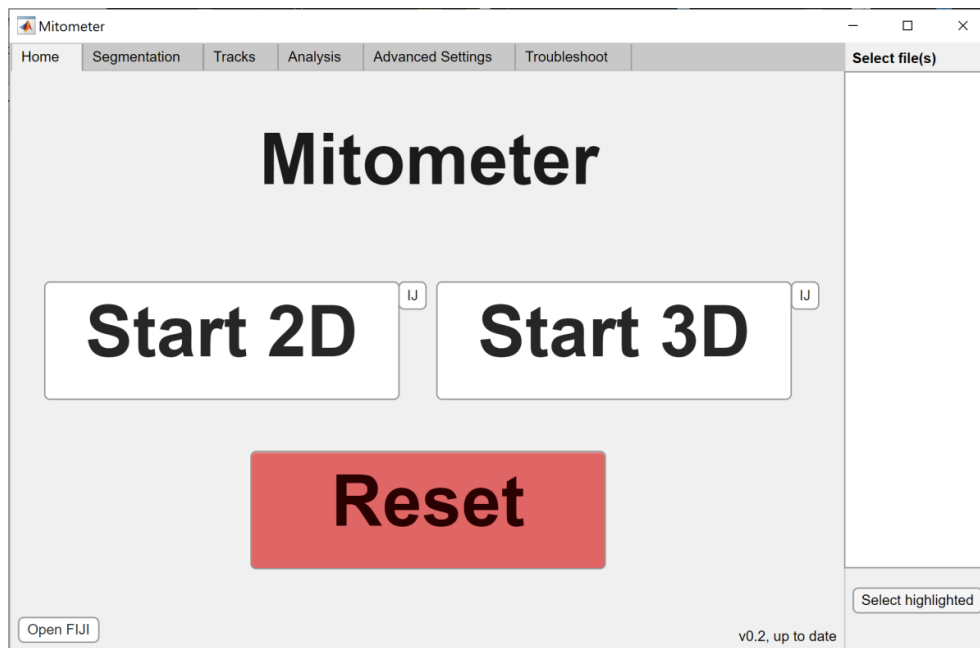
### C.1.3 Source code

All functions used in the Mitometer app are included in the Source Code folder. This includes the app's App Designer GUI, titled "GUI".

## C.2 UI tutorial

### C.2.1 Home tab

An instance of Mitometer can take as an input either 2D or 3D images:



#### C.2.1.1 Start 2D

1. Input pixel size and time between each temporal frame.
  2. Upload one or more Tif image stacks with temporal frames as the stack.
- Runs segmentation and tracking on each file in order of selection.
  - Uploaded files will be shown in the right column under "Select file(s)"

**Note:** You can analyze additional 2D files by pressing on Add 2D and following steps 1 and 2 again.

What is your pixel size, in microns per pixel?

0.0879

What is your time between frames, in seconds?

1

OK Cancel

### C.2.1.2 Start 3D

1. Input pixel size, time between each temporal frame, number of spatial planes, and axial distance between the spatial planes.

What is your pixel size, in microns per pixel?

0.105

What is your time between frames, in seconds?

10

How many z-planes in the stack?

21

What is the axial distance, in microns?

0.45

OK Cancel

2. Upload one or more Tif image stacks with the temporal and spatial frames as the stack. Order should follow  $z \rightarrow t$ , i.e. all sequential (bottom to top) z-planes for time 1, followed by all sequential z-planes for time 2 (Note: This is the default order for LSM files).
- Runs segmentation and tracking on each file in order of selection.
  - Uploaded files will be shown in the right column under “Select file(s)”

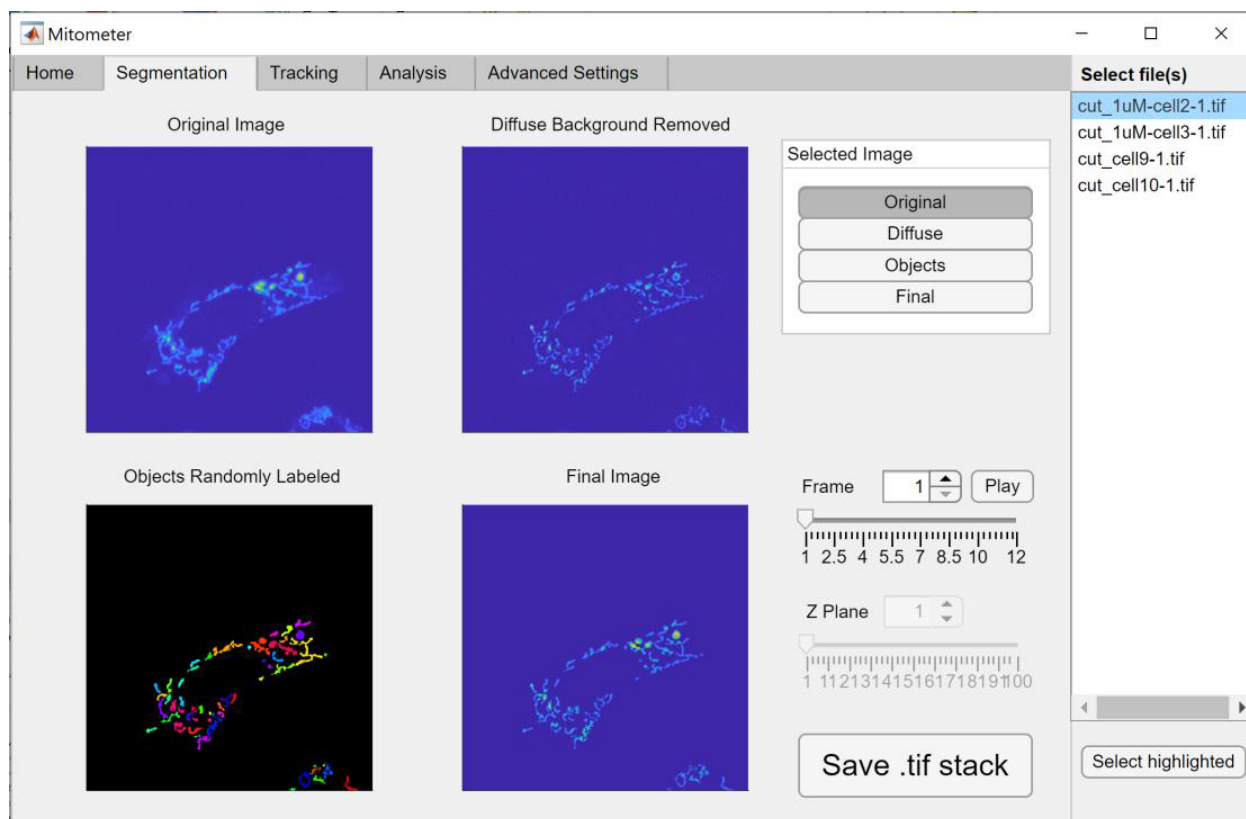
- Note: You can analyze additional 3D files by pressing on Add 3D and following steps 1 and 2 again.

#### **C.2.1.3 Reset**

- Reloads Mitometer.

## C.2.2 Segmentation Tab

After the processing from the home page is finished, visualization of mitochondria segmentation for each individual file will be available.



### C.2.2.1 Visualize

1. Select the file you wish to visualize under the “Select file(s)” menu.
  2. Press the “Select highlighted” button.
- The software allows visualization of the uploaded image, the image after diffuse background removal, randomly colored connected components (mitochondria), and the final segmented image.

- To scrub through frames of the images:
  1. Select the image you wish you view under “Selected Image”
  2. Use the frame spinner, slider, or play button to view temporal frames.
- In 3D, you can view different spatial frames by changing the spinner or slider next to “Z Plane”.

#### **C.2.2.2 Save images**

To save the image stack to a tif file:

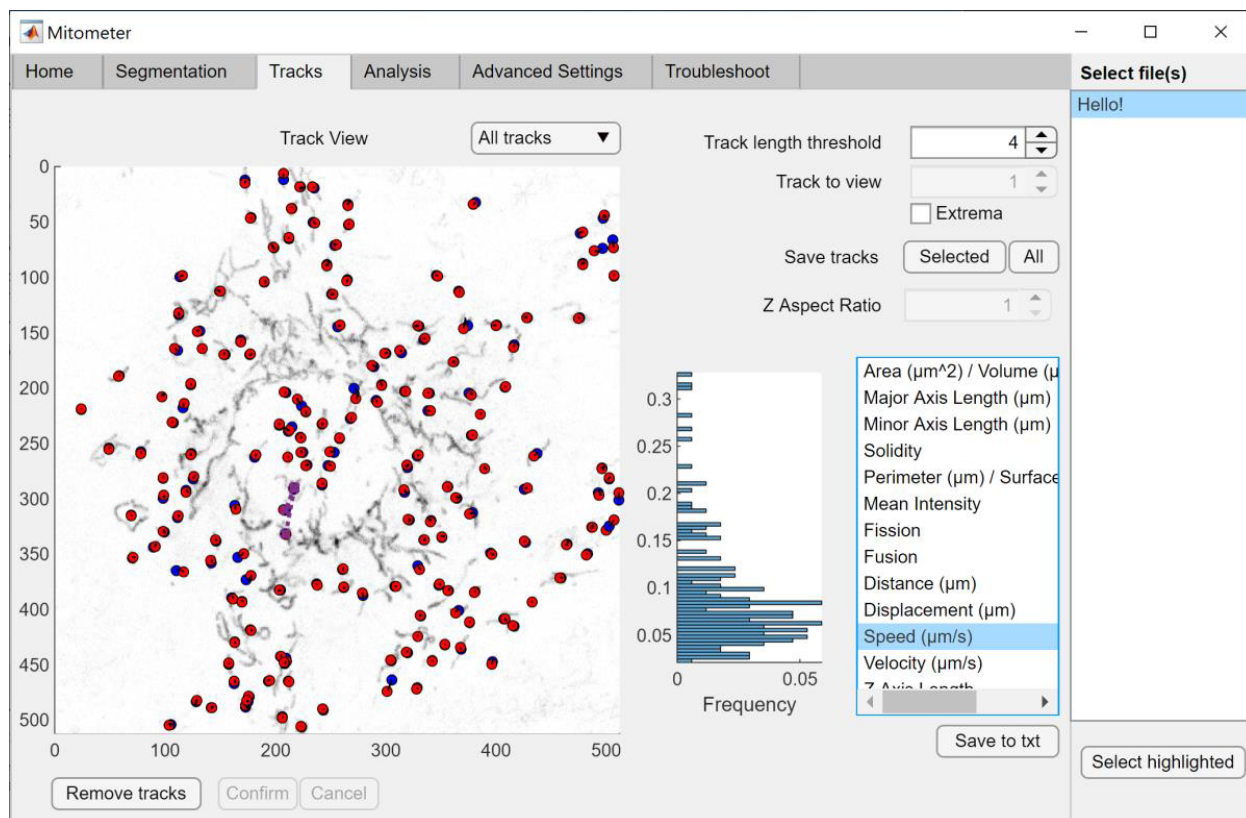
1. Select the image you wish to save under “Selected Image”.
2. Press the “Save .tif stack” button.

To save a single spatiotemporal frame:

1. Hover over the image you wish to save.
2. Use the MATLAB menu that appears above the image.

## C.2.3 Tracking tab

After the processing from the home tab is finished, visualization of mitochondria tracks for each individual file will be available.



### C.2.3.1 Visualize

1. Select the file you wish to visualize under the “Select file(s)” menu.
  2. Press the “Select highlighted” button.
  3. Select the feature you want to visualize and it will appear as a histogram with the feature value as the y-axis, and the normalized frequency in the x-axis.
- The software allows visualization of all tracks, confident tracks, a single track (one track at a time), perinuclear tracks, and telenuclear tracks (as defined by below and



above the Otsu’s threshold, respectively, of the histogram of mitochondrial distances from the mitochondrial aggregate center of mass).

- In 3D, you can change the aspect ratio of the Z plane in respect to the X-Y plane by changing the spinner next to “Z Aspect Ratio”.
- To remove tracks containing less than a specified number of points, change the spinner next to “Track length threshold”
- When “Single track” is selected, you can change the selected track by changing the spinner value next to “Track to view”.
- Track starting points are shown in blue, track ending points are shown in red, fission events are shown in purple, and fusion events are shown in green.
- Outlines of mitochondria at every frame can be visualized by enabling the “Extrema” checkbox

#### **C.2.3.2 Remove tracks**

To remove specific tracks:

1. Press the “Remove tracks” button.
2. Click a track or draw a region around the tracks you wish to remove.
3. Press the “Confirm” button to remove the selected tracks.
4. Press the “Cancel” button to cancel.

### C.2.3.3 Save feature data

To save the feature data of an individual file (refer to Section 3. Output, for information on the saved data):

1. Select the type of track you wish to save under “Track View” (default is all tracks).
2. Select a track length threshold (default is 1).
3. Click on the feature you would like to save.
4. Press the “Save to txt” button.
5. Select where to save the data.

Feature data will be saved in a .txt file.

### C.2.3.4 Save tracks

To save the track data (refer to Section 3. Output, for information on the saved data):

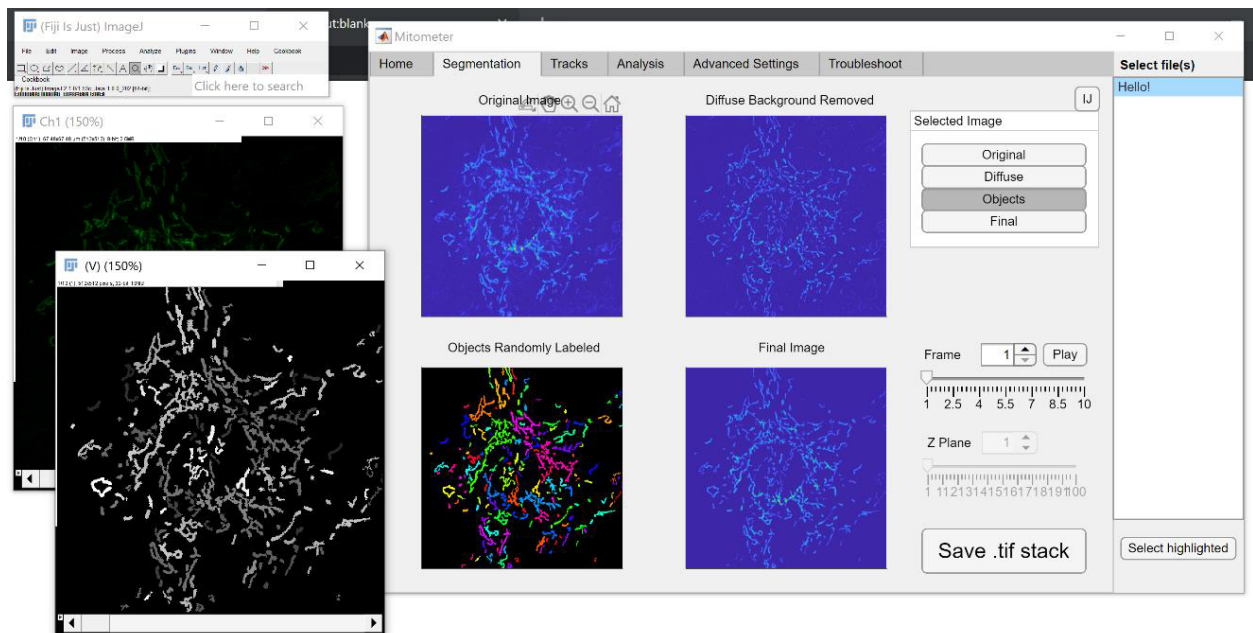
1. Select the type of track you wish to save under “Track View” (default is all tracks).
  2. Select a track length threshold (default is 1).
- To save specific file(s)
    1. Select one or more files you wish to save under the “Select file(s)” menu.
    2. Press the “Select highlighted” button.
    3. Press the “Selected” button next to “Save tracks”.
  - To save all files

1. Press the “All” button next to “Save tracks”.

Track data will be saved in a .mat file.

### C.2.3.5 Open in ImageJ

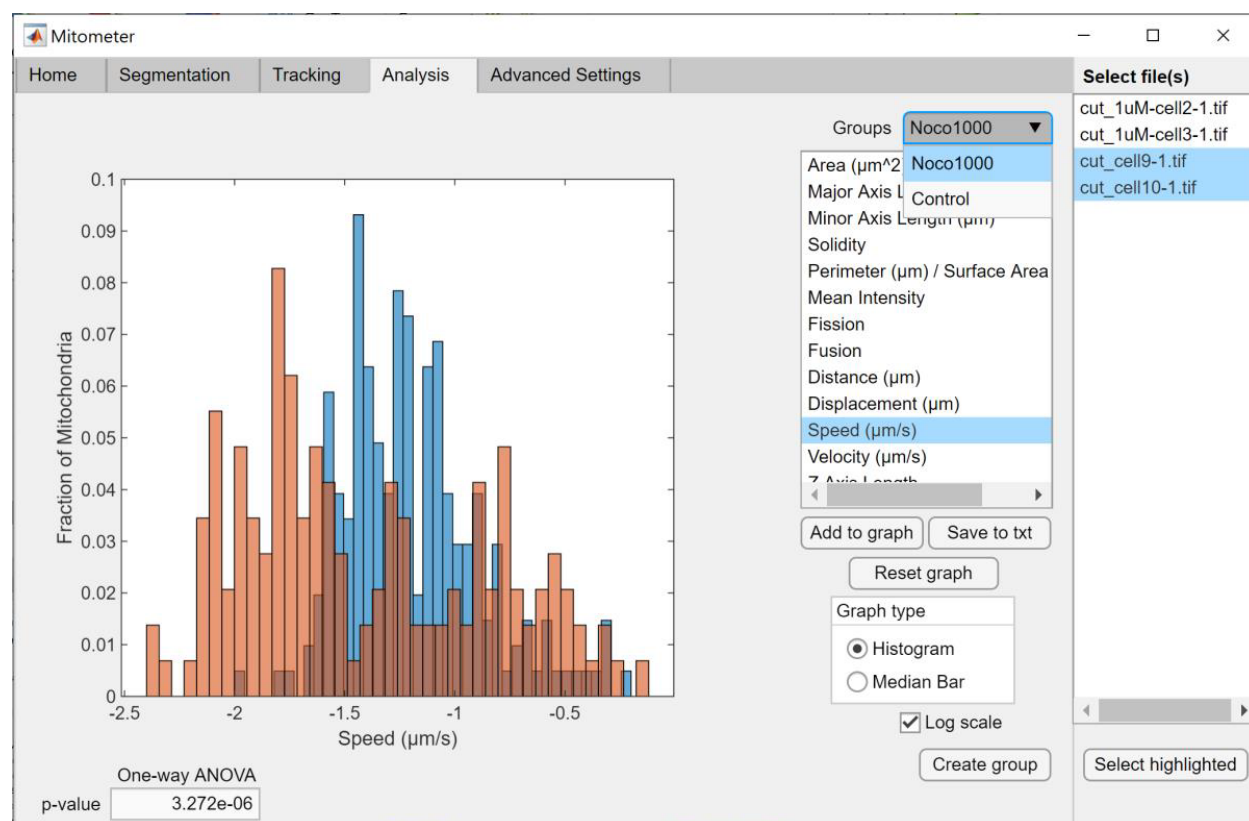
To open segmented files in ImageJ, first follow steps in section 4: ImageJ Guide.



1. Open Fiji through Mitometer.
2. On the “Segmentation” tab, select the image to transfer to ImageJ under “Selected Image”
3. Click the IJ button.

## C.2.4 Analysis tab

After the processing from the home tab is finished, preliminary analysis of basic mitochondrial morphological, motility, and dynamic features between files and conditions will be available.



### C.2.4.1 Visualize

1. Select the file(s) whose features you wish to visualize under the “Select file(s)” menu.
  - (a) E.g. select all files of your control group.
2. Press the “Select highlighted” button.
3. Press the “Create group” button.

A screenshot of a software dialog box. At the top, there are standard window controls (minimize, maximize, close). Below these is a dropdown menu currently showing 'All tracks'. Underneath the dropdown is a label 'Min track length' followed by a spinner control showing the value '1'. Below the spinner is a text input field with the placeholder text 'name'. At the bottom of the dialog is a button labeled 'Create group'.

4. Select whether you wish to analyze all tracks, confident tracks, perinuclear tracks, or telenuclear tracks (default is all tracks).
  5. Select a track length threshold (default is 1).
  6. Name your group.
  7. Repeat 1-6 for each condition/group you wish to compare.
  8. Select the first group to compare under the “Groups” dropdown.
  9. Select the feature you wish to analyze.
    - (a) Note: Z Axis Length is only available in 3D.
  10. Press “Add to graph” to visualize the data.
  11. Repeat steps 8-10 for each condition/group you wish to compare.
- The software allows visualization of either histogram distributions or bar graphs of median values of normal or logarithmically transformed data.
  - Statistical comparison between groups is done via a One-way ANOVA.
  - Clear off all groups from the graph by clicking the “Reset graph” button.

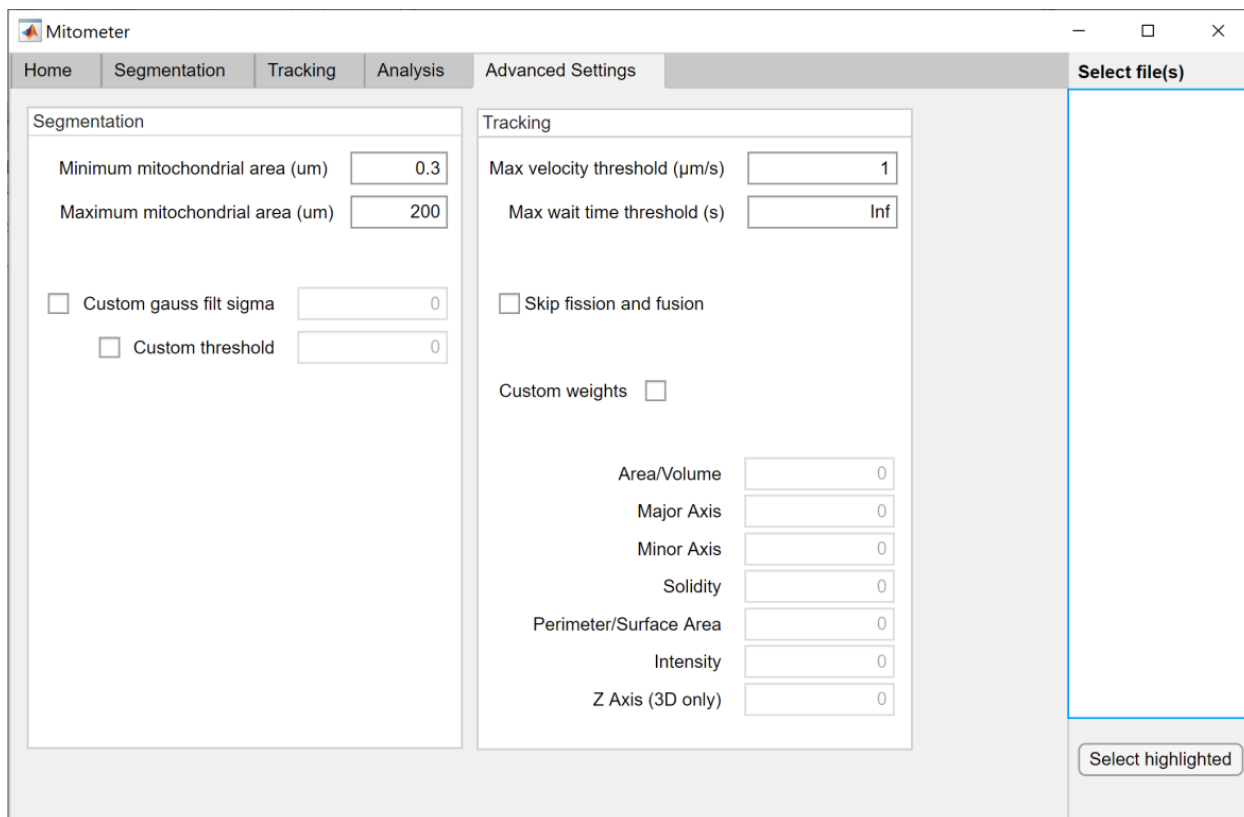
#### C.2.4.2 Save feature data

To save the feature data (refer to Section 3. Output, for information on the saved data):

1. Select the file(s) whose features you wish to save under the “Select file(s)” menu.
  - (a) E.g. select all files of your control group.
2. Press the “Select highlighted” button.
3. Press the “Create group” button.
4. Select whether you wish to save all tracks, confident tracks, perinuclear tracks, or telenuclear tracks (default is all tracks).
5. Select a track length threshold (default is 1).
6. Name your group.
7. Select the group to save under the “Groups” dropdown.
8. Select the feature(s) you wish to save.
  - (a) Note: Z Axis Length is only available in 3D.
9. Press the “Save to txt” button
  - (a) Your data will be saved to a comma delimited text file where each row is a track, and each column is a frame.
10. Repeat 1-9 for each condition/group you wish to save.

## C.2.5 Advanced settings tab

Before processing files from the Home tab, it is possible to adjust both segmentation and tracking parameters, though the default parameters are recommended.



### C.2.5.1 Segmentation settings

- **Minimum mitochondrial area** is the minimum area threshold for a connected component to be analyzed as a mitochondrion.
- **Maximum mitochondrial area** is the maximum area threshold for a connected component to be analyzed as a mitochondrion.
- **Custom gauss filt sigma** is the standard deviation used in the 3x3 gaussian filter after the diffuse background subtraction, but before the mask creation.

- **Custom threshold** is the threshold level (1-256) used for creating a mask from the gaussian filtered image.

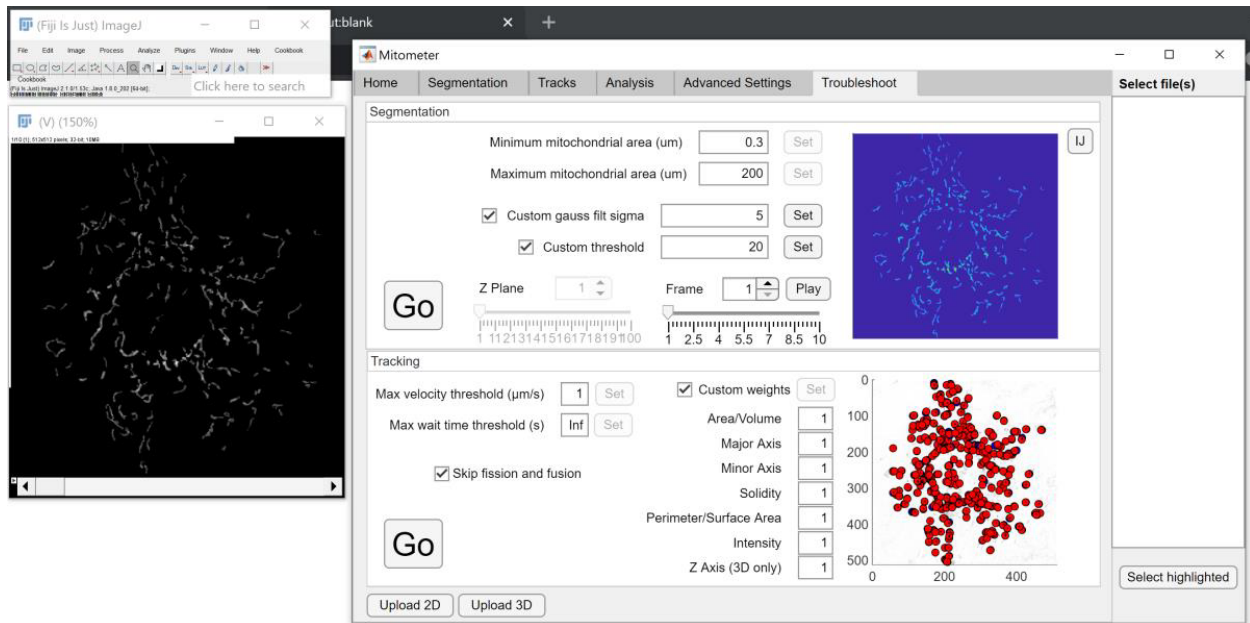
#### C.2.5.2 Tracking settings

- **Max velocity threshold** is the maximum speed a mitochondrion can travel between frames.
- **Max wait time threshold** is the amount of time the algorithm will attempt to assign an unassigned track to a mitochondrion.
- **Skip fission and fusion** will skip fission and fusion assignments and speeds up processing if these features are not needed.
- **Custom weights** allows you to choose the cost matrix weighting for each mitochondrial morphological feature, and will speed up processing.



## C.2.6 Troubleshoot tab

If a particular image does not segment or track correctly, you can use the troubleshooting tab to find parameters that work better.



### C.2.6.1 Segmentation

1. Manually enter any parameters you would like to test for troubleshooting.
2. If a custom gaussian filter sigma or threshold is desired, enable the checkbox next to the respective parameter.
3. Press the “Go” button in the segmentation section.
4. If the output image seems reasonable, click on the “Set” button next to the changed parameters. This will update Mitometer to use these parameter settings from the Home tab.

**Note:** You can open the segmented image through Fiji using the “IJ” button if Fiji has been opened as described.

### C.2.6.2 Tracking

1. Once you have a segmented image, you can troubleshoot tracking parameters.
2. Manually enter any parameters you would like to test for troubleshooting.
3. If custom morphology parameter weights are desired, enable the checkbox next to the respective parameter.
4. If you wish to skip fission and fusion events, enable the checkbox next to this option.
5. Press the “Go” button in the tracking section.
6. If the output image seems reasonable, click on the “Set” button next to the changed parameters. This will update Mitometer to use these parameter settings from the Home tab.

## C.3 Output

### C.3.1 Tracking output

Saving a file's data from the tracking tab will result in a .mat file of many essential and extra data from that file's segmentation and tracking processes. Opening the .mat file in MATLAB will produce a variable named "trackList". This variable is a 1xN structure where N is the number of tracks in the file. Each track has the following 1xM fields, where M is the number of frames in the track:

2D	3D	Description
Extrema	ConvexHull	The coordinates of the extrema or convex hull points comprising the mitochondrion.
PixelIdxList	VoxelIdxList	The indices of every pixel comprising the mitochondrion.
WeightedCentroid	WeightedCentroid	The intensity weighted centroid of the mitochondrion.
NPA	NPA	The number of potential track assignments (NPA) to which the mitochondrion can be assigned to.
label	label	The mitochondrion's corresponding label number in the object image.
OGid	OGid	The ID of the mitochondrion before thresholding based off of track length.
confident	confident	Whether the assignment was confident (1) or not (0) during that frame.

lost	lost	Whether the track was lost (1) or not (0) during that frame.
frame	frame	The frame number corresponding to vectors' column.
Area	Volume	The area or volume of the mitochondrion at that frame in microns.
Solidity	Solidity	The solidity of the mitochondrion, which is the ratio of the mitochondrion's area to the area of its convex hull.
Perimeter	SurfaceArea	The perimeter or surface area of the mitochondrion in microns.
MeanIntensity	MeanIntensity	The mean intensity (1-256) of the mitochondrion.
MajorAxisLength	MajorAxisLength	The major axis length of the mitochondrion in microns.
MinorAxisLength	MinorAxisLength	The minor axis length of the mitochondrion in microns.
N/A	ZAxisLength	The z axis length of the mitochondrion in microns.
fission	fission	Gives the track number from which the mitochondrion fissioned or not (0).
fusion	fusion	Gives the track number from which the mitochondrion fissioned or not (0).

Table C.1: Mitometer variable outputs.

## C.3.2 Analysis output

Saving a file's data from the analysis tab will result in a .txt file of the selected features. The file is comma delimited and is easily opened with programs such as excel for more complex analysis. Each row is a mitochondrion track, and each column is a frame.

**Tip:** When pasting data from the text file into Excel, you can split up the columns by going to Data → Text to Columns → Delimited → Comma → Finish.

	A	B	C	D	E	F	G	H	I	J	K	L	M	N
1	NaN	1.2725	1.943656	1.523594	1.266761	2.006349	1.667239	1.377713	2.048795	1.593618	1.308946	2.038551		
2	NaN	1.208822	1.544856	1.048964	1.095376	1.461058	0.9107	1.1357	1.494793	0.900321	1.180305	1.437488		
3	NaN	1.074291	NaN	NaN	NaN	NaN	NaN	NaN	NaN	NaN	NaN	NaN		
4	NaN	1.792011	2.397811	1.711376	1.701149	2.351433	1.697275	1.6847	2.372194	1.679803	1.689315	2.359027		
5	NaN	1.560341	NaN	NaN	NaN	NaN	NaN	NaN	NaN	NaN	NaN	NaN		
6	NaN	1.990875	2.398678	NaN	NaN	NaN	NaN	NaN	NaN	NaN	NaN	NaN		
7	NaN	1.525899	2.158879	2.479721	1.526825	2.149661	2.44891	1.521204	2.166943	2.450092	1.507271	2.169932		
8	NaN	1.500386	NaN	NaN	NaN	NaN	NaN	NaN	NaN	NaN	NaN	NaN		
9	NaN	1.176961	1.300796	1.728709	1.152218	1.29084	1.730694	1.235552	1.370773	1.879617	1.275637	1.326263		
10	NaN	2.242773	2.537148	1.55419	2.268708	NaN	NaN	NaN	NaN	NaN	NaN	NaN		
11	NaN	0.547989	NaN	NaN	NaN	NaN	NaN	NaN	NaN	NaN	NaN	NaN		
12	NaN	2.299607	2.516505	0.824453	1.838687	1.954818	1.240615	1.960344	1.965859	1.222244	1.972632	1.966559		
13	NaN	0.748416	0.859991	1.113405	0.729297	0.846035	1.103676	0.719283	0.853777	1.111012	0.703239	0.852129		
14	NaN	1.469227	1.782647	2.22407	1.419084	1.753111	2.201968	1.44824	1.790848	2.322956	1.509205	1.781958		
15	NaN	1.536997	2.440882	2.468642	1.563895	2.428105	2.412837	NaN	NaN	NaN	NaN	NaN		
16	NaN	0.571665	0.663849	0.475066	0.467473	0.669424	0.505067	0.469417	0.887349	0.660455	0.609961	0.712658		
17	NaN	2.003436	NaN	NaN	NaN	NaN	NaN	NaN	NaN	NaN	NaN	NaN		
18	NaN	2.329453	2.864803	2.014319	2.149923	2.906542	NaN	NaN	NaN	NaN	NaN	NaN		
19	NaN	2.673729	2.708184	NaN	NaN	NaN	NaN	NaN	NaN	NaN	NaN	NaN		
20	NaN	2.01415	1.721614	NaN	NaN	NaN	NaN	NaN	NaN	NaN	NaN	NaN		
21	NaN	0.910934	0.728513	0.576027	0.902643	0.726063	0.582043	0.911637	0.730477	0.605298	0.924285	0.737088		
22	NaN	0.829998	1.329902	1.248205	NaN	NaN	NaN	NaN	NaN	NaN	NaN	NaN		
23	NaN	2.437601	2.115633	1.173225	2.180313	1.752868	1.415622	2.218848	1.776078	1.388526	2.194726	1.78751		
24	NaN	1.640247	2.662405	2.323329	1.542253	NaN	NaN	NaN	NaN	NaN	NaN	NaN		
25	NaN	1.452479	2.100656	1.541014	1.477376	2.425761	NaN	NaN	NaN	NaN	NaN	NaN		
26	NaN	2.801797	2.720138	1.755648	2.77391	2.777087	1.745815	2.630396	2.534952	1.780146	2.692742	2.796582		
27	NaN	0.674591	1.102714	0.784105	0.687207	NaN	NaN	NaN	NaN	NaN	NaN	NaN		
28	NaN	1.12327	1.371656	1.556143	1.136257	NaN	NaN	NaN	NaN	NaN	NaN	NaN		
29	NaN	2.23182	NaN	NaN	NaN	NaN	NaN	NaN	NaN	NaN	NaN	NaN		
30	NaN	1.149299	1.768658	NaN	NaN	NaN	NaN	NaN	NaN	NaN	NaN	NaN		
31	NaN	1.602813	NaN	NaN	NaN	NaN	NaN	NaN	NaN	NaN	NaN	NaN		

## C.4 ImageJ guide

### C.4.1 Prerequisites

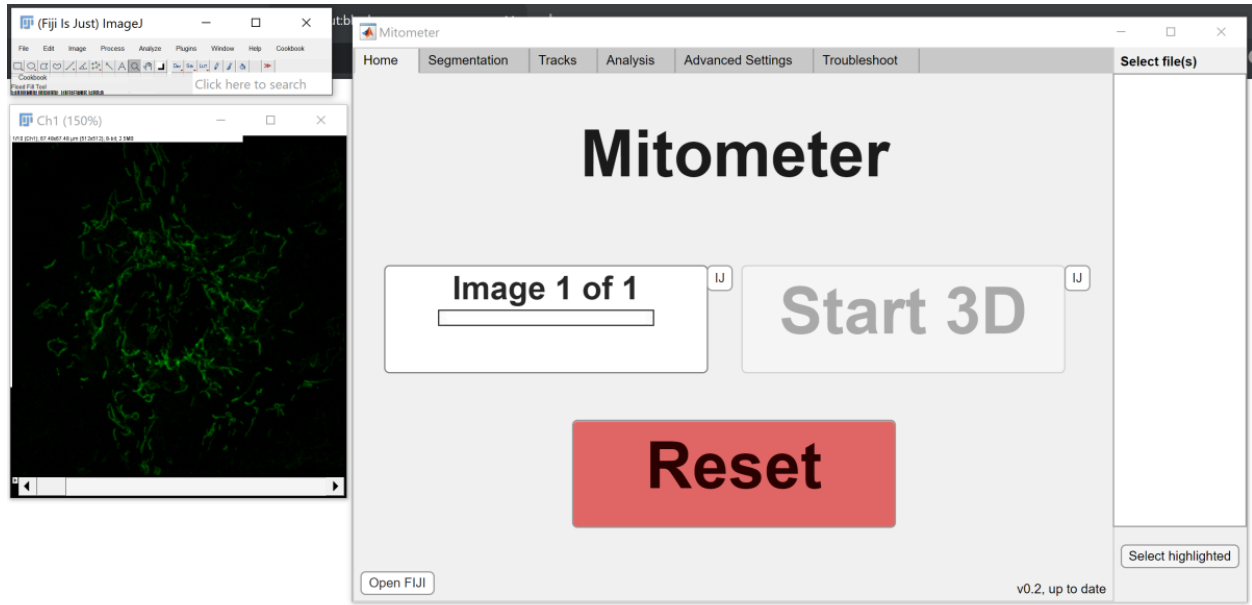
1. Download FIJI (<https://imagej.net/Fiji>)
2. Open FIJI
3. Go to Help → Update
  - (a) Wait for the status check to finish
4. Open Manage update sites
5. Enable ImageJ-MATLAB
6. Click close
7. Click Apply changes on ImageJ Updater.
8. Close FIJI.

**Note:** You only need to do this once.

### C.4.2 Mitometer

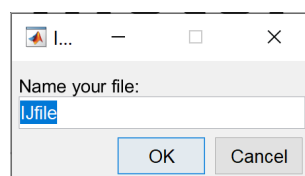
1. Click “Open FIJI” in the home tab.
2. Select your FIJI scripts folder.
  - (a) On Mac: Select the folder where the FIJI app is located (likely in the “Applications” folder).
  - (b) On PC: Select the FIJI scripts folder (default is Documents → Fiji.app → scripts).
  - (c) An ImageJ toolbar should open.

3. Open the image you wish to analyze as you would normally through ImageJ
4. On the Mitometer Home tab, click the IJ button next to Start 2D if you have opened a 2D image, and next to Start 3D if you have opened a 3D image.



#### C.4.2.1 Start 2D

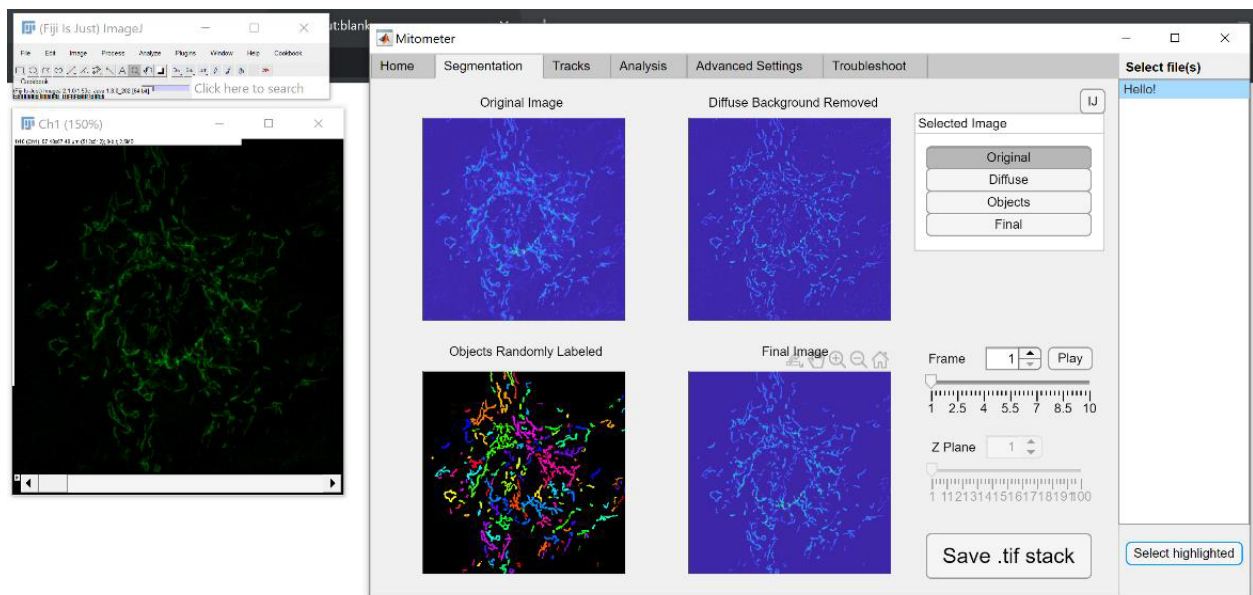
1. Input pixel size and time between each temporal frame.
2. Name your file.
  - Uploaded files will be shown in the right column under “Select file(s)”
  - **Note:** You can analyze additional 2D files by again pressing on IJ with a different file open.



### C.4.2.2 Start 3D

1. Input pixel size, time between each temporal frame, number of spatial planes, and axial distance between the spatial planes.
2. Name your file.
  - Uploaded files will be shown in the right column under “Select file(s)”
  - **Note:** You can analyze additional 3D files by pressing on IJ with a different file open.

**Note:** As long as you don’t quit out of Fiji, you can keep using it through Mitometer.





## **C.5 Requirements**

### **C.5.1 Windows**

#### **C.5.1.1 Operating systems**

- Windows 10 (version 1803 or higher)
- Windows 7 Service Pack 1
- Windows Server 2019
- Windows Server 2016

#### **C.5.1.2 Processors**

- Minimum: Any Intel or AMD x86-64 processor
- Recommended: Any Intel or AMD x86-64 processor with four logical cores and AVX2 instruction set support

#### **C.5.1.3 RAM**

- Minimum: 4 GB
- Recommended: 8 GB

### **C.5.2 Mac**

#### **C.5.2.1 Operating systems**

- macOS Catalina (10.15)

- macOS Mojave (10.14)

### **C.5.2.2 Processors**

- Minimum: Any Intel x86-64 processor
- Recommended: Any Intel x86-64 processor with four logical cores and AVX2 instruction set support

### **C.5.2.3 RAM**

- Minimum: 4 GB
- Recommended: 8 GB

## **C.5.3 Linux**

### **C.5.3.1 Operating systems**

- Ubuntu 20.04 LTS
- Ubuntu 18.04 LTS
- Ubuntu 16.04 LTS
- Debian 10
- Debian 9
- Red Hat Enterprise Linux 8
- Red Hat Enterprise Linux 7 (minimum 7.5)

- SUSE Linux Enterprise Desktop 12 (minimum SP2)
- SUSE Linux Enterprise Desktop 15
- SUSE Linux Enterprise Server 12 (minimum SP2)
- SUSE Linux Enterprise Server 15

#### **C.5.3.2 Processors**

- Minimum: Any Intel or AMD x86-64 processor
- Recommended: Any Intel or AMD x86-64 processor with four logical cores and AVX2 instruction set support

#### **C.5.3.3 RAM**

- Minimum: 4 GB
- Recommended: 8 GB

### **C.5.4 All**

Mitometer has been tested only on Windows 10 and macOS Catalina with MATLAB R2020a and R2020b.

## C.6 License

This project is covered under the **GNU General Public 3.0 License**.

# Appendix D

## Automated mitochondria segmentation and tracking in live-cell time-lapse images: Supplementary materials

The main text for this appendix can be found in [Chapter 6](#).

## D.1 Open-source mitochondria analysis algorithms self described as automated

### D.1.1 Mitochondrial Network Analysis (MiNA)

[Valente et al. (2017)]:

<https://github.com/StuartLab/MiNA>

MiNA uses a GUI to make use of existing ImageJ plugins in order to quantify mitochondrial morphology. The analysis is optimized for 2D but has limited functionality for 3D, especially for visualization purposes. The output gives only cell-wide aggregate mitochondrial data and does not allow temporal analysis. We define the technique as semi-automated as it requires the user to select a thresholding operation. It also prompts the user to optionally select a median filter, unsharp mask, or local contrast enhancement. The benefit is that the implementation of MiNA is completely free, using code written in Java and Python, implemented in ImageJ. To use MiNA in an operator-independent manner, we processed the validation files using the default settings, corresponding to an Otsu threshold and no optional parameters selected.

### D.1.2 MitoGraph

[Viana et al. (2015)]:

<https://github.com/vianamp/MitoGraph>

MitoGraph calculates 3D volume and intracellular structures of organelles in living cells, but especially optimized for tubular mitochondrial networks. We were able to use the software in 2D for validation purposes. It allows analysis of only a single temporal frame, thus giving

no motility measurements. Additionally, there is no GUI, running only through command lines. A benefit, again, is that the software is completely free, written in C++.

### D.1.3 Mytoe

[Lihavainen et al. (2012)]:

<https://sites.google.com/view/andreriabeirolab/home/software>

Mytoe is a software to analyze mitochondrial dynamics and structure. The Mytoe software was not available at the link listed in the publication. We assume the software listed on the corresponding author's website is up to date. Mytoe is able only to analyze 2D mitochondrial fluorescence time stacks and presents data in terms of nodes and branches as well as individual mitochondria. Mytoe's MATLAB GUI is not fully functional, perhaps due to its construction on an older version of MATLAB. It is also unclear how the temporal aspect is incorporated into the algorithm. When a single temporal stack is selected for analysis, all temporal frames appear, however, when multiple temporal stacks are selected for analysis, only a single temporal frame of each stack appears. The manual and publication make solving this problem unclear. We thus chose to analyze temporal stacks individually on a stack-by-stack basis for the motility validation, aggregating speed data for each frame and using a rank sum comparison to the ground truth. The software also does not record tracks between frames, and instead uses an optical flow algorithm between only two adjacent frames at a time, thus we omit lifetime comparisons. Mytoe is written in MATLAB but has a standalone Windows version which does not require MATLAB, though this limits the user to only the preestablished source code.

### D.1.4 Mitochondrial Single Particle Tracking (MitoSPT)

[Kandel et al. (2015)]:

<https://github.com/kandelj/MitoSPT>

MitoSPT is a software used mainly to characterize the distribution of whole-cell mitochondrial movement in 2D but can also give limited information on individual mitochondria within the cell. MitoSPT requires a pre-processing step for each image through ImageJ through a custom macro. In this macro, however, a user-defined threshold is required. For our purposes, we used the auto-threshold value for the segmentation experiments. Additionally, in the MATLAB GUI, MitoSPT required several operator-dependent inputs, such as minimum and maximum mitochondrial area, and maximum track length. MitoSPT was also limited in its output from the GUI. Although the program creates a list of individual points derived from mitochondria along with their corresponding coordinates at each time frame, the output gives only distance and angle traveled. It does not output individual tracks, nor does it output morphometric data. To accommodate the program for validation purposes, we implemented additional outputs within the source code derived from the distance vectors to give the speeds and lifetime of each tracked point. MitoSPT also purports being able to capture fission and fusion events, but this feature does not appear in the GUI. Additionally, the described method requires high temporal resolution, as it analyzes adjacent frames for component overlap to determine these mitochondrial dynamics. MitoSPT also uses MATLAB and does not have a standalone version.

### D.1.5 QuoVadoPro (QVP)

[Basu and Schwarz (2020)]:

<https://github.com/ThomasSchwarzLab/QuoVadoPro>



QVP is a set of ImageJ macros used to segment, quantify, and visualize intracellular organelle motion by quantifying the variance of pixel illumination across time. QVP requires by default file-by-file segmentation (though a batch analysis is relatively easy to implement) and user input of multiple parameters, including a gaussian smoothing radius, a threshold value, a time smoothing value, and a minimum particle size. For comparability and automation purposes, we used the default values, or the values recommended in the manual if presented, i.e. a gaussian smoothing radius of 5, a threshold of 9000, a time smoothing of 1, and a minimum particle size of 1. QVP also requires a number of substacks in which to split the time series, which we left as the default of 1. QVP does not analyze morphometrics and gives as a motility metric only the motility score, which is a quantification of the pixel illumination variance, on an image-wide basis, and does not give frame-by-frame quantification. Thus, a comparable analysis to object-based methods was not possible. QVP also does not analyze fission and fusion events. QVP is written as an ImageJ macro file and implemented as an ImageJ plugin.

### D.1.6 Mitochondrial Segmentation Network (MitoSegNet)

[Fischer et al. (2020)]:

<https://github.com/MitoSegNet>

MitoSegNet is a pretrained deep learning segmentation model used to segment and analyze mitochondrial morphometrics. MitoSegNet handles batch input and requires no user-input for parameters, eliminating bias. It handles only 2D images and does not allow analysis of temporal variation. It allows quantification and visualization of individual mitochondrial morphometrics but does not quantify motility metrics or fission and fusion events. MitoSegNet is written in Python and runs on a standalone software.

### D.1.7 MTrack2

[Klopfenstein and Vale (2004)]:

<https://github.com/fiji/MTrack2>

MTrack2 is a 2D tracking software which uses ImageJ's built-in particle analyzer plugin to link particles between frames. It works only for 2D images and gives centroid positions of objects in a binary image. It cannot handle multiple files within the plugin but is relatively easy to code for batch analysis. It does not output morphological features, nor does it handle fission and fusion events. The GUI is relatively limited, relying on ImageJ's templates and results page for the output. MTrack2 is written in Java and implemented as an ImageJ plugin.

### D.1.8 TrackMate

[Tinevez et al. (2017)]:

<https://github.com/fiji/TrackMate>

TrackMate is a segmentation and tracking algorithm designed with modularity and scriptability in mind. It is specifically suited for round spots and particles, and thus its use on mitochondria is limited. It can handle 2D and 3D inputs, and outputs morphometrics limited to particle diameter and average intensity, among a few others, as well as motility metrics such as displacement, speed, and track merges and splits. Because of its specific design for round objects, medium to long mitochondria tend to be segmented into multiple objects. The plugin also requires an input of an estimated blob diameter and a threshold, parameters whose ideal values can vary greatly in mitochondria. TrackMate is written in Java and is implemented as an ImageJ plugin.

Tool	<i>Mitometer</i>	MiNA	Mito-Graph	MyToe	MitoSPT	QVP	Mito-SegNet	MTrack2	Track Mate
<b>Automated</b>	Full	Semi	Full	Semi	Semi	Semi	Full	Semi	Semi
<b>2D</b>	Yes	Yes	Yes	Yes	Yes	Yes	Yes	Yes	Yes
<b>3D</b>	Yes	Lim	Yes	No	No	Lim	No	No	Yes
<b>Temporal Analysis</b>	Yes	No	No	Lim	Lim	Lim	No	Yes	Yes
<b>Individual Mito</b>	Yes	No	Lim	Lim	Lim	No	Yes	Yes	Lim
<b>Morpho-metric</b>	Yes	Lim	Lim	Lim	No	No	Yes	No	Lim
<b>Motility Metrics</b>	Yes	No	No	Lim	Yes	Lim	No	Lim	Yes
<b>Fission/Fusion</b>	Yes	No	No	No	Lim	No	No	No	Lim
<b>GUI</b>	Yes	Yes	No	Lim	Lim	Lim	Yes	Lim	Yes
<b>Language</b>	Mat	Python/Java/IJ	C++	Mat	Mat	IJ	Python	Java/IJ	Java/IJ

Figure D.1: Comparison of Mitometer to existing open-source methods self-described as automated. We compared features and validation experiments between 5 different mitochondrial analysis software that are open source and self-proclaimed as automated, including Mitometer. We define a software as fully automated if the required inputs do not introduce operator bias, and if it can handle batch input. For example, if a software requires only pixel size, it is considered fully automated, however if it additionally requires the user to specify a median filter size, it is only semi-automated. Likewise, if a software can only perform analysis on one image before requiring additional user-input, we define it as only semi-automated. We also assess its ability to analyze mitochondria in 2D and 3D images, and if it can handle temporal stacks. We also assess if the software fully quantifies and output data of individual mitochondria at each time frame, rather than cell-wide or stack-wide outputs. Furthermore, we assess the software’s ability to output morphological and motility metrics, and if it can analyze fission and fusion events. Finally, we assess the usability and simplicity of the GUI and the software’s corresponding language.

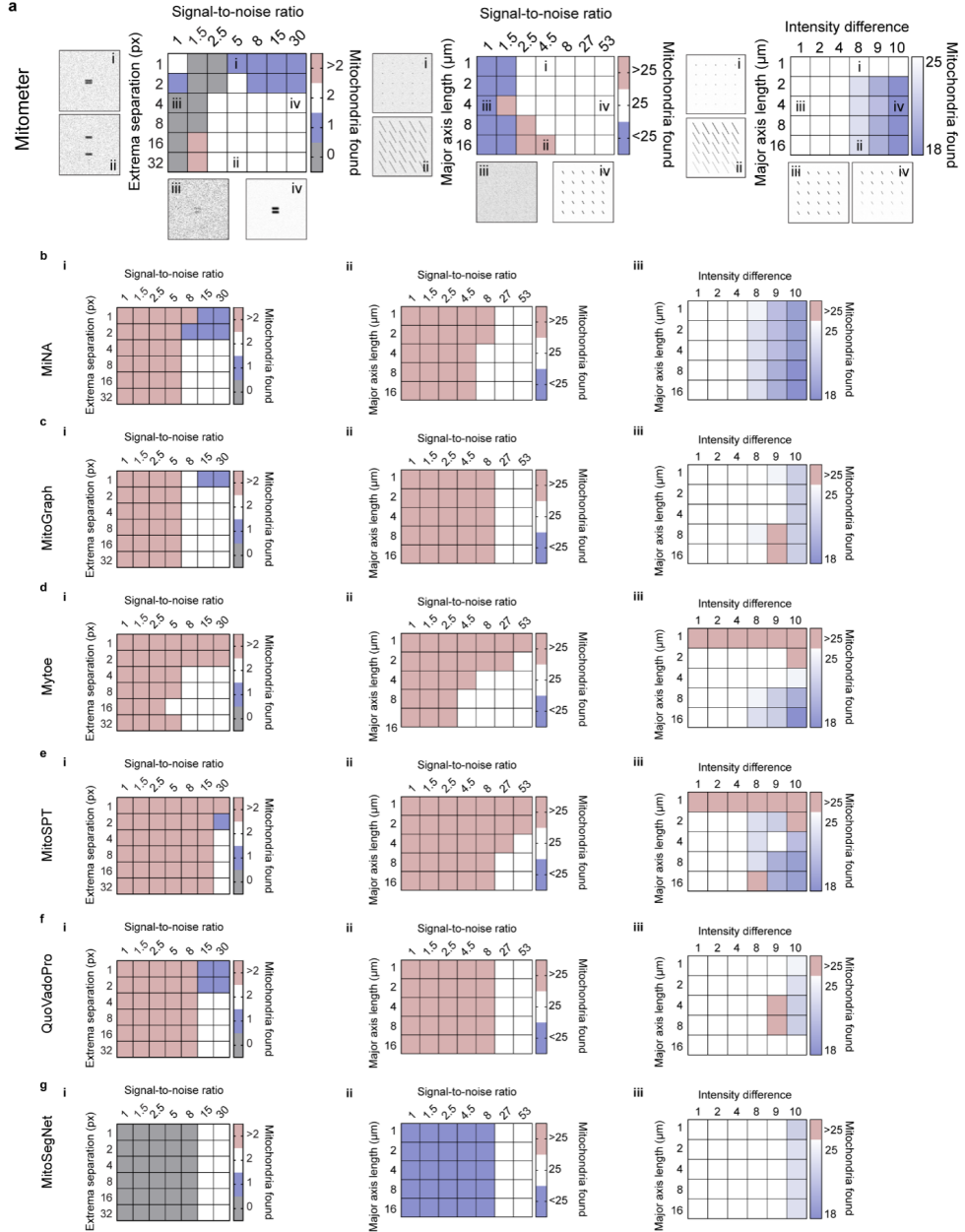


Figure D.2: Segmentation validation comparison of Mitometer to existing open-source methods self-described as automated. **a**, Mitometer validation data reprinted from Fig. 6.7 for reference. For comparison, validation data for MiNA (**b**), MitoGraph (**c**), Mytoe (**d**), MitoSPT (**e**), QuoVadoPro (**f**), and MitoSegNet (**g**) segmentation algorithms are shown. For each software, we present data of the number of mitochondria from a simulated image of 2 adjacent mitochondria at increasing separations and signal-to-noise ratios (i), of 25 mitochondria at increasing major axis lengths and signal-to-noise ratios (ii), and of 25 mitochondria at increasing major axis lengths and intensity differences (iii).  $n=3$  independent trials.

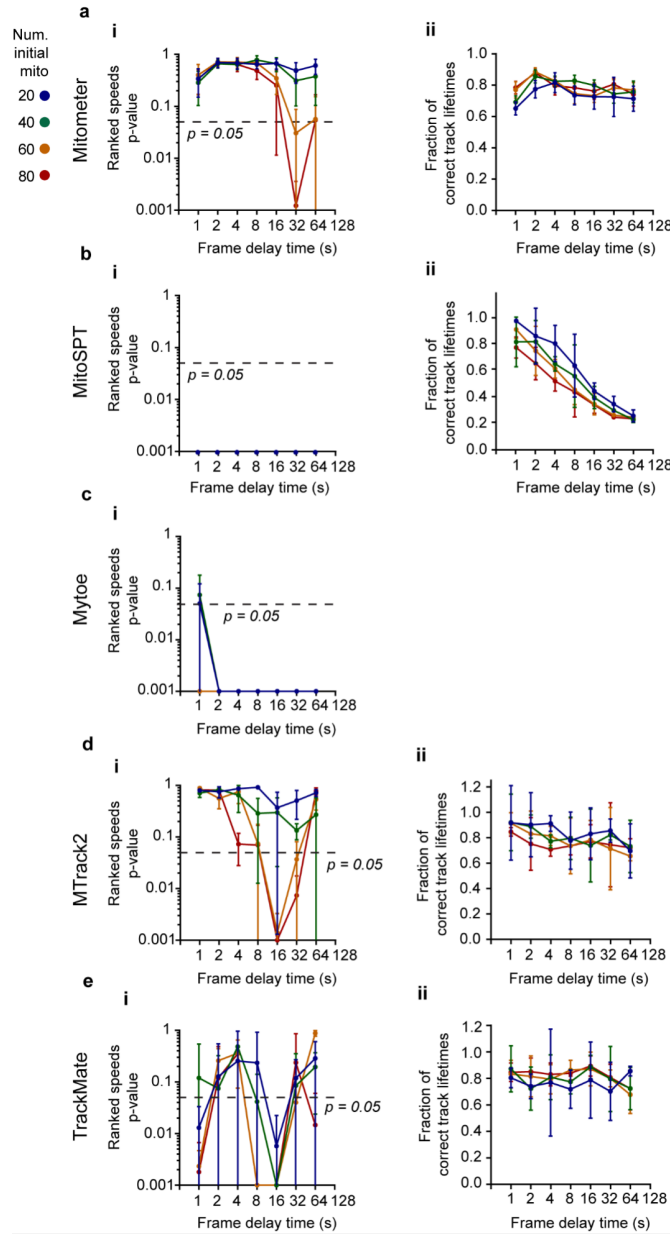


Figure D.3: Tracking validation comparison of Mitometer to existing open-source methods self-described as automated. **a**, Mitometer validation data reprinted from Fig. 3 for reference. For comparison, validation data for Mytoe (**b**), MitoSPT (**c**), MTrack2 (**d**), and TrackMate (**e**) tracking algorithms are shown. For each software, we present data of the comparison in speed of the algorithm against the ground truth values as quantified by a two-sided Wilcoxon rank sum test's p-value (i), and for MitoSPT we show the fraction of tracks with the correct lifetimes (ii). Mytoe's fraction of tracks with the correct lifetimes is omitted as the software is incapable of tracking components over more than two frames. (i) Points below 0.001 are rounded to 0.001. Data are presented as means with 95% confidence intervals.  $n=10$  independent trials.

## D.2 Diffuse background removal (diffuseBgRemove.m)

To preserve the complex shapes and varying sizes of mitochondria, we avoid the use of a median filter with a definitive size. Instead, we create an adaptive filter that encompasses a range of circular median filter sizes based on the pixel size of the image. The radius varies from a minimum of  $0.3\ \mu\text{m}$ , the set minimum area of a mitochondrion, to a maximum of  $1\ \mu\text{m}$ , a size which gives a diameter above the minor axis length of a mitochondrion, but not so large as to increase the run time unnecessarily. This is important, as choosing a maximum size below the minor axis length of a mitochondrion may lead to the algorithm classifying the mitochondrion as the background, and ultimately leading to its removal.

We begin by creating two-dimensional disk filters using MATLAB's `fspecial` function. We use this disk filter in MATLAB's `ordfilt2` function using the median value as the order, thereby creating a median disk filter. We iterate through this process to create multiple median disk filters in radius steps of 1 pixel from the minimum radius to the maximum radius to create a stack of median disk filters. We add the original image into the stack as well. We then find the stack-wide minimum value for each pixel to create the diffuse background image and subtract this from the original image. We repeat this process for each frame and each z-slice in the case of 3D imaging to remove the diffuse background image from the entire fluorescence image stack.

### D.2.1 diffuseBgRemove.m

---

```
function [ImBgRemoved,ImMinMed,ImMedFiltered] =  
    diffuseBgRemove(Im,minCircleFiltSize,maxCircleFiltSize)  
  
    ImMinMed = zeros(size(Im),class(Im));  
    ImBgRemoved = zeros(size(Im),class(Im));
```

```

minCircleFilt = max(2,minCircleFiltSize);

loading = waitbar(0,'Please
    wait...','CreateCancelBtn','setappdata(gcf,'canceling',1)');
setappdata(loading,'canceling',0);
pause(.0002)

for frameNum = 1:size(Im,3)

    %We add the original image into the stack as well.
    ImMedFiltered(:,:,1) = Im(:,:,frameNum);
    circleFilt = cell(1,round(maxCircleFiltSize) - round(minCircleFilt));

    circleFiltNum = 1;

    %We iterate through this process to create multiple median disk filters
    %in radius steps of 1 pixel from the minimum radius to the maximum
    %radius to create a stack of median disk filters.
    for circleSize = round(minCircleFilt):round(maxCircleFiltSize)
        %
        if getappdata(loading,'canceling')
            delete(loading)
            break
        end
        waitbar(circleSize/round(maxCircleFiltSize),loading,sprintf('Median
            filter %d of %d for frame %d of
            %d.',circleSize,round(maxCircleFiltSize),frameNum,size(Im,3)));
        pause(.0002)
    end
end

```

```

%
circleFiltNum = circleFiltNum + 1;

% We begin by creating a two-dimensional disk filters using MATLAB's
    fspecial function. We use this disk filter in MATLAB's ordfilt2
    function using the median value as the order, thereby creating a
    median disk filter.

circleFilt{circleFiltNum-1} = fspecial('disk',circleSize)>0;
ImMedFiltered(:,:,circleFiltNum) = ordfilt2( ImMedFiltered(:,:,1),
    round(0.5*numel( find(circleFilt{ circleFiltNum-1}))), circleFilt{
    circleFiltNum-1}, 'symmetric');
end

%We then find the stack-wide minimum value for each pixel to create the
    diffuse background image and subtract this from the original image.
ImMinMed(:,:,frameNum) = min(ImMedFiltered,[],3);

ImBgRemoved(:,:,frameNum) = ImMedFiltered(:,:,1)-ImMinMed(:,:,frameNum);

%We repeat this process for each frame and each z-slice in the case of 3D
    to remove the diffuse background image from the entire fluorescence
    image stack.
end
delete>Loading)

end

```

---



## D.3 Parameter optimization

To correctly optimize the Gaussian filter sigma and absolute threshold for stability, we first evaluate the intensity values in the image. We use Otsu's thresholding and verify its effectiveness metric to determine whether it is satisfactory (80% effective) to use rather than iterating through intensity values. If it is not satisfactory (80% effective) we calculate the entire stack's 80<sup>th</sup> quantile of intensities above 2 and use that as the upper limit for thresholding.

We also limit the Gaussian filter's sigma between 0.33 and 0.5 with iterations in steps of 0.01. We choose these values as we want to keep the Gaussian filter's size to a 3x3 kernel. We choose a minimum sigma of greater than 0.32 as it has a center value of 0.97 and edge values of 0.0074, essentially making it and anything below it useless as a filter. We choose a maximum sigma of 0.5 as, in general, the rule of thumb is to limit the filter size to 3 times the sigma on either side of the center (making it  $6 \times 0.5$  for a size of 3). This is because the tails of the Gaussian have values that are effectively 0 after three sigma, and anything greater than 0.5 with a filter size of 3 produces a noticeably non-Gaussian filter.

We then iterate through the first 10 timeframes (or all frames if the total number of timeframes is less than 10) for each sigma and intensity value. We calculate the number of mitochondria and the median area of all mitochondria that are within the area threshold in each temporal frame. We calculate the standard deviation of the median area of the mitochondria and the mean and standard deviation of the number of mitochondria across all temporal stacks for each Gaussian sigma and absolute threshold value. We take the z-score of each of these mitochondrial parameters to build up our cost matrix. To ensure choosing a stable value, we run the cost matrix through a symmetric 3x3 median filter, which acts to remove any outlying regions. We then select the minimum value of this cost matrix to set our sigma and threshold values.

Finally, we run the kernel over the entire temporal stack and create a mask using the threshold value, which we then apply to the original image to obtain the stack that will be used for tracking. In the case of 3D time lapse images, we are able to remove pane-specific artifacts by removing any components that appear in only one plane. This process will not affect mitochondria so long as the z-distance is kept to a reasonable step-size.

### D.3.1 optimizeSigmaThresh.m

---

```
function [sigmaOptimal,threshOptimal,costs] =
    optimizeSigmaThresh(ImBgRemoved,minArea,maxArea)

numFrames = min(size(ImBgRemoved,3),10);

% We use Otsu's thresholding and verify its effectiveness metric to determine
% whether it is satisfactory (>80% effective) to use rather than iterating
% through intensity values. If it is not satisfactory (<80% effective) we
% calculate the entire stack's 80th quantile of intensity and use that as
% the upper limit for thresholding.
[t,em] = graythresh(uint8(ImBgRemoved));
if em > 0.8 && round(t*max(ImBgRemoved(:))) ~= 0
    intensityQuantile = round(t*max(ImBgRemoved(:)));
    threshMatrix = intensityQuantile;
else
    intensityQuantile = quantile(ImBgRemoved(ImBgRemoved~=0),0.8);
    threshMatrix = (2:1:intensityQuantile);
end

%We also limit the gaussian filter's standard deviation between 0.33 and
```

```

%0.5. We choose these values as we want to keep the gaussian filter's size
%to a 3x3 kernel. We choose a minimum standard deviation of greater than
%0.32 as it has a center value of 0.97 and edge values of 0.0074,
%essentially making it and anything below it useless as a filter. We choose
%a maximum standard deviation of 0.5 as, in general, the rule of thumb is
%to limit the filter size to 3 times the standard deviation on either side
%of the center (making it 6*0.5 for a size of 3). This is because the tails
%of the Gaussian have values that are effectively 0 after three standard
%deviations, and anything greater than 0.5 with a filter size of 3 produces
%a non-Gaussian filter.

sigmaMatrix = (0.33:0.01:0.5);

numComponents = zeros([length(threshMatrix),length(sigmaMatrix),numFrames]);
medianArea = zeros([length(threshMatrix),length(sigmaMatrix),numFrames]);

loading = waitbar(0,'Please
    wait...','CreateCancelBtn','setappdata(gcf,'canceling',1)');
setappdata(loading,'canceling',0);
pause(.0002)

for sigma = 1:length(sigmaMatrix)
    ImGaussFiltered = gaussFilter(ImBgRemoved,sigmaMatrix(sigma));
    for thresh = 1:length(threshMatrix)

        %
        if getappdata(loading,'canceling')
            delete(loading)
            break
        end
    end
end

```

```

waitbar((thresh+length(threshMatrix)*(sigma-1))/
    (length(sigmaMatrix)*length(threshMatrix)), loading,
    sprintf('Testing parameter %d of %d.',
    (thresh+length(threshMatrix)*(sigma-1)),
    (length(sigmaMatrix)*length(threshMatrix))));
pause(.0002)
%

ImMask = thresholdImage(ImGaussFiltered,threshMatrix(thresh));

%We then iterate through the first 10 timeframes (or all frames if
%the total number of timeframes is less than 10) for each standard
%deviation and intensity value.
for frameNum = 1:numFrames
    CCPreThresh = bwconncomp(ImMask(:,:,frameNum));
    statsPreThresh = regionprops(CCPreThresh,'Area');
    %We calculate the number of mitochondria and the median area of
    %all mitochondria that are within the area threshold in each
    %temporal frame.
    if nargin > 1
        keptComponents = find([statsPreThresh.Area]>minArea &
            [statsPreThresh.Area]<maxArea);
        numComponents(thresh,sigma,frameNum) = length(keptComponents);
        medianArea(thresh,sigma,frameNum) =
            nanmedian([statsPreThresh(keptComponents).Area]);
    else
        keptComponents = find([statsPreThresh.Area]>1);
        numComponents(thresh,sigma,frameNum) = length(keptComponents);
    end
end

```

```

        medianArea(thresh,sigma,frameNum) =
            nanmedian([statsPreThresh(keptComponents).Area]);
    end
end
end
end

%We calculate the standard deviation of the median area of the mitochondria
%and the mean and standard deviation of the number of mitochondria across
%all temporal stacks for each Gaussian sigma and absolute threshold value.
meanArea = nanmean(medianArea,3);
stdNum = nanstd(numComponents,[],3);
stdArea = nanstd(medianArea,[],3);
stdArea(isnan(stdArea)) = nanmean(stdArea(:));
meanNum = nanmean(numComponents,3);

%We take the z-score of each of these mitochondrial parameters to build up
%our cost matrix.
normStdArea = zscore(stdArea,0,'all');
normStdNum = zscore(stdNum,0,'all');
normMeanNum = zscore(meanNum,0,'all');

%To ensure choosing a stable value, we run the cost matrix through a
%symmetric 3x3 median filter, which acts to remove any outlying regions.
costMatrix = medfilt2(normStdArea + normStdNum - 0.5*normMeanNum,'symmetric');
costMatrix(costMatrix==0) = 1e4;

%We then select the minimum value of this cost matrix to set our sigma and
%threshold values.
minVal = min(costMatrix,[],'all');

```

```

[rowMin,colMin] = find(costMatrix == minVal);

threshOptimal = threshMatrix(floor(median(rowMin)));
sigmaOptimal = sigmaMatrix(floor(median(colMin)));

costs.stdArea = stdArea;
costs.stdNum = stdNum;
costs.meanNum = meanNum;
costs.normStdArea = normStdArea;
costs.normStdNum = normStdNum;
costs.normMeanNum = normMeanNum;
costs.costMatrix = costMatrix;
costs.numComponents = numComponents;
costs.medianArea = medianArea;
costs.rowMin = rowMin;
costs.colMin = colMin;

delete>Loading)

end

```

---

## D.4 Calculating the cost matrix

To find the differences in distance and mitochondrial morphological features, we compare these parameters from mitochondria found in the current time frame to those of existing tracks. In the case of distance differences, we take the differences in x, y, and z (in 3D) intensity weighted centroid positions. We then use the square root of the squared sums as the distance.

$$\Delta D_{i,j} = \sqrt{(x_j - x_i)^2 + (y_j - y_i)^2 + (z_j - z_i)^2} \quad (\text{D.1})$$

Where “i” is a mitochondrion in the current time frame, “j” is an existing track, “x”, “y”, and “z” are the x, y, and z-coordinates of the intensity weighted centroid, respectively, and “ $\Delta D$ ” is the distance difference. For the other features, we simply take the difference in the feature’s value between the current time frame’s mitochondria to those of existing tracks (e.g. the difference in surface area) divided by the existing track’s value, producing a normalized difference.

$$\Delta F_{i,j} = \frac{F_i - F_j}{F_j} \quad (\text{D.2})$$

Where “i” is a mitochondrion in the current time frame, “j” is an existing track, and “F” is the feature in question. For 2D the features are area, major axis length, minor axis length, solidity, perimeter, and mean intensity. For 3D the features are volume, major axis length, minor axis length, z axis length, solidity, surface area, and mean intensity. These difference values are then squared, and the z-score is calculated. Any differences between mitochondria and tracks that do not meet the maximum velocity and search time thresholds are set to infinity to avoid assignment. These z-scored morphological features are then

weighted (equally in the first iteration, and confidently in the second) and summed.

$$C_{i,j} = \Delta Z D_{i,j} + \sum_{ZF=1}^n w_F \Delta Z F_{i,j} \quad (\text{D.3})$$

Where “ZD” is the squared z-score normalized distance difference, “ZF” is the squared z-score normalized feature in question,”  $w_F$ ” is the feature in question’s weighting, “n” is the total number of features, and “ $C_{i,j}$ ” is the cost of assignment between mitochondrion i and track j. The cost matrix is then appended to a diagonal matrix of a dynamic value for new track assignments to create the final cost matrix. This diagonal matrix’s value depends on the costs of assignment for confident assignments. Confident costs are those that minimize the individual mitochondrion’s assignment cost, as well as minimize the global assignment cost of all mitochondria. The diagonal matrix is first set to 1 and is updated at each frame to the 98<sup>th</sup> quantile of a running list of costs for the confident assignment

#### D.4.1 trackMitochondria.m

---

```
function [track, mitoCoM, extra] = trackMitochondria(Im, ImOG, weights,
    micronPerPixel, secondsPerFrame, distThreshMicrons, frameThreshSeconds,
    stdRange, skipDyn)

numFrames = size(Im,3);

% User Parameters
distThresh = (distThreshMicrons/micronPerPixel)*secondsPerFrame;
frameThresh = round(frameThreshSeconds/secondsPerFrame);

% Other Parameters
wArea = weights(1);
wMajAx = weights(2);
```



```

wMinAx = weights(3);
wSol = weights(4);
wPeri = weights(5);
wInt = weights(6);
startCost = 1;

%%%%%%%%%%%%%%%%%%%%%%%%%%%%%%%%%%%%%%%%%%%%%%%%%%%%%%%%%%%%%%%%%%%%%%%%
%%%%%%%%%%%%%%%%%%%%%%%%%%%%%%%%%%%%%%%%%%%%%%%%%%%%%%%%%%%%%%%%%%%%%%%%
%%%%%%%%%%%%%%%%%%%%%%%%%%%%%%%%%%%%%%%%%%%%%%%%%%%%%%%%%%%%%%%%%%%%%%%%
%%Assign Tracks
% Initialize
extra = struct();
CC = cell(1,numFrames);
L = cell(1,numFrames);
mito = cell(1,numFrames);
numMito = zeros(1,numFrames);
NN = cell(1,numFrames);
NNExtrema = cell(1,numFrames);
firstUsableFrame = true;
secondUsableFrame = false;
mitoCoM = struct();
distanceMatrix = cell(1,numFrames);
areaMatrix = cell(1,numFrames);
majAxMatrix = cell(1,numFrames);
minAxMatrix = cell(1,numFrames);
solMatrix = cell(1,numFrames);
periMatrix = cell(1,numFrames);
intMatrix = cell(1,numFrames);
frameMatrix = cell(1,numFrames);

```

```

NPA = cell(1,numFrames);
distanceMatrixThresholded = cell(1,numFrames);
distanceMatrixSq = cell(1,numFrames);
areaMatrixSq = cell(1,numFrames);
majAxMatrixSq = cell(1,numFrames);
minAxMatrixSq = cell(1,numFrames);
solMatrixSq = cell(1,numFrames);
periMatrixSq = cell(1,numFrames);
intMatrixSq = cell(1,numFrames);
distanceMatrixZ = cell(1,numFrames);
areaMatrixZ = cell(1,numFrames);
majAxMatrixZ = cell(1,numFrames);
minAxMatrixZ = cell(1,numFrames);
solMatrixZ = cell(1,numFrames);
periMatrixZ = cell(1,numFrames);
intMatrixZ = cell(1,numFrames);
differenceMatrix = cell(1,numFrames);
assignTrackMatrix = cell(1,numFrames);
matchedTrack = cell(1,numFrames);
confident = cell(1,numFrames);

firstFrame = 1;

runningConfidentCosts = [];

loading = waitbar(0,'Please
    wait...','CreateCancelBtn','setappdata(gcf,'canceling',1)');
setappdata(loading,'canceling',0);
pause(.0002)

```

```

for frameNum = 1:numFrames

    %
    if getappdata>Loading, 'canceling')
        delete>Loading)
        break
    end

    waitbar(frameNum/numFrames,Loading,sprintf('Tracking frame %d of
        %d.',frameNum,numFrames));
    pause(.0002)
    %

    %Get stats for each mitochondrion in each frame.
    CC{frameNum} = bwconncomp(Im(:,:,frameNum));
    L{frameNum} = labelmatrix(CC{frameNum});
    mito{frameNum} = regionprops(CC{frameNum}, Im(:, :, frameNum), 'Area',
        'Centroid', 'Solidity', 'MaxFeretProperties', 'Extrema',
        'MeanIntensity', 'WeightedCentroid', 'MajorAxisLength',
        'MinorAxisLength', 'Perimeter', 'PixelIdxList');
    numMito(frameNum) = length(mito{frameNum});

    %Keep iterating through frames until one with mitochondria appears.
    if ~sum(numMito)
        firstFrame = firstFrame+1;
        continue
    end
end

```

```

%Get the nearest neighbor distances based on intensity weighted centroids
    and based on extrema.

NN{frameNum} = getNN(mito{frameNum});
NNExtrema{frameNum} = getNNExtrema(mito{frameNum});

%Correct the angles of the mitochondria and assign NN, frame, and
    initiliaze other parameters.
for mitoNum = 1:numMito(frameNum)
    mito{frameNum}(mitoNum).MaxFeretAngle =
        angle0to180(180-mito{frameNum}(mitoNum).MaxFeretAngle);
    mito{frameNum}(mitoNum).NN = NN{frameNum}(mitoNum);
    mito{frameNum}(mitoNum).NNExtrema = NNExtrema{frameNum}(mitoNum);
    mito{frameNum}(mitoNum).frame = frameNum;
    mito{frameNum}(mitoNum).NPA = 0;
    mito{frameNum}(mitoNum).confident = 1;
    mito{frameNum}(mitoNum).lost = 0;
    mito{frameNum}(mitoNum).fission = 0;
    mito{frameNum}(mitoNum).fusion = 0;
    mito{frameNum}(mitoNum).label = mitoNum;
end

if firstUsableFrame
    firstUsableFrame = false;
    secondUsableFrame = true;

%Create a track from all mito in the first frame
    track = mito{frameNum};

%Keep track of mito center of mass in the first frame

```

```

binaryOG = true(size(ImOG(:,:,frameNum)));
labeledOG = logical(binaryOG);
CoMstats =
    regionprops(labeledOG,ImOG(:,:,frameNum),'WeightedCentroid');
mitoCoM(frameNum).centroid = CoMstats.WeightedCentroid;
mitoCoM(frameNum).x = CoMstats.WeightedCentroid(1);
mitoCoM(frameNum).y = CoMstats.WeightedCentroid(2);

continue
end

%Keep track of mito center of mass
binaryOG = true(size(ImOG(:,:,frameNum)));
labeledOG = logical(binaryOG);
CoMstats = regionprops(labeledOG,ImOG(:,:,frameNum),'WeightedCentroid');
mitoCoM(frameNum).centroid = CoMstats.WeightedCentroid;
mitoCoM(frameNum).x = CoMstats.WeightedCentroid(1);
mitoCoM(frameNum).y = CoMstats.WeightedCentroid(2);

%Get the costs for the cost matrix
distanceMatrix{frameNum} = getDistanceMatrix(mito{frameNum},track);
areaMatrix{frameNum} = getDeltaMatrix(mito{frameNum},track,'Area');
majAxMatrix{frameNum} =
    getDeltaMatrix(mito{frameNum},track,'MajorAxisLength');
minAxMatrix{frameNum} =
    getDeltaMatrix(mito{frameNum},track,'MinorAxisLength');
solMatrix{frameNum} = getDeltaMatrix(mito{frameNum},track,'Solidity');
periMatrix{frameNum} = getDeltaMatrix(mito{frameNum},track,'Perimeter');

```

```

intMatrix{frameNum} =
    getDeltaMatrix(mito{frameNum},track,'MeanIntensity');

%Get the search time threshold matrix
frameMatrix{frameNum} = getFrameMatrix(mito{frameNum},track);

%Threshold out distances if it surpasses the max velocity or search time
distanceMatrixThresholded{frameNum} = distanceMatrix{frameNum};

distanceMatrixThresholded{frameNum}(distanceMatrix{frameNum}>distThresh)
    = Inf;
distanceMatrixThresholded{frameNum}(frameMatrix{frameNum}>frameThresh) =
    Inf;

%Get number of possible assignments for each mito.
NPA{frameNum} = sum(~isinf(distanceMatrixThresholded{frameNum}),2);
for mitoNum = 1:numMito(frameNum)
    mito{frameNum}(mitoNum).NPA = NPA{frameNum}(mitoNum);
end

%Square the difference matrices
distanceMatrixSq{frameNum} = distanceMatrixThresholded{frameNum}.^2;
areaMatrixSq{frameNum} = areaMatrix{frameNum}.^2;
majAxMatrixSq{frameNum} = majAxMatrix{frameNum}.^2;
minAxMatrixSq{frameNum} = minAxMatrix{frameNum}.^2;
solMatrixSq{frameNum} = solMatrix{frameNum}.^2;
periMatrixSq{frameNum} = majAxMatrix{frameNum}.^2;
intMatrixSq{frameNum} = intMatrix{frameNum}.^2;

```

```

solMatrixSq{frameNum}(isinf(solMatrixSq{frameNum})) =
    max(solMatrixSq{frameNum}(~isinf(solMatrixSq{frameNum})));
solMatrixSq{frameNum}(isnan(solMatrixSq{frameNum})) =
    max(solMatrixSq{frameNum}(~isnan(solMatrixSq{frameNum})));

%Z-score of the difference matrices to normalize variables
distanceMatrixZ{frameNum} = distanceMatrixSq{frameNum};
areaMatrixZ{frameNum} = distanceMatrixSq{frameNum};
majAxMatrixZ{frameNum} = distanceMatrixSq{frameNum};
minAxMatrixZ{frameNum} = distanceMatrixSq{frameNum};
solMatrixZ{frameNum} = distanceMatrixSq{frameNum};
periMatrixZ{frameNum} = distanceMatrixSq{frameNum};
intMatrixZ{frameNum} = distanceMatrixSq{frameNum};

distanceMatrixZ{frameNum}(~isinf( distanceMatrixSq{frameNum})) = zscore(
    distanceMatrixSq{frameNum}(~isinf(
        distanceMatrixSq{frameNum})),0,'all');
areaMatrixZ{frameNum}(~isinf( distanceMatrixSq{frameNum})) = zscore(
    areaMatrixSq{frameNum}(~isinf( distanceMatrixSq{frameNum})),0,'all');
majAxMatrixZ{frameNum}(~isinf( distanceMatrixSq{frameNum})) = zscore(
    majAxMatrixSq{frameNum}(~isinf( distanceMatrixSq{frameNum})),0,'all');
minAxMatrixZ{frameNum}(~isinf( distanceMatrixSq{frameNum})) = zscore(
    minAxMatrixSq{frameNum}(~isinf( distanceMatrixSq{frameNum})),0,'all');
solMatrixZ{frameNum}(~isinf( distanceMatrixSq{frameNum})) = zscore(
    solMatrixSq{frameNum}(~isinf( distanceMatrixSq{frameNum})),0,'all');
periMatrixZ{frameNum}(~isinf( distanceMatrixSq{frameNum})) = zscore(
    periMatrixSq{frameNum}(~isinf( distanceMatrixSq{frameNum})),0,'all');
intMatrixZ{frameNum}(~isinf( distanceMatrixSq{frameNum})) = zscore(
    intMatrixSq{frameNum}(~isinf( distanceMatrixSq{frameNum})),0,'all');

```

```

%Create a cost matrix of the z-scores and append newTrackMatrix
differenceMatrix{frameNum} = distanceMatrixZ{frameNum} + (wArea *
    areaMatrixZ{frameNum}) + (wMajAx * majAxMatrixZ{frameNum}) + (wMinAx *
    minAxMatrixZ{frameNum}) + (wSol * solMatrixZ{frameNum}) + (wPeri *
    periMatrixZ{frameNum}) + (wInt * intMatrixZ{frameNum});
tempDifferenceMatrix = differenceMatrix{frameNum};
tempDifferenceMatrix(tempDifferenceMatrix==Inf) = nan;
if ~secondUsableFrame
    startCost = quantile(runningConfidentCosts,0.98,'all');
end
secondUsableFrame = false;
if isnan(startCost)
    startCost = 1;
end
newTrackMatrix = diag(ones(size(tempDifferenceMatrix,1),1))*startCost;
newTrackMatrix(newTrackMatrix==0) = Inf;

assignTrackMatrix{frameNum} = [differenceMatrix{frameNum},newTrackMatrix];

%Assign mitochondria to tracks
for assignCol = 1:size(assignTrackMatrix{frameNum},2)
    if ~sum(~isinf(assignTrackMatrix{frameNum}(:,assignCol))) ||
        ~sum(~isnan(assignTrackMatrix{frameNum}(:,assignCol)))
        assignTrackMatrix{frameNum}(:,assignCol) = 100;
    end
end
matchedTrack{frameNum} = matchpairs(assignTrackMatrix{frameNum},1e9);

```



```

%Find high confidence assignments, where minimum assignment value per row
    is the same as the cost matrix minimization assignment

[M,I] = min(assignTrackMatrix{frameNum},[],2);

[~,idx] = sort(matchedTrack{frameNum}(:,1));
sortedMatches = matchedTrack{frameNum}(idx,:);

confident{frameNum} = (sortedMatches(:,2) == I);
for mitoNum = 1:numMito(frameNum)
    mito{frameNum}(mitoNum).confident = confident{frameNum}(mitoNum);
end

allConfidentCosts = M(confident{frameNum});
nonNewConfidentCosts =
    allConfidentCosts(I(confident{frameNum})<length(track));
runningConfidentCosts = [runningConfidentCosts;nonNewConfidentCosts];
%add mito to tracks / make new tracks
tempTrack = track;
for matchNum = 1:length(matchedTrack{frameNum}(:,1))
    mitoMatch = sortedMatches(matchNum,1);
    trackMatch = sortedMatches(matchNum,2);
    if trackMatch <= length(tempTrack)
        track(trackMatch) =
            addToTrack(mito{frameNum}(mitoMatch),track(trackMatch));
    else %prepare to check for fission and create a new track
        newTrack = length(track)+1;
        track(newTrack) = mito{frameNum}(mitoMatch);
    end
end
end
end

```

```

%Get Dynamics of tracks

[mitoDynamics,~] = getDynamics(micronPerPixel,secondsPerFrame,track);

speedStats = getDynamicStats(mitoDynamics.speed);

angleStats = getDynamicStats(mitoDynamics.travelAngle);

%%%%%%%%%%%%%%%%%%%%%%%%%%%%%%%%%%%%%%%%%%%%%%%%%%%%%%%%%%%%%%%%%%%%%%%%%%%%%%
%%%%%%%%%%%%%%%%%%%%%%%%%%%%%%%%%%%%%%%%%%%%%%%%%%%%%%%%%%%%%%%%%%%%%%%%%%%%%%
%%%%%%%%%%%%%%%%%%%%%%%%%%%%%%%%%%%%%%%%%%%%%%%%%%%%%%%%%%%%%%%%%%%%%%%%%%%%%%

%%Clean Up Track Gaps

checkClean = 0;

tracktotal = length(track);

cleanNum = 0;

cleanCoV = 0.2;

run = 1;

while ~checkClean

    cleanNum = cleanNum+1;

    lostNum = 1;

    newNum = 1;

    for trackNum = 1:length(track)

        %

        if getappdata>Loading,'canceling')

            delete>Loading)

            break

        end

```

```

waitbar(trackNum/length(track),loading,sprintf('Cleaning track %d of
    %d.',trackNum,length(track)));
pause(.0002)
%

%Make a list of lost tracks
if (track(trackNum).frame(end) == max([track.frame]))
    continue
end
lostList(lostNum, :) = [trackNum, track(trackNum).frame(end),
    speedStats.mean(trackNum), speedStats.std(trackNum),
    speedStats.CoV(trackNum), angleStats.mean(trackNum),
    angleStats.std(trackNum), angleStats.CoV(trackNum)];
lostCoords(lostNum,:) =
    [trackNum,track(trackNum).WeightedCentroid(end-1),
    track(trackNum).WeightedCentroid(end)];
lostNum = lostNum+1;

%Make a list of new tracks
if (track(trackNum).frame(1) == firstFrame)
    continue
end
newList(newNum, :) = [trackNum, track(trackNum).frame(1),
    speedStats.mean(trackNum), speedStats.std(trackNum),
    speedStats.CoV(trackNum), angleStats.mean(trackNum),
    angleStats.std(trackNum), angleStats.CoV(trackNum)];
newCoords(newNum, :) = [trackNum,
    track(trackNum).WeightedCentroid(1),
    track(trackNum).WeightedCentroid(2)];

```

```

newNum = newNum+1;
end

if exist('newList') && exist('lostList') && sum(sum(~isnan(newList))) &&
sum(sum(~isnan(lostList)))
%Threshold based on search time
newLostFrameMatrix = zeros(size(newList,1),size(lostList,1));

for newTrackNum = 1:newNum-1
    newLostFrameMatrix(newTrackNum,:) =
        newList(newTrackNum,2)-lostList(:,2)';
end
newLostFrameMatrixHold = newLostFrameMatrix;
newLostFrameMatrix(newLostFrameMatrix<1) = Inf;
newLostFrameMatrix(newLostFrameMatrix>frameThresh) = Inf;

%Threshold based on maximum travel distance
newLostDistanceMatrix = inf(size(newList,1),size(lostList,1));

for newTrackNum = 1:newNum-1
    for lostTrackNum = 1:lostNum-1
        if isinf(newLostFrameMatrix(newTrackNum,lostTrackNum))
            continue
        end
        newLostDistanceMatrix(newTrackNum,lostTrackNum) =
            norm(newCoords(newTrackNum,2:3) -
                lostCoords(lostTrackNum,2:3));
    end
end
end

```

```

newLostDistanceMatrix(newLostDistanceMatrix>distThresh) = Inf;

for newTrackNum = 1:newNum-1
    holdRow = newLostDistanceMatrix(newTrackNum,:);
    if numel(holdRow(~isinf(holdRow)))==1 &&
        track(newList(newTrackNum,1)).NPA(1)==1
        newLostDistanceMatrix(newTrackNum,:) =
            newLostDistanceMatrix(newTrackNum,:)*1E-9;
    end
end

%Combine tracks and look at coefficient of variation
newLostCoVMatrix = inf(size(newList,1),size(lostList,1));

for newTrackNum = 1:newNum-1
    for lostTrackNum = 1:lostNum-1
        if isinf(newLostDistanceMatrix(newTrackNum,lostTrackNum))
            continue
        elseif newList(newTrackNum) == lostList(lostTrackNum)
            continue
        end

        tempTrack = addToTrack(track(newList(newTrackNum,1)),
            track(lostList(lostTrackNum,1)));

        tempDynamics =
            getDynamics(micronPerPixel,secondsPerFrame,tempTrack);
        tempDynamicsAngle = getDynamicStats(tempDynamics.travelAngle);

        tempCoVMean = mean([tempDynamicsAngle.CoV]);
    end
end

```

```

    if tempCoVMean == 0
        newLostCoVMatrix(newTrackNum,lostTrackNum) = Inf;
        continue
    end

    newLostCoVMatrix(newTrackNum,lostTrackNum) = tempCoVMean;
end

holdRow = newLostCoVMatrix(newTrackNum,:);
if numel(holdRow(~isinf(holdRow)))==1 &&
    track(newList(newTrackNum,1)).NPA(1)==1
    newLostCoVMatrix(newTrackNum,:) =
        newLostCoVMatrix(newTrackNum,:)*-100;
end
end

newLostDistanceMatrix(newLostCoVMatrix>cleanCoV) = Inf;

if numel(newLostCoVMatrix(~isinf(newLostCoVMatrix)))

    extra.newLostDistanceMatrix{cleanNum} = newLostDistanceMatrix;
    matchedGaps = matchpairs(newLostDistanceMatrix,distThresh);
    if numel(matchedGaps)

        %Assign tracks in descending order to avoid messing up indices
        [~,idx] = sort(matchedGaps(:,2),'descend'); % sort just the
            first column
    end
end

```

```

        sortedGaps = matchedGaps(idx,:); % sort the whole matrix using
            the sort indices
        for gapNum = 1:size(matchedGaps,1)
            newTrackGap = newList(sortedGaps(gapNum,1));
            lostTrackGap = lostList(sortedGaps(gapNum,2));
            track(lostTrackGap) =
                addToTrack(track(newTrackGap),track(lostTrackGap));
        end

        %Delete tracks in descending order to avoid messing up indices.
        removedTracks = sort(matchedGaps(:,1),'descend');
        for trackRemove = 1:length(removedTracks)
            track(newList(removedTracks(trackRemove))) = [];
        end
    end
end

end

trackCount(run) = tracktotal;
run = run+1;
if length(track) == tracktotal
    checkClean = 1;
else
    tracktotal = length(track);
end
end

%%%%%%%%%%%%%%%%%%%%%%%%%%%%%%%%%%%%%%%%%%%%%%%%%%%%%%%%%%%%%%%%%%%%%%%%
%%%%%%%%%%%%%%%%%%%%%%%%%%%%%%%%%%%%%%%%%%%%%%%%%%%%%%%%%%%%%%%%%%%%%%%%
%%%%%%%%%%%%%%%%%%%%%%%%%%%%%%%%%%%%%%%%%%%%%%%%%%%%%%%%%%%%%%%%%%%%%%%%

```

```

if nargin<9

    %%Fission
    numTracks = length(track);

    %Parameters
    if nargin > 7
        stdRangeFission = stdRange;
    else
        stdRangeFission = 1;
    end

    CVpercFission = 0.01;

    %Initialize
    fissionTrack =
        zeros(length(track)-length(mito{firstFrame}),length(track));
    extremaFission =
        inf(length(track)-length(mito{firstFrame}),length(track));
    fissionMatrix =
        zeros(length(track)-length(mito{firstFrame}),length(track));

    %Only check track after the first frame, since no fission can occur b4
    then
        newTrackIdx = ((length(mito{firstFrame}))+1):numTracks);

    %Check for fission
    for trackNum = 1:length(newTrackIdx)

```



```

%
if getappdata>Loading, 'canceling')
    delete>Loading)
    break
end

waitbar(trackNum/length(newTrackIdx),Loading,sprintf('Checking
    fission of new track %d of %d.',trackNum,length(newTrackIdx)));
pause(.0002)
%

fissionTrackFirst = zeros(frameThresh,length(track));
extremaFissionFirst = nan(frameThresh,length(track));

frameDifference = track(newTrackIdx(trackNum)).frame(1)-frameThresh;
frameCheck =
    (max(1,frameDifference):track(newTrackIdx(trackNum)).frame(1)-1);
for frameNum = 1:length(frameCheck)

    for checkTrack = 1:(newTrackIdx(trackNum)-1)
        if length(track(newTrackIdx(trackNum)).Area)>2 &&
            sum(track(checkTrack).frame==frameCheck(frameNum)) &&
            ~nnz(~track(newTrackIdx(trackNum)).confident) &&
            ~nnz(~track(checkTrack).confident)

            %Now check the extrema and assign a fission event to the
            %closest existing track that withstood thresholding
            extremaFissionFirst(frameNum,checkTrack) =
                getExtremaMatrixFission( track(newTrackIdx(trackNum)),
                    track(checkTrack), frameCheck(frameNum));
        end
    end
end

```

```

        %only check track which are within search time from fission
        event
        fissionTrackFirst(frameNum,checkTrack) = 1;
    end
end
end

%Can only undergo fission with tracks that have a value within the
%search time, this is our search threshold. The rows are the new
    tracks
%(index corresponds to values in newTrackIdx). The cols are the
%existing tracks. Anything above 0 is checked against the new track.
fissionTrack(trackNum,:) = sum(fissionTrackFirst);

extremaFission(trackNum,:) = nanmean(extremaFissionFirst);
extremaFission(isnan(extremaFission)) = Inf;

%Fission events must create a track that has the area of the old track
%before fission minus the area of the old track after fission, within
%one standard deviation and a coefficient of variance above 1.
[fissionMatrix(trackNum,:),fissionExtra(trackNum)] =
    checkFissionArea(newTrackIdx(trackNum), track, stdRangeFission,
    CVpercFission);

maskFission = ((fissionTrack>0).*fissionMatrix);
maskFission(maskFission == 0) = Inf;

extremaFissionThresholded = extremaFission.*maskFission;

```

```

        extremaFissionThresholded(extremaFissionThresholded>distThresh) = Inf;

end

% extremaFissionThresholded

%Assign fission

if ~isempty(newTrackIdx)
    [fissionMin,fissionIndex] = min(extremaFissionThresholded,[],2);
    for trackNum = 1:length(newTrackIdx)
        if ~isinf(fissionMin(trackNum))
            track(newTrackIdx(trackNum)).fission(1) =
                fissionIndex(trackNum);
        end
    end
end

end

%%%%%%%%%%%%%%%%%%%%%%%%%%%%%%%%%%%%%%%%%%%%%%%%%%%%%%%%%%%%%%%%%%%%%%%%%%%%%%
%%%%%%%%%%%%%%%%%%%%%%%%%%%%%%%%%%%%%%%%%%%%%%%%%%%%%%%%%%%%%%%%%%%%%%%%%%%%%%
%%%%%%%%%%%%%%%%%%%%%%%%%%%%%%%%%%%%%%%%%%%%%%%%%%%%%%%%%%%%%%%%%%%%%%%%%%%%%%
%%Fusion

%Parameters

if nargin > 7
    stdRangeFusion = stdRange;
else
    stdRangeFusion = 1;
end

CVpercFusion = 0.01;

```

```

lostTracks = zeros(1,numTracks);

lostTrackNum = 0;
for trackNum = 1:numTracks
    if track(trackNum).frame(end)~=numFrames
        lostTrackNum = lostTrackNum + 1;
        lostTracks(trackNum) = 1;
    end
end

%Initialize
fusionTrack = zeros(lostTrackNum,length(track));
extremaFusion = inf(lostTrackNum,length(track));
fusionMatrix = zeros(lostTrackNum,length(track));

lostTrackIdx = find(lostTracks);

%Check for fusion
for trackNum = 1:length(lostTrackIdx)

    %
    if getappdata>Loading,'canceling')
        delete>Loading)
        break
    end

    waitbar(trackNum/length(lostTrackIdx),Loading,sprintf('Checking
        fusion of lost track %d of %d.',trackNum,length(lostTrackIdx)));
    pause(.0002)

    %

```

```

fusionTrackFirst = zeros(frameThresh,length(track));
extremaFusionFirst = nan(frameThresh,length(track));

frameDifference = frameThresh+
    track(lostTrackIdx(trackNum)).frame(end);
frameCheck = (track(lostTrackIdx(trackNum)).frame(end) + 1 :
    min(frameDifference,numFrames));

for frameNum = 1:length(frameCheck)
    for checkTrack = (lostTrackIdx(trackNum)+1):length(track)
        if length(track(lostTrackIdx(trackNum)).Area)>2 &&
            sum(track(checkTrack).frame==frameCheck(frameNum)) &&
            ~nnz(~track(lostTrackIdx(trackNum)).confident) &&
            ~nnz(~track(checkTrack).confident)
            %Now check the extrema and assign a fission event to the
            %closest existing track that withstood thresholding
            extremaFusionFirst(frameNum,checkTrack) =
                getExtremaMatrixFusion( track(lostTrackIdx(trackNum)),
                track(checkTrack), frameCheck(frameNum));

            %only check track which are within search time from fission
            event
            fusionTrackFirst(frameNum,checkTrack) = 1;
        end
    end
end

%Can only undergo fusion with tracks that have a value within the

```

```

%search time, this is our search threshold. The rows are the lost
    tracks

%(index corresponds to values in lostTrackIdx). The cols are the
%existing tracks. Anything above 0 is checked against the lost track.
fusionTrack(trackNum,:) = sum(fusionTrackFirst);

extremaFusion(trackNum,:) = nanmean(extremaFusionFirst);
extremaFusion(isnan(extremaFusion)) = Inf;

%Fusion events must lose a track that has the area of the fused track
%after fusion plus the area of the fused track before fission, within
%one standard deviation and a coefficient of variance above 1.
[fusionMatrix(trackNum,:),fusionExtra(trackNum)] =
    checkFusionArea(lostTrackIdx(trackNum), track, stdRangeFusion,
    CVpercFusion);

maskFusion = ((fusionTrack>0).*fusionMatrix);
maskFusion(maskFusion == 0) = Inf;

extremaFusionThresholded = extremaFusion.*maskFusion;
extremaFusionThresholded(extremaFusionThresholded>distThresh) = Inf;

end

%Assign fission
if ~isempty(lostTrackIdx)
    [fusionMin,fusionIndex] = min(extremaFusionThresholded,[],2);

```

```

        for trackNum = 1:length(lostTrackIdx)
            if ~isinf(fusionMin(trackNum))
                track(lostTrackIdx(trackNum)).fusion(end) =
                    fusionIndex(trackNum);
            end
        end
    end
end

extra.fissionTrack = fissionTrack;
extra.extremaFission = extremaFission;
extra.fissionMatrix = fissionMatrix;
if ~isempty(newTrackIdx)
    extra.fissionExtra = fissionExtra;
    extra.fissionMin = fissionMin;
    extra.fissionIndex = fissionIndex;
    extra.newTrackIndex = newTrackIdx;
end

extra.fusionTrack = fusionTrack;
extra.extremaFusion = extremaFusion;
extra.fusionMatrix = fusionMatrix;
if ~isempty(lostTrackIdx)
    extra.fusionExtra = fusionExtra;
    extra.fusionMin = fusionMin;
    extra.fusionIndex = fusionIndex;
    extra.lostTrackIndex = lostTrackIdx;
end
end
end

```

```

for trackNum = 1:length(track)

    track(trackNum).MajorAxisLength =

        track(trackNum).MajorAxisLength*micronPerPixel;

    track(trackNum).MinorAxisLength =

        track(trackNum).MinorAxisLength*micronPerPixel;

    track(trackNum).Perimeter = track(trackNum).Perimeter*micronPerPixel;

    track(trackNum).Area = track(trackNum).Area*micronPerPixel^2;

end

%%%%%%%%%%%%%%%%%%%%%%%%%%%%%%%%%%%%%%%%%%%%%%%%%%%%%%%%%%%%%%%%%%%%%%%%%%%%%%
%%%%%%%%%%%%%%%%%%%%%%%%%%%%%%%%%%%%%%%%%%%%%%%%%%%%%%%%%%%%%%%%%%%%%%%%%%%%%%
%%%%%%%%%%%%%%%%%%%%%%%%%%%%%%%%%%%%%%%%%%%%%%%%%%%%%%%%%%%%%%%%%%%%%%%%%%%%%%

extra.CC = CC;

extra.L = L;

extra.mito = mito;

extra.numMito = numMito;

extra.NN = NN;

extra.NNExtrema = NNExtrema;

extra.distanceMatrix = distanceMatrix;

extra.areaMatrix = areaMatrix;

extra.majAxMatrix = majAxMatrix;

extra.minAxMatrix = minAxMatrix;

extra.solMatrix = solMatrix;

extra.periMatrix = periMatrix;

extra.intMatrix = intMatrix;

extra.frameMatrix = frameMatrix;

extra.NPA = NPA;

extra.distanceMatrixThresholded = distanceMatrixThresholded;

extra.distanceMatrixSq = distanceMatrixSq;

```



```

extra.areaMatrixSq = areaMatrixSq;
extra.majAxMatrixSq = majAxMatrixSq;
extra.minAxMatrixSq = minAxMatrixSq;
extra.solMatrixSq = solMatrixSq;
extra.periMatrixSq = periMatrixSq;
extra.intMatrixSq = intMatrixSq;
extra.distanceMatrixZ = distanceMatrixZ;
extra.areaMatrixZ = areaMatrixZ;
extra.majAxMatrixZ = majAxMatrixZ;
extra.minAxMatrixZ = minAxMatrixZ;
extra.solMatrixZ = solMatrixZ;
extra.periMatrixZ = periMatrixZ;
extra.intMatrixZ = intMatrixZ;
extra.differenceMatrix = differenceMatrix;
extra.assignTrackMatrix = assignTrackMatrix;
extra.matchedTrack = matchedTrack;
extra.confident = confident;
delete>Loading)
end

```

---

## D.4.2 getDistanceMatrix.m

---

```

function distanceMatrix = getDistanceMatrix(mito,track)

numMito = length(mito);
numTracks = length(track);

%initialize

```

```

xTrack = zeros(1,numMito);
yTrack = zeros(1,numMito);
xDiff = zeros(numMito,numTracks);
yDiff = zeros(numMito,numTracks);

for mitoNum = 1:numMito
    xTrack(mitoNum) = mito(mitoNum).WeightedCentroid(1);
    yTrack(mitoNum) = mito(mitoNum).WeightedCentroid(2);
end

for trackNum = 1:numTracks
    xDiff(:,trackNum) = xTrack'-track(trackNum).WeightedCentroid(end,1);
    yDiff(:,trackNum) = yTrack'-track(trackNum).WeightedCentroid(end,2);
end

distanceMatrix = sqrt((xDiff.^2)+(yDiff.^2));
end

```

---

### D.4.3 getDeltaMatrix.m

---

```

function deltaMatrix = getDeltaMatrix(mito,track,field)

numMito = length(mito);
numTracks = length(track);

%initialize
deltaMatrix = zeros(numMito,numTracks);

deltaMito = [mito.(field)];

```

```

%we simply take the difference in the feature's value between the current
%time frame's mitochondria to those of existing tracks (e.g. the difference
%in surface area) divided by the existing track's value, producing a
%normalized difference.

for trackNum = 1:numTracks
    deltaMatrix(:,trackNum) = (deltaMito' - track(trackNum).(field)(end)) ./
        (track(trackNum).(field)(end));
end
end

```

---

## D.5 Determining maximum search time threshold

The maximum search time threshold is the maximum number of temporal frames between which a mitochondrion can be assigned to an unassigned track. To determine this threshold, we analyze mitochondrial tracks of three independent TMRM-labelled MDA-MB-231 cells at varying search time thresholds. As expected, we find that as we increase the search time threshold, the percentage of optimal mitochondrial tracks increases while the mean speed of mitochondrial tracks and the total number of tracks decreases (Fig. D.4a-c). These results indicate setting a higher search time threshold will give more reliable results. We note, however, that after a certain search time threshold, the change in these parameters is minimal. As reducing the search time threshold is beneficial for increasing run time efficiency, we quantify the lack of significant change in parameters by calculating the Wilcoxon rank sum test p-value of the mean speeds of mitochondrial tracks of adjacent search time thresholds. We find that above a search time threshold of 6 frames, the p-value surpasses 0.05, though it reaches a more stable value after a search time threshold of 20 frames, equivalent to  $\frac{1}{6}$  of the total frames (Fig. D.4d). Therefore, we recommend using the default search time

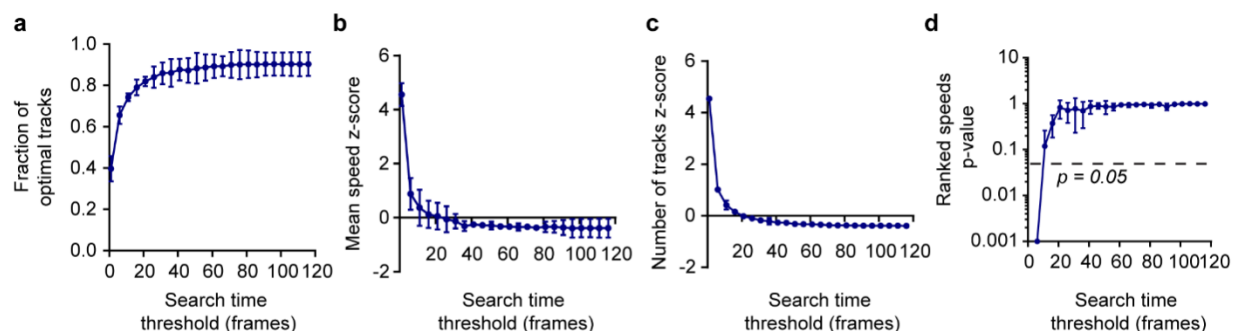


Figure D.4: Effect of search time threshold on variation in resulting mitochondrial tracks. The fraction of total resulting mitochondrial tracks comprised of optimal tracks (a), the z-score normalized mean speed of mitochondrial tracks (b), and the z-score normalized total number of mitochondrial tracks (b) as a function of the search time threshold. d, The p-value of a two-sided Wilcoxon test between the ranked mean speeds of all mitochondrial tracks in the corresponding search time threshold and the previous search time threshold. Points below 0.001 are rounded to 0.001. Data are presented as means with 95% confidence intervals. n=3 cells.

threshold encompassing all frames, but at a minimum using  $\frac{1}{6}$  of the total frames if a higher computational efficiency is required.

## D.6 Optimize feature weighting

The weighting of each mitochondrial morphological feature depends on the coefficient of variation (CoV) within confident tracks and between confident tracks. A confident track is a track made up entirely of confident assignments. If a morphological feature changes greatly within the confident tracks, it will have a lesser weighting, whereas if it varies greatly between confident tracks, it will have a greater weighting. For each individual confident track, we calculate the CoV of each feature within that track, the intraCoV.

$$intraCoV_{i,F} = \frac{\sigma_{i,F}}{\mu_{i,F}} \quad (D.4)$$

Where " $\sigma_{i,F}$ " is the standard deviation of feature F of confident track i, " $\mu_{i,F}$ " is the mean of feature F of confident track i, and "intraCoV<sub>i,F</sub>" is the intraCoV of feature F of confident track i. We also build a vector of mean values for each feature of each confident track. We then calculate the CoV of each feature for all tracks, the interCoV.

$$interCoV_F = \frac{\bar{\sigma}_F}{\bar{\mu}_F} \quad (D.5)$$

Where " $\sigma_F$ " is the standard deviation of the mean values of feature F for all confident tracks, " $\mu_F$ " is the mean of the mean values of feature F for all confident tracks, and "interCoV<sub>F</sub>" is the interCoV of feature F. We then weight each feature as the ratio of the interCoV to the mean intraCoV and normalize each weight by the sum of the weights to produce a final sum weighting of 1.

$$w_F = interCoV_F : \overline{intraCoV_F} \quad (D.6)$$

$$w'_F = \frac{w_F}{\sum w} \quad (\text{D.7})$$

Where “ $w_F$ ” is the pre-normalized weighting for feature F and “ $w'_F$ ” is the normalized weighting for feature F.

### D.6.1 getTrackingWeights.m

---

```
function [weights,allPerfectTracks,perfectTrackIdx] = getTrackingWeights(track)

    perfectTrack = zeros(1,length(track));

    for trackNum = 1:length(track)

        if sum(track(trackNum).confident)==length(track(trackNum).confident) &&
            length(track(trackNum).frame)>1
            perfectTrack(trackNum) = 1;
        end
    end

    perfectTrackIdx = find(perfectTrack);
    allPerfectTracks = track(find(perfectTrack));

    %Initialize
    meanArea = zeros(1,length(allPerfectTracks));
    meanMajorAxis = zeros(1,length(allPerfectTracks));
    meanMinorAxis = zeros(1,length(allPerfectTracks));
    meanSolidity = zeros(1,length(allPerfectTracks));
    meanPeri = zeros(1,length(allPerfectTracks));
    meanMeanIntensity = zeros(1,length(allPerfectTracks));
```

```

intraAreaCoV = zeros(1,length(allPerfectTracks));
intraMajAxCoV = zeros(1,length(allPerfectTracks));
intraMinAxCoV = zeros(1,length(allPerfectTracks));
intraSolCoV = zeros(1,length(allPerfectTracks));
intraPeriCoV = zeros(1,length(allPerfectTracks));
intraMeanIntCoV = zeros(1,length(allPerfectTracks));

for trackNum = 1:length(allPerfectTracks)
    meanArea(trackNum) = mean(allPerfectTracks(trackNum).Area);
    meanMajorAxis(trackNum) =
        mean(allPerfectTracks(trackNum).MajorAxisLength);
    meanMinorAxis(trackNum) =
        mean(allPerfectTracks(trackNum).MinorAxisLength);
    meanSolidity(trackNum) = mean(allPerfectTracks(trackNum).Solidity);
    meanPeri(trackNum) = mean(allPerfectTracks(trackNum).Perimeter);
    meanMeanIntensity(trackNum) =
        mean(allPerfectTracks(trackNum).MeanIntensity);

    intraAreaCoV(trackNum) = std(allPerfectTracks(trackNum).Area)
        /mean(allPerfectTracks(trackNum).Area);
    intraMajAxCoV(trackNum) = std(allPerfectTracks(trackNum).MajorAxisLength)
        /mean(allPerfectTracks(trackNum).MajorAxisLength);
    intraMinAxCoV(trackNum) = std(allPerfectTracks(trackNum).MinorAxisLength)
        /mean(allPerfectTracks(trackNum).MinorAxisLength);
    intraSolCoV(trackNum) = std(allPerfectTracks(trackNum).Solidity)
        /mean(allPerfectTracks(trackNum).Solidity);
    intraPeriCoV(trackNum) = std(allPerfectTracks(trackNum).Perimeter)
        /mean(allPerfectTracks(trackNum).Perimeter);

```



```

        intraMeanIntCoV(trackNum) = std(allPerfectTracks(trackNum).MeanIntensity)
            /mean(allPerfectTracks(trackNum).MeanIntensity);
end

interAreaCoV = nanstd(meanArea(:))/nanmean(meanArea(:));
interMajAxCoV = nanstd(meanMajorAxis(:))/nanmean(meanMajorAxis(:));
interMinAxCoV = nanstd(meanMinorAxis(:))/nanmean(meanMinorAxis(:));
interSolCoV = nanstd(meanSolidity(:))/nanmean(meanSolidity(:));
interPeriCoV = nanstd(meanPeri(:))/nanmean(meanPeri(:));
interMeanIntCoV = nanstd(meanMeanIntensity(:))/nanmean(meanMeanIntensity(:));

avIntraAreaCoV = nanmean(intraAreaCoV);
avIntraMajAxCoV = nanmean(intraMajAxCoV);
avIntraMinAxCoV = nanmean(intraMinAxCoV);
avIntraSolCoV = nanmean(intraSolCoV);
avIntraPeriCoV = nanmean(intraPeriCoV);
avIntraMeanIntCoV = nanmean(intraMeanIntCoV);

areaWeight = interAreaCoV/avIntraAreaCoV;
majAxWeight = interMajAxCoV/avIntraMajAxCoV;
minAxWeight = interMinAxCoV/avIntraMinAxCoV;
solWeight = interSolCoV/avIntraSolCoV;
periWeight = interPeriCoV/avIntraPeriCoV;
meanIntWeight = interMeanIntCoV/avIntraMeanIntCoV;

sumWeights =
    areaWeight+majAxWeight+minAxWeight+solWeight+periWeight+meanIntWeight;

areaWeightNorm = areaWeight/sumWeights;

```

```
majAxWeightNorm = majAxWeight/sumWeights;  
minAxWeightNorm = minAxWeight/sumWeights;  
solWeightNorm = solWeight/sumWeights;  
periWeightNorm = periWeight/sumWeights;  
meanIntWeightNorm = meanIntWeight/sumWeights;  
  
weights = [areaWeightNorm, majAxWeightNorm, minAxWeightNorm, solWeightNorm,  
           periWeightNorm, meanIntWeightNorm];  
end
```

---

## D.7 Gap closing (trackMitochondria.m)

As our algorithm stabilizes the cost of new track creation towards an average value, mitochondria that travel in an outlying manner, such as those being quickly and directionally transported, intrinsically have a higher probability to mistakenly be assigned to new tracks. The gap closing scheme serves to better reconstruct accurate tracks by combining probable tracks that have been newly formed with tracks that have been lost within the search time and maximum velocity thresholds. Two scenarios arise for gap closing.

1. Only one new track and one lost track are within the thresholds. In this case, the tracks are combined.
2. Multiple new and/or lost tracks are within the thresholds. In this case, we define a probable connection as a nearby new and lost track whose combined travel angle produces a final CoV of less than 10%. In the case of 3D, the mean CoV of the xy, xz, and yz travel angles are used.

$$CoV_{\theta_{xy},i} = \frac{\sigma_{\theta_{xy},i}}{\mu_{\theta_{xy},i}}, \quad CoV_{\theta_{yz},i} = \frac{\sigma_{\theta_{yz},i}}{\mu_{\theta_{yz},i}}, \quad CoV_{\theta_{xz},i} = \frac{\sigma_{\theta_{xz},i}}{\mu_{\theta_{xz},i}} \quad (D.8)$$

$$CoV_{\theta_f,i} = \frac{1}{3} * (CoV_{\theta_{xy},i} + CoV_{\theta_{yz},i} + CoV_{\theta_{xz},i}) \quad (D.9)$$

Where “ $\sigma_{\theta_{xy},i}$ ,  $\sigma_{\theta_{yz},i}$ ,  $\sigma_{\theta_{xz},i}$ ” are the standard deviations of the xy, yz, xz travel angles for combined new and lost track i, “ $\mu_{\theta_{xy},i}$ ,  $\mu_{\theta_{yz},i}$ ,  $\mu_{\theta_{xz},i}$ ” are the mean values of the xy, yz, xz travel angles for the combined new and lost track i, and “ $CoV_{\theta_{xy}}$ ,” “ $CoV_{\theta_{yz}}$ ,” “ $CoV_{\theta_{xz}}$ ,” “ $CoV_{\theta_f,i}$ ” are the xy, yz, xz and final coefficients of variation for the travel angles of the combined new and lost track i.

Any combined tracks with a final travel angle CoV less than 10% are considered possible candidates for gap closure. All possible candidates between new and lost tracks are added to a cost matrix whose costs are the weighted centroid distances between the new track's starting position and the lost track's ending position. The final combinations are assigned to globally minimize the cost matrix. This entire process is repeated until the final number of tracks remains constant.

## D.8 Fission and fusion

Fission event classification is strict to ensure a low false positive rate. A new track is only classified as having arisen due to fission if it has at least 2 tracked frames post-fission and it must be a confident track. Additionally, only confident tracks with at least 2 tracked frames are checked as possible candidates from which it has fissioned. It must, of course, also meet the search time and maximum velocity thresholds.

In the case of fission and fusion, we calculate the maximum velocity thresholds for extrema distances, rather than intensity weighted centroid distances. We begin by calculating the extrema distances between all new tracks and existing tracks within the search time threshold. To reduce computational complexity in 2D we sample only 8 points for comparison: the top, top-left, top-right, right, left, bottom-left, bottom-right, and bottom-most points of each mitochondrion. To reduce computational complexity in 3D we sample only the points which make up the convex hull of the mitochondrion.

Those fission candidates who meet all the aforementioned requirements are then analyzed for volume differences. Specifically, the fission candidate's mean volume after the new track's first time frame and the new track's mean volume are summed together and subtracted from the fission candidate's mean volume before the new track's first time frame. If the absolute value of the resulting volume is within one standard deviation of the square root of the sum squared standard deviations of the post, pre, and new tracks' mean volumes, and the product of the coefficients of variation of the post, pre, and new tracks is less than 1%, the candidate is retained.

$$\Delta V = |\bar{V}_{pre} - \bar{V}_{post} + \bar{V}_{new}| \quad (\text{D.10})$$

$$\sigma_f = \sqrt{\sigma_{pre}^2 + \sigma_{post}^2 + \sigma_{new}^2} \quad (D.11)$$

$$CoV_f = CoV_{pre} * CoV_{post} * CoV_{new} \quad (D.12)$$

Where “ $V_{pre}$ ”, “ $V_{post}$ ”, “ $V_{new}$ ”, “ $\sigma_{pre}$ ”, “ $\sigma_{post}$ ”, “ $\sigma_{new}$ ”, and “ $CoV_{pre}$ ”, “ $CoV_{post}$ ”, “ $CoV_{new}$ ” are the mean volumes, standard deviations, and coefficients of variation for the fission candidate before and after the new track’s first frame, and for the new track, respectively. Candidate is retained if

$$\Delta V < \sigma_f \text{ and } CoV_f < 0.01$$

The new track is then assigned as having undergone fission with the candidate with the closest extrema distance. Unlike track assignments and gap closures, multiple new tracks can be assigned to a single candidate.

The process for fusion event classification is similar, and equally strict to ensure a low false positive rate. A lost track is only classified as having disappeared due to fusion if it has at least 2 tracked frames pre-fusion and it must be a confident track. Additionally, only confident tracks with at least 2 tracked frames are checked as possible fusion candidates. It must, of course, also meet search time and maximum velocity thresholds.

Those fusion candidates who meet all the aforementioned requirements are then analyzed for volume differences. Specifically, the fusion candidate’s mean volume before the lost track’s last time frame and the lost track’s mean volume are summed together and subtracted from the fusion candidate’s mean volume after the lost track’s last time frame. If the absolute value of the resulting volume is within one standard deviation of the square root of the

sum squared standard deviations of the post, pre, and new tracks' mean volumes, and the product of the coefficients of variation of the post, pre, and new tracks is less than 1%, the candidate is retained.

$$\Delta V = |\bar{V}_{post} - \bar{V}_{pre} + \bar{V}_{lost}| \quad (D.13)$$

$$\sigma_f = \sqrt{\sigma_{post}^2 + \sigma_{pre}^2 + \sigma_{lost}^2} \quad (D.14)$$

$$CoV_f = CoV_{post} * CoV_{pre} * CoV_{lost} \quad (D.15)$$

Where “ $V_{post}$ ”, “ $V_{pre}$ ”, “ $V_{lost}$ ”, “ $\sigma_{post}$ ”, “ $\sigma_{pre}$ ”, “ $\sigma_{lost}$ ”, and “ $CoV_{post}$ ”, “ $CoV_{pre}$ ”, “ $CoV_{lost}$ ” are the mean volumes, standard deviations, and coefficients of variation for the fission candidate after and before the lost track's last frame, and for the lost track, respectively. Candidate is retained if

$$\Delta V < \sigma_f \text{ and } CoV_f < 0.01$$

The lost track is then assigned as having fused with the candidate with the closest extrema distance. Again, unlike track assignments and gap closures, multiple lost tracks can be assigned to a single candidate.

### D.8.1 getExtremaMatrixFission.m

---

```
function extremaMatrix = getExtremaMatrixFission(newTrack, track, frameNum)

numTracks = length(track);
```

```

%initialize
extremaMatrix = zeros(1,numTracks);

for trackNum = 1:numTracks
    frameIdx = find(track(trackNum).frame==frameNum);
    if ~frameIdx
        extremaMatrix(1,trackNum) = Inf;
    else
        xExtrema = track(trackNum).Extrema(:,frameIdx*2-1);
        yExtrema = track(trackNum).Extrema(:,frameIdx*2);
        DistMatX = inf(size(track(trackNum).Extrema,1),
            size(newTrack.Extrema,1));
        DistMatY = inf(size(track(trackNum).Extrema,1),
            size(newTrack.Extrema,1));
        for newExtremaNum = 1:size(newTrack.Extrema,1)
            DistMatX(:,newExtremaNum) = xExtrema -
                newTrack.Extrema(newExtremaNum,1);
            DistMatY(:,newExtremaNum) = yExtrema -
                newTrack.Extrema(newExtremaNum,2);
        end
        DistMat = sqrt(DistMatX.^2+DistMatY.^2);

        extremaMatrix(1,trackNum) = min(DistMat,[],'all');
    end
end
end

```

---



## D.8.2 getExtremaMatrixFusion.m

---

```
function extremaMatrix = getExtremaMatrixFusion(lostTrack,track,frameNum)

numTracks = length(track);

%initialize
extremaMatrix = zeros(1,numTracks);
for trackNum = 1:numTracks
    frameIdx = find(track(trackNum).frame==frameNum);
    if ~frameIdx
        extremaMatrix(1,trackNum) = Inf;
    else
        xExtrema = track(trackNum).Extrema(:,frameIdx*2-1);
        yExtrema = track(trackNum).Extrema(:,frameIdx*2);
        DistMatX = inf(size(track(trackNum).Extrema,1),
            size(lostTrack.Extrema,1));
        DistMatY = inf(size(track(trackNum).Extrema,1),
            size(lostTrack.Extrema,1));
        for lostExtremaNum = 1:size(lostTrack.Extrema,1)
            DistMatX(:,lostExtremaNum) = xExtrema -
                lostTrack.Extrema(lostExtremaNum,1);
            DistMatY(:,lostExtremaNum) = yExtrema -
                lostTrack.Extrema(lostExtremaNum,2);
        end
        DistMat = sqrt(DistMatX.^2+DistMatY.^2);

        extremaMatrix(1,trackNum) = min(DistMat,[],'all');
    end
end
```

```
end  
end
```

---

### D.8.3 checkFissionArea.m

---

```
function [fissionMatrix, extra] =  
    checkFissionArea(newTrackNum, track, stdRange, CVperc)  
    numTracks = length(track);  
  
    %Initialize  
    preArea = inf(1, numTracks);  
    postArea = inf(1, numTracks);  
    newArea = inf(1, numTracks);  
    preStd = inf(1, numTracks);  
    postStd = inf(1, numTracks);  
    newStd = inf(1, numTracks);  
  
    newTrack = track(newTrackNum);  
  
    for trackNum = 1:numTracks  
        frameMax = newTrack.frame(1);  
        if sum(track(trackNum).frame < frameMax) &&  
            sum(track(trackNum).frame >= frameMax)  
            index = find(track(trackNum).frame < frameMax);  
        else  
            continue  
        end
```

```

prefission = track(trackNum).Area(1:index(end));
postfission = track(trackNum).Area(index(end)+1:end);

if nnz(~track(trackNum).confident(1:index(end))) ||
    nnz(~track(trackNum).confident(index(end)+1:end)) ||
    length(prefission) < 2 || length(postfission) < 2
    continue
end

preArea(trackNum) = nanmean(track(trackNum).Area(1:index(end)));
postArea(trackNum) = nanmean(track(trackNum).Area(index(end)+1:end));
newArea(trackNum) = nanmean(newTrack.Area);

preStd(trackNum) = nanstd(track(trackNum).Area(1:index(end)));
postStd(trackNum) = nanstd(track(trackNum).Area(index(end)+1:end));
newStd(trackNum) = nanstd(newTrack.Area);
end

areaDiff = abs(preArea-(postArea+newArea));
stdTotal = sqrt(preStd.^2+postStd.^2+newStd.^2);
coeffVarMatrixPost = postStd./postArea;
coeffVarMatrixPre = preStd./preArea;
coeffVarMatrixNew = newStd./newArea;
coeffVarMatrix = coeffVarMatrixPost.*coeffVarMatrixPre.*coeffVarMatrixNew;
coeffVarMatrix(isnan(coeffVarMatrix)) = Inf;
possibleFissionMatrix = areaDiff<(stdTotal*stdRange);
fissionMatrix = possibleFissionMatrix.*(coeffVarMatrix<CVperc);
fissionMatrix(isnan(fissionMatrix)) = 0;

```

```

extra.preArea = preArea;
extra.postArea = postArea;
extra.newArea = newArea;
extra.preStd = preStd;
extra.postStd = postStd;
extra.newStd = newStd;
extra.areaDiff = areaDiff;
extra.stdTotal = stdTotal;
extra.coeffVarMatrixPost = coeffVarMatrixPost;
extra.coeffVarMatrixPre = coeffVarMatrixPre;
extra.coeffVarMatrixNew = coeffVarMatrixNew;
extra.coeffVarMatrix = coeffVarMatrix;
extra.possibleFissionMatrix = possibleFissionMatrix;
extra.fissionMatrix = fissionMatrix;

end

```

---

## D.8.4 checkFusionArea.m

---

```

function [fusionMatrix,extra] =
    checkFusionArea(lostTrackNum,track,stdRange,CVperc)

numTracks = length(track);

%Initialize
preArea = inf(1,numTracks);
postArea = inf(1,numTracks);
lostArea = inf(1,numTracks);
preStd = inf(1,numTracks);
postStd = inf(1,numTracks);

```

```

lostStd = inf(1,numTracks);

lostTrack = track(lostTrackNum);

for trackNum = 1:numTracks
    frameMin = lostTrack.frame(end);
    if sum(track(trackNum).frame>frameMin) &&
        sum(track(trackNum).frame<=frameMin)
        index = find(track(trackNum).frame>frameMin);
    else
        continue
    end

    prefusion = track(trackNum).Area(1:index(1)-1);
    postfusion = track(trackNum).Area(index(1):end);

    if nnz(~track(trackNum).confident(1:index(1)-1)) ||
        nnz(~track(trackNum).confident(index(1):end)) || length(prefusion) < 2
        || length(postfusion) < 2
        continue
    end

    preArea(trackNum) = nanmean(prefusion);
    postArea(trackNum) = nanmean(postfusion);
    lostArea(trackNum) = nanmean(lostTrack.Area);

    preStd(trackNum) = nanstd(track(trackNum).Area(1:index(1)-1));
    postStd(trackNum) = nanstd(track(trackNum).Area(index(1):end));
    lostStd(trackNum) = nanstd(lostTrack.Area);
end

```

```

areaDiff = abs(postArea-(preArea+lostArea));
stdTotal = sqrt(preStd.^2+postStd.^2+lostStd.^2);
coeffVarMatrixPost = postStd./postArea;
coeffVarMatrixPre = preStd./preArea;
coeffVarMatrixLost = lostStd./lostArea;
coeffVarMatrix = coeffVarMatrixPost.*coeffVarMatrixPre.*coeffVarMatrixLost;
coeffVarMatrix(isnan(coeffVarMatrix)) = Inf;
possibleFusionMatrix = areaDiff<(stdTotal*stdRange);
fusionMatrix = possibleFusionMatrix.*(coeffVarMatrix<CVperc);
fusionMatrix(isnan(fusionMatrix)) = 0;

extra.preArea = preArea;
extra.postArea = postArea;
extra.lostArea = lostArea;
extra.preStd = preStd;
extra.postStd = postStd;
extra.lostStd = lostStd;
extra.areaDiff = areaDiff;
extra.stdTotal = stdTotal;
extra.coeffVarMatrixPost = coeffVarMatrixPost;
extra.coeffVarMatrixPre = coeffVarMatrixPre;
extra.coeffVarMatrixLost = coeffVarMatrixLost;
extra.coeffVarMatrix = coeffVarMatrix;
extra.possibleFusionMatrix = possibleFusionMatrix;
extra.fusionMatrix = fusionMatrix;

```

end

---

## D.9 Simulation of artificial mitochondria (generateMitochondria.m, generateMitoMovement.m)

We simulate mitochondria by generating rectangles with parameters derived from mitochondrial morphological parameters of MDA-MB-231 cells labelled with MitoTracker DeepRed and from randomly generated values:

1. A lognormal distribution is fit to the cells' mitochondrial major axis lengths, resulting in a log mean of  $0.518344 \mu\text{m}$  and a log standard deviation of  $0.336479 \mu\text{m}$ , with maximum and minimum log values of  $1.4885 \mu\text{m}$  and  $-0.0990 \mu\text{m}$  (Fig. D.5a).
2. The cells' median mitochondrial minor axis length value of  $1.1555 \mu\text{m}$  divided by 2 is used as the simulated minor axis length (Fig. D.5b).
3. The initial position of the mitochondria is randomly selected by a uniform distribution within  $[(\text{Frame Size})/3, \text{Frame Size}-(\text{Frame Size})/3]$ .
4. Mitochondria are randomly rotated by a uniform distribution between  $[0, \pi]$ .
5. Mitochondria 8-bit intensities are randomly generated by a normal distribution of 100 with a standard deviation of 1.

We also simulate artificial mitochondrial motion, based both on parameters derived from mitochondrial motility parameters of MDA-MB-231 cells labelled with MitoTracker DeepRed and from randomly generated values:

1. We first iterate randomly through the list of existing mitochondria which neither disappeared nor fused with another mitochondrion.
2. We give the mitochondrion a chance to disappear.

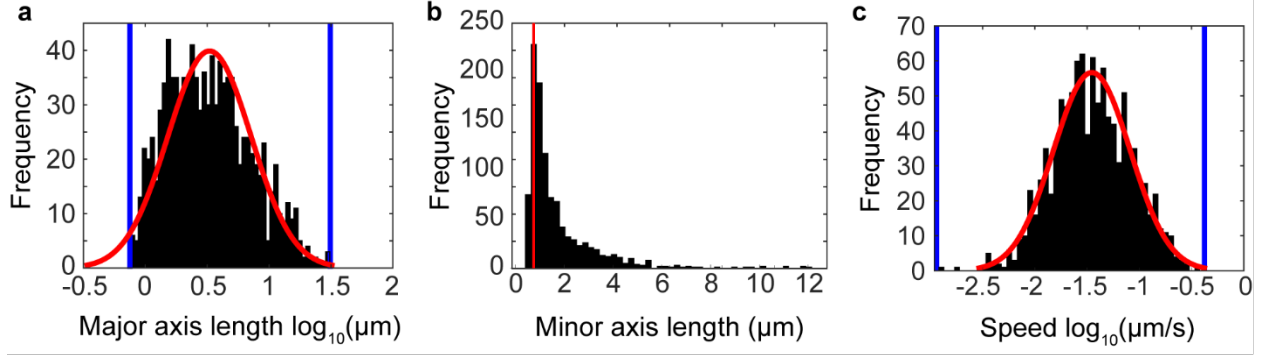


Figure D.5: Experimental parameters used for simulation generation. MDA-MB-231 cells labelled with MitoTracker DeepRed and its distribution (black bars) of major axis lengths with a lognormal fit (red line) and min and max values (blue lines) (a), the minor axis lengths with its median value divided by 2 (red line) (b), and speed with a lognormal fit (red line) and min and max values (blue lines) (c).

3. If the mitochondrion did not disappear, we generate a speed from a lognormal distribution fit to the experimental cells' mitochondrial speed data, resulting in a log mean of  $-1.45484 \mu\text{m/s}$ , a log standard deviation of  $0.367769 \mu\text{m/s}$ , and a minimum and maximum log speed value of  $-2.9010 \mu\text{m/s}$  and  $-0.4621 \mu\text{m/s}$ , respectively (Fig. D.5c).
4. The mitochondria are directionally displaced in the direction of their maximum Feret angle, with a 22.39% chance to move backwards, which is derived from the median directionality value of the experimental cells.
5. The mitochondrion is then rotated from a normal distribution with its maximum Feret angle as the mean, and a standard deviation of 1 degree multiplied by the seconds between frames.
6. The mitochondrion's intensity value is regenerated via a normal distribution with its previous frames' intensity as the mean, and a standard deviation of 0.1.

In the case where fusion is possible:

1. A list of overlapping mitochondria is generated.



2. Any overlapping mitochondria are given a chance to fuse together if they meet the following criteria:
  - (a) The two mitochondria did not overlap in the first frame.
  - (b) Neither mitochondrion has already undergone fusion.
  - (c) The sum of the two mitochondrial major axes do not exceed the maximum log value of  $1.4885 \mu\text{m}$ .
3. If the two mitochondria meet the aforementioned criteria:
  - (a) The two major axis lengths are summed and used as the mean to generate the new mitochondrion's major axis length from a normal distribution with a standard deviation of 0.1.
  - (b) The mean value of the two intensity weighted centroid positions is used to generate the new mitochondrion's weighted centroid position.

In the case where fission is possible:

1. Mitochondria are given the chance to undergo fission if they meet the following criteria:
  - (a) The mitochondrion has not already undergone fission or fusion.
  - (b) The mitochondrion is not lost.
  - (c) The mitochondrion's major axis length divided by 2 is greater than its minor axis length.
2. If the mitochondrion meets the aforementioned criteria:
  - (a) A new mitochondrion is generated with a major axis length generated from a uniform distribution between of the minor axis length and half the major axis length of the mitochondrion from which it fissioned.

- (b) The major axis length of the mitochondrion from which it fissioned is reduced by the major axis length of the new mitochondrion.
- (c) The new mitochondrion's centroid is placed at the old mitochondrion's centroid plus a displacement of the new mitochondrion's major axis multiplied by 2.
- (d) The old mitochondrion's centroid is placed at the old mitochondrion's centroid minus the sum of its generated travel distance and the new and old mitochondria's major axis lengths.

### D.9.1 generateMitochondria.m

---

```
function [mitoIm,mitoSim] = generateMitochondria(numMito, imageSize,
micronPerPixel, frameNum, lengthMultiplier, intensityMultiplier)

im = ones(imageSize,imageSize);

mainFig = figure;
set(mainFig, 'MenuBar', 'none')
set(mainFig, 'ToolBar', 'none')

mitoIm = zeros(imageSize,imageSize,numMito,'uint8');
for mitoNum = 1:numMito

    imshow(im)

    axis image off

    hold on

    %generate Major Axis Length from lognormal distribution

    mu = 0.518344;

    sigma = 0.336479;
```

```

MajAxlog = normrnd(mu,sigma);
while MajAxlog > 1.4885 || MajAxlog < -0.0990
    MajAxlog = normrnd(mu,sigma);
end

%Major axis from the log normal distribution above
a = 10^MajAxlog/micronPerPixel/4*lengthMultiplier;

%Minor axis is the median of control values
%Override minorAxis
b = 1.1555/micronPerPixel/4;

%random initial position (constrained)
x0 = unifrnd(imageSize/3,imageSize-imageSize/3);
y0 = unifrnd(imageSize/3,imageSize-imageSize/3);

%rotate mitochondrion
rotate = -unifrnd(0,pi)-(pi/2);

%fill in the mitochondria and plot them.
drawMito([x0,y0],a*2,b*2,rotate)

%Make the plot into an image.
ax = gca;
ax.Units = 'pixels';
pos = ax.Position;
rect = [pos(1),pos(2),pos(3),pos(4)];
f = getframe(gcf,rect);
[X,~] = frame2im(f);

```

```

%inverse colors for tracking.
tempMitoIm = 1-X(:,:,1);

%override Intensity
intensity = normrnd(100,1);

mitoIm(:,:,mitoNum) = tempMitoIm*intensity;

%get mito properties (will be slightly different than generated and
%plotted stats)
CCSim = bwconncomp(mitoIm(:,:,mitoNum));
mito = regionprops(CCSim,mitoIm(:,:,mitoNum), 'Area', 'Centroid',
    'Eccentricity', 'MaxFeretProperties', 'Extrema', 'MeanIntensity',
    'WeightedCentroid', 'MajorAxisLength', 'MinorAxisLength', 'Perimeter',
    'PixelIdxList');

%Correct the angles of the mitochondria and assign NN, frame, and
%initiliaze other parameters.
mito.MaxFeretAngle = angle0to180(180-mito.MaxFeretAngle);
mito.NN =0;
mito.NNExtrema = 0;
mito.frame = frameNum;
mito.NPA = 0;
mito.confident = 1;
mito.lost = 0;
mito.fission = 0;
mito.fusion = 0;
mito.a = a;

```

```

    mito.b = b;
    mito.rotate = rotate;
    mito.intensity = intensity;
    mito.trueCoords = [x0,y0];
    mito.overlap1 = 0;

    if numMito == 1
        mitoSim = mito;
    else
        mitoSim(mitoNum) = mito;
    end

    hold off

end

close

end

```

---

## D.9.2 generateMitoMovement.m

---

```

function [newMitoIm,newMito] = generateMitoMovement(mito, frameSize,
    micronPerPixel, secondsPerFrame, frameNum, speedMultiplier, lostChance,
    fusionChance, fissionChance)

    im = ones(frameSize,frameSize);

    mainFig = figure;
    set(mainFig, 'MenuBar', 'none')
    set(mainFig, 'Toolbar', 'none')

```

```

newMitoIm = zeros(frameSize,frameSize,length(mito),'uint8');

newMito = mito;

travelDistanceAll = zeros(1,length(mito));

randMitoList = (1:length(mito));
randMitoList = randMitoList(randperm(length(randMitoList))));

for mitoNum = randMitoList
    %skip if already disappeared or fused
    imshow(im)
    axis image off
    hold on

    if mito(mitoNum).lost(end) || mito(mitoNum).fusion(end)

        continue
    end

    %Chance to disappear
    if rand<lostChance
        mito(mitoNum).lost(end) = 1;
        newMito(mitoNum).lost(end) = 1;
        continue
    end

    %generate speed from log normal distribution

```

```

mu = -1.45484;
sigma = 0.367769;
travelDistanceLog = normrnd(mu,sigma);
while (travelDistanceLog < -2.9010) || (travelDistanceLog > -0.4621)
    travelDistanceLog = normrnd(mu,sigma);
end

travelDistance =
    10^travelDistanceLog*secondsPerFrame/micronPerPixel*speedMultiplier;
%chance for backwards movement
if rand < 0.2239
    travelDistance = -travelDistance;
end
travelDistanceAll(mitoNum) = travelDistance;

%rotate mitochondrion
rotate = normrnd(mito(mitoNum).rotate(end),deg2rad(1)*secondsPerFrame);

%move mitochondrion in direction of rotation
newX = mito(mitoNum).trueCoords(1)+travelDistance*cos(rotate);
newY = mito(mitoNum).trueCoords(2)+travelDistance*sin(rotate);

%fill in the mitochondria and plot them.
drawMito([newX,newY], normrnd(mito(mitoNum).a*2,0.1),
    normrnd(mito(mitoNum).b*2,0.1), rotate)

%Make the plot into an image.
ax = gca;
ax.Units = 'pixels';

```

```

pos = ax.Position;
rect = [pos(1),pos(2),pos(3),pos(4)];
f = getframe(gcf,rect);
[X,~] = frame2im(f);

%inverse colors for tracking.
tempMitoIm = 1-X(:,:,1);
newMitoIm(:,:,mitoNum) = tempMitoIm*normrnd(mito(mitoNum).intensity,0.1);

%get mito properties (will be slightly different than generated and
%plotted stats)
CCNew = bwconncomp(newMitoIm(:,:,mitoNum));
newMitoTemp = regionprops(CCNew, newMitoIm(:,:,mitoNum), 'Area',
    'Centroid', 'Eccentricity', 'MaxFeretProperties', 'Extrema',
    'MeanIntensity', 'WeightedCentroid', 'MajorAxisLength',
    'MinorAxisLength', 'Perimeter', 'PixelIdxList');

%Correct the angles of the mitochondria and assign NN, frame, and
%initiliaze other parameters.
newMitoTemp.MaxFeretAngle = angle0to180(180-newMitoTemp.MaxFeretAngle);
newMitoTemp.NN =0;
newMitoTemp.NNExtrema = 0;
newMitoTemp.frame = frameNum;
newMitoTemp.NPA = 0;
newMitoTemp.confident = 1;
newMitoTemp.lost = 0;
newMitoTemp.fission = 0;
newMitoTemp.fusion = mito(mitoNum).fusion;
newMitoTemp.a = mito(mitoNum).a;

```



```

newMitoTemp.b = mito(mitoNum).b;
newMitoTemp.rotate = rotate;
newMitoTemp.intensity = mito(mitoNum).intensity;
newMitoTemp.trueCoords = [newX,newY];
newMitoTemp.overlap1 = mito(mitoNum).overlap1(end);

newMito(mitoNum) = newMitoTemp;

hold off
end

overlap = zeros(length(newMito),length(newMito));

%check if there is overlap
for mitoNum = 1:length(newMito)
    if mito(mitoNum).lost(end) || mito(mitoNum).fusion(end)
        continue
    end
    for overlapCheck = mitoNum:length(newMito)
        if overlapCheck == mitoNum
            continue
        end
        overlap(mitoNum,overlapCheck) =
            sum(ismember(mito(mitoNum).PixelIdxList,
                mito(overlapCheck).PixelIdxList));
    end
end

%chance for fusion if there is overlap

```

```

for mitoNum = randMitoList

    if mito(mitoNum).lost(end) || mito(mitoNum).fusion(end)

        continue

    end

    if ~nnz(overlap(mitoNum,:))

        continue

    end

    for overlapNum = find(overlap(mitoNum,:))

        if mito(mitoNum).overlap1 == 1 || ~overlap(mitoNum,overlapNum) ||

            sum(mito(mitoNum).fusion) || sum(mito(overlapNum).fusion) ||

            sum(mito(overlapNum).fusion)

            continue

        end

        if mito(overlapNum).lost(end)

            continue

        end

        if mito(mitoNum).frame(end) == 1

            mito(overlapNum).overlap1(:) = 1;

            newMito(overlapNum).overlap1 = 1;

            mito(mitoNum).overlap1(:) = 1;

            newMito(mitoNum).overlap1 = 1;

            continue

        end

        temp = rand;

        if temp < fusionChance && ~newMito(mitoNum).fusion(end) &&

            ~newMito(overlapNum).fusion(end) && ~mito(overlapNum).fusion(end)

            && ~mito(mitoNum).fusion(end) &&

```

```

(newMito(mitoNum).a+newMito(overlapNum).a)<111.5812 %max mito
length

imshow(im)

axis image off

hold on

newMito(mitoNum) = mito(mitoNum);
newMito(mitoNum).fusion(end) = overlapNum;
overlap(mitoNum,:) = 0;
overlap(:,overlapNum) = 0;
newMitoIm(:,:,mitoNum) = zeros(frameSize,frameSize);

newMito(overlapNum) =
    simulateFusion(newMito(mitoNum),newMito(overlapNum));

newX = newMito(overlapNum).trueCoords(1);
newY = newMito(overlapNum).trueCoords(2);
%fill in the mitochondria and plot them.
drawMito([newX,newY], normrnd(newMito(overlapNum).a*2,0.1),
    normrnd(newMito(overlapNum).b*2,0.1),
    newMito(overlapNum).rotate)

%Make the plot into an image.
ax = gca;
ax.Units = 'pixels';
pos = ax.Position;
rect = [pos(1),pos(2),pos(3),pos(4)];
f = getframe(gcf,rect);

```

```

[X,~] = frame2im(f);

%inverse colors for tracking.
tempMitoIm = 1-X(:,:,1);
newMitoIm(:,:,overlapNum) =
    tempMitoIm*normrnd(newMito(overlapNum).intensity,0.1);

%get mito properties (will be slightly different than generated and
%plotted stats)
CCNew = bwconncomp(newMitoIm(:,:,overlapNum));
newMitoTemp = regionprops(CCNew, newMitoIm(:, :, overlapNum),
    'Area', 'Centroid', 'Eccentricity', 'MaxFeretProperties',
    'Extrema', 'MeanIntensity', 'WeightedCentroid',
    'MajorAxisLength', 'MinorAxisLength', 'Perimeter',
    'PixelIdxList');

%Correct the angles of the mitochondria and assign NN, frame, and
%initiliaze other parameters.
newMitoTemp.MaxFeretAngle =
    angle0to180(180-newMitoTemp.MaxFeretAngle);
newMitoTemp.NN = newMito(overlapNum).NN;
newMitoTemp.NNExtrema = newMito(overlapNum).NNExtrema;
newMitoTemp.frame = newMito(overlapNum).frame;
newMitoTemp.NPA = newMito(overlapNum).NPA;
newMitoTemp.confident = 1;
newMitoTemp.lost = newMito(overlapNum).lost;
newMitoTemp.fission = newMito(overlapNum).fission;
newMitoTemp.fusion = newMito(overlapNum).fusion;
newMitoTemp.a = newMito(overlapNum).a;

```

```

        newMitoTemp.b = newMito(overlapNum).b;
        newMitoTemp.rotate = newMito(overlapNum).rotate;
        newMitoTemp.intensity = newMito(overlapNum).intensity;
        newMitoTemp.trueCoords = [newX,newY];
        newMitoTemp.overlap1 = mito(mitoNum).overlap1;
        newMito(overlapNum) = newMitoTemp;

        hold off

        continue

    end

end

end

%chance to undergo fission
for mitoNum = randMitoList
    if mito(mitoNum).lost(end) || mito(mitoNum).fusion(end)
        continue
    end
    if frameNum < 3
        continue
    end
    if rand>=fissionChance || newMito(mitoNum).fission ||
        newMito(mitoNum).lost || newMito(mitoNum).a/2<newMito(mitoNum).b
        continue
    end

    imshow(im)
    axis image off
    hold on

```

```

fissionMito = newMito(mitoNum);

fissionMito.a = unifrnd(newMito(mitoNum).b,newMito(mitoNum).a/2);

newMito(mitoNum).a = newMito(mitoNum).a-fissionMito.a;

oldX = newMito(mitoNum).trueCoords(1) +(fissionMito.a*2)
    *cos(newMito(mitoNum).rotate);

oldY = newMito(mitoNum).trueCoords(2) +(fissionMito.a*2)
    *sin(newMito(mitoNum).rotate);

newX = fissionMito.trueCoords(1) -(travelDistanceAll(mitoNum)
    +newMito(mitoNum).a +fissionMito.a) *cos(newMito(mitoNum).rotate);

newY = fissionMito.trueCoords(2) -(travelDistanceAll(mitoNum)
    +newMito(mitoNum).a +fissionMito.a) *sin(newMito(mitoNum).rotate);

fissionMitoIm = zeros(frameSize,frameSize);

%fill in the mitochondria and plot them.
drawMito([newX,newY],normrnd(fissionMito.a*2,0.1),
    normrnd(fissionMito.b*2,0.1), fissionMito.rotate)

%Make the plot into an image.
ax = gca;
ax.Units = 'pixels';
pos = ax.Position;
rect = [pos(1),pos(2),pos(3),pos(4)];
f = getframe(gcf,rect);
[X,~] = frame2im(f);

%inverse colors for tracking.
tempMitoIm = 1-X(:,:,1);

```

```

fissionMitoIm(:, :) = tempMitoIm*normrnd(fissionMito.intensity,0.1);

hold off

imshow(im)

axis image off

hold on

%fill in the mitochondria and plot them.

drawMito([oldX,oldY],normrnd(newMito(mitoNum).a*2,0.1),

    normrnd(newMito(mitoNum).b*2,0.1), newMito(mitoNum).rotate)

%Make the plot into an image.

ax = gca;

ax.Units = 'pixels';

pos = ax.Position;

rect = [pos(1),pos(2),pos(3),pos(4)];

f = getframe(gcf,rect);

[X,~] = frame2im(f);

%inverse colors for tracking.

tempMitoIm = 1-X(:, :, 1);

newMitoIm(:, :, mitoNum) =

    tempMitoIm*normrnd(newMito(mitoNum).intensity,0.1);

%get mito properties (will be slightly different than generated and

%plotted stats)

CCNew = bwconncomp(fissionMitoIm(:, :));

newMitoTemp = regionprops(CCNew,fissionMitoIm(:, :), 'Area', 'Centroid',

    'Eccentricity', 'MaxFerretProperties', 'Extrema', 'MeanIntensity',

```

```

        'WeightedCentroid', 'MajorAxisLength', 'MinorAxisLength', 'Perimeter',
        'PixelIdxList');

CCOld = bwconncomp(newMitoIm(:,:,mitoNum));
oldMitoTemp = regionprops(CCOld, newMitoIm(:, :, mitoNum), 'Area',
    'Centroid', 'Eccentricity', 'MaxFeretProperties', 'Extrema',
    'MeanIntensity', 'WeightedCentroid', 'MajorAxisLength',
    'MinorAxisLength', 'Perimeter', 'PixelIdxList');

%Correct the angles of the mitochondria and assign NN, frame, and
%initiliaze other parameters.
newMitoTemp.MaxFeretAngle = angle0to180(180-newMitoTemp.MaxFeretAngle);
newMitoTemp.NN =0;
newMitoTemp.NNExtrema = 0;
newMitoTemp.frame = frameNum;
newMitoTemp.NPA = 0;
newMitoTemp.confident = 1;
newMitoTemp.lost = 0;
newMitoTemp.fission = mitoNum;
newMitoTemp.fusion = 0;
newMitoTemp.a = fissionMito.a;
newMitoTemp.b = fissionMito.b;
newMitoTemp.rotate = fissionMito.rotate;
newMitoTemp.intensity = fissionMito.intensity;
newMitoTemp.trueCoords = [newX,newY];
newMitoTemp.overlap1 = fissionMito.overlap1;

numMitoTotal = length(newMito);
newMito(numMitoTotal+1) = newMitoTemp;

```



```

newMitoIm(:,:,numMitoTotal+1) = fissionMitoIm;

%Correct the angles of the mitochondria and assign NN, frame, and
%initiliaze other parameters.

oldMitoTemp.MaxFerretAngle = angle0to180(180-oldMitoTemp.MaxFerretAngle);
oldMitoTemp.NN = newMito(mitoNum).NN;
oldMitoTemp.NNExtrema = newMito(mitoNum).NNExtrema;
oldMitoTemp.frame = frameNum;
oldMitoTemp.NPA = newMito(mitoNum).NPA;
oldMitoTemp.confident = newMito(mitoNum).confident;
oldMitoTemp.lost = newMito(mitoNum).lost;
oldMitoTemp.fission = newMito(mitoNum).fission;
oldMitoTemp.fusion = newMito(mitoNum).fusion;
oldMitoTemp.a = newMito(mitoNum).a;
oldMitoTemp.b = newMito(mitoNum).b;
oldMitoTemp.rotate = newMito(mitoNum).rotate;
oldMitoTemp.intensity = newMito(mitoNum).intensity;
oldMitoTemp.trueCoords = [oldX,oldY];
oldMitoTemp.overlap1 = newMito(mitoNum).overlap1;

newMito(mitoNum) = oldMitoTemp;

hold off

end

end

```

---

## D.10 Abbreviated data for each cell type

	<b>Model</b>	<b>Cancerous</b>	<b>ER/PR+</b>	<b>Age</b>	<b>Gender</b>	<b>Black/White</b>
<b>MCF-10A</b>	Cell line	No	+	36	F	W
<b>Patient 72</b>	Mammoplasty	No	+	46	F	W
<b>Patient 76</b>	Mammoplasty	No	+	25	F	B
<b>Patient 08</b>	Mammoplasty	No	+	18	F	W
<b>Patient 99</b>	Mammoplasty	No	+	36	F	W
<b>Patient 97</b>	Mammoplasty	No	+	25	F	B
<b>MCF-7</b>	Cell line	Yes	+	69	F	W
<b>T-47D</b>	Cell line	Yes	+	54	F	N/A
<b>MDA-MB-231</b>	Cell line	Yes	-	51	F	W
<b>MDA-MB-468</b>	Cell line	Yes	-	51	F	B
<b>BT-549</b>	Cell line	Yes	-	72	F	W
<b>HCI-010</b>	PDX	Yes	-	N/A	F	N/A
<b>HCI-002</b>	PDX	Yes	-	N/A	F	N/A

Figure D.6: Abbreviated data for each cell type.

## D.11 Examples of mitochondria motility and morphology features

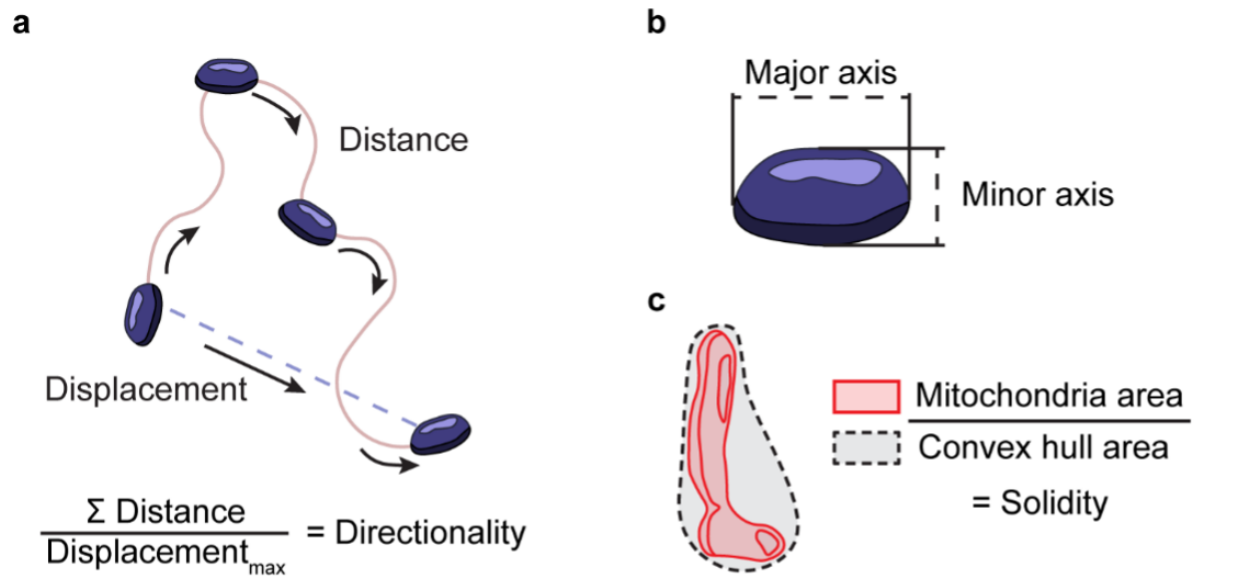


Figure D.7: **a**, The directionality of a mitochondrion is defined as the total distance traveled divided by the maximum displacement of the track. Using the maximum rather than final eliminates considering retrograde and anterograde motion. **b**, The major and minor axis of a mitochondrion is defined as the major and minor axis of an ellipse, respectively, with the same normalized second central moment as the mitochondrial component. **c**, The solidity of a mitochondrion is defined as the total mitochondrion's area divided by the area of the convex hull, which is the smallest convex polygon that can contain the region.

## D.12 Morpho and motility metrics of mitochondria of individual cell lines in 2D and 3D

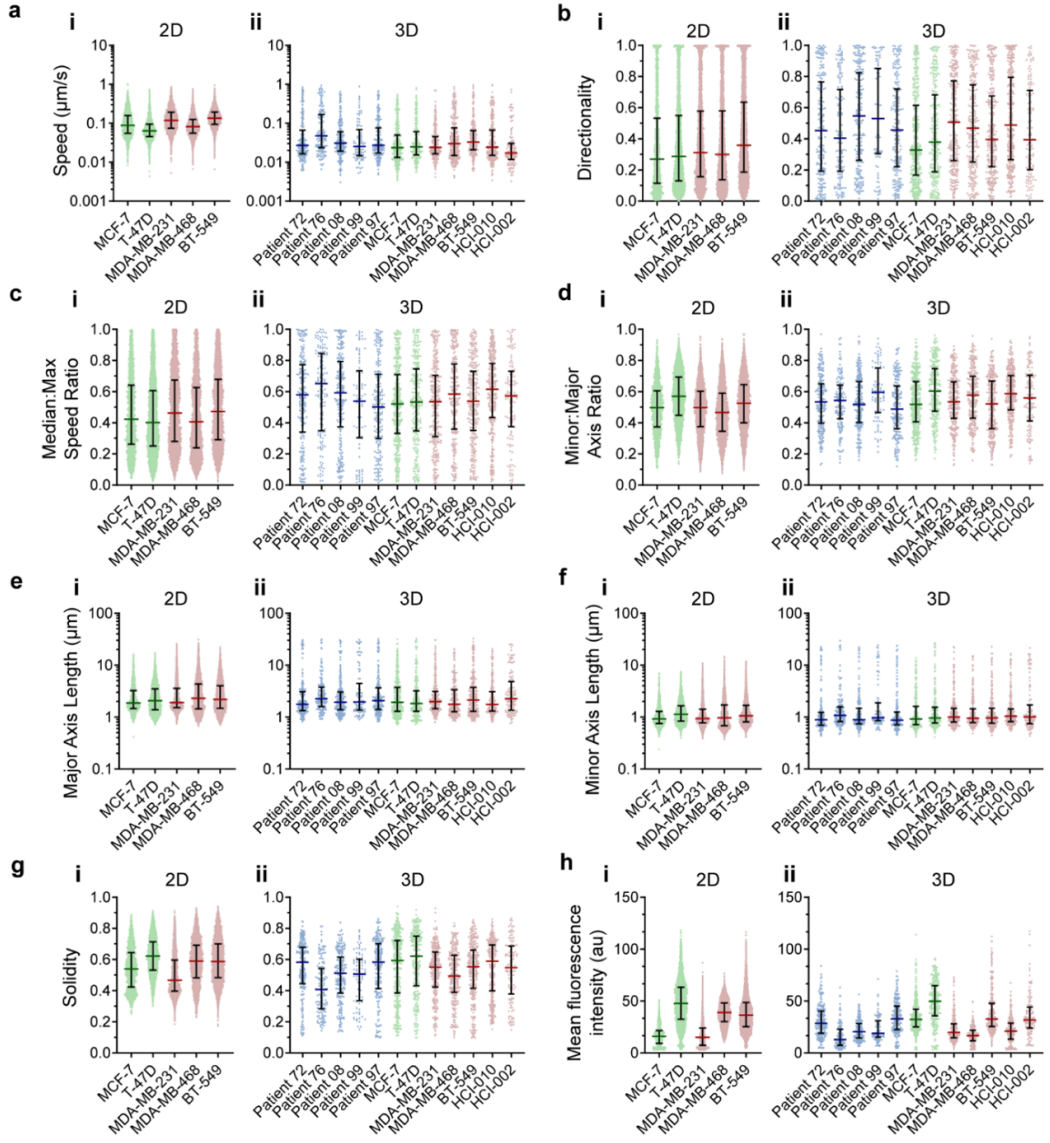


Figure D.8: Distributions of mitochondrial speed (a), directionality (b), median:max speed ratio (c), minor:major axis ratio (d), major axis length (e), minor axis length (f), solidity (g), and mean fluorescence intensity (h) in 2D (i) and 3D (ii) culture conditions.  $n=2191$ , 5874, 4168, 4561, and 6293 distinct mitochondrial tracks for MCF-7, T-47D, MDA-MB-231, MDA-MB-468, and BT-549 in 2D cultures, respectively.  $n=207$ , 147, 223, 87, 204, 410, 261, 292, 267, 298, 338, and 124 distinct mitochondrial tracks for patients 72, 76, 08, 99, 97, MCF-7, T-47D, MDA-MB-231, MDA-MB-468, BT-549, HCI-010, and HCI-002 in 3D cultures, respectively. Data are median  $\pm$  interquartile ranges.

## D.13 An example of a random forest classifier with N decision trees

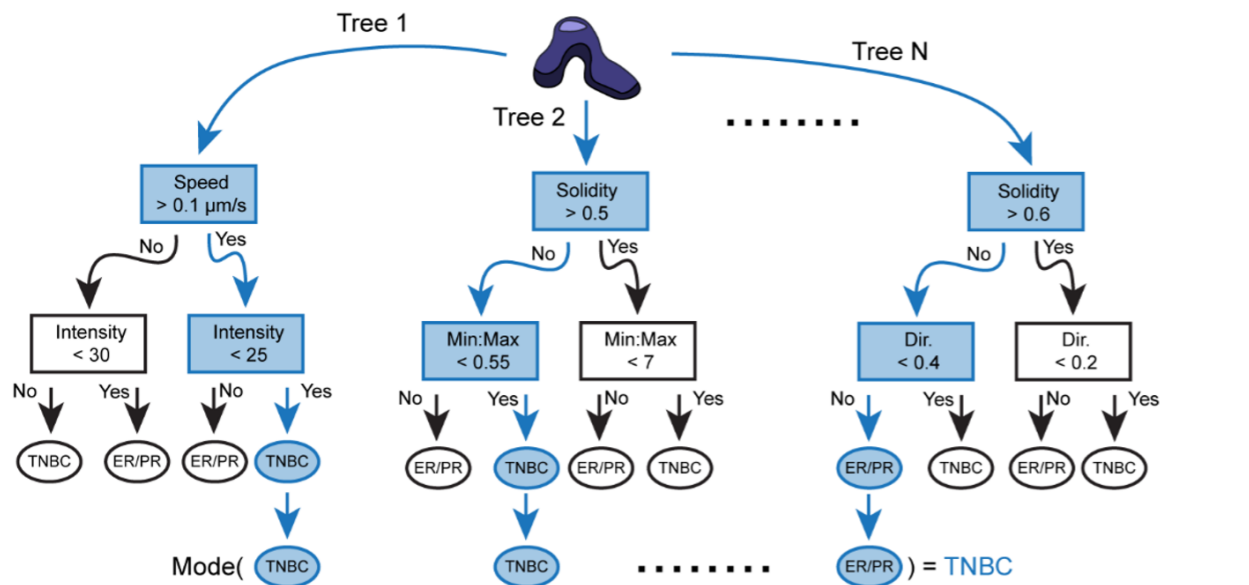


Figure D.9: Each tree in this example is made of two nodes. Decision tree 1 splits classification on speed and intensity, tree 2 on solidity and min:max speed ratio, and tree N on solidity and directionality. In this example the mitochondrion has a speed above  $0.1 \mu\text{m/s}$  and an intensity below 25, so tree 1 classifies it as coming from a TNBC cell. The mitochondrion also has a solidity below 0.5 and min:max speed ratio below 0.55, so tree 2 classifies it as coming from a TNBC cell. The mitochondrion also has a directionality below 0.4, so tree N classifies it as coming from an ER/PR+ cell. The mode of the classifications of all trees is taken as the final classification. In this case, the random forest classifies the mitochondrion as coming from a TNBC cell.

## D.14 Random forest parameters

Features	Morphology	Motility	Both
<b>Min:Max Axis Ratio</b>	+	-	+
<b>Solidity</b>	+	-	+
<b>Mean Intensity</b>	+	-	+
<b>Median Speed</b>	-	+	+
<b>Med:Max Speed Ratio</b>	-	+	+
<b>Directionality</b>	-	+	+
<b>2D AUC</b>	0.68	0.63	0.77
<b>3D AUC</b>	0.77	0.55	0.80

Figure D.10: Inputs for random forest classification of cancer subtype

Parameter Name	Value
<b>n_estimators</b>	300
<b>criterion</b>	"gini"
<b>max_depth</b>	None
<b>min_samples_split</b>	2
<b>min_samples_leaf</b>	1
<b>min_weight_fraction_leaf</b>	0
<b>max_features</b>	sqrt(n_features)
<b>max_leaf_nodes</b>	None
<b>min_impurity_decrease</b>	0
<b>min_impurity_split</b>	None
<b>bootstrap</b>	TRUE
<b>oob_score</b>	FALSE
<b>n_jobs</b>	None
<b>random_state</b>	None
<b>verbose</b>	0
<b>warm_start</b>	FALSE
<b>class_weight</b>	None
<b>ccp_alpha</b>	0
<b>max_samples</b>	None

Figure D.11: Scikit-learn random forest hyperparameters

## D.15 Object-based FLIM of NADH

Traditionally, FLIM of NADH requires a pixel-wise averaging of many frames of fluorescence data, as the quantum yield of NADH is quite low. In the case of highly dynamic mitochondria, the averaged pixels include lifetime data of the cytoplasm/nucleus if the mitochondrion moves out of that pixel. Because our tracking method is object-based it provides a list of pixel indices of which each mitochondrion occupies. Using these indices, rather than pixel-wise frame averaging, we build a list of phase and modulation values of Fourier transformed photon arrival times for each mitochondrion, whose averages lie within the universal circle.